SYNTHESIS, CHARACTERIZATION AND REACTIVITY OF TRANSITION METAL CONTAINING ZEOLITES

by

Joseph A. Rossin

Dissertation submitted to the Faculty of the

Virginia Polytechnic Institute and State University

in partial fulfillment of the requirements for the degree of

DOCTOR OF PHILOSOPHY

in

Chemical Engineering

APPROVED:

M. E. Davis, Chairman

G. Gibbs

B. Hanson

A. Squires

G. Wills

May 4, 1986

Blacksburg, Virginia

SYNTHESIS, CHARACTERIZATION AND REACTIVITY OF TRANSITION METAL CONTAINING ZEOLITES

by

Joseph A. Rossin

Committee Chairman: Mark E. Davis
Chemical Engineering

(ABSTRACT)

Transition metal containing zeolites (zeolite A and ZSM-5) were prepared by addition of various transition metal containing substrates to zeolite synthesis gels. Crystal growth data were recorded in order to determine the influence of the transition metal species on the rate of crystal growth. X-ray diffraction, oxygen adsorption, FTIR and SEM were utilized to evaluate crystal purity. X-ray photoelectron spectroscopy (XPS), chemical analysis and electron microprobe analysis were performed in order to ascertain the position (intrazeolitic versus surface) and homogeneity of the transition metal. It was concluded that intrazeolitic transition metals were produced by the novel procedure presented in this work.

1-Hexene hydroformylation by rhodium zeolite A showed intrazeolitic rhodium to migrate to the external surface of the zeolite. However, in the presence of a solution and surface rhodium poison, intrazeolitic rhodium was found to hydroformylate 1-hexene exclusively to heptanal.

Ruthenium containing zeolite A was evaluated under CO-hydrogenation conditions. No migration of intrazeolitic ruthenium to the external surface of the zeolite was observed over the course of the reaction. The product distribution obtained for this catalyst did not follow a log normal behavior. Also, loss of zeolite crystallinity was observed following the reaction.

Cobalt ZSM-5 was evaluated under CO-hydrogenation conditions. No migration of cobalt to the external surface of the zeolite occurred. XPS analysis of the catalyst following various stages of the reaction indicated that intrazeolitic cobalt was not reduced to the zero valent state. Consequently, the non-zero valent cobalt was not capable of hydrogenating carbon monoxide.

ACKNOWLEDGEMENTS

Probably the hardest part of writing the dissertation is the acknowledgements, as many people have provided assistance for me during the course of this work; either through their friendship, their teachings or both. I'd like to thank the Nation Science Foundation, the American Chemical Society, Pratt Fellowship and Cunningham Fellowship for financial support. I am grateful to the colorado Regional NMR Center for assistance with the ^{13}C-MASNMR work. Special thanks is also be given to and and for laboratory discussion and the countless assistance you have provided me with. deserves much thanks for his patience in construction of the synthesis vessels.

Of the people I've had the privilege to be associated with during my career at Virginia Tech, I'd like to thank for having the honors of breaking me in; for being a friend as well as an associate; for always being there when I needed to talk; for computer troubleshooting; for his "library" time idea, for being an outstanding weightlifter, bodybuilder and all around good guy; for the excitement in New Orleans; for teaching me his "country club" mannerism; for always being a ray of sunshine; and for being my weightlifting partner all these years. Special thanks goes out to the Virginia Tech Weightlifting Club

and especially members of the Virginia Tech Powerlifting Team, my home away from research.

I thank my parents, and for their understanding and support.

I came to Virginia Tech with an understanding of Zeolite synthesis. This was due to the teachings of I thank you for being my friend and providing direction for me in life. Lastly, I'd like to thank Professor Mark Davis for his guidance, support and caring. I know you are a demanding individual, but this is only because you want your students to be successful not only in chemical engineering but in life as well. It is from your ideals and teachings that I have learned. You have had and will always have my utmost respect.

TABLE OF CONTENTS

LIST OF TABLES

LIST OF FIGURES

I INTRODUCTION

Over the past dacade, considerable attention has been placed on the development of zeolite supported transition metal catalysts. Zeolite possess excellent properties for support of catalytically active metals. First, zeolites have a very large surface area, on the order of 800 m^2/g, over which transition metals may be finely dispersed. Secondly, the structure of the zeolite allows for exclusion of molecules beyond a critical diameter, as the pore size (typically between 3 and 8Å) is approximately the size of small molecules. This "shape selective" characteristic adds a new dimension to catalyst design. Zeolites also possess excellent thermal stability, with most being stable at temperatures in excess of 800°C (1). Finally, most zeolites can be produced at relatively low costs using simple procedures.

Transition metal zeolites are traditionally prepared by cation exchange or metal carbonyl sublimation (see, for example 2-6). These techniques reportedly place the transition metal within the cavities of large pore, low silica zeolites such as faujasite and mordenite, but locate the majority of the transition metal on the external surface in the case of small pore zeolites, such as zeolite A and erionite[1], and high silica zeolites, such as ZSM-5 (4). If reaction selectivity enhancements from transition metal containing zeolites catalysts are to be achieved,

---

[1] Often times, the transition metal complex is too large to penetrate the zeolie structure (4).

near exclusive location of the transition metal within the zeolite channel system will be required. This is because small quantities of metal located on the external surface may be many times more reactive than intrazeoltic metal. This may be due to either diffusion limitations or ensemble effects[2]. Thus, small quantities of metal located on the surface of zeolites may result in masking any selectivity enhancements produced by intrazeolitic catalysis.

Zeolites A and ZSM-5 are very interesting and potentially very useful materials for intrazeolitic catalysis. Zeolite A possesses 11.8Å cages which are accessed through 5Å windows. Due to the size of the aperature, only linear hydrocarbons may be transported through the structure. Thus, this zeolite has the possibility of being very useful in reactions where both linear and branched hydrocarbons are produced and the desired product is the linear isomer. For zeolite A, the pore size is both an advantage as well as a handicap. The handicap being that many transition metals, such as ruthenium, rhodium, platinum, iron, etc. are restricted from the structure due to the size of their ion exchange complexes. ZSM-5 is a high silica zeolite which possesses the unusual catalytic property (in the acid form) of being able to transform alcohols (7) and olefins (8) into aromatic hydrocarbons. It has been postulated (9) that if either the alcohol or olefin synthesis function could be placed in the proximity

---

[2] For example, studies involving Fischer-Tropsch catalysts have revealed that the reactivity decreases as the metal particle size is also decreased (10,11). Only very small particles (6 to 8Å) may be contained within zeolite cavities.

of the acid site, exposure of the catalyst to syn-gas would result in unprecedented selectivity to aromatic hydrocarbons. The drawback associated with placing alcohol or olefin synthesis metals within ZSM-5 is the hydrophobicity of the high silica surface. Since many cation exchange complexes involving transition metals are hydrophilic in nature, a large portion of the transition metal complexes become located on the external surface following ion exchange (12). In addition, the high silica surface of ZSM-5 does not provide a large number of anionic sites. This places severe limitations on the quantity of transition metal which may be ultimately placed within ZSM-5.

Transition metals such as ruthenium, rhodium, palladium, etc. cannot be cation exchanged into zeolite A due to the size of the exchange complex. Shannon et al. (4) have demonstrated this to be the case for rhodium, as virtually none of the rhodium was located within zeolite A following cation exchange. Nickel could not be exclusively located within zeolite A via cation exchange (5), as the resulting material (6.5 wt%) was found to be a very active benzene hydrogenation catalyst[3]. In addition, Breck (13) has presented data which suggests that many metals of catalytic interest (e.g. Cr) cannot be readily incorporated within zeolite A via cation exchange.

Since a number of transition metals cannot be ion exchanged into zeolite A, attempts have been made to synthesize zeolite A in the presence

---

[3] Benzene is much too large to penetrate the 5Å windows of zeolite A.

of transition metal amines (14,15,16). Platinum containing zeolite A was prepared by addition of $Pt(NH_3)_4Cl_2$ to the zeolite A synthesis gel (14). The resulting material was 0.10 wt% Pt. The location of the platinum was probed via catalytic reactions involving normal and branched olefins. The results of this experiment indicated that platinum was located on both the surface and within the zeolite. That is, the preparation technique did not exclusively locate platinum within the zeolite.

The majority of the transition metal ZSM-5 materials reported in literature have been prepared for the purpose of developing a Fischer-Tropsch catalyst (see, for example 3,17,18,19). These materials were prepared via cation exchange or carbonyl sublimation with the resulting materials being typically 5 to 10 wt% transition metal. Whenever particle size studies were conducted with these materials, the average particle size was found to be many times larger than the channel size could accommodate (2,3,17). Shannon et al. (4) has presented strong evidence to indicate that rhodium can only be partially exchanged into ZSM-11[4] even at low rhodium loadings (0.9 wt%).

As in the case of zeolite A, attempts have been made to locate transition metals exclusively within ZSM-5 by adding transition metal complexes to the synthesis gel. These complexes have included iron oxides (20), transition metal hydroxides (21) and polyaromatic transition metal

---

[4] ZSM-11 is identical to ZSM-5 with the exception of the tortuosity of one of the channels. The channel dimensions and framework compositions are identical.

compounds (22). Results of these studies indicate that neither addition of iron oxide nor the transition metal hydroxide to the synthesis gel locates a significant portion of the metal within the ZSM-5 channel system. Addition of the polyaromatic compounds to the synthesis gel does locate the transition metal exclusively within the channels. The drawback from this technique is that the compounds are expensive to synthesis and a large quantity of the compound placed into the synthesis gel is not recovered with the product crystal.

Olefin hydroformylation involves reaction of an olefin with carbon monoxide and hydrogen to yield aldehydes. The desired product from the hydroformylation of an α-olefin is the linear aldehyde. However, hydroformylation of an α-olefin typically produces both linear and branched aldehydes (23). Olefin hydroformylation has traditionally been performed with either homogeneous cobalt or rhodium catalysts (23). Recently, studies have been conducted in an attempt to locate the homogeneous catalysts within zeolites (24,25). These attempts involved locating rhodium within the large cavities of faujasite. It has been postulated (25) that the rhodium complexes could be "trapped" within the 13A cage[5] and would thus provide comparable selectivity as the homogeneous catalysts. Further, the entrapped rhodium species would be capable of higher operation temperatures (compared to homogeneous catalysts) while making the catalyst/product separation trivial.

---

[5] This cage is accessed through 8Å ports.

Catalytic investigations of the rhodium faujasite catalysts showed these materials to leach rhodium from the zeolite (24,26,27). Also, the rhodium utilization of these materials was reported to be poor (25), and that intrazeolitic rhodium could not be activated in the vapor phase hydroformylation of propylene (25,28). None-the-less, a selectivity enhancement was observed in the vapor phase hydroformylation of propylene (25,29). These studies noted that the regioselectivity (ratio of normal to branched aldehydes) was increased from 1/1 (homogeneous catalyst) to 2/1 (rhodium faujasite). It may be possible that the reactivity of intrazeolitic rhodium is much less than that of surface rhodium and that in these cases, surface rhodium dominated the product spectrum.

The CO-hydrogenation reaction (also referred to as Fischer-Tropsch) involves reaction of CO and hydrogen over a transition metal catalyst to yield a wide spectrum of paraffins, olefins and alcohols. The stoichiometric Fischer-Tropsch reactions are as follows (30,31,32)[6]:

Paraffins: $nCO + (2n+1)H_2 = C(n)H(2n+1) + nH_2O$

Olefins: $nCO + 2nH_2 = C(n)H(2n) + nH_2O$

Alcohols: $nCO + 2nH_2O = C(n)H(2n+1)OH + (n-1)H_2O$

This reaction is very unselective, as the product distribution obeys traditional polymerization kinetics and can be modeled by the following equation:

---

[6] The notation C(n) indicates carbon of length n

$$\text{Log}[M(n)] = n\log\alpha + \text{Log}[(\alpha-1)/\alpha] \qquad (1)$$

where M(n) is the mole fraction of C(n) and α is the chain growth probability.

Group VIII transition metals will catalyze the Fischer-Tropsch reactions, with ruthenium, iron and cobalt being the most reactive (33). These metals can be supported on metal oxides (e.g. TiO_2, Al_2O_3, etc.) or zeolites. The Fischer-Tropsch product distribution can be altered through variations in the catalyst preparation (10,11,34) or reaction conditions (10,11,33). Despite these changes, the resulting product distribution still may be predicted by equation 1.

The Fischer-Tropsch reaction could become very important provided a catalyst could be developed which would selectively yield light olefins or gasoline range hydrocarbons. This is because syn-gas can be readily derived from coal (35) which is believed to comprise over 65% of the worlds recoverable fossil fuel resources (36). Fischer-Tropsch catalysts selective towards the formation of light hydrocarbons (C_1-C_5) have been reported (37-40). These catalysts employ very small metal particles (>20Å) supported on either metal oxides or within zeolite Y (in this case, the product was 95% methane). For the cases involving metal oxide supports, the excellent selectivity towards light hydrocarbons could not be maintained due to sintering of the metal particles (39). For the zeolite Y based Fischer-Tropsch catalysts, the product distributions were only reported following a short time after start-up. No indication as to

catalytic stability following long periods of exposure has been provided. Fraenkel and Gates (40) have shown CoCd A to be a selective Fischer-Tropsch catalyst, however, reaction rates were extremely low.

Bifunctional catalysts have been also found to function as selective Fischer-Tropsch catalysts (3,9). These catalysts combined the hydrocarbon synthesis function of the transition metal with the acid function of ZSM-5. For these catalysts, excellent conversion of syn-gas to gasoline range hydrocarbons (C_7-C_{12}) high in aromaticity has been demonstrated (9).

As reported in the literature, a number of studies have involved transition metal zeolites. However, few synthesis techniques are available which provide near exclusive location of transition metals within zeolites, and the vast majority of the catalytic activity observed from transition metal zeolites is due to catalysis occurring at the zeolite surface. The purpose of this study is to develop a technique which will provide near exclusive location of transition metals within zeolites. The main topics of this research will involve the synthesis of transition metal zeolites and the subsequent investigation of these new materials as shape selective catalysts. Of interest will be zeolite selectivity, activity, metal mobility and stability. The two zeolites used in this study are zeolite A and ZSM-5. Test reactions employed here are olefin hydroformylation and CO-hydrogenation.

II LITERATURE REVIEW

II.A Zeolite A

II.A.1 Zeolite A Synthesis

The synthesis of zeolite A involves dissolving an aluminum species in a solution of sodium hydroxide and water. To this solution, a silica species dissolved in water is next added. Typical aluminum species include sodium aluminate (41-45) and aluminum hydroxide (42). Sodium aluminate is the preferred material (42). Typical silica species include colloidal silica solutions (42,43), sodium silicate (45), silica gel (46) and tetraethyl ortho-silicate (44). The resulting synthesis gel is heated to temperatures typically between 85 and 110°C (42-45,47), with crystallization being complete in less than 5 hours. Breck (48), in a review of the literature, reports that zeolite A can be synthesized at temperatures ranging from 25 to 150°C. Early syntheses of zeolite A were performed with agitation in glass flasks operating with reflux (43-45). Later synthesis investigations were carried out in teflon lined autoclaves at autogeneous pressure (37,39,49), as glass was found to be dissolved by the caustic synthesis solution.

The composition region for zeolite A was investigated in early synthesis studies. Barrer et al. (42) varied the SiO_2/Al_2O_3 ratio of the synthesis gel from 1 to 12 (integer values) while the Na_2O/Al_2O_3 ratios were 2, 3 and 4 (Na_2O contribution from NaOH). The gel compositions listed in their study did not report the H_2O/Al_2O_3 ratio. The reaction

temperatures employed were 60, 85, 110, 150, 200 and 250°C. Their results showed excellent yields of zeolite A at temperatures of 85 and 110°C for SiO_2/Al_2O_3 equal to 1 and 2. Crystallization was noted to be more rapid for gels prepared with a Na_2O/Al_2O_3 ratio of 4. At temperatures of 150°C and above, zeolite A was no longer formed. Also, increasing the SiO_2/Al_2O_3 ratio to 3 and above resulted in poor or no yield of zeolite A.

The composition region for zeolite A was also investigated by Regis et al. (43). These authors varied both the SiO_2/Al_2O_3 and Na_2/Al_2O_3 ratios while allowing the gels to react at 100°C for 1 day. Again, the H_2O/Al_2O_3 ratio was not reported. It was noted in this study that for the composition x Na_2O-Al_2O_3-y SiO_2, zeolite A was best synthesized from gels with x = 3 and y = 1 and x = 2 and y = 2. Figure 1 shows the phase relationship observed in this work. The phase relation reported by Kosinko (50) is shown in Figure 2. Note that both of these studies appear to agree on the SiO_2/Al_2O_3 ratio while differing on the sodium content. As the figures show, the system of Kostinko appears to favor a higher sodium concentration than the system reported by Regis et al.

Ciric (45) studied the influence of the NaOH concentration on the zeolite A synthesis for the compositions:

A) xNa_2O-Al_2O_3-2.47 SiO_2-350 H_2O
B) yNa_2O-Al_2O_3-2.47 SiO_2-575 H_2O

where x was varied between 0.46 and 4.6 and y was varied between 0.25 and 6.0. In all cases, the synthesis temperature was 100°C. From his study,

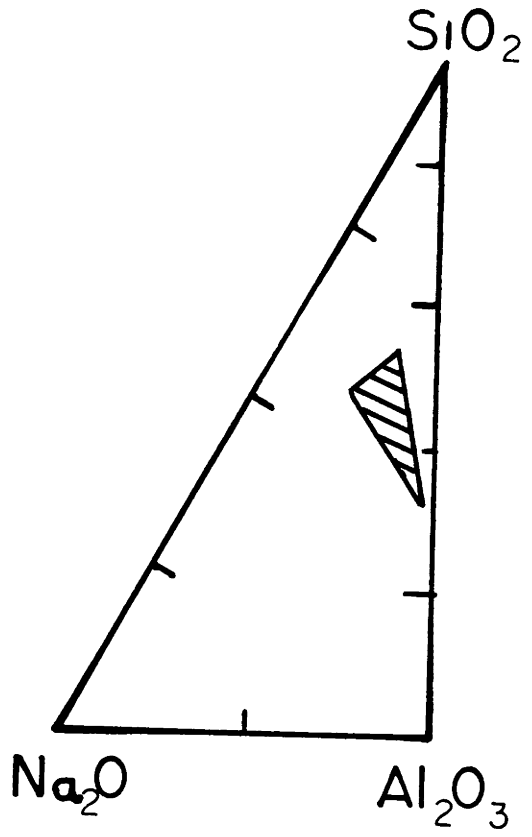

Figure 1: Phase Relation for the Crystallization of Zeolite A (43).

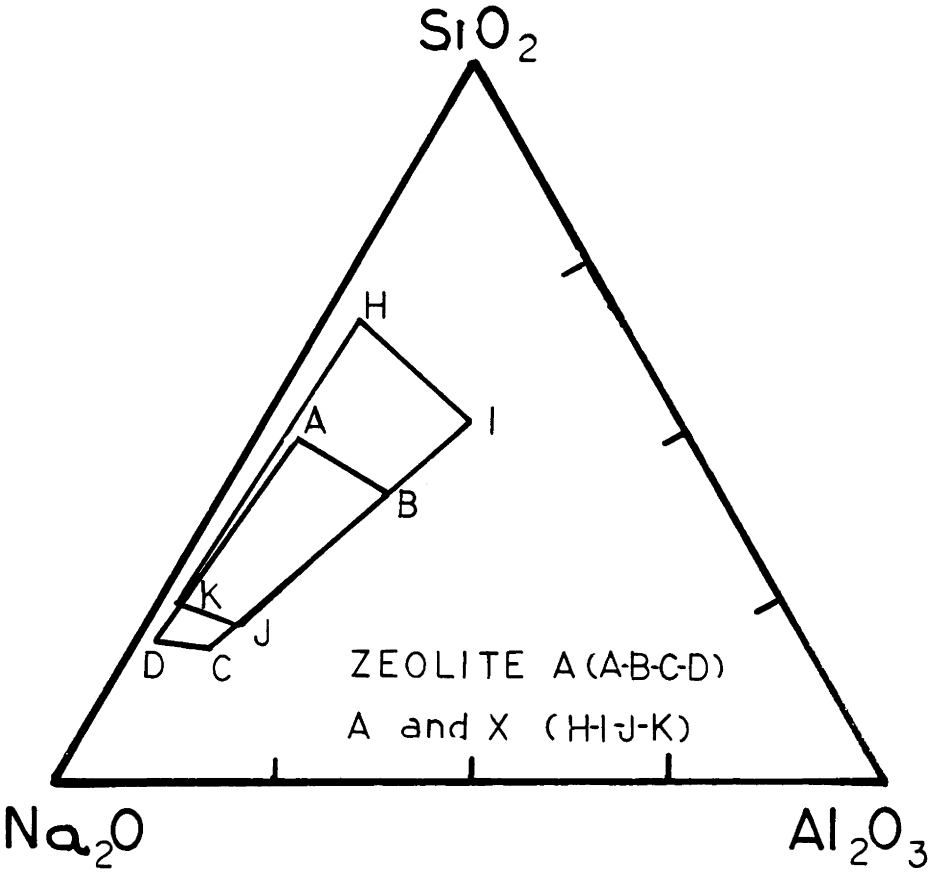

Figure 2: Phase Relation for the Crystallization of Zeolite A (50).

Ciric concluded that syntheses performed with SiO_2/Al_2O_3 ratios above 2.0 produced both zeolite A and an amorphous species, and that increasing the caustic resulted in dissolution of the excess silica (amorphous).

The zeolite A crystalline phase is metastable. It will readily undergo a phase transformation to zeolite P and sodalite if left in contact with the synthesis solution for extended periods of time (42,43,48). Typically, zeolite A will transform to zeolite P in a high silica gel, while transformation to sodalite occurs at high NaOH concentrations (48).

In summary, synthesis investigations have shown that zeolite A is best produced from gels with SiO_2/Al_2O_3 ratios between 1 and 2, with the ratio of Na_2O/Al_2O_3 between 0.5 and 4.0, and with temperatures between 85 and 110°C.

The cation(s) present in the zeolite A synthesis gel influence the nature of the gel. The sodium ions are thought to provide structure direction during the zeolite A synthesis. That is, the sodium ions are thought to order the silicon and aluminum in the synthesis gel so as to produce the zeolite A structure. Zeolite A cannot be grown in the absence of sodium, as replacement of sodium by lithium, potassium and calcium does not yield zeolite A (51,52). Zeolite A can however be synthesized from mixtures of cations, such as Na-K and Na-Li (48). These studies also showed sodium to be the preferred cation for zeolite A synthesis.

Zeolite A synthesized with the aforementioned compositions produces a structure with a SiO_2/Al_2O_3 ratio very nearly equal to 2.0 (42,43,47). Zeolite A with SiO_2/Al_2O_3 ratios greater than 2.0 have been synthesized. Synthesis of these materials involved addition of tetramethylammonium hydroxide (TMAOH) to the gel (41,46). These molecular sieves are referred to as zeolite N-A and ZK-4. Synthesis of the high silica zeolite A requires approximately 24 hours at about 150°C whereas zeolite A requires only 1-4 hours at 100°C. The high silica A-type zeolites are produced from synthesis gels with SiO_2/Al_2O_3 ratios from 4 to 11, TMA_2O/Al_2O_3 ratios from 9 to 30, Na_2O/Al_2O_3 ratios from 0 .5 to 1.5 and H_2O/Al_2O_3 ratios from 100 to 350. Typically, the product crystals synthesized within this composition range possess a SiO_2/Al_2O_3 ratio of 1.4 to 1.7 (41). The reason for the increased SiO_2/Al_2O_3 ratio stems from the physical constraints of the zeolite A α-cage. Analysis of these materials following synthesis has shown the TMA^+ cation to be present within the β-cage, occupying a charge balancing site. The size of the TMA^+ cation limits the number of cations which can be present within the cage. The sodium ions are required to balance the remaining aluminium charges. Because the number of cations per unit cell is limited, the resulting zeolite becomes more siliceous (53).

Zeolite A is known to grow in the presence of seed crystals (44,45,47,48). The seed crystals reduce the nucleation time and increase the rate of crystal growth by supplying growth sites (44,45,47). Thompson and Dyer (47) illustrated the pronounced effects of "seeding" a synthesis gel. They attempted to react a very dilute gel and produced no zeolite

phase. The addition of "seed" crystals to this gel resulted in crystal growth onto the seed material only. No new crystals were observed.

The mechanism for crystallization of zeolite A was first proposed by Flanigen and Breck to be a solid-solid phase transformation reaction (44). Later studies by Kerr (44) and Ciric (45) showed the synthesis to involve the liquid phase and involve an ordering of gel phase silica and alumina species around active growth sites. This mechanism involves the dilution of the amorphous solid (gel) into the alkaline solution to form soluble, active species. The concentration of these species in solution remains nearly constant throughout most of the crystal growth process. The constant concentration results from the species being formed from the amorphous solid and removed via crystal growth. The decrease in the rate of crystal growth near completion is the result of the decrease in solution phase active species as the amorphous solid is consumed.

Kerr (44) proposed the following reaction sequence based on the above mechanism:

Amorphous Solid =fast=> Solution Species
Solution Species + Nuclei (or Zeolite Crystal) =slow=> Zeolite A

Kerr also showed that the rate of crystallization could be modeled assuming first order kinetics: $LnZ = kt + lnZ_0$ where Z is defined as the percent zeolite, t is time and k is the first order rate constant. This model shows that the rate of crystallization is a function of the quantity of nuclei or crystals present in the system. Ciric (45) attempted to explain the crystal growth behavior by accounting for mass transfer of

the active species to the active growth site. His attempts to model this phenomena failed. Both Kerr and Ciric noted in their studies that the concentration of OH^- ions in solution increased the rate of crystal growth.

Breck (54) proposed that the silica in solution existed as a hydrated monomer, $Si(OH)_4$. Dissolution of the gel involved simultaneous hydration-depolymerization, catalyzed by the presence of a strong base. The synthesis mechanism of Breck is consistent with that proposed by Ciric and Kerr and is presented in Figure 3. The hydrated sodium ion acts as a template, which serves to replicate the basic building units of the zeolite A structure.

II.A.2 Zeolite A Structure

The crystal structure of zeolite A was first determined by Breck and co-workers and reported in 1956 (55). The structure of this novel synthetic zeolite was determined by combining X-ray diffraction data with the adsorption properties of the material. The X-ray diffraction pattern for zeolite A in the sodium form is shown in Figure 4 and the d-spacings are reported in Table 1 for Na A and Ca A. Zeolite A is comprised of three basic units, these being the α-cage, the β-cage and the double four membered ring (D4R), as shown in Figure 5. The four membered rings connect the truncated octahedra (β-cage) so as to produce the α-cage. Eight β-cages constitute the true unit cell of zeolite A, with each β-cage occupying the corner of a cube, as shown in Figure 6. The β-cage encloses a

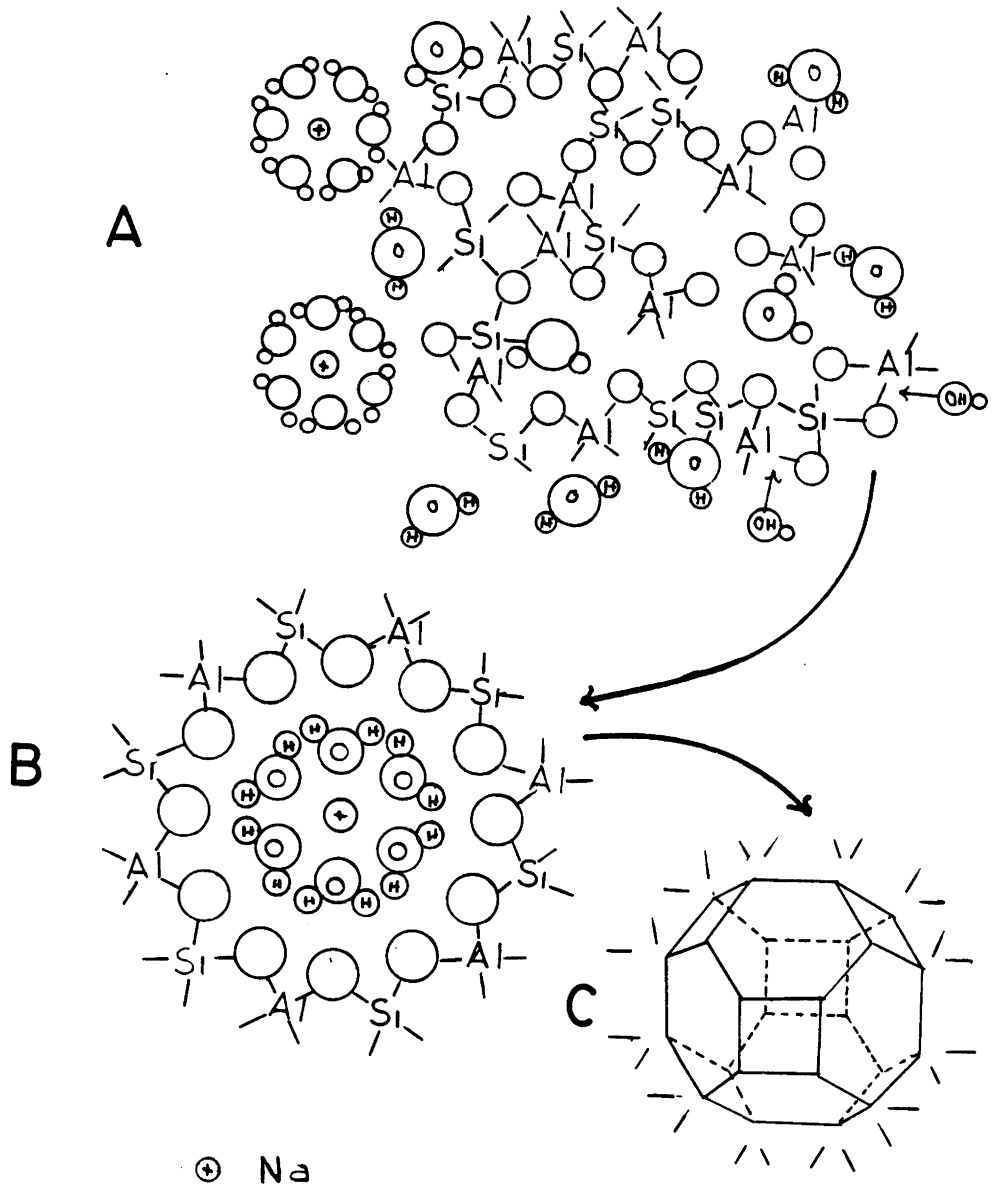

Figure 3: Proposed Mechanism for the Synthesis of Zeolite A (54). In C, the intersections of the lines represent T-atoms (Si,Al) and the lines represent oxygne atoms.

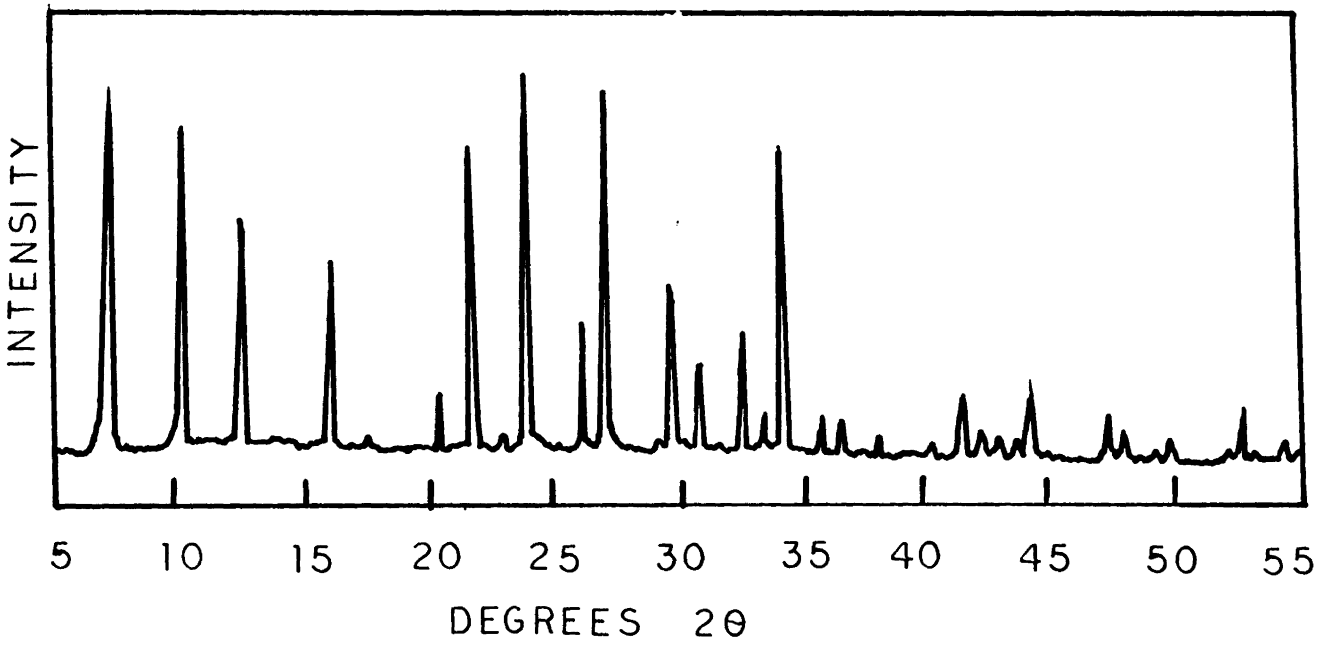

Figure 4: X-Ray Diffraction Pattern for Zeolite A (56).

Table 1
X-Ray Data for Zeolites Na A and Ca A (66)

Na A		Ca A	
d(Å)	I/I_0	d(Å)	I/I_0
12.29	100	12.24	100
8.71	69	8.66	39
7.11	35	7.08	13
----	--	6.12	12
5.51	25	5.48	20
5.03	2	5.00	4
4.36	6	----	--
4.107	36	4.084	35
-----	--	3.875	2
3.714	53	3.696	34
-----	--	3.539	4
3.417	16	3.398	18
3.293	47	3.276	38
2.987	55	2.972	32
2.904	9	2.888	9
2.754	12	2.741	7
2.688	4	2.676	3
2.626	22	2.614	24
2.515	5	2.502	7
2.464	4	2.451	7
2.371	3	2.359	3
2.289	1	-----	--
2.249	3	2.238	3
2.177	7	2.166	8
2.144	10	2.141	8
2.113	3	2.103	5
2.083	4	2.074	2
2.053	9	2.042	4

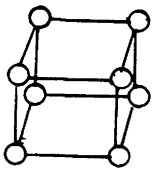

D4R

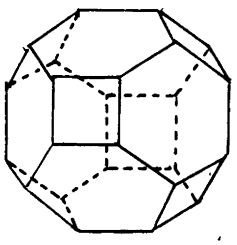

β-CAGE

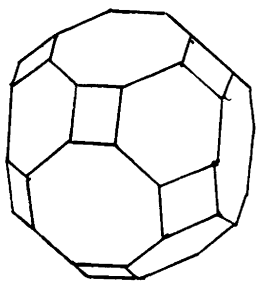

α-CAGE

Figure 5: Structure Units of Zeolite A (57). Cornors represent T-atoms while the lines are oxygen atoms.

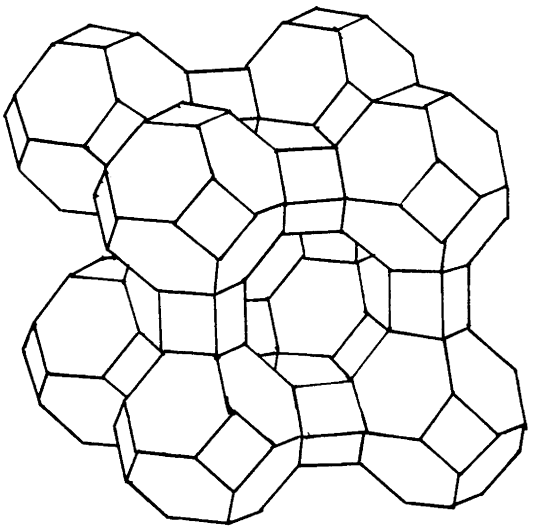

ZEOLITE A

Figure 6: The Structure of Zeolite A.

6.6 Å cavity which is accessible through the 2.2 Å window of the six-membered rings. The small size of this aperture results in exclusion of molecules such as oxygen (O_2); however, smaller molecules such as water may enter. The α-cage is 11.4 Å in diameter. It is accessed through the 8-membered rings which are formed via connection of the β-cages with the D4R. The size of this opening is 4.2 Å, as determined by X-ray diffraction. Mass transfer through the 8-membered rings is limited only to linear hydrocarbons. Branched hydrocarbons, with a minimum critical diameter of 5.0 Å are excluded (55-57). Zeolite A in the potassium form is commonly referred to as 3A, while the sodium and calcium forms are referred to as 4A and 5A, respectively.

As stated earlier, the true unit cell is composed of eight β-cages linked by 4-membered rings. The β-cage is; however, the repeating unit in the zeolite A structure. The β-cage is therefore referred to as the pseudo-unit cell, whose composition is $[Me_{12}O/n][(AlO_2)_{12}(SiO_2)_{12}]\cdot N\ H_2O$ (55-57). Here, Me refers to the charge balancing cation of valency n and N refers to the number of water molecules per unit cell, typically between 24 and 30, depending on the charge balancing cation. The SiO_2/Al_2O_3 ratio for zeolite A was found to be 1.92±0.09 for samples prepared over a wide range of compositions (55). The SiO_2/Al_2O_3 ratio of 2 suggests that the structure is comprised of alternating SiO_2 and AlO_2 tetrahedra. Thus, each Si atom has four neighboring Al atoms and each Al atom has four neighboring Si atoms. This scheme was proposed and is consistent with Loewenstein's rule which states that two aluminum atoms cannot share the same oxygen atom while retaining a coordination of 4 (55). The proposed

ordering of Reed and Breck was later verified by ^{29}Si-MASNMR (magic angle spinning NMR) studies (59). SiO_2/Al_2O_3 ratios less than 2 are due to occluded aluminum species. The nature of the occluded aluminum species has been postulated to be either Al_2O_3 or $NaAlO_2$ (57).

There are 12 sodium ions located within the hydrated sodium A unit cell. Eight of these ions are located near the center of the 6-membered rings, inside the α-cage. The remaining 4 ions are associated with the 8-membered rings, which are the openings to the α-cage. When dehydrated, the 8 sodium ions located near the center of the 6-membered rings are displaced 0.4 Å towards the center of the α-cage. Three of the remaining sodium ions are displaced 1.2 Å from the center of the 8-membered rings partially blocking the aperture and hence regulating the pore size. The remaining sodium is postulated to be opposite the 4-membered ring. Cation exchange of 8 unipositive sodium ions with 4 dipositive calcium ions results in vacant cation positions near the 8-membered ring. Consequently, the apertures are completely open and capable of admitting larger molecules (57).

The volume of zeolite A has been calculated as 151 $Å^3$ for the β-cage and 775 $Å^3$ for the α-cage. Pore volumes have been measured directly from adsorption of various molecules. O_2 and H_2O adsorptions are commonly employed as a method of pore volume determination. The type of cation in the zeolite A structure can influence the measured pore volume greatly. The measured pore volume of Na A and Ca A via O_2 adsorption

(135mm, -196°C) were found to be 0.213 and 0.242 cm^3/g-zeolite, respectively (57).

II.A.3 Physical Properties of Zeolite A

The morphology of the zeolite A crystals is cubic. The size of the cubes typically range from 1 to 5μ, although crystals as great as 25μ have been grown. Attempts to grow larger crystals results in twinning or the formation of aggreates (55,58).

Zeolite A has been characterized with IR spectroscopy by Flanigen et al. (60). The IR spectrum of sodium A is shown in Figure 7. The band assignments for this spectrum and that of calcium A are reported in Table 2. As the table shows, there are some subtle differences between the two spectra.

The nature of the charge balancing cation in zeolite A is very important as it can greatly influence the physical properties of the material. Cation exchange of the as synthesized Na A material is typically performed by slurrying the zeolite in a 0.1-0.2 N solution of 100% excess (for complete exchange) ion at 25°C (13,58). For univalent ions, the order of decreasing selectivity for exchange was found to be $Ag>Tl>Na>K>NH_4>Rb>Li>Cs$, while for divalent cations, the order was $Zn>Sr>Ba>Ca>Co>Ni>Cd>Hg>Mg$ (13,58). Breck et al. (58) noted that Cs^+ could only be exchanged at a 31% level, and that no exchange for trivalent

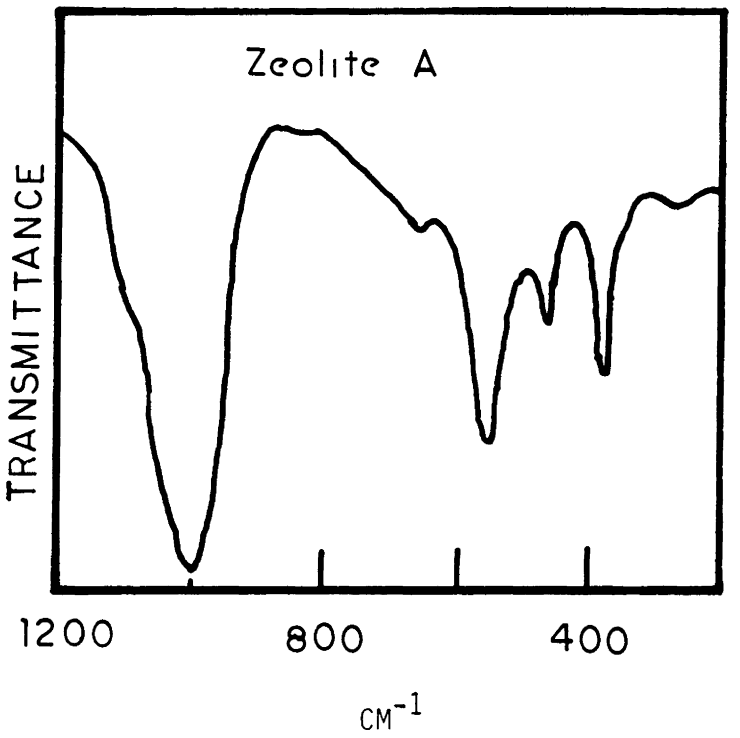

Figure 7: IR Spectrum of Zeolite Sodium A (60).

Table 2
Infrared Spectral Data for Zeolite A (60)

Zeolite	Asymmetric T-O Stretch			Symmetric T-O Stretch		
Na A	1090vwsh	1050vwsh	995s			660vw
Ca A	1130vwsh	1055vwsh		742vwsh	705vwsh	665vw

Zeolite	Dbl. Rings	T-O Bend	Pore Openings?	
Na A	550ms	464m	378ms	260vwb
Ca A	542ms	460m	376m	

s = strong; ms = medium strong; m = medium; vw = very weak;
sh = shoulder; b = broad

Ce^{+3} or Fe^{+3} could be achieved. Attempts to exchange Rh^{+3} within zeolite Na A resulted in rhodium located on the zeolite surface (4).

The stability of the A-type structure, with a SiO_2/Al_2O_3 ratio of 2.0, is dependent upon the charge balancing cations. For divalent cations, the structure stability decreases with an increase in the ionic radii. For monovalent cations, the stability of the A-type structure increases as the ionic radii of the cation is increased. For example, Na A recrystallizes to a β-cristobalite-type structure when exposed to air at 800°C for 2 hours, while Ca A retains its structure at the same conditions (61). Exposing the zeolite to steam at elevated temperatures also results in loss of crystallinity. Degradation of the structure in the presence of water vapor occurs via dealumination at the outer surface and proceeds inward (62). In the protonated form, zeolite A is very unstable, especially when exposed to water vapor (63). Exchange of both Na A and Ca A by NH_4Cl at a 75% level resulted in complete structural collapse.

The adsorption properties of zeolite A are very dependent upon the charge balancing cation. In the sodium form, zeolite A will adsorb (at room temperature) molecules the size of ethane, ethylene and propylene. However, molecules such as propane and cyclopropane are excluded. The fact that propylene is adsorbed and propane is excluded suggests that the structure is more selective towards unsaturated hydrocarbons than saturated (55). Zeolite Na A will exclude all hydrocarbons of C_4 and greater.

The effective pore size of the Na A zeolite is therefore between 4.2 and 4.75 Å, based on the kinetic diameters of the molecules adsorbed.

In the calcium form, zeolite A possesses a larger effective pore size than Na A. Ca A will readily adsorb molecules such as n-butane and CCl_2F_2. Thus, the effective pore size of Ca A is between 5.0 and 5.6 Å (55). Larger linear chain hydrocarbons, up to C_{14}, have been adsorbed by zeolite Ca A at room temperature and atmospheric pressure. Figure 8 illustrates the kinetic diameter of some simple hydrocarbons while Table 3 reports the adsorption capacity of various molecules within zeolites Na A and Ca A.

As shown in Figure 9, the adsorption of gases by zeolite A, and hence the effective pore size, is temperature dependent. This effect could be the result of vibrations of the structure. As the temperature is increased (80 K to 300 K), an increase in vibrational amplitude of 0.1 to 0.2 Å is expected (55). As the size of the aperture is increased with temperature, molecules which were originally rejected may now readily enter the structure.

From adsorption studies, it is evident that the effective pore size, as defined by the calculated critical dimensions of molecules, can be larger or smaller than the physical dimensions of the 8-membered ring (4.2 Å)[7]. This phenomena was explained by Breck et al. (58) to be due to an

---

[7] It should be noted that the dimensions of the 8 membered ring is

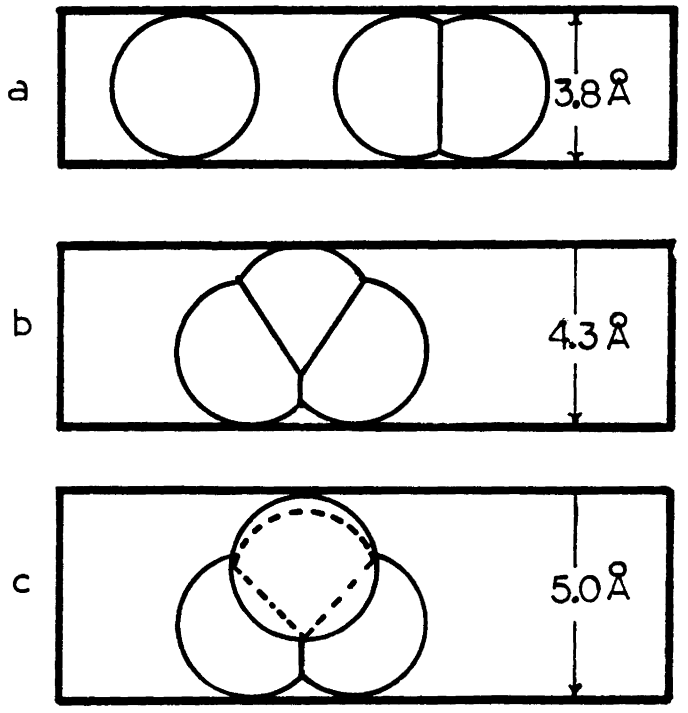

Figure 8: Kinetic Diameter of A) Methane, Ethane; B) Propane and C) iso-Butane (58).

Table 3
Adsorption Capacity of Na A and Ca A Zeolites
(from 58)

Adsorbate	Critical Diameter	Temperature	Pressure	G/G-Zeolite Na A	G/G-Zeolite Ca A
O_2	2.8 A	-196°C	132 mmHg	0.254	0.307
		-183	750	0.252	0.276
N_2	3.0	-196	700	0.006	0.239
$n\text{-}C_3H_7OH$	---	room	700	0.037	0.197
C_2H_6	4.2	room	700	0.074	0.087
C_2H_4	4.25	room	700	0.084	0.091
C_2H_8	4.89	room	600	0.017	0.130
C_2H_6	5.00	room	700	0.116	0.136
1-butene	5.10	room	400	0.029	0.154

NOte: Critical diameter is defined as the diameter of the circumscribed circle of cross section of minimum area.

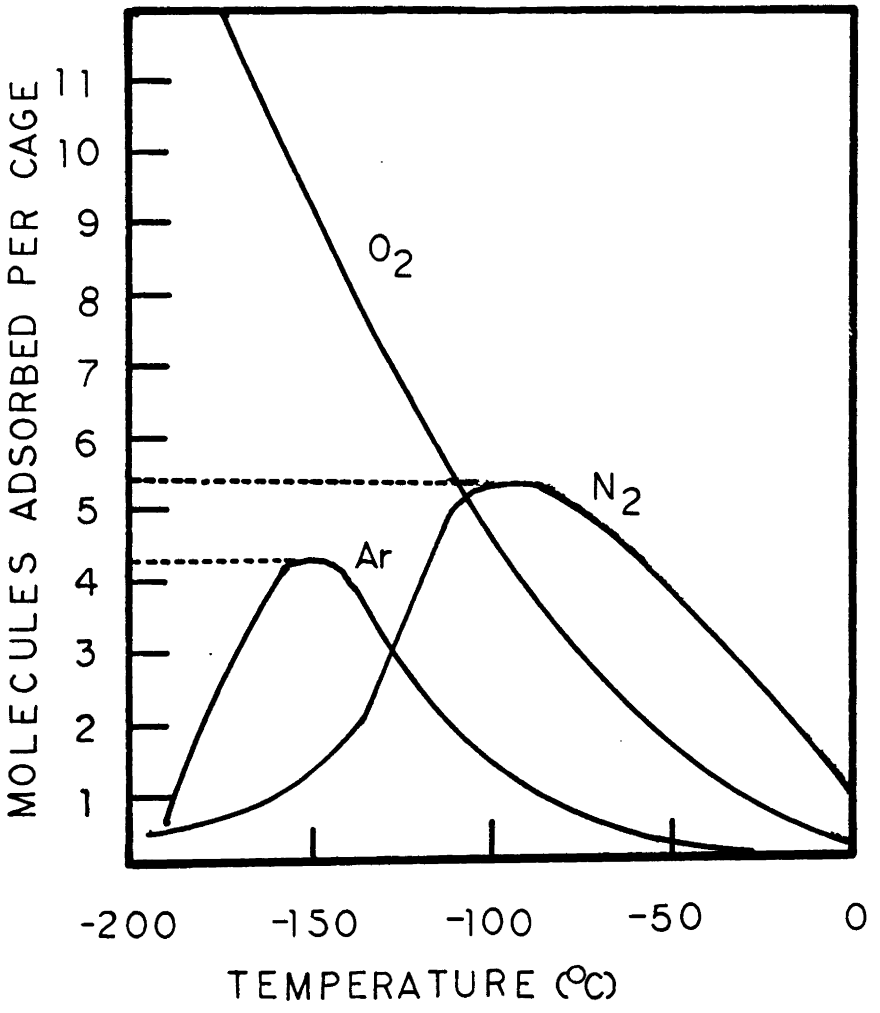

Figure 9: Gas Adsorption Isobars for Na A (58).

energy barrier existing at the entrance to the 8 membered ring. A physical blockage of the channel by the position of the sodium ions has also been suggested (57).

The ionic nature of the zeolite A surface results in strong attractions, and hence high heats of adsorption for polar molecules. This has been demonstrated by the rapid uptake of water at very low pressures (55).

II.A.4 Metal Incorporation Techniques for Zeolite A

Typically, catalytically active metals such as Ag^{+}, Co^{+2} and Ni^{+2} can be incorporated into the A-type pore system by conventional cation exchange. Cation exchange techniques involving these metals do not, however, exclusively locate the metal within the zeolite pore system. For example, a 6.5 wt% Ni A zeolite was shown to be a very active benzene hydrogenation catalyst (5). Since benzene is excluded from the A structure, these results suggest that the catalysis is occurring via surface Ni and that the cation exchange did not place Ni exclusively within the zeolite. On the other hand, $Co^{0}Cd^{+2}$ A (cobalt introduced via ion exchange and reduced via cadmium metal vapor) did show selectivity as a Fischer-Tropsch catalyst (31). These results suggest that the cobalt was located within the pore structure. Cation exchange of Na A with $RhCl_3$-$3H_2O$ re-

---

calculated from X-ray diffraction data. These dimensions will change with temperature due to an increase in vibrational energy.

sulted in near exclusive location of rhodium onto the zeolite surface (4). The surface rhodium is due to the fact that the hydrated rhodium ion has a larger diameter than the 8-membered rings.

If the zeolite A structure is to be employed as a shape selective catalyst, the metal(s) of interest must be located almost exclusively within the pore structure. In depth analysis of metal location following cation exchange of zeolite A has only been performed in a few isolated cases. However, based on ion exchange equilibrium curves and data supplied by Breck (13), many metals of catalytic interest cannot be easily incorporated into the A-type pore structure. Metals such as Ru, Rh, Pt and Pd are excluded due to the physical size of their hydrated ions.

Attempts to place metals of catalytic interest into zeolite A which could not be incorporated via ion exchange have been made. These attempts have involved growing the A-type structure around the metal of interest (14). Platinum containing zeolite A was prepared by addition of tetraammine platinous chloride $[Pt(NH_3)_4Cl_4]$ to the zeolite A synthesis gel. The resulting catalyst (>0.1 wt% Pt) was washed with a 0.2 N NaCl solution and distilled water. Catalytic combustion of both n- and i-butane resulted in extensive oxidation (formation of CO_2) of both reactants, indicating that some platinum was present on the zeolite surface. Following a more extensive washing procedure, the catalyst was found to combust propylene, while leaving i-butane unreacted. These results suggest that the co-crystallization technique produced at least some intrazeolitic platinum.

The PtNa A catalyst prepared according to Chen (14) was exchanged into the calcium form by Chen and Weisz (15). The authors noted in their study that the diffusivity ratio of trans 2-butene to cis 2-butene was approximately 200 at 26°C in zeolite A. Thus, the hydrogenation activity of a mixed stream of cis,trans 2-butene over the PtCa A material should selectively convert the trans hydrocarbon over the cis. The catalyst tested was reported to be less than 0.1 wt% platinum. The experimentally observed selectivity determined from the ratio of the rate constants [K(trans)/K(cis)] was 7.0, 4.3 and 3.3 at temperatures of 98, 103 and 120°C, respectively. These results further indicated that the platinum, when added to the zeolite A synthesis gel, does in fact incorporate within the zeolite A pore structure.

Transition metal containing zeolite alpha was prepared by addition of metal amines, such as $[Pt(NH_3)_4]Cl_2$, to the synthesis gel (16). Rhodium zeolite alpha was prepared by addition of $[Rh(NH_3)_5Cl]Cl$ to the zeolite alpha synthesis gel. The resulting material was 0.18 wt% rhodium. The location of the rhodium (intrazeolitic versus surface) was investigated through a simple olefin hydrogenation experiment. The rhodium zeolite alpha was exposed to a 1:1 mixture of 1-butene : i-butene at 340°F. At these conditions, 75% of the 1-butene had undergone hydrogenation while only 4.2% of the i-butene had reacted. Since i-butene cannot penetrate the 5Å channels of zeolite A, any hydrogenation of this material is the result of surface rhodium. 1-butene easily diffuses into

zeolite A. Since the conversion of 1-butene was much greater than the conversion of i-butene, it was concluded that the synthesis technique resulted in the formation of intrazeolitic rhodium.

II.B ZSM-5

II.B.1 ZSM-5 Synthesis

The synthesis of ZSM-5 was first reported in 1972 (64). The crystallization of ZSM-5 can be accomplished with a wide range of reaction mixtures. The preparation of the ZSM-5 synthesis gel typically involves dissolving an aluminum containing compound in an aqueous alkaline metal hydroxide solution. This solution is then added to another aqueous solution containing an organic cation and dissolved silica. The resulting gel is then placed in an autoclave and heated to temperatures between 150 and 200°C under autogeneous pressure. The types of the reaction components vary greatly as can be seen from Table 4. Mostowicz and Sand (65) performed an extensive investigation into the reactivity of various types of silicas. Their study showed sodium silicate to be slightly more reactive than the colloidal silica solution (Ludox AS-30) and much more reactive than fumed silica or precipitated silica. No studies have been reported in the open literature regarding the reactivity of the various aluminas listed in Table 4. Sodium aluminate appears to be the preferred source of alumina, with aluminum sulfate and aluminum hydroxide being employed whenever it was desired to synthesize ZSM-5 in a sodium free environment.

Table 4
ZSM-5 Synthesis Reagents

Silica	Reference
Colloidal silica solution	65,67,68,69 70,71
Fumed silica	65
Precipitated silica	65,72,64
Sodium silicate	65,73
Potassium silicate	65,73

Alumina	Reference
Aluminum hydroxide gel	65,72
Aluminum sulfate	71
Sodium aluminate	64,69,70,71
Aluminum nitrate	75

Organic Cation	Reference
TPAOH	64,65,67,71
TPABr	65,69,71,72,76,77
Triethyl-n-propylammonium bromide	76
n-Propylamine	77
1,2;1,3;1,4;1,5;1,6-Diaminoethane	77
Tetrabutylphosphonium chloride	73
Oxyethyllactamide	78

Alkali Cation	Reference
Sodium hydroxide	64,68,69,70,71 76,79
Potassium hydroxide	65,79
Lithium hydroxide	65,79
Calcium hydroxide	65
Barium hydroxide	65
Strontium hydroxide	65

The tetrapropylammonium cation (TPA) is the preferred organic cation in the synthesis of ZSM-5. Mostowicz and Sand (65) have shown TPABr to be much more reactive than TPAOH. The other organic cations which lead to the synthesis of ZSM-5 (listed in Table 4) illustrate the relative nonspecificity of the organic cation in the ZSM-5 crystallization process. Also, it has been shown that ZSM-5 can be synthesized in the presence a variety of alkaline earth cations (65,79). These studies have shown sodium to be the most reactive alkaline earth cation (80).

The gel compositions employed in the synthesis of ZSM-5 can vary over a wide range. Table 5 lists compositions for the synthesis of ZSM-5 in the sodium/silica/alumina/TPA/water system. ZSM-5 can also be synthesized in the absence of alumina and is denoted as silicalite (73,81). The composition range for the synthesis of ZSM-5, as covered by the patent of Argauer and Landolt (64), is listed in Table 6. Note that the composition range covered in this patent indicates that both sodium and TPA are necessary for crystallization of ZSM-5.

II.B.1a Influence of Aluminum on the Synthesis of ZSM-5

Data in the literature indicate that alumina is not necessary for the synthesis of ZSM-5 (81). Excessive quantities of alumina in the synthesis gel; however, can hinder the crystal growth process to the point where complete crystallization is no longer achievable (64,72).

Table 5
ZSM-5 Gel Compositions in the $Na_2O/SiO_2/Al_2O_3/TPA/H_2O$ System.

Na_2O	SiO_2/Al_2O_3	TPA	H_2O	Reference
3.75	29	55.7	1486	64
12.50	90	9.4	2087	65,69
29.5	87.7	9.4	3491	72
160.7	24.4	314	14545	70
25.6	22	922	42240	82
----	100	40 to 60	8100	71

Note: values reported for Na_2O, TPA and H_2O are per 96 (Si+Al) atoms.

Table 6
Gel Composition Range for Synthesis of ZSM-5 (64)

SiO_2/Al_2O_3	5 to 100
OH^-/SiO_2	0.07 to 10.0
TPA/(TPA + Na)	0.2 to 0.95
H_2O/OH^-	10 to 300

Mostowicz and Sand (65) have shown an increase in the activation energy of nucleation, from 8.5 to 32.0 kcal/mol-K, upon reducing the gel phase SiO_2/Al_2O_3 ratio from 90 to 70. This data suggested to the authors that the ZSM-5 structure accommodates silicon preferentially. The influence of alumina present in the synthesis gel was studied in more detail by Ghamami and Sand (72). For the system $4(TPA)_2O\text{-}6(NH_4)_2O\text{-}Al_2O_3\text{-}28Si_2O\text{-}750H_2O$, only 38% crystallization was achieved in 152 hours at 180°C. Increasing the SiO_2/Al_2O_3 ratio to 59 in the same system brought about 92% crystallinity in 102 hours. The authors noted that as the SiO_2/Al_2O_3 ratio was increased from 49 to 59, 69, 90 and ∞, the nucleation time was decreased and the crystallization rate was increased significantly. The change in SiO_2/Al_2O_3 ratio also altered the crystal morphology.

II.B.1b Influence of the Organic Cation on the Synthesis of ZSM-5

The organic cation present in the ZSM-5 synthesis gel supplies structure direction (77). A number of organic cations (listed in Table 4) have been found to direct the synthesis of ZSM-5. Kulkarni et al. (76) demonstrated the synthesis of ZSM-5 from triethyl-n-propylamine (TEPA) with the gel composition $4.38(TEPA)_2O\text{-}27.6Na_2O\text{-}Al_2O_3\text{-}87.7Si_2O\text{-}3262H_2O$. Crystals resulting from this gel composition were analyzed by X-ray diffraction, IR spectroscopy and conversion of methanol. The results of these analyses proved to be characteristic of ZSM-5. The rate of crystal growth using TEPA was compared to that using TPA, and the data showed that the TEPA rate was much slower than that of TPA. Also of note was that

the phase transformation of ZSM-5 to α-quartz was more rapid in the TEPA system.

Nakamoto and Takahashi (78) demonstrated the synthesis of ZSM-5 from oxyethyllactamide (OEL). Their study employed the synthesis gel composition[8] $13.7(Na,OEL)_2O$-Al_2O_3-$42.5SiO_2$-$936.4H_2O$-$11.0Na_2SO_4$ reacted under autogeneous pressure at 150°C. The ratio of sodium (from sodium hydroxide) to sodium plus OEL was varied from zero to one. Their study showed ZSM-5 to be formed exclusively only when the Na/(Na+OEL) ratio was between 0.6 and 0.7. When the ratio was between 0.7 and 0.85, both ZSM-5 and mordenite co-existed. At a ratio above 0.85, only mordenite was formed, while at a ratio below 0.6, no zeolite phase could be crystallized. The product ZSM-5 crystals synthesized from OEL were compared to ZSM-5 crystallized from TPA with the same gel composition. SEM showed a distinct difference in crystalline morphology. The X-ray diffraction pattern of the ZSM-5 crystallized in the OEL system showed resolution of the two peaks in the 2θ=23.00 region, while the TPA ZSM-5 showed only one broad peak. This result suggested to the authors that the OEL ZSM-5 was a more perfect crystal.

Hou and Sand (73) demonstrated that ZSM-5 could be synthesized in the presence of tetrabutylphosphonium chloride (TBP). The following synthesis gel composition was employed:

---

[8] The notation (Na,OEL) is used to signify the sum of Na plus OEL.

$$40(TBP)\text{-}(33\text{-}x)Na_2O\text{-}xK_2O\text{-}Al_2O_3\text{-}110SiO_2\text{-}7150H_2O\text{-}22H_2SO_4$$

In this study, x was varied between 0 and 33. Synthesis gels prepared from this composition were reacted at temperatures between 100 and 220°C. At temperatures between 100 and 130°C, ZSM-11 was formed exclusively, while at temperatures between 150 and 180°C, only ZSM-5 was formed. For these experiments, no specific values of x were reported. Their data also showed that when the ratio K/(Na+K) was 0.05 and above, ZSM-5 was more favorably produced.

ZSM-5 may be synthesized in the absence of organic cations (83,84). In the patent literature, Plank et al. (83) synthesized ZSM-5 by addition of seed crystals to the synthesis gel. The composition range covered by the patent is reported in Table 7. The examples in this patent showed that the best results were obtained whenever an alcohol was also present in the gel. Narita et al. (84) investigated the effects of acetone on the synthesis of ZSM-5 from seed crystals. The gel composition used in this study was[9] $15,20Na_2O\text{-}Al_2O_3\text{-}100SiO_2\text{-}4600H_2O$, with the quantity of seed crystals (0.19μ) employed being 0.36 wt%. The amount of acetone added to the synthesis gel was varied from 0 to 12% by weight. The purpose of acetone is to inhibit the excessive gelation of the reaction mixture. This study showed acetone was required in order to obtain complete crystallization. As shown in Figure 10, 4.7 wt% acetone appeared to be

---

[9] 15,20 is indicates that the Na_2O/Al_2O_3 ratios employed were either 15 or 20.

Table 7
Composition Range for Synthesis of ZSM-5 from Seed Crystals (83)

	Broad	Preferred
Seed	0.01 to 10%	1 to 6% (wt)
OH^-/SiO_2	0.07 to 1.0	0.1 to 0.8
H_2O/OH^-	10 to 300	10 to 300
SiO_2/Al_2O_3	5 to 100	10 to 60
ROH/Al_2O_3	0 to 400	0 to 300
NH_4OH/Al_2O_3	0 to 250	0 to 150

Note: R represents hydrocarbon of length 2 to 5

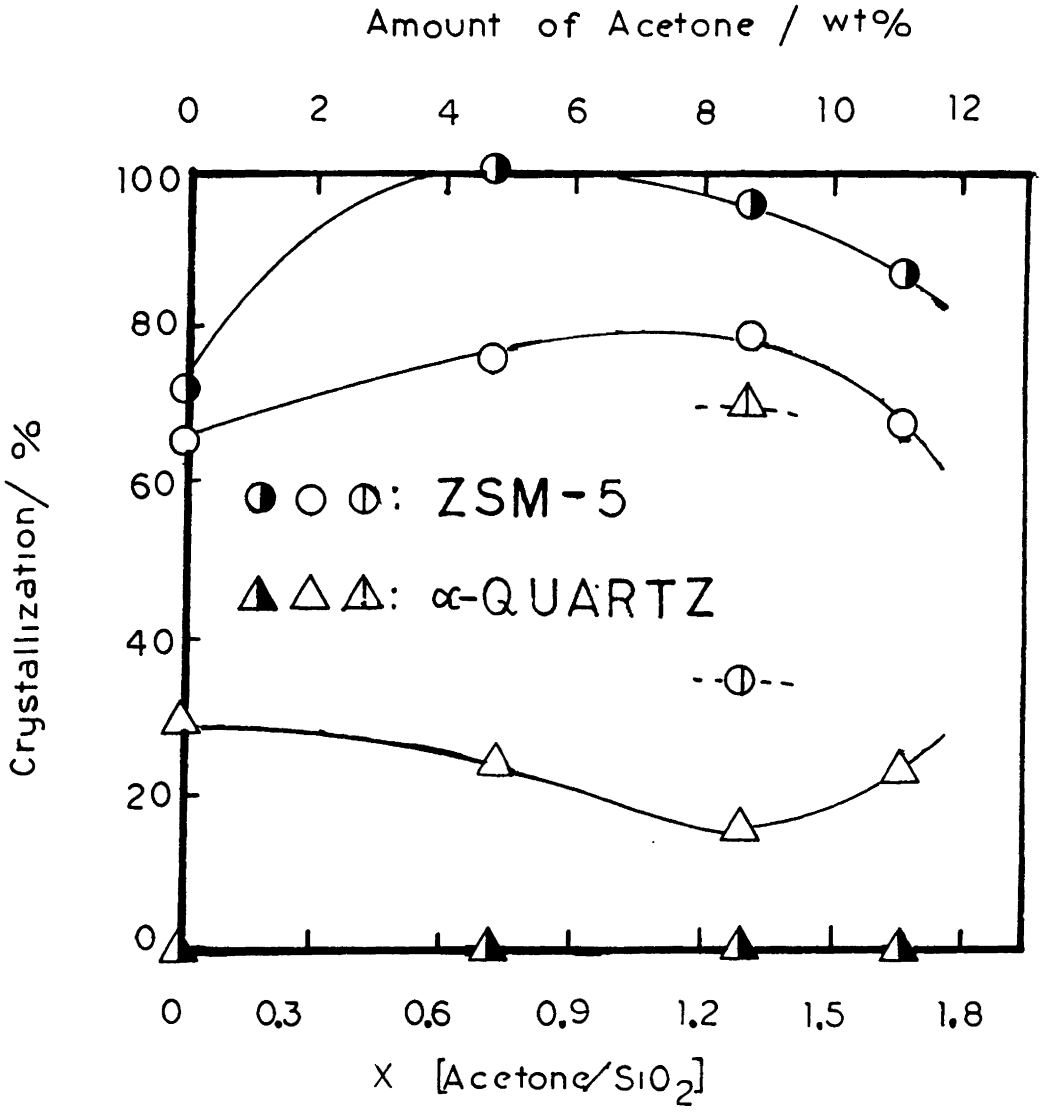

Figure 10: Effects of the Amount of Acetone on the Crystallization of ZSM-5 and α-quartz in the yNa_2O-0.01Al_2O_3-SiO_2-46 H_2O-x Acetone Seed System at 190 C (84).

◑ ▲ y = 0.15, time = 12 hrs;
○ △ y = 0.20, time = 24 hrs;
◐ ◭ y = 0.20, time = 72 hrs.

optimum. X-ray anlaysis of the ZSM-5 crystals grown from the seed crystals displayed a split in the 2θ=23.00 region. This split was not observed in the seed crystals. Therefore, the product crystals grown from the seed material were of high purity. The authors also showed that the addition of alumina to the synthesis gel is necessary, as no crystalline yield was obtained from an alumina free gel.

II.B.1c Influence of the Alkali Cation on the Synthesis of ZSM-5

The effects of the alkali cation type on the synthesis of ZSM-5 have been studied (65,79). Mostowicz and Sand (65) attempted ZSM-5 synthesis with Na, Li, K, Ca, Sr and Ba hydroxides employing the gel composition $12(Me)_2O$-Al_2O_3-$90SiO_2$-$4.5(TPA)_2O$-$2000H_2O$, where Me refers to the alkaline earth cation. For the sodium, lithium and potassium systems, the time required to achieve nucleation differed, but the rates of crystal growth were fast in all cases. In the barium and strontium systems, complete crystallization was not achieved, with 80% being the maximum observed. In no case was ZSM-5 crystallized from calcium hydroxide.

Nastro and Sand (79) studied the influence of lithium, sodium and potassium in the synthesis of ZSM-5. The gel compostion employed by the authors was $4(TPA)_2O$-$38(NH_4)_2O$-$x(Li,Na,K)_2O$-Al_2O_3-$59Si_2O$-$750H_2O$ with x assuming values of 0.50, 1.0 and 1.5 for lithium; 0.25, 0.85 and 1.5 for sodium and 0.32, 1.0 and 1.5 for potassium. Syntheses were conducted at 177°C. The crystals obtained in the different cation systems did not display the same X-ray diffraction patterns, as the relative intensities

of the peaks varied. The reason for this change was not investigated. SEM's of the product crystals showed crystals grown in the sodium and potassium system to be nearly equivalent in size and morphology, while crystals produced in the lithium system were much larger and untwinned (lath-shaped). Complete crystallization was not achieved in the lithium system, as portions of unreacted gel remained. From these results it was theorized that fewer nuclei formed in the Li_2O-$(NH_4)_2O$ system.

The synthesis of ZSM-5 in the $(NH_4)_2O$ system was investigated by Ghamami and Sand (72). This study included the determination of the kinetics of crystallization and the crystal growth of ZSM-5 as a function of $NH_4/(NH_4+TPA)$. The gel compostion was:

$$x(TPA)_2O\text{-}(10\text{-}x)(NH_4)_2O\text{-}Al_2O_3\text{-}59SiO_2\text{-}750H_2O$$

where x was either 0, 2, 4, 6, 8 and 10. Results of this study showed that as the $NH_4/(NH_4+TPA)$ ratio decreased, the induction period decreased and the rate of crystal growth became more rapid. At x = 0 (no TPA), no crystallization could be achieved. This indicated that the ammonium hydroxide did not perform an important role in the formation of ZSM-5; i.e. the NH_4 did not appear to supply structure direction, as its presence in the synthesis gel hindered the crystallization process. It is also important to note that upon calcination, the resulting ZSM-5 synthesized in the $(NH_4)_2O$ system were in the protonated form.

II.B.2 ZSM-5 Crystal Growth Mechanism

The mechanism which governs the crystallization of ZSM-5 has received considerable attention due to the wide range of compositions and reactants from which this material can be synthesized. The role of the various reagents which make up the ZSM-5 synthesis gel is not well understood. For example, the organic cation is thought to provide the structure direction and therefore be essential in the synthesis of ZSM-5. Additional studies have shown that structure direction may be supplied from seed crystals. Thus, the presence of the organic cation in the gel is not required (83,84).

The quarternary ammonium cation can influence the product zeolite in three ways. The organic cation can influence the gel chemistry so that 1) a different zeolite structure is produced; 2) zeolite will crystallize where the reaction mixture would otherwise remain amorphous; 3) the chemical composition of the product zeolte is altered (145). The organic cation is postulated to have a structure directing effect; i.e. it orders about itself silicon and aluminum atoms. The structure directing effect has been termed "templating" due to the organic cation's ability to "template" the channel system[10] (84).

---

[10] The ZSM-5 material is a classic example of "templating", as its 3-dimensional 10-ring channel system allows the nitrogen body of the TPA to occupy the channel intersections, with the "arms" stretching into the channels (77,85,86).

The growth mechanism of ZSM-5 appears to involve Si,Al clathration of the hydrophobic organic cation (81). That is, the tetra-alkylammonium cation orders around itself silicate and aluminate tetrahedral units. This ordering is accomplished by successive displacement of hydrogen bonded water (84). The clathrated tetra-alkylammonium cation has been postulated to be the precursor in the synthesis of ZSM-5 (81,87).

Scholle et al. (87) employed various spectroscopic techniques in an attempt to understand the synthesis mechanism of ZSM-5. The crystallization of the synthesis gel employed in this study required 8 days. In the early stages of the crystallization process (0.5 to 1 day), the presence of double 5-membered rings was shown, along with an aluminum rich aluminosilicate phase. A schematic of the double 5-membered ring is shown in Figure 11. The presence of the double 5-membered rings is consistent with the findings of Boxhoorn et al. (82). These double 5-membered ring structures have been postulated to be formed via interactions between gel phase silica and alumina species and the TPA cation (82). The double 5-membered ring does not stabalize the TPA, however[11]. Stabilization occurs when the double 5-membered rings unite, forming what the authors refer to as TPA-ZSM-5 entities. These species are postulated to be between 20 and 50 Å (approximately the size of one unit cell). Jacobs et al. (88) have also shown the that the X-ray amorphous "ZSM-5 like" species are present in the early stages of the crystallization

---

[11] Stabilization implies that the TPA is trapped within the ZSM-5 channel structure.

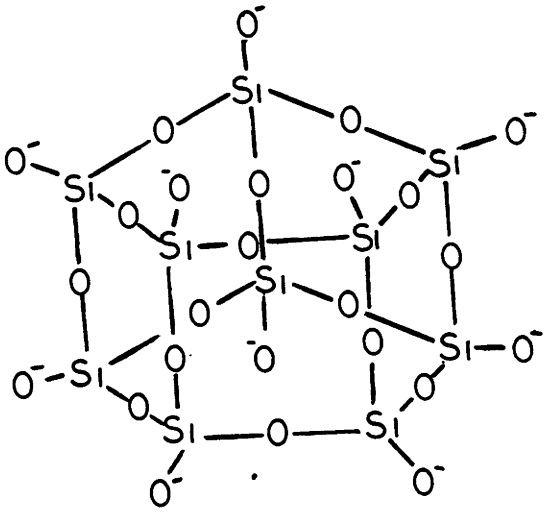

Figure 11: Schematic Representation of the Double 5-Membered Ring (82).

process, as illustrated in Figure 12. This figure shows that following 3 days, virtually all the gel phase Si,Al has been coordinated into ZSM-5 microstructures (what the authors refer to as X-ray amorphous ZSM-5). During the crystallization times of three to five days, all the TPA-ZSM-5 entities are formed prior to their combining to form larger crystals which can be detected by X-ray diffraction. The build-up of these large crystals is due to the combining of the TPA-ZSM-5 entities (87). This may explain the change in crystal size with time, as shown in Figure 13.

The crystallization process (or details of this process) as described by Scholle et al. (87), Flanigen et al. (81), Boxhoorn et al. (82) and Derouane et al. (84) have suggested that the TPA is responsible for ordering gel phase silicon and aluminum atoms. The presence of sodium in the ZSM-5 synthesis gel also plays an important role in the synthesis of ZSM-5. Nastro et al. (80) have shown that as the alkali metal cation concentration in the synthesis gel is increased, the number of TPA cations present per channel intersection decreases. Their work also shows that sodium favors the formation of secondary building units in solution. Thus, a complex interaction between sodium and TPA may exist. Additional studies involving the synthesis of ZSM-5 from seed crystals (83,84) suggest that sodium may play a structure directing role as well.

II.B.3 ZSM-5 Crystal Structure

The crystal structure of ZSM-5 was determined first by Kokotailo et al. (89) and reported in 1978. They determined the structure from model building, single crystal studies and powder X-ray diffraction data. A

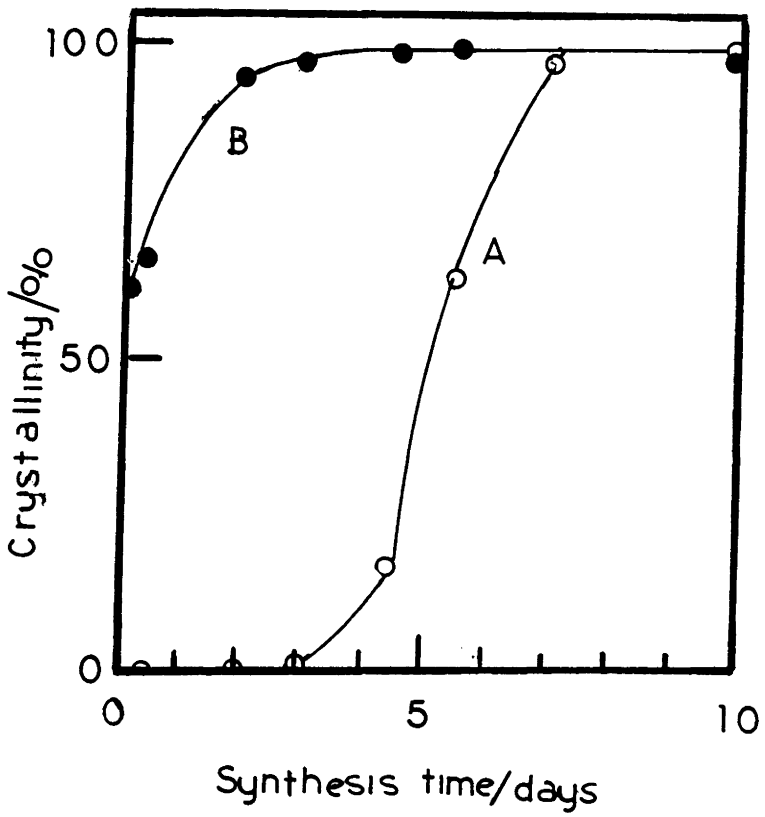

Figure 12: Change of the Crystallinity of ZSM-5 Materials with Time (88). A) X-Ray crystallinity; B) IR crystallinity.

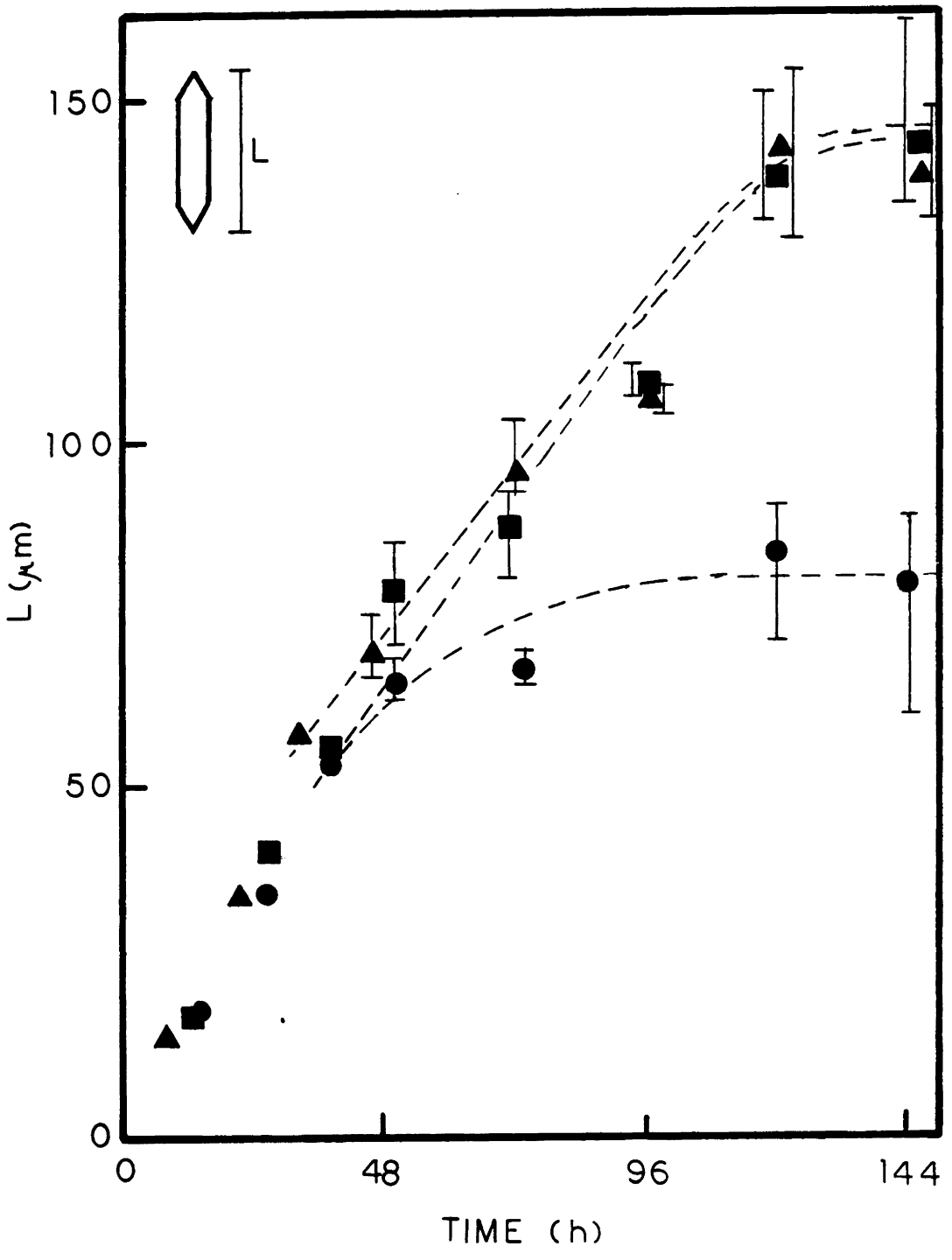

Figure 13: Length of the Crystals of ZSM-5 Produced in Systems with Li_2O (79). ● $0.5Li_2O$, ■ $1.0\ Li_2O$; ▲$1.5\ Li_2O$.

representation of the ZSM-5 structure is shown in Figure 14. As the figure shows, there are two interconnecting channel systems which allows for three dimensional mass transfer. One channel system is sinusoidal and runs parallel to the [001] plane while the second channel system is straight and runs parallel to the [010] plane. Both channel systems consist of ten membered rings, as can be seen from the skeletal diagram of the [010] plane shown in Figure 15. The sinusoidal channels are circular and measure 5.2±0.2 Å while the straight channels are elliptical and measure 5.7-5.8 Å X 5.1-5.2 Å (81). The crystal structure of ZSM-5 is orthorhombic (68,81). The unit cell of ZSM-5 consists of 96 T-atoms, with the unit cell composition being x Na-x Al-(96-x) Si-192 O-16 H_2O. x is typically less than 27 and is equal to 0 for the case of silicalite.

The crystal symmetry of ZSM-5 may be altered from orthorhombic to monoclinic (89-92) through various treatments. The X-ray diffraction patterns of the ZSM-5 in the two symmetries mainly differ by the appearance of a doublet at 2θ= 23.2° Additional doublets have also been observed at 2θ = 24.4°, 29.2° and 48.6° (91).

II.B.4 Physical properties of ZSM-5

The morphology of the ZSM-5 zeolite can vary according to the synthesis conditions employed (69). These crystals display morphologies ranging from sub-micron aggreates (93) to large, lath-shaped particles in excess of 100μ (79). Most commonly, the ZSM-5 crystals are euhedral (lath-shaped with penetration twin). Foger et al.(94) have noted that the morphology of ZSM-5 is an important property, as they have shown it

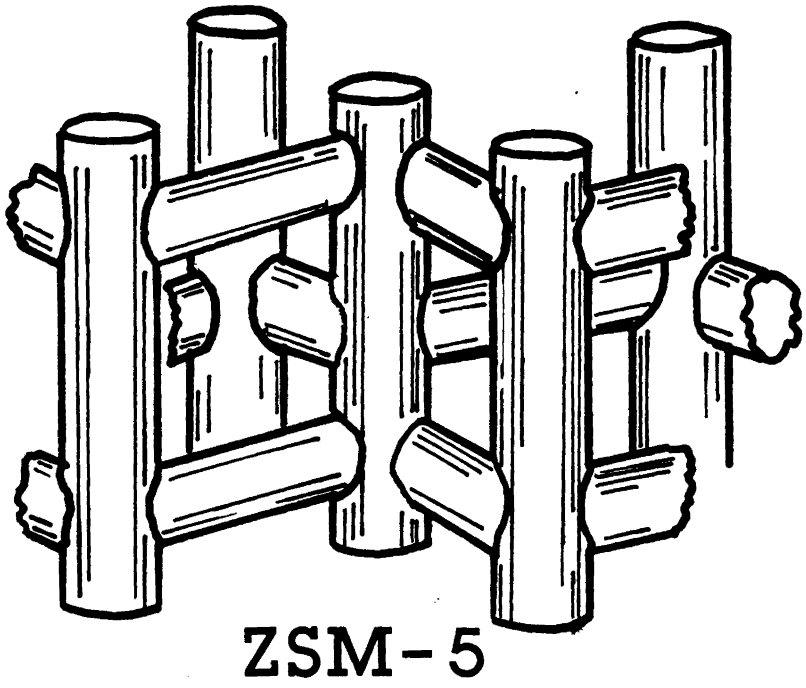

Figure 14: The Channel Structure of ZSM-5 (89).

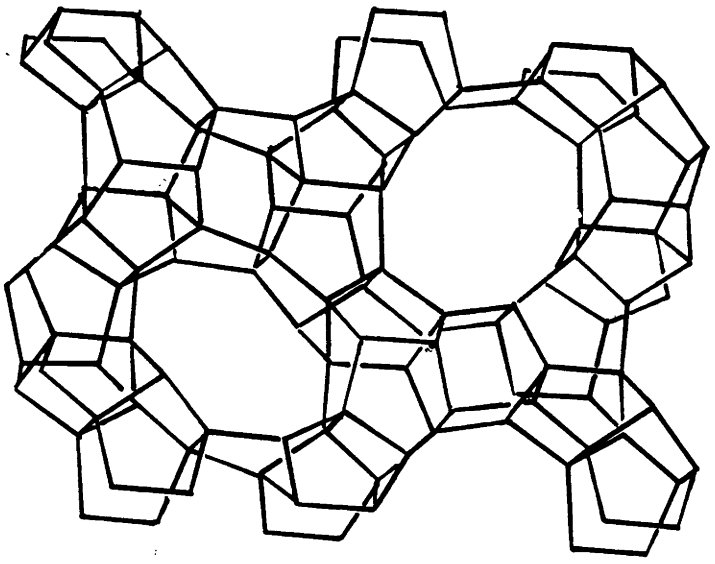

Figure 15: Skeletal Diagram of the (010) Face of the ZSM-5 Unit Cell (89). Oxygen atoms are not shown. T-atoms are represented by the intersection of lines.

to influence the catalytic and sorption properties. This is due to the relative lengths of the straight and zig-zag channels present in the crystal. Their results showed the straight channels to favor the transport of large molecules due to the increased tortuosity of the zig-zag channels.

The X-ray diffraction pattern of ZSM-5, unlike that of faujasite, is not altered significantly by the SiO_2/Al_2O_3 ratio (95). The crystal structure of ZSM-5 is typically indexed to orthorhombic symmetry, however, certain preparations can result in lowering the crystal symmetry to monoclinic (89-92). The characteristic X-ray diffraction patterns of ZSM-5 exibiting monoclinic and orthorhombic symmetry are shown in Figures 16A and 16B. Note that as the symmetry is lowered, the resolution in the $2\theta = 23.0°$ and 24.6° region has increased. The lack of resolution in this region is the result of lattice faults and defects, therefore, it has been suggested that crystals displaying the monoclinic symmetry are more "perfect" (78).

Infrared spectroscopy detects short order molecular interactions and thus distances. These distances are only slightly different for zeolites in the same group, thus making structure determination from IR spectroscopy impossible (60,96). None-the-less, IR spectroscopy is an important tool in the characterization of ZSM-type molecular sieves. The IR spectrum of ZSM-5 is shown in Figure 17. The band at 460 cm^{-1} has been assigned to the internal vibrations of Si,AlO_4 tetrahedra. This band is observed also in SiO_2 and quartz (60,96). The band at 550 cm^{-1} is char-

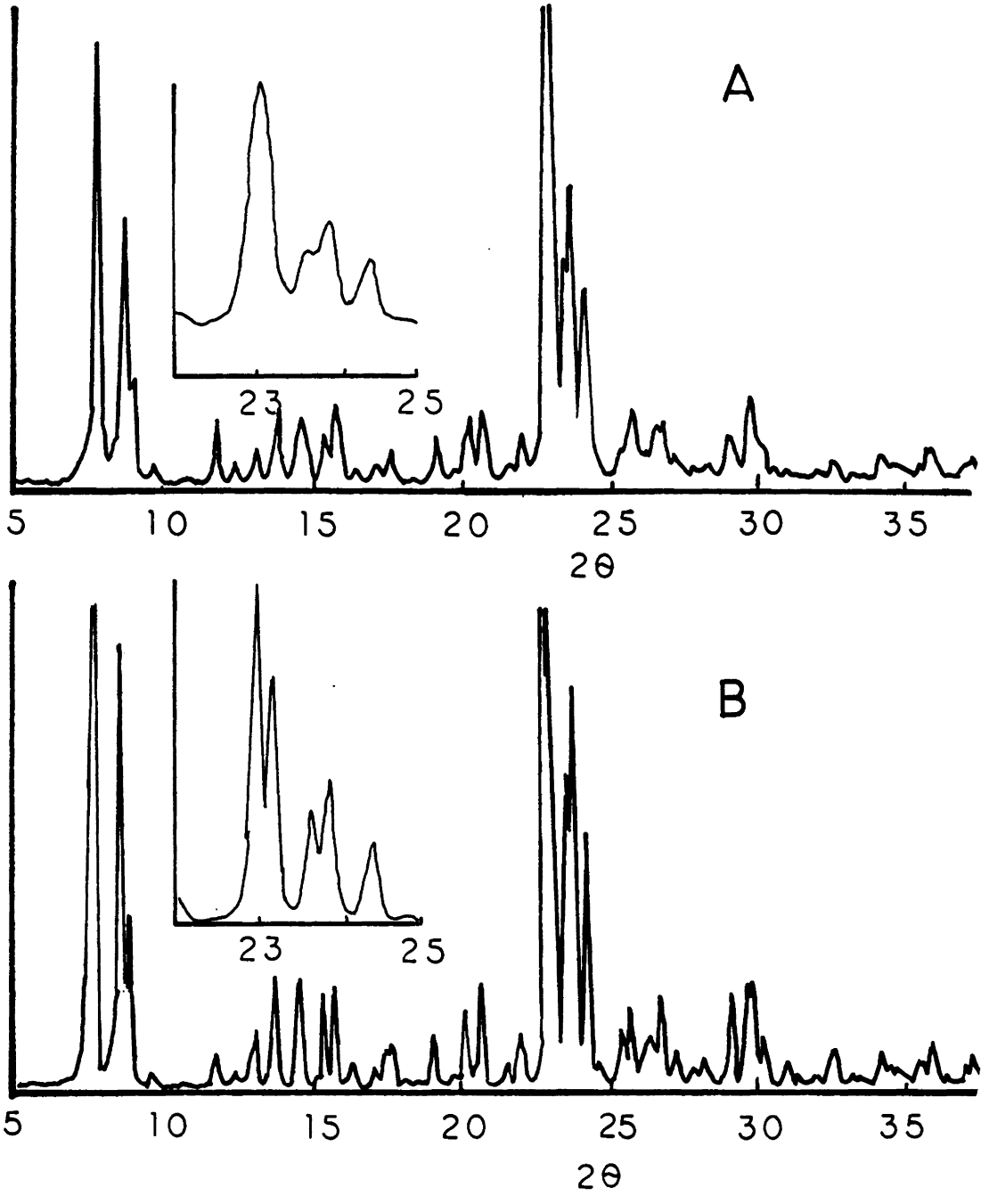

Figure 16: X-Ray Diffraction Pattern of ZSM-5 (78). A) Orthorhomb symmetry; B) Monoclinic symmetry.

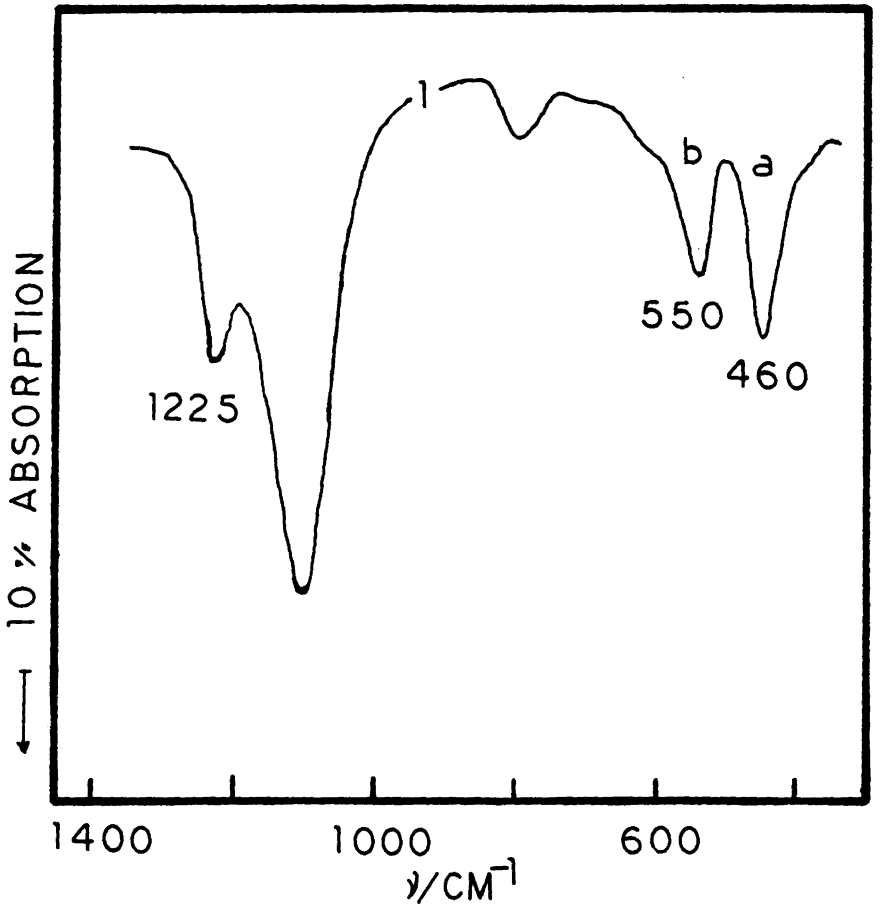

Figure 17: IR Spectrum of ZSM-5 (96). The bands labeled a and b are referenced in text.

acteristic of ZSM-type material (ZSM-5 and ZSM-11) and has been assigned to external vibration modes of chainletts of tetrahedra. The vibration occurring between 1200-1150 cm^{-1} is attributed to an external asymmetric stretching vibration (96). Because SiO_2 does not show an absorbance in the 550 cm^{-1} region, the ratio of the bands A to B (as labeled in Figure 15) has been shown to be an excellent probe for purity of the ZSM zeolites[12]. For well crystallized ZSM-5, the intensity of the bands ratioed A to B is approximately 0.70 (87,88,96). Van der Gaag et al. (97) have indicated that this ratio should be greater than 0.80 rather than 0.70. Thus, if amorphous SiO_2 is present or the ZSM-5 contains intergrowth with ZSM-11, the band ratio will be less than 0.70. The band present at 1225 cm^{-1} in Figure 17 is due to the presence of the five membered rings.

Unlike the A-type zeolites, ZSM-5 possesses excellent thermal stability, which is not highly dependent on the cation exchange form. ZSM-5 is stable in air at temperatures in excess of 1100°C (81). It is also highly resistant to the attack of most mineral acids (81).

Another characteristic property of ZSM-5 is it hydrophobic surface (81,95,98). This is a very important property, as with hydrophilic catalysts, water will cover the surface of the catalyst and prevent adsorption of organic molecules. With ZSM-5, the water will be repelled

---

[12] ZSM zeolites include ZSM-5, ZSM-8, Silicalite, ZSM-11 etc.

by the surface. The degree of hydrophobicity of ZSM-5 is a function of the SiO_2/Al_2O_3 ratio, as shown in Figure 18.

In the protonated form, ZSM-5 has been shown to be a strong acid catalyst, as demonstrated by its cracking activity of n-butane (99). The cracking activity of ZSM-5 reported in that study was comparable to acidified Y's and mordenites. The acidity of protonated ZSM-5 (H/ZSM-5) may be varied by varying the SiO_2/Al_2O_3 ratio (98). This is because increasing the silica content of the zeolite will result in stronger acid sites. For H/ZSM-5, the maximum in acidity was observed at a SiO_2/Al_2O_3 ratio of 94 (98). The acid form of ZSM-5 has also been found to catalyze such reactions as xylene synthesis (100), dehydration of methanol (7,101) and oligomerizaion (8).

One of the major concerns in acid catalysis is the solid's ability to resist coke formation. Resistence to coke formation is one of the most important properties of ZSM-5. This was demonstrated by Dejaifve et al. (101) in a study involving the methanol dehydration reaction. For this reaction, the H/ZSM-5 retained approximately the same activity over the course of the reaction (80 minutes) while H-offretite and H-mordenite were found to completely deactivate in less than 60 and 30 minutes, respectively. Analysis of the catalyst following reaction showed carboneous deposits to be formed primarially on the external surface of the ZSM-5. Coke precursors are polyaromatic and cannot be formed inside the ZSM-5 channels due to the restrictive transition state molecular shape selec-

Attention Patron:

Page 61 omitted from numbering

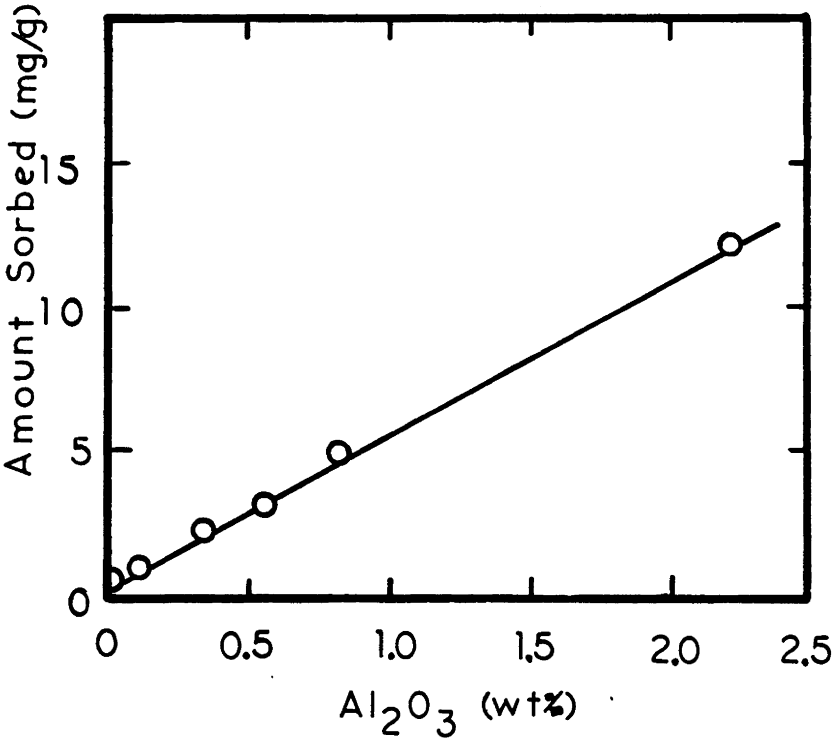

Figure 18: Effects of Aluminum Content on Water Sorption of H/ZSM-5 at P/P_o = 0.006 (95).

tivity of this zeolite. In other words, the intermediate species leading to the coke precursor cannot be formed due to size constraints.

The exchange of inorganic cations into ZSM-5 shows a different behavior than that observed for the low silica zeolites (e.g. faujasite and zeolite A). This behavior was demonstrated by Chu and Dwyer (12). They found the selectivity towards monovalent inorganic cations to be $Cs^+ > H_3O^+ > NH_4^+ > K^+ > Ag^+ > Na^+ > Li^+$. This observed selectivity is proportional to the bare ionic radii; that is, the greater the radii, the greater the selectivity. This could be due to the weak anionic field strength of the ZSM-5 cavities. It was also shown that the higher the valency of the cation, the lower its selectivity towards exchange in ZSM-5. This behavior is the direct opposite of that observed for low silica zeolites. This lower selectivity with increase in charge was attributed to either the greater hydrated energy of the polyvalent cation or the low AlO_4 tetrahedra site density.

Olson et al. (95) have shown a stoichiometric correlation to exist (1 Cs^+ per AlO_4^- site) in the exchange of Cs^+ for H^+ in H/ZSM-5 over a range of SiO_2/Al_2O_3 ratios. This study shows that the cation exchange properties of ZSM-5 are related to the aluminum content of the material. Chester et al. (102) noted that the as-synthesized ZSM-5 contains cations (Na^+ + TPA^+) well in excess of that required to balance the tetrahedral framework aluminum. They also noted that the total cation content appeared to be independent of the SiO_2/Al_2O_3 ratio. These sites numbered approximately 2 to 4 per unit cell. The authors postulated the aluminum

independent cation exchange sites to be either occluded silicate ions or trapped OH^- or $SiOH^-$ which are part of the framework but not associated with aluminum atoms. The authors note that these sites are easily destroyed by an acid medium, such as cation exchange with NH_4^+, thus leaving only aluminum dependent exchange sites.

The pore volume of ZSM-5 has been measured by oxygen adsorption (81,95). The pore volume for ZSM-5 was found to be 0.18 cm^3/g, which is slightly less than that determined for silicalite, 0.19 cm^3/g (81,95).

The cation form of ZSM-5 has been shown by Wu and Ma (103) to influence the adsorption properties of ZSM-5. The authors measured the equilibrium adsorption of benzene, n-hexane, p-xylene, methanol and dimethylether over ZSM-5 at 30°C as a function of the charge balancing cation. The cations which the authors investigated were Li, Na, K, Rb and Cs. As was expected, the adsorption capacity decreased as the cationic radii was increased, however, the rate of diffusion of these hydrocarbons was not effected. This lead the authors to conclude that the cations were located at the channel intersections, not blocking the pore openings.

ZSM-5 is accessible to branched hydrocarbons, aromatic hydrocarbons up to the size of durene (1,2,4,5-tetramethyl benzene) and long chain hydrocarbons, based on adsorption and reaction data. The largest branched hydrocarbon which may gain access to ZSM-5 is neopentane (kinetic diameter of 6.2Å), as small quantities have been adsorbed at room temperature (81).

Xylenes, tri and tetra substituted methyl benzenes have been observed in the product stream following the reaction of H/ZSM-5 with methanol. These hydrocarbons possess kinetic diameters greater than what the channel system appears to be capable of accommodating. Foger et al. (94) has suggested that this effect may be due to the molecules "adjusting" so as to fit the cross section of the channel or the molecule being compressed by the field within the channels. For straight chain hydrocarbons, there does not appear to be a "cut-off", as Garwood (8) has shown that linear hydrocarbons greater than C_{30} have been formed via oligomerization of terminal olefins over H/ZSM-5.

II.B.5 Transition Metal Incorporation Techniques with ZSM-5

There are three techniques presented in open literature which have been reported to produce intrazeolitic transition metals with ZSM-5. These include cation exchange, carbonyl sublimation and synthesis of ZSM-5 in the presence of transition metal substrates. The majority of the transition metal ZSM-5's prepared by cation exchange and carbonyl sublimation were in the neighborhood of 5 to 10 wt% metal (2,3,17,18,19). The primary use of these catalysts was for Fischer-Tropsch chemistry. Although the authors of some of these studies concluded that the reaction chemistry was due to intrazeolitic metals, the majority of these studies did not deal with the location of the metal (surface or internal).

An extensive study involving the ion exchange of cobalt(II) nitrate with ZSM-5 has been performed by Rao (2) and Stencel et al. (3). In these studies, Co/ZSM-5 was prepared up to 9 wt% cobalt. Following cation ex-

change, the two samples (5.9 and 9.0 wt% cobalt) were analyzed by X-ray diffraction. The results of these analyses showed crystallites of cobalt oxide to be present on the surface of the ZSM-5. These crystallites were approximately 250 to 300 Å in size (3). The 9.0 and 5.9 wt% samples were then washed with a dilute HCl solution so as to remove the surface cobalt crystallites. Chemical analyses performed on these crystals revealed the cobalt loading to be 1.2 wt%, regardless of the initial coblalt content (2). X-ray analysis of the washed materials indicated no crystallites to be present on the zeolite surface. The XPS spectra of the Co2p(3/2) photoelectron region displayed a higher than normal binding energy of 783.2 eV, which suggested that the cobalt was in a highly oxidized environment (3). This catalyst was then exposed to Fischer-Tropsch reaction conditions and found to be inactive. Following contact with H_2 at 450°C, the XPS spectrum showed only a slight shift in binding energy of the cobalt (0.7 eV), indicating that the cobalt could not be reduced. From these results the authors concluded that inside the ZSM-5 are highly dispersed Co^{2+} species. This study suggested that only a portion of the cobalt could be cation exchanged into the ZSM-5.

Dhere and DeAngelis (6) also performed an indepth characterization of Co/ZSM-5 prepared both by cobalt(II) nitrate exchange and cobalt carbonyl sublimation. Both materials were approximately 9.0 wt% cobalt following impregnation. For the cobalt nitrate exchange, X-ray diffraction analysis revealed the presence of 350 Å particles of Co_3O_4 particles on the surface. The catalyst prepared by sublimation of cobalt carbonyl yielded a very fine dispersion of cobalt oxide, which was not

detected by X-ray. Following reduction with hydrogen, cobalt particles of 150 A were observed on the surface of this material.

ZSM-11 possesses near identical properties as ZSM-5, with the exception that its channel system consists of two straight channels whereas the channel system of ZSM-5 consists of straight and zig-zag channels. It was shown by Shannon et al. (4) that at a 1.6 and 0.9 wt% rhodium loading, rhodium could only be partially exchanged into ZSM-11.

In addition to the cobalt studies, Rao (2) performed experiments which lead to a well characterized Fe/ZSM-5. These materials were prepared by sublimation of $Fe_3(CO)_{12}$ and exchange with iron nitrate solution. Analysis of the resulting Fe/ZSM-5 by X-ray diffraction showed that both preparations resulted in iron on the surface, as evidenced by the >60Å particles of γ-Fe_2O_3.

Attempts to incorporate transition metals into ZSM-5 during crystal growth have been undertaken (20,21,22). Sano et al. (20) added Fe_3O_4 to the ZSM-5 synthesis gel in an effort to synthesize intrazeolitic iron for Fischer-Tropsch catalysis. In their preparations, the ratio of iron in the gel to product ZSM-5 was 0.33 (1.33 in one instance). Analysis of the material following synthesis showed Fe_2O_3 crystals of appreciable size (peaks observed in the X-ray diffraction pattern). The catalyst was then washed in a dilute HCl solution for 5 days. Following this washing, no Fe_2O_3 peaks were present in the X-ray pattern. XPS analysis of the washed material showed only traces of iron to be present in the superfi-

cial region (approximately 50 Å). The washed Fe/ZSM-5 was then ground, and the XPS spectra was again recorded. This spectra showed an appreciable quantity of Fe to be present while the intensity of the silicon peak remained unchanged. From this analysis, the authors concluded that the Fe_2O_3 crystallites were "enveloped" in the ZSM-5. CO hydrogenation activity was then recorded for this material and the catalytic results were compared to a physical mixture of Fe_2O_3 and H/ZSM-5. The results of this study showed the Fe/ZSM-5 to be more selective in the C_2-C_5 region. This behavior was attributed to the shape selective characteristicts of the ZSM-5.

Rankal and Valyocalk (22) describe a procedure for preparing transition metal containing ZSM-5 by employing transition metal organic cations, which are shown in Figure 19. The transition metals were shown to be incorporated into the ZSM-5 structure during crystal growth. The metals claimed by the patent are copper, cobalt, lithium, vanadium, iron and ruthenium. All reported preparations require large quantities of transition metal organic cations. It should be noted that these orgainc cations, as shown in Figure 19, are too bulky to fit into the ZSM-5 channel system. Thus, their incorporation is more than likely the result of the molecules undergoing some sort of degradation during the synthesis process.

Dodwell (21) performed syntheses of ZSM-5 in the presence of transition metal hydroxides. The metals investigated in his study were iron, nickel, copper, chromium, platinum, paladimun, rhodium, ruthenium, cobalt

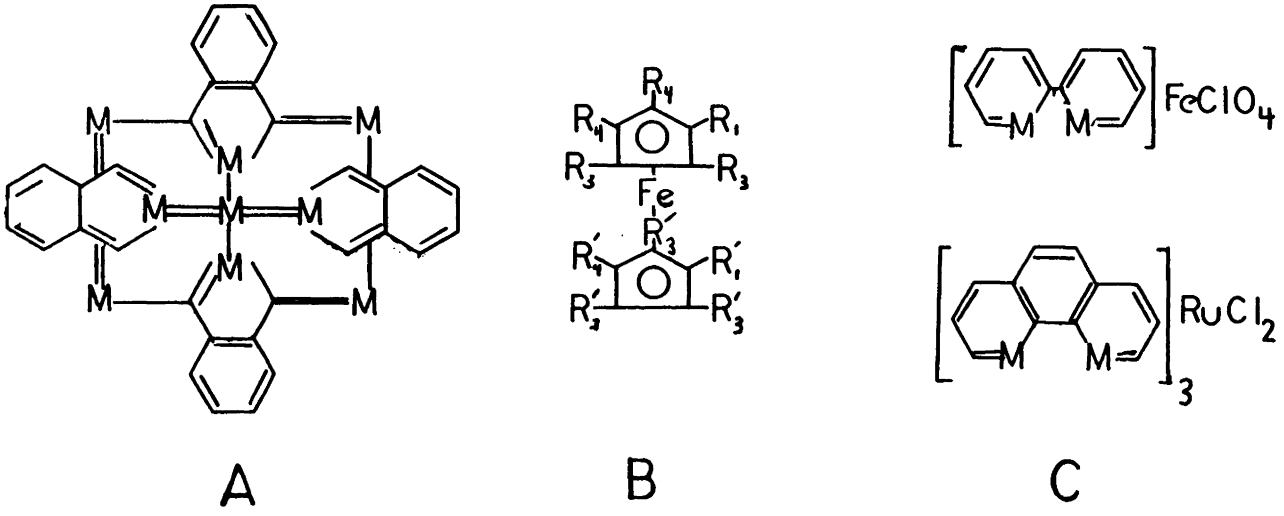

Figure 19: Transition Metal Organic Cations Employed in the Synthesis of ZSM-5 (22).

and tin. With the exception, of cobalt, ruthenium and chromium, the presence of the transition metal in the synthesis gel did not impede the crystal growth rate. Visual inspection of the product crystals showed them to be speckled with clumps of amorphous metal oxides. Microprobe analysis showed regions of high concentrations of transition metal, while the surface showed a substantial concentration of the transition metal. Analysis of internal layers of the ZSM-5 crystals showed that small quantities of the transition metal had in fact been incorporated during the crystal growth process.

II.C Olefin Hydrofomylation by Zeolite Catalysts

The hydroformylation of 1-hexene proceeded according to the reaction sequence shown in Figure 20. As the figure indicates, the two side reactions of 1-hexene which may occur are hydrogenation and skeletal isomeration. In addition, the isomer hexenes (t,c-2-hexene and t,c-3-hexene) may undergo hydroformylation to yield the product aldehydes shown in Figure 20. The hydroformylation of internal olefins proceeds much slower than that of terminal olefins (23). These alkenes may undergo hydrogenation to yield n-hexane. Another reaction which may occur involving product aldehydes is the aldol condensation reaction. In this reaction, to aldehydes combine to produce an ether. An example of this reaction is shown in Figure 20. The product aldehydes may also be hydrogenated to alcohols. Both the aldol condensation reaction and the hydrogenation of aldehydes are favored at higher reaction temperatures (23). A detailed review of non-zeolites supported hydroformylation cat-

1-Hexene Hydorformylation:

$CH_3(CH_2)_3CH{=}CH_3 + H_2 + CO \longrightarrow CH_3(CH_2)_3CH_2CH_2CHO$ heptanal

$\longrightarrow CH_3(CH_2)_3CHCH_3$ (CHO) 2-methyl hexanal

1-Hexene Isomeration:

$CH_3(CH_2)_3CH{=}CH_3 \longleftrightarrow CH_3CH_2CH_2CH{=}CHCH_3$ c,t-2-hexene

c,t 2-hexene $\longleftrightarrow CH_3CH_2CH{=}CHCH_2CH_3$ c,t-3-hexene

Hydroformylation of Internal Olefins:

c,t-2-hexene $\longrightarrow CH_3(CH_2)_3CHCH_3$ (CHO) 2-methylhexanal

$\longrightarrow CH_3CH_2CH_2CHCH_2CH_3$ (CHO) 2-ethylpentanal

c,t-3-hexene $\longrightarrow CH_3CH_2CH_2CHCH_2CH_3$ (CHO) 2-ethylpentanal

Aldol Condensation:

$H_2 + 2\ CH_3(CH_2)_4CH_2CHO \longrightarrow [CH_3(CH_2)_4CH_2CH]_2O + H_2$

Hydrogenation of Alkene:

Alkene $+ H_2 \longrightarrow CH_3(CH_2)_4CH_3$ n-hexane

Hydrogenation of Aldehyde:

$CH_3(CH_2)_3CH_2CH_2CHO + \frac{1}{2}H_2 \longrightarrow CH_3(CH_2)_3CH_2CH_2CHOH$

Figure 20: Possible Reactions of 1-Hexene.

alysts have been presented by and Wender and Pino (23). Since it was the focus of this study to investigate the hydroformylation of rhodium zeolite catalysts, the literature review will be focused in this area.

Rode (25) and Mantovani et al. (24) have postulated that zeolite encapsulated rhodium carbonyls will have certain advantages over homogeneous catalysts. When employing homogeneous catalysts, separation of catalyst and product can be costly. By "hetrogenizing" the homogeneous catalyst, product/catalyst separation becomes trivial. Also, in theory at least, the encapsulated rhodium species would be capable of higher temperatures of operation which would allow for greater catalyst activity. It has also been postulated that these catalysts would be capable of maintaining the high selectivity associated with homogeneous catalysts. Faujasite (zeolites X and Y) has received considerable attention as a support for rhodium hydroformylation catalysts (24,25,28,29,104). Rode (25) has stated that ideally, the transition metal encaged within the faujasite type zeolite will form a cluster within the supercage, where it will be unable to diffuse from the structure due to tertiary size. The cage structure of faujasite is shown in Figure 21. As the figure shows, the 13Å supercage is entered through 8Å ports. This type of structure is postulated to provide a suitable "cage" for which a rhodium cluster may be immobilized.

Mantovani et al. (24) cation exchanged rhodium into zeolite Na Y and employed the resulting catalyst in the hydroformylation of 1-hexene. This reaction was performed in the liquid phase using n-hexane as the solvent.

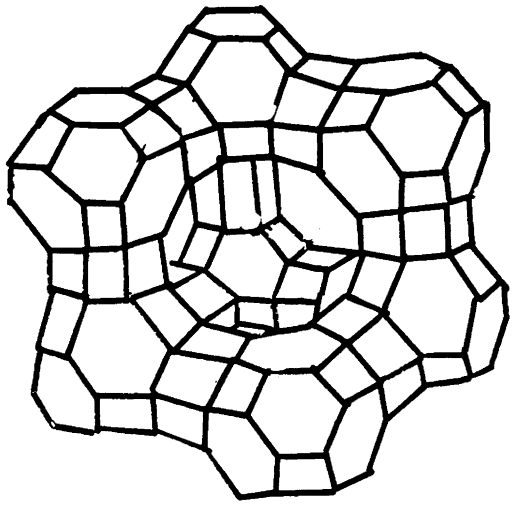

Figure 21: Structural Representation of Faujasite.

The reaction temperature was varied between 50 and 130°C with the overhead H_2/CO (1:1) pressure being varied between 30 and 100 atm. The RhNa Y catalyst was found to be active towards the hydroformylation of 1-hexene, achieving high conversions. At these conversions (>80%) all three possible aldehydes (heptanal, 2-methylhexanal and 2-ethylpentanal) were present. The regioselectivity (ratio of normal to branched aldehydes; n/b) is similar to that obtained from homogeneous catalysts at similar reaction conditions.

Rhodium loss and catalytic acvtivity were investigated over the course of eight catalytic cycles[13]. Rhodium was lost from the catalyst throughout the cycles while conversion of 1-hexene remained nearly constant following the first cycle. Rhodium elution from supported faujasite has also been reported elsewhere (27,28). Mantovani et al. (24) stated that the observed rhodium loss is not severe and that rhodium zeolites are promising as hydroformylation catalysts.

Davis et al. (105) performed liquid phase hydroformylation studies similar to those of Mantovani et al. In this study, the catalytic activity of RhX, RhY and RhA were investigated at 50°C under 300 atm CO/H_2 (1:1). Rhodium elution into solution was observed for all zeolites supported catalysts investigated in this study. The behavior of the RhCa A (2%) catalyst was almost identical to that of the homogeneous rhodium

---

[13] Catalytic cycle refers to the catalyst being used for a batch reaction run, recovered followed by reuse.

catalyst [$Rh_6(CO)_{16}$]. This indicated that the majority of the rhodium originally associated with zeolite A had eluted into solution. This result was not surprising, as rhodium cannot be cation exchanged into zeolite A (4).

Takahashi and Kobayashi (28) performed vapor phase hydroformylation studies involving ethylene and propylene. These studies were performed for the purpose of establishing whether all the active sites formed within the zeolite cavity are effectively utilized. A RhNa Y catalyst was employed in this study and was demonstrated to be active towards the hydroformylation of both olefins. Once steady-state was achieved, the catalyst activity remained constant for over one month. Based on a comparison of reaction rates between propylene and ethylene, the conclusion was drawn that two active hydroformylation sites existed on the Y zeolite. The first site is postulated to be at the external surface of the zeolite while the second site is postulated to be within the structure very near the external surface. Both ethylene and propylene are easily diffused into faujasite, and butyraldehyde was found to desorb from the zeolite faster than propionaldehyde. Thus, diffusion could not account for the greater reactivity of ethylene. Propylene hydroformylation was believed to have occurred at the external surface of the zeolite or within cavities very near the surface. Ethylene, due to its smaller molecular size, was able to undergo hydroformylation at interior as well as external sites. The inability of the internal sites to hydroformylate propylene was attributed to the active complex being very large.

Davis et al. (29) compared the reactivity of zeolites X and Y towards hydroformylation of propylene in the vapor phase. These catalysts were first exposed to flowing CO at 120°C followed by exposure to 1 atm propylene/H_2/N_2/CO (3/3/2/1) at 130-170°C. The regioselectivity of the X and Y zeolites were found to be comparable (2:1 and 1.9:1, respectively) at 150°C. Exposing the RhX catalyst to 3 atms of CO at 120°C resulted in the reduction of Rh(III) to Rh(I) while exposing the RhY catalyst to the same environment resulted in the reduction of Rh(III) to Rh(0).

Under steady state conditions, the reaction rate did not appear to decline over the remaining 20 hours of the run. This indicates that catalyst deactivity and/or rhodium loss are not significant. The selectivity obtained from these catalysts are a significant improvement over that obtained from homogeneous catalysts (n/b = 1). This improved selectivity may be due to zeolite acting as a ligand. Analysis of the catalysts following reaction by infrared spectroscopy indicated that different rhodium species were supported on the two zeolites. It is believed that zeolite X supported a geminal dicarbonyl, $Rh(CO)_2^+$, while zeolite Y supported Rh_6CO_{16}. It is postulated that these species may transform to yield the same hydroformylation catalyst, as the reaction rates of hydroformylation determined for Rh X and Rh Y were similar.

Rode (25) performed an extensive study into the vapor phase hydroformylation of propylene over rhodium faujasites. This work coupled infrared spectroscopy with reaction studies in an attempt to locate and understand the active rhodium species associated with the faujasite cat-

alysts. The results of this study showed that rhodium zeolites are able to form stable hydroformylation catalysts at 80-150°C under 1 atmosphere total pressure. Also, it was shown that the selectivity to n-buteraldehyde achieved with the zeolite catalysts is twice that achieved in the homogeneous phase. IR spectroscopy studies of the RhY catalyst exposed to CO indicated that $Rh_6(CO)_{16}$ is formed and is located within the α-cage. These studies have also suggested the possibility that $Rh(CO)_2^+$ species may be located within the α-cage of zeolite X; however, the location of this species was not proven conclusively. The formation of the catalytically active species as proposed by Rode are shown in Figure 22. As the figure shows the active species is postulated to be a rhodium hydride. A rhodium hydride active species has also been postulated for homogeneous rhodium hydroformylation catalysts (23). In addition, Rode has indicated that the utilization of zeolitic rhodium is poor, at 1 atm and that the active sites appears to be located on the exterior surface of the zeolite.

II.D Fischer-Tropsch Synthesis

II.D.1 Fischer-Tropsch Chemistry

In Fischer-Tropsch synthesis, syn-gas, namely CO and hydrogen, are converted to a wide variety of olefins and paraffins, along with

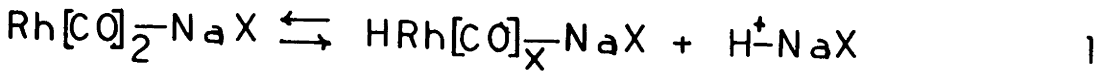

1

2

Figure 22: Proposed Reaction Pathway leading to the Formation of the Active Rhodium Complex Associated with Zeolites X and Y (25).

oxygenates. The stoichiometric Fischer-Tropsch reactions are as follows (30,32,40)[14]:

Paraffins: $nCO + (2n+1)H_2 = C(n)H(2n+1) + nH_2O$

Olefins: $nCO + 2nH_2 = C(n)H(2n) + nH_2O$

Alcohols: $nCO + 2nH_2O = C(n)H(2n+1)OH + (n-1)H_2O$

The above reactions are highly exothermic (30). There are also two important side reactions which normally accompany the Fischer-Tropsch synthesis. The first reaction is the water-gas-shift (WGS) reaction, which involves the reaction of water and CO to form CO_2 and hydrogen (30,31,106-109). This reaction proceeds according to:

WGS: $H_2O + CO = CO_2 + H_2$

For this reaction, the water is supplied from the Fischer-Tropsch synthesis. The second side reaction is the Boudouard reaction, where CO reacts to yield CO_2 and elemental carbon (30,31):

Boudouard: $2CO = CO_2 + C$

This reaction normally results in the poisoning of the active surface sites.

---

[14] The notation C(n) indicates carbon of length n

The Fischer-Tropsch reactions are typically carried out between 200 and 350°C under 1 to 20 atmospheres CO/H_2. The ratio of CO/H_2 in the feed stream is typically 1.0 to 0.2. Table 8 lists a range of Fischer-Tropsch reaction conditions as performed over various catalysts.

Group VIII transition metals have been found to be the most reactive towards Fischer-Tropsch synthesis. Vannice (33) studied the catalytic activity of all group VIII metals except osmium supported on η-Al_2O_3. In his studies, the effects of metal dispersion were taken into account when the turnover numbers were determined. All reactions were carried out at atmospheric pressure with the H_2/CO ratio being varied from 0.6 to 15. The reaction temperatures employed varied between 210 and 280°C. The rates of reaction for the various metals at 275°C are reported in Table 9. As the table shows, the activity of the metal decreases according to the series Ru>Fe>Ni>Co>Rh>Pd>Pt>Ir. This series may be misleading, as the catalyst loading employed by Vannice varied considerably. Additional studies (10,11,34) have shown reaction rates of supported metal catalysts to be influenced by the metal loading. In some instances, increases in reactivity of over two orders of magnitude have been reported for a 2 to 3 fold change in catalyst loading (11).

Ruthenium was observed to produce the highest average molecular weight hydrocarbons while nickel, palladium, iridium and platium yielded primarially methane. The ordering of the metals based on the average molecular weight of the hydrocarbons was Ru>Fe>Co>Rh>Ni>Ir>Pt>Pd. Also,

Table 8
Selected Fischer-Tropsch Reaction Conditions

Catalyst	Temperature	Pressure	H_2/CO	Reference
Ru Y	200°C	10 atm	3/2	110
Co/SiO_2	225-400	1	2/1	34
Co/TiO_2	250	10	33/5	111
Co,Fe/ZSM-5	280	20	2/1,1/1	2,3,18,112,113
Fe+H/ZSM-5	320	13.6	2/1	19
Fe Y	285	NR[1]	1/1	114
CoCd A	150-287	6	1/1	40
Ru Y	220	1	2/1	115

[1] Not reported

Table 9
CO Hydrogenation Kinetics of Supported Transition Metals (33)

Catalyst	N X 10^3
5% Ru/Al_2O_3	325
15% Fe/Al_2O_3	160
5% Ni/Al_2O_3	38
2% Co/Al_2O_3	28
1% Rh/Al_2O_3	17
2% Pd/Al_2O_3	13
1.75% Pt/Al_2O_3	3.4
2% Ir/Al_2O_3	2.6

Note: Turnover number in units of moles CO reacted per site per second at 275°C.

gasoline range hydrocarbons are usually most abundant with iron, cobalt and ruthenium catalysts (2,3,10,17,18,109,112,116).

II.D.2 Hydrocarbon Product Distribution

The hydrocarbon product distribution obtained when CO and hydrogen are reacted over supported transition metal catalysts usually follows a log-normal behavior, ofter referred to as Schultz-Flory behavior (10,11,17,34,117). The mole fraction of hydrocarbon produced of length n can be predicted from the following equation:

$$\text{Log}[M(n)] = n\text{Log}\alpha + \text{Log}[(1-\alpha)/\alpha]$$

where M(n) is the mole fraction of C(n), n is the chain length and α is the chain growth probability. α is defined as the rate of chain propagation divided by the rate of propagation plus termination (116). This equation is derived from polymerization kinetics and is presented in detail elsewhere (118). Figure 23 illustrates a typical Schultz-Flory distribution for hydrocarbons produced over Co/Al_2O_3. This figure compares the product distribution obtained from two different catalysts with chain growth probabilities of 0.9 and 0.7. Note from this figure that the larger values of α yields a larger quantity of higher molecular weight hydrocarbons. Note also from this figure that both the C_1 and C_2 fraction do not fit the Schultz-Flory model, as the methane fraction is greater than expected while the C_2 fraction is less than expected. This behavior has been observed by several investigators (10,11,17,116,118). The

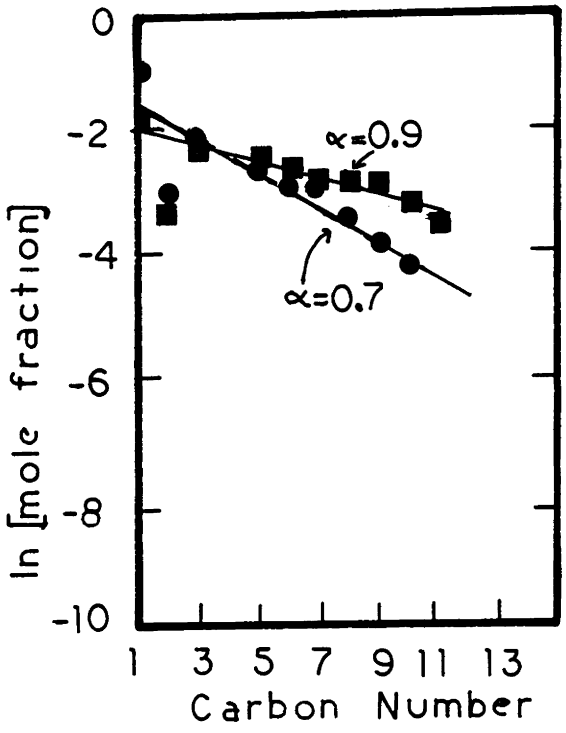

Figure 23: Typical Schultz-Flory Product Distribution (11). Co/Al_2O_3 catalyst reacted at 200 C under 1 atm CO/H_2 (2/1). ● 3% cobalt and ■ 8% cobalt.

higher than expected yield of methane has been attributed to the existence of a second set of sites capable of forming only methane. The higher than expected methane yield has also been attributed to hydrogenolysis of light olefins (116). The lower than expected yield of C_2 has been attributed to the insertion of ethylene into growing chains (116).

The product distribution obtained from supported metal Fischer-Tropsch catalysts typically consists of linear α-olefins and n-paraffins (109,119,120). The olefin to paraffin ratio is dependent on both the H_2 partial pressure (121) and the reaction pressure (120,121). Kellner and Bell (121) have shown that for Ru/Al_2O_3 catalysts, the olefin/paraffin ratio decreased with increasing H_2 partial pressure. This was attributed to the greater fraction of adsorbed hydrogen present on the catalyst surface. For these same catalysts, Kellner and Bell (121) noted that increasing the reaction temperature from 180 to 250°C also altered the olefin/paraffin ratio. At 1 atm H_2/CO (3/1) a maximum in the olefin/paraffin ratio was observed at 255°C. For ruthenium supported in Na Y, Chen et al. (120) observed that the olefin/paraffin ratio decreased over the temperature range of 220-320°C, as shown in Figure 24.

The chain growth probability, α, can greatly influence the hydrocarbon product distribution, as illustrated in Figure 25. As this figure shows, large values of α result in a greater fraction of higher molecular weight hydrocarbons. The chain growth probability can be influenced by temperature and H_2/CO ratio (116). Table 10 reports the effects of temperature on α for a ruthenium catalyst (the support type is

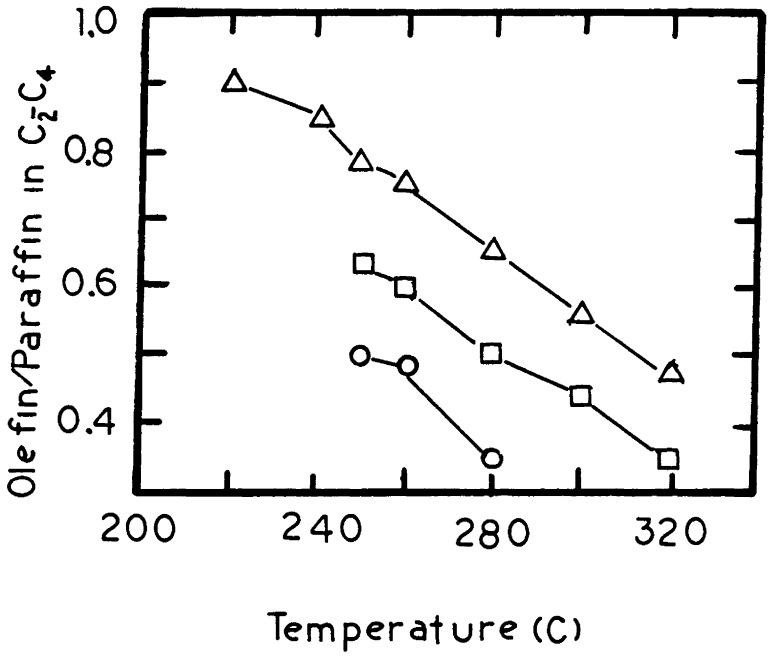

Figure 24: Influence of Temperature on Olefin/Paraffin Ratio of three different Ru/Al_2O_3 Catalysts (120).

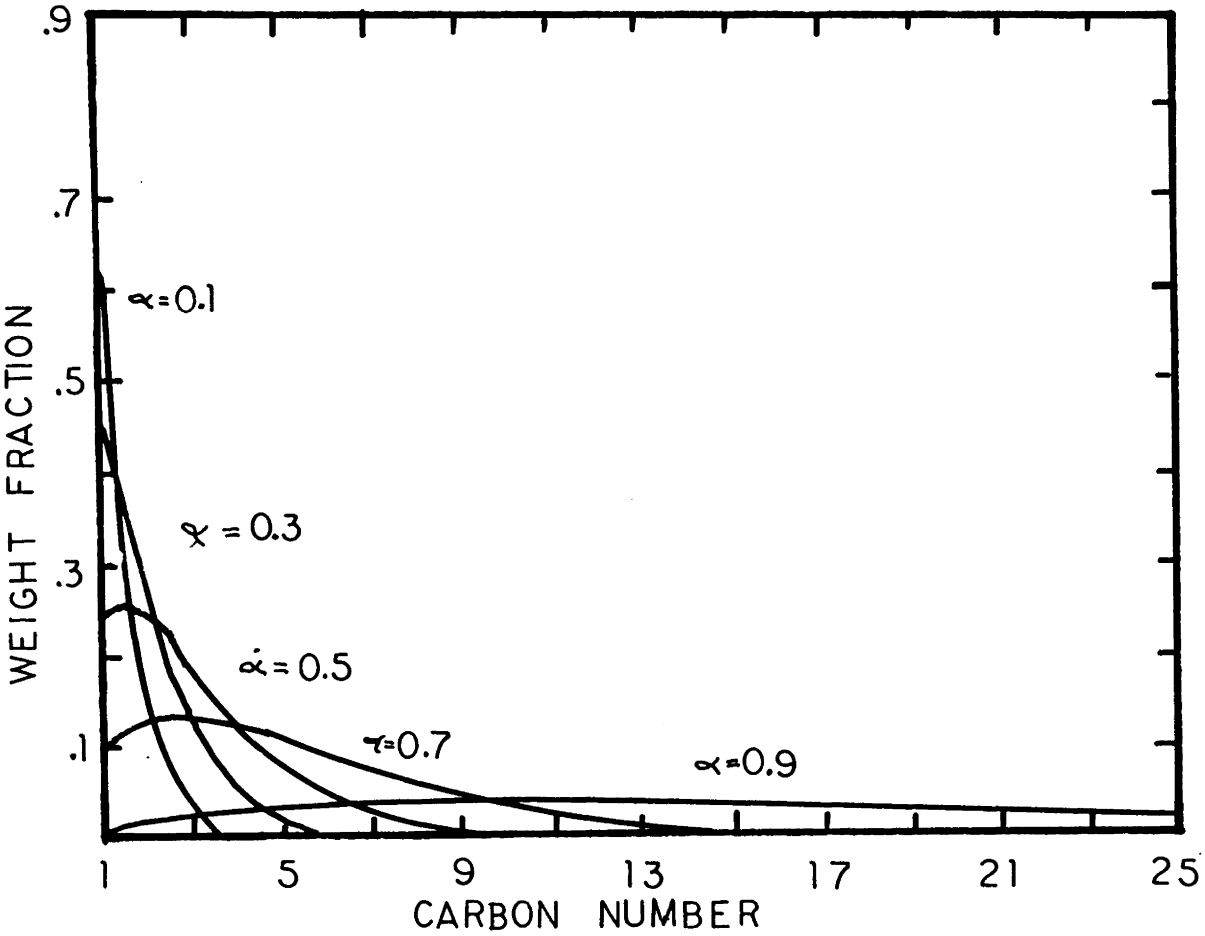

Figure 25: Influence of Chain Growth Probability on Hydrocarbon Product Distribution.

Table 10
Influence of Temperature and H_2/CO Ratio on α

T/K	α
509	0.769
529	0.732
551	0.634
573	0.366

Note: Data recorded for a ruthenium catalyst (116).

H_2/CO	α
3	0.47
2	0.51
1	0.56

Note: Data recorded for a 1% Ru/Al_2O_3 catalyst (116).

not provided) and the influence of H_2/CO ratio on α for a Ru/Al_2O_3 catalyst. As these tables show, the chain growth probability decreases with an increase in temperature and H_2/CO ratio.

As the previous experimental results have shown, CO-hydrogenation reactions yield a spectrum of products, even when operated at low conversion. A valuable Fischer-Tropsch catalyst would be one which would deviate from Schultz-Flory kinetics so as to yield either light olefins or gasoline range (C_5-C_{12}) hydrocarbons (122). This is because syn-gas can be derived from coal, which comprises about 65% of the worlds fossil fuel resources (36). Schultz-Flory kinetics can be circumvented through secondary reactions of the Fischer-Tropsch products, e.g. cracking, oligomerization and hydrogenolysis (31,116). It has been shown that by combining the Fischer-Tropsch activty of a transition metal catalyst with the secondary effects of an acid catalyst that a non-Schultz-Flory product distribution may be obtained (9,31). Non-Schultz-Flory behavior can result from primary effects as well. Primary effects refer to the Fischer-Tropsch reactions. This has been demonstrated by using catalysts of very small metal particles encaged in Y zeolites (31,41,115,116,120,123) or carbonyls supported on amorphous oxides (37,38,39,124). These results have lead Jacobs and co-workers (31,41,109,116,123) and Commereuc et al. (39) to postulate that for a monodispersed metal particle size distribution, a very narrow product distribution may result. This is because the particle size is thought to limit the length of the largest hydrocarbon which may be formed upon

it. The effect of metal particle size on the Fischer-Tropsch product distribution is next discussed in more detail.

II.D.3 Particle Size Effects with Non-Zeolite Supports

The effects of transition metal particle size on the behavior of well characterized Fischer-Tropsch catalysts have been studied by Kellner and Bell (10), Fu and Bartholomew (11) and Reuel and Bartholomew (34). In all cases, a Schultz-Flory product distribution was obtained. Dispersion was shown to effect the reaction rate and chain growth probability, however.

Kellner and Bell (10) investigated the effects of dispersion on Ru/Al_2O_3 catalysts. In this study, the catalyst loading was varied between 1.3 and 11.1 wt% ruthenium. In all cases, the reactions were performed at 1 or 10 atm H_2/CO (2/1) and 205°C. The decrease in dispersion of ruthenium resulted in a rapid increase in reaction rate, as shown in Figure 26. In this figure, the $C_{11}+$ hydrocarbon fraction did not follow the log-normal behavior outlined by the light hydrocarbons. This was attributed to sampling artifacts, e.g. line condensation. Note from this figure that the dispersion does not interfere with the log-normal behavior of the product distribution. However, the chain growth probability was altered slightly with changes in dispersion. α increased from 0.63 to 0.70 as the dispersion decreased from 0.82 to 0.67. Below a dispersion of 0.67, α remained constant at 0.70. The dispersion was also shown to influence the olefin to paraffin ratio. Whenever the dispersion was below

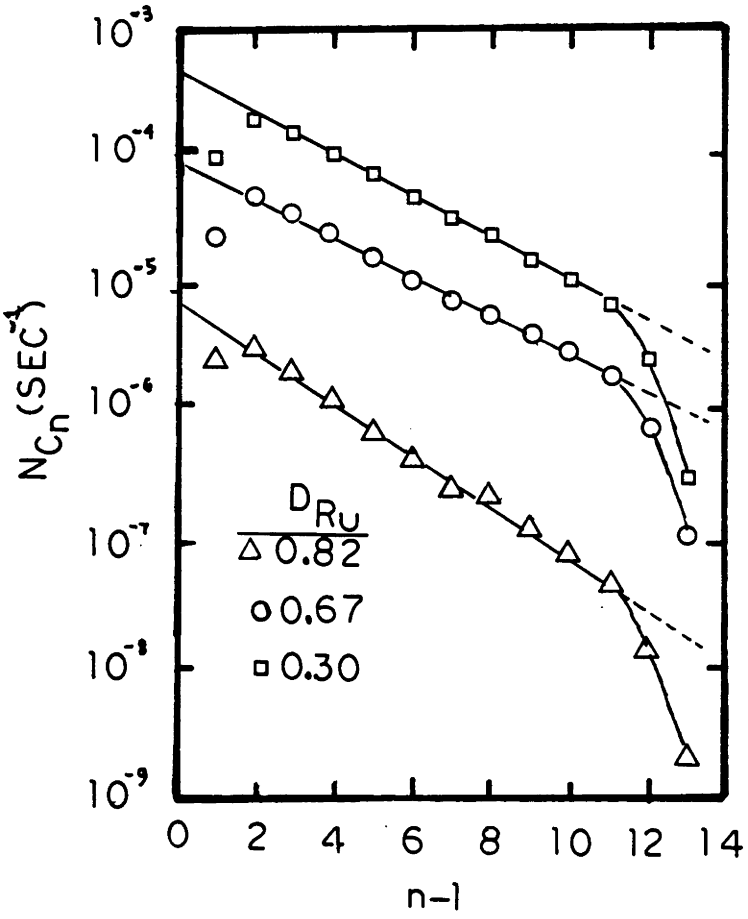

Figure 26: Influence of Ruthenium Particle Dispersion on Turnover Number (N) and Hydrocarbon Product Distribution (10).

0.6-0.7, the olefin to paraffin ratio was only weakly dependent on dispersion. For higher dispersed catalysts, the olefin to paraffin ratio rapidly decreased with increasing dispersion.

The decreased activity with increasing dispersion was postulated to be a result of a decrease in the number of sites suitable for CO-hydrogenation. Kellner and Bell noted that 14Å particles were present when the dispersion was 0.7. These particles were small enough to expect interactions between the support and the ruthenium particles (10). These support effects are postulated to result in a reduction in the density of the d orbital of the ruthenium atoms at the particle surface. This decreases the degree of back donation of charge from the d orbital of the ruthenium to the π^* (π antibonding) orbital of chemisorbed CO, resulting in reducing the degree to which the C-O bond was weakened. Dissociation of molecularly adsorbed CO is a major step in the synthesis of hydrocarbons over ruthenium. As the degree of back donation of d electrons was decreased, the C-O bond strength was increased which reduces the ability of the chemisorbed CO to dissociate. Thus, the reaction rate declines as shown in Figure 26.

Fu and Bartholomew (11) studied the effects of cobalt particle size on the CO-hydrogenation reaction. These reaction studies were performed under 1 atm H_2/CO (2/1) at temperatures between 200 and 250°C. In all cases, the conversion was maintained in the 5 to 10% range. The catalysts employed in this study were Co/Al_2O_3 with the cobalt loading being varied between 3 and 25%. Their study showed the extent of reduction to increase

with an increase in metal loading. That is, the higher loaded catalysts were more easily reduced. Dispersion was also observed to decrease as the catalyst loading was increased. The hydrocarbon product distribution consisted of primarially C_3-C_8 olefins and C_1-C_{15} paraffins. In all cases, Schultz-Flory behavior was followed. The chain growth probability was found to decrease as the catalyst loading decreased (dispersion increased). This is illustrated in Figure 23. These findings are similar to those of Kellner and Bell (10). A ten fold increase in specific activity was observed as the catalyst loading increased from 3 to 25% cobalt. The dispersion decreased from 15 to 6.7% over this range. Also, as the dispersion on a 3% Co/Al_2O_3 catalyst was varied from 15 to 30%, the turnover frequency decreased by a factor of 7. These results suggested that the CO-hydrogenation activity of Co/Al_2O_3 is structure (of the cobalt particles) sensitive (11).

The increase in average carbon number and catalyst activity with decreasing dispersion was attributed to changes in the adsorption strength of CO and carbon containing intermediates. Reuel and Bartholomew (125) have shown a shift from relatively weakly bonded carbonyl species to strongly bonded linear and bridged CO species as the dispersion is decreased. Therefore, as the dispersion is decreased, the residence time of the adsorbed CO species or hydrocarbon intermediate on the particle is increased. This in turn increases the average carbon number of the product, as shown in Figure 27.

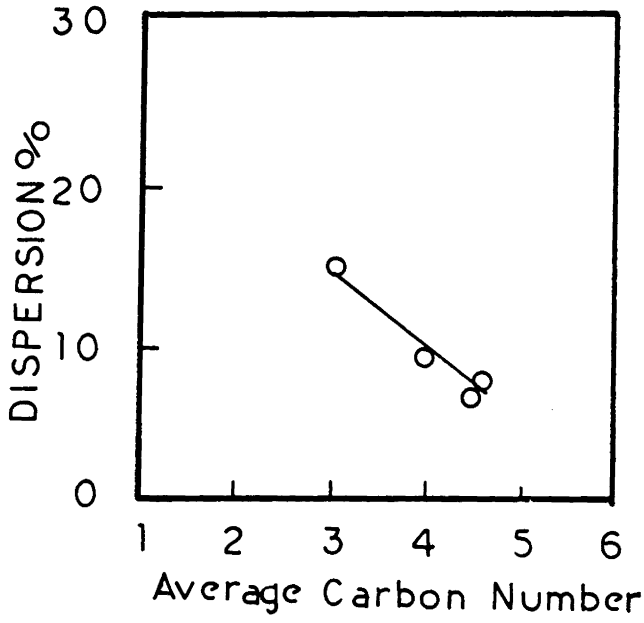

Figure 27: Correlation Between Dispersion and Average Carbon Number (125).

Reuel and Bartholomew (34) have shown that support type as well as dispersion of the cobalt phase will alter the hydrocarbon product distribution. For these studies, cobalt was supported on either SiO_2, Al_2O_3, TiO_2, MgO or carbon. In all reaction studies, the pressure was 1 atm H_2O/CO (2/1) and the temperature was varied from 175 to 400°C. Their results showed the production of CO_2 to increase with an increase in dispersion. Also, the average hydrocarbon length increased as dispersion was decreased. This is exemplified by a 100 fold decrease in activity as dispersion was increased from 4.5 to 86%.

High rates of CO_2 production were observed for well dispersed, poorly reduced catalysts. This was attributed to the formation of cobalt oxides, possibly spinels (CO associated with support oxygen). These particles are inert to CO-hydrogenation but are very active for the WGS reaction (34). The authors concluded from their study that well dispersed, low loaded catalysts contain a large fraction of stable surface oxides. Also, Chin and Hercules (126) have reported that cobalt in tetrahedral coordination, such as spinels, cannot be reduced by hydrogen.

It is interesting to note from these studies that while variations in dispersion effected the reaction rate, chain growth probability, olefin/paraffin ratio and average hydrocarbon chain length, Schultz-Flory behavior was still followed. Deviation from Schultz-Flory behavior has been reported only with supported metal carbonyls [non-zeolite supports] (37,38,39,124).

CO-hydrogenation catalysts have been prepared by depositing transition metal carbonyls on non-zeolite supports (37,38,39,124). The resulting catalysts were of low transition metal loadings (typically between 0.35 and 1.2 wt%) and exibited high selectivity to light hydrocarbons (C_1-C_5) when exposed to CO and H_2, CO and H_2O and ethylene. These studies have indicated that supported metal carbonyls serve as a precursor for Fischer-Tropsch catalysts. These carbonyl clusters limit the chain growth and hence yield a high selectivity to light hydrocarbons. It should also be noted that these materials were not reduced with hydrogen prior to reaction.

Smith et al. (37) supported $Ru_3(CO)_{12}$, $Os_3(CO)_{12}$, $Os_6(CO)_{18}$, $Rh_4(CO)_{12}$, $Rh_6(CO)_{16}$, and $Ir_4(CO)_{12}$ on η-Al_2O_3. These supported clusters were found to have remained intact at temperatures of 250°C, which was the temperature that many of the reactions were performed. Heating the supported carbonyls in the presence of CO resulted in the formation of CO_2, H_2 and various hydrocarbons. The hydrocarbon product distribution was influenced mostly by the water content of the support. Evidence was shown to indicate that, upon heating the catalyst, the carbonyl ligands reacted with either the hydroxyl (OH^-) groups of the support or adsorbed water to produce CO_2 and H_2O. The hydrogen then further reacted with the supported clusters to produce hydrocarbons from the carbonyls or carbide intermediates.

The hydrocarbon product distribution for $Rh_6(CO)_{16}$ supported on η-Al_2O_3 is reported in Table 11. The pretreatment temperature of the

Table 11
Influence of Alumina Pretreatment on the Composition of the Hydrocarbon Fraction (37)

Pretreatment Temperature	Hydrocarbon %					
	CH_4	C_2H_6	C_2H_4	C_3H_8	C_3H_6	$1\text{-}C_4H_8$
200	4	1	55	1	7	5
300	7	1	32	1	5	7
500	6	1	40	1	2	15
900	9	1	22	1	9	8

Pretreatment Temperature	Hydrocarbon %	
	$t\text{-}2\text{-}C_4H_8$	$c\text{-}2\text{-}C_4H_8$
200	19	10
300	31	18
500	20	17
900	33	19

Note: Data for $Rh_6(CO)_{16}$ at 200°C under 600 torr CO. Data recorded following 24 hours.

support influenced the water content. The results reported in Table 11 were obtained at 200°C following 24 hours exposure to 600 torr CO. Note from this table the high yield of butenes and ethylene.

Commereuc et al. (39) reported the Fischer-Tropsch activity of iron carbonyls supported on γ-Al_2O_3, La_2O_3, SiO_2 and MgO. The catalytic activity was measured under 10 atm CO/H_2 (1/1) at temperatures between 180 and 270°C. During the first few hours of reaction, a very high selectivity towards propylene was observed (up to 45 wt%). This selectivity declined slowly with time, as can be seen from Figure 28. At 48 hours, long chain hydrocarbons were observed. Before exposing the catalyst to CO and H_2, the metal particle size was determined to be less than 20Å. Following the run, however, large iron particles (250 to 500Å) were present. This result indicated that the low molecular weight olefins are produced when small iron particles are present, whereas larger hydrocarbons are present when large iron particles exist. These results appear to concure with those of Jacobs and co-workers (31,41,109,116,123) regarding limitations of the hydrocarbon chain length imposed by small metal particles.

Hugues et al. (124) proposed a mechanism which may govern the formation of light hydrocarbons over supported metal carbonyls. In this study, $Fe_3(CO)_{12}$ was supported on MgO and exposed to either CO and H_2 (1/2) or ethylene. Prior to reaction, the carbonyl was decomposed under vacuum (10^{-4} torr) at 130°C to yield a 1.8 wt% Fe/MgO catalyst. Upon exposure to syn-gas, the catalyst was found to be very selective towards

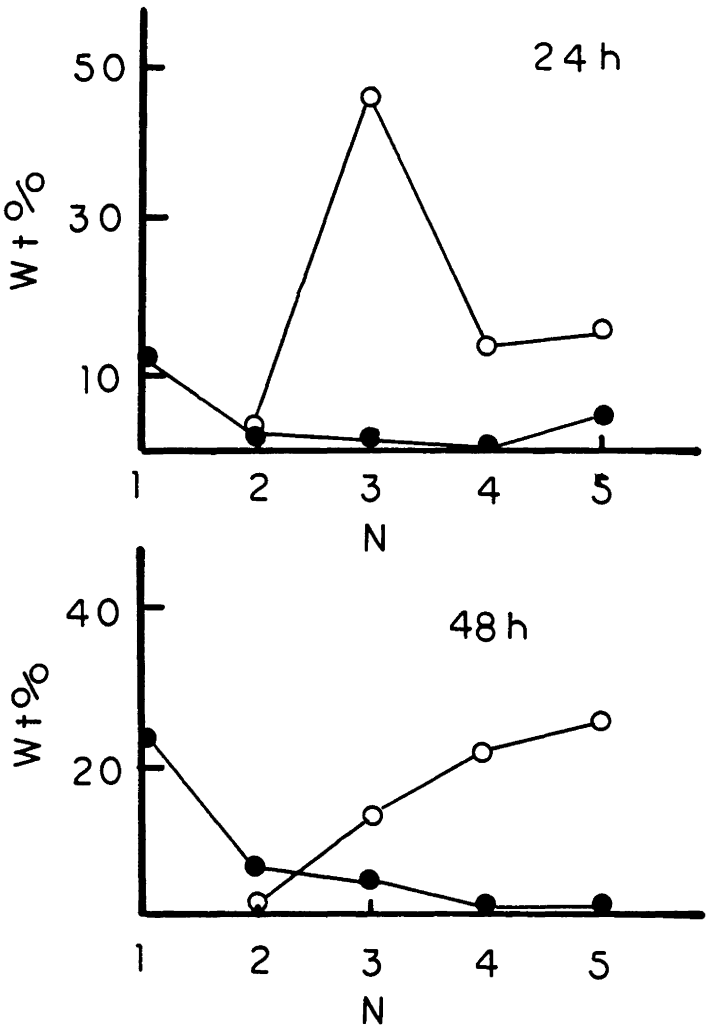

Figure 28: Selectivity Obtained in the Fischer-Tropsch Synthesis over Fe/Al_2O_3 Catalysts (39).
○ olefins; ● paraffins.

production of propylene (up to 45 wt%) while yielding only small quantities of ethylene. This implied that ethylene could be a primary product which undergoes a secondary reaction leading to the formation of propylene. Exposure of a similar catalyst to ethylene at 170°C resulted in the formation of propylene (70 wt%) with small yields of methane and butenes. Figure 29 reports the elementary reactions proposed by Hugues et al. leading to the formation of of methane, propylene and 1-butene from ethylene. As the figure shows, methane is formed from ethylene via cleavage of the double bond. Propylene is formed via reaction between a metal carbide and ethylene while 1-butene is formed through interactions between a surface carbide and propylene.

II.D.4 Particle Size Effects with Zeolite Supports

Fraenkel and Gates (40) have reported $Co^0Cd(II)$ A to behave as a shape selective Fischer-Tropsch catalyst. This catalyst was prepared by cation exchange of Na A with cobalt followed by reduction with cadmium vapor. Reaction of this catalyst at 151°C and 6 atm CO/H_2 (1/1) resulted in the production of only propylene. The rate of reaction was 0.4 CO molecules reacted per cobalt atom per hour. This rate was essentially constant over the 17.5 hours of the experiment. Examination of the catalyst by IR following this experiment showed cobalt carbonyl complexes to be present within the catalyst. No bridging CO was observed. The product distribution lead to the conclusion that $Co^0Cd(II)$ A can function as a selective Fischer-Tropsch catalyst.

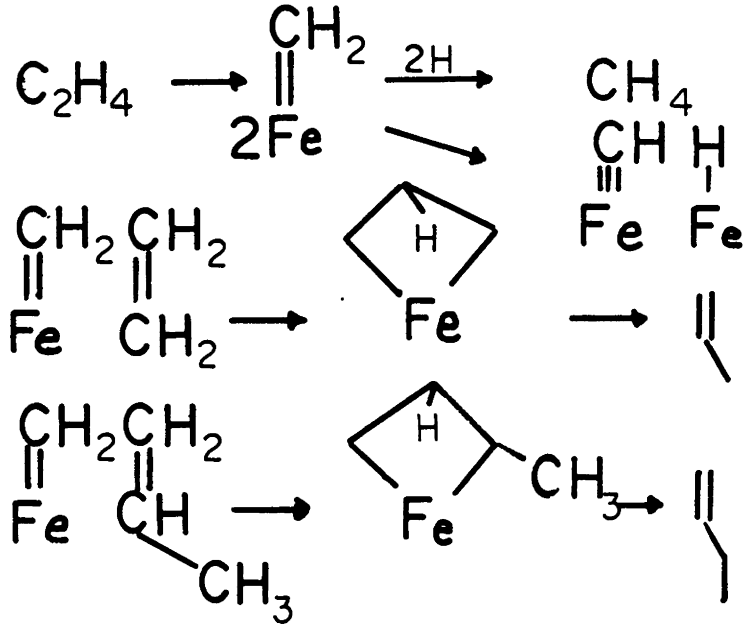

Figure 29: Proposed Reaction Sequence for the Formation of Methane, Propylene and 1-butene from Ethylene Reacted over Fe/Al_2O_3 (124).

Extensive studies have been conducted which have reported ruthenium zeolite Y to behave as a shape-selective Fischer-Tropsch catalyst (31,41,109,116,123). The shape-selective behavior of this catalyst has been attributed to a metal particle size effect. These works have lead to the conclusion that small metal particles limit the maximum size of the hydrocarbon which may be synthesized upon it.

During the reaction of H_2/CO over Ru Y catalysts, structural degradation leading to the formation of holes was observed (123). These holes are nothing more than intracrystalline voids and were discovered following the exposure of Ru Y to wet hydrogen (14). After exposure to reaction conditions the ruthenium particle size distribution was determined by temperature programmed oxidation (TPO) and transmission electron microscopy (TEM). The TPO analysis indicated that ruthenium crystallites were present which were larger than the zeolite cage could accommodate. Further analysis by TEM showed that ruthenium particles, approximately 25 to 40Å, to be present within the zeolite. These particles appeared to be centered within intracrystalline voids brought about by the reduction of the ruthenium coupled with the presence of water. The reduction of ruthenium within the zeolite proceeds as follows:

$$Ru^{+3}(ZO^-)_3 + 3/2H_2 = Ru^0 + 3ZOH$$

where ZO^- represents the zeolite framework. Thus the reduction of the ruthenium transforms the zeolite to an acid zeolite. The acid form is not stable at elevated temperatures in the presence of water vapor, as

partial hydrolysis of aluminum may occur (127). The presence of water during the reduction (catalyst reduced in wet hydrogen) apparently destroyed the zeolite in the vicinity of the ruthenium atoms creating intracrystalline voids. The ruthenium particles are postulated to have sintered into these voids.

Nijs et al. (123) prepared several Ru Y catalysts through cation exchange with $Ru(NH_3)_6Cl_3$. Temperature programmed oxidation (TPO) was used to determine the size of the ruthenium particles. The results revealed that ruthenium particles could be located in either the zeolite supercage, in holes within the structure or on the external surface of the crystal. In their study, the average ruthenium particle size was varied between 13 and 140 Å. The particle size was found to be a function of the extent of cation exchange and the form (sodium or lanthanum) of the zeolite. Exposure of these catalysts to 10 atm H_2/CO (1.5/1) at 200°C showed the reaction rate to be a function of the ruthenium particle size, as reported in Table 12. These findings are consistent with those for ruthenium and cobalt supported on γ-Al_2O_3 (10,11,34). The influence of the metal particle size on the reaction rate demonstrates that the Fischer-Tropsch reaction is structure sensitive.

For the first two catalysts reported in Table 12 [Ru(60)Y and Ru(20)Y][15], long chain hydrocarbons were produced. The Ru(60)Y produced hydrocarbons greater than C_{12}, as reported in Figure 30d, while the

---

[15] The number in parenthesis refers to the percent cation exchange.

Table 12
Turnover Number (N) for CO Conversion at 473K and Particle Size of Ruthenium Metal (123)

Catalyst	N X 10^6, s^{-1}	Average Particle Size, A
Ru(60) Y	520	140
Ru(20) Y	300	40
Ru(14)LaNa Y	210	20
Ru(14)La Y	140	13

Notes: Turnover number is of CO molecules converted per unit time per ruthenium surface atom. Particle sizes determined from transmission electron microscopy, except in the case of Ru(14)La Y, where the particle size was determined from chemisorption data.

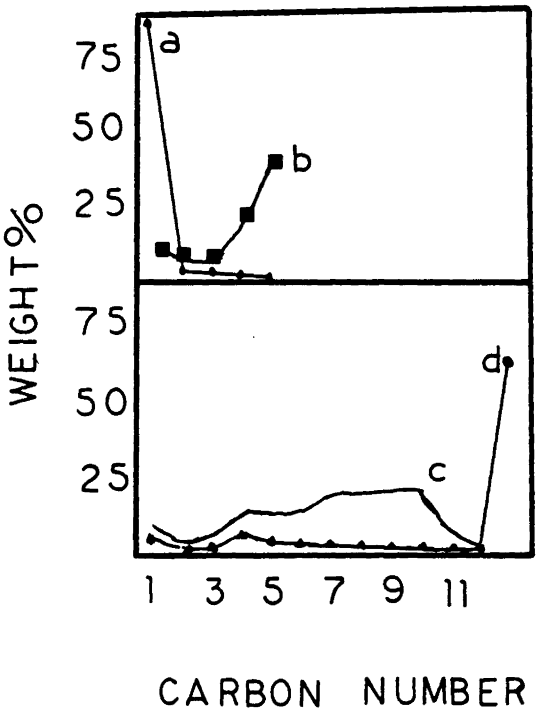

Figure 30: Hydrocarbon product Distribution for Catalysts Reported in Table 12 (123). a) Ru(14)La Y; b) Ru(14)NaLa Y; c) Ru(20) Y d) Ru(60)Y.

Ru(20)Y exibited a cut-off[16] at C_{10}. The Ru(14)LaNaY limited the hydrocarbon production to C_5. Note from Figure 30a that C_5 is the most abundant hydrocarbon present. Also, notice that the Ru(14)LaY yielded predominantly methane (95%). This high methane yield was attributed to the presence of ruthenium within the supercage; i.e. no holes were formed in the support due to the added structural stability resulting from the lanthanum. The activity and selectivity of the Ru(20)Y and the Ru(14)LaNaY was attributed to ruthenium particles present within zeolitic holes. Finially, note that the distributions shown in Figure 30 were obtained after only 1200 seconds on line.

Chen et al. (120) performed an extensive characterization and Fischer-Tropsch catalytic evaluation of zeolite Ru Y. In their study, average particle sizes as small as 13Å were reported (measured by hydrogen adsorption). The authors also note that the presence of a few large particles on the zeolite surface may result in a significant increase in the calculated average particle size. Infrared spectral analysis of Ru Y exposed to CO indicated that interactions between the ruthenium particles and the zeolite support were present, as evidenced by a decrease in the wavelength of the CO stretching frequency. Fischer-Tropsch reactions were next conducted over the characterized Ru Y catalyst. The effects of metal particle size on conversion are illustrated in Figure 31. As the figure shows, an increase in particle size results in an increase in

---

[16] Cut-off refers to the hydrocarbon after which no hydrocarbons of greater chain length were observed.

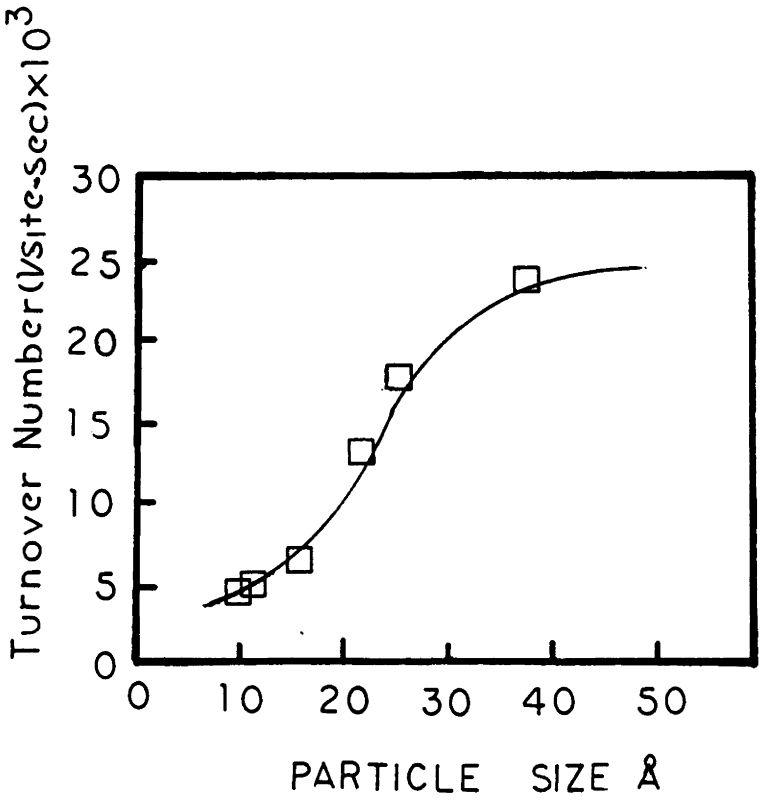

Figure 31: Particle Size Effect on Turnover Number over Ru/Na Y (120). 250 C, 1 atm H_2/CO = 1.0.

reaction rate. Start-up behavior of the Ru Y catalysts are shown in Figure 32. As the figure shows, all catalysts were very stable and reached steady-state in approximately 30 minutes. During the first 30 minutes, the selectivity was observed to shift to higher molecular weight hydrocarbons. Following 30 hours of exposure to syn-gas, the catalysts were regenerated with hydrogen and the experiment was repeated. Again, a similar start-up behavior was observed. The results of this experiment indicated that the shift in selectivity observed early into the run was not due to sintering of ruthenium but rather due to a transient species which formed early into the run. Unfortunately, Chen et al. (120) did not present the complete hydrocarbon product distribution.

Leith (115) investigated various cation exchanged forms of ruthenium Y zeolites as Fischer-Tropsch catalysts. The reaction studies in this experiment employed a "bracketing" technique, where the reduced catalyst was exposed to H_2/CO (2/1) for 15 minutes[17] followed by purging with hydrogen at 350°C for 1 hour. Following hydrogen exposure, the catalyst was next exposed to syn-gas and the procedure was repeated. Two types of Ru Y catalysts were prepared and are designated Y I and Y II. The Y I catalysts were prepared via cation exchange with $RuCl_3$-$3H_2O$ while the Y II catalysts were prepared by ion exchange with $Ru(NH_3)_6Cl_3$. The average rutheinum particle size was determined by hydrogen up-take prior to and following reaction. These results are reported in Table 13. As the table shows, the Y II catalysts possessed the smaller average particle

---

[17] It is reported that steady state was reached at this time.

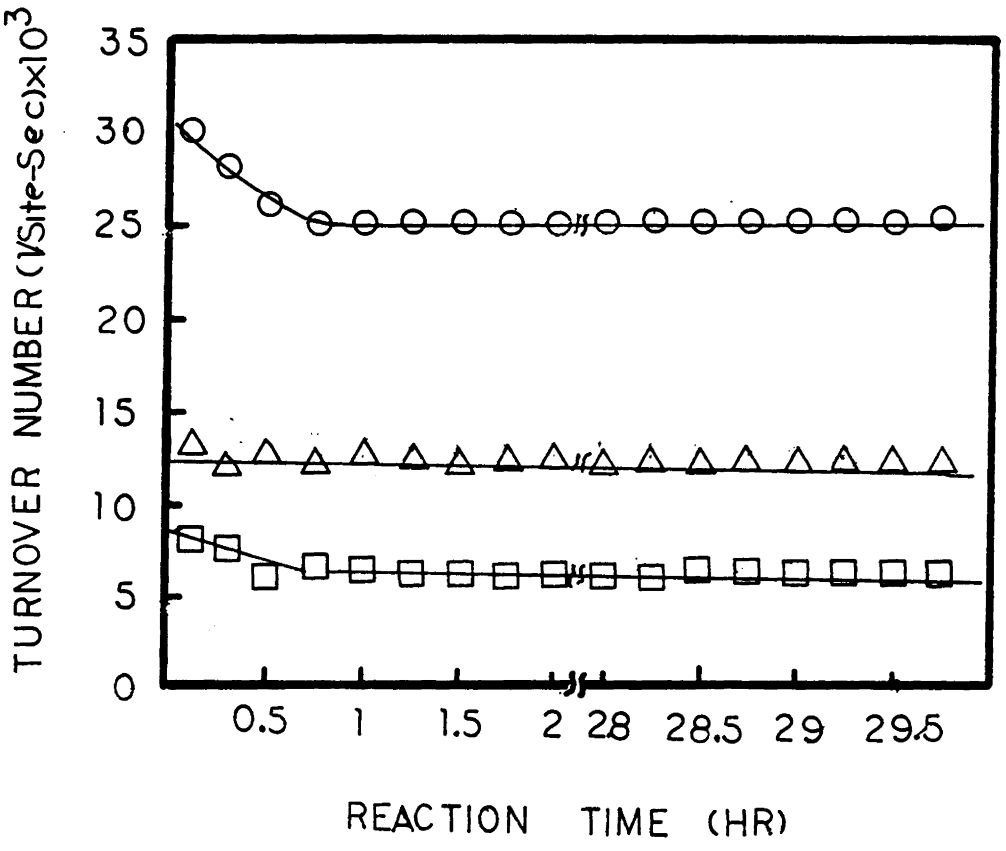

Figure 32: Stability of Three Ru Y catalysts (120). 250 C, 1 atm CO/H_2 = 1.0.

Table 13
Hydrogen Chemisorption on Supported Ruthenium Catalysts (115)

Catalyst	Average Crystallite Size (Å) Fresh	Used
RuNa Y I	49	46
RuMg Y I	43	49
RuLa Y I	21	20
$RuNH_4$ Y I	40	32
RuNa Y II	12	20
RuMg Y II	14	26
RuLa Y II	16	20
$RuNH_4$ Y II	23	17

size. The table also shows the average ruthenium particle size to increase following exposure to reaction on the Y II catalysts. For the Y I catalysts, the average ruthenium particle size did not alter significantly following exposure to reaction.

Using the bracketing technique described earlier, Leith was able to maintain the catalytic activity of the Y I catalysts through 8 cycles. For this same treatment, the activity of the Y II catalysts was shown to increase greatly over the course of 8 cycles. Figure 33 reports the product distribution following repeated exposures for a typical Y II catalyst. As the figure shows, the methane selectivity of the first exposure is very high. The selectivity decreased sharply following initial exposure. A more gradual decrease is observed thereafter. Note also from this figure that for the first exposure only C_1 and C_2 hydrocarbons were observed in the product stream. This may not be due to a particle size effect, as conversion for this run was extremely low. The shift in selectivity and reactivity of the Y II catalysts were attributed to sintering of ruthenium atoms into holes. These holes were assumed to be present based on the work of Jacobs and co-workers (see, for example 14,123). An increase in activity with an increase in ruthenium particle size was reported also in this study. This increase in activity was attributed to an increase in the number of sites which are capable of performing CO hydrogneation. The charge balancing cations associated with the Y I and Y II catalysts were reported to effect the catalytic activity. This effect was attributed to either an alteration in

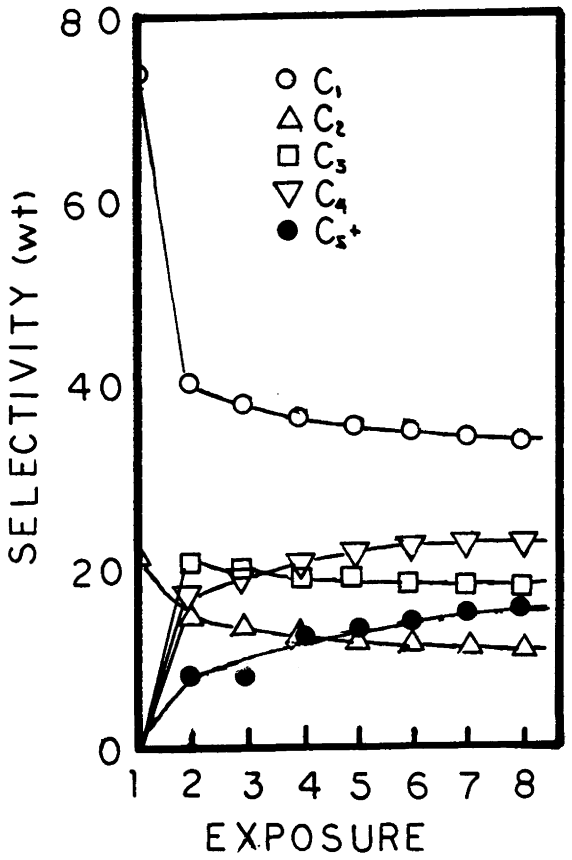

Figure 33: Product Distribution Following Repeated Usage of a Typical Y II Catalyst (115).

dispersion of the ruthenium or an alteration in the support-ruthenium interaction.

It appears that small metal particles, either synthesized via metal carbonyl sublimation (37,38,39,124) or by location within the supercage or holes in zeolite Y (31,41,109,116,123) can function as selective (to light hydrocarbons) Fischer-Tropsch catalysts. A drawback of these catalysts may be maintaining selectivity. Commereuc et al. (39) showed that when the small iron particles are deposited on MgO, they migrate together during the reaction and cause a shift in the product distribution away from light hydrocarbons. Jacobs and co-workers (31,41,109,116,123) only report selectivity early into the run (e.g. 1200 seconds) and give no indication as to whether selectivity is maintained. Fraenkel and Gates (40) have reported CoCd A to maintain selectivity over the course of the reaction (17.5 hours), but the reactivity was extremely low. Since small metal particles have been shown to be selective towards Fischer-Tropsch synthesis, emphasis should be directed towards development of supports which will impede the sintering of metal particles.

II.D.5 Non-Schultz-Flory Behavior via Secondary Reactions

The log-normal product distribution which is typical of the Fishcer-Tropsch reaction has been circumvented by combining the CO-hydrogenation properties of a transition metal with the acidic properties of zeolites. Thus, light olefins are able to undergo oligomerization leading to branched and/or aromatic hydrocarbons while

long chain hydrocarbons will crack. This results in a high fraction of products being formed in the C_7-C_{12} range (9). These bifunctional catalysts have employed Ru, Fe and Co as the CO-hydrogenation catalyst and ZSM-5 zeolite as the acid site (2,3,9,17,18,19,20,116). Ru, Fe and Co were chosen due to their ability to yield long chain hydrocarbons (10,11,33,118). ZSM-5 is a strong acid catalyst and possesses a unique ability to transform olefins and oxygenates to aromatics (7,8). In addition, ZSM-5 is highly resistant to coke formation (101).

Transition metal/ZSM-5 catalysts were prepared by either physically mixing the transition metal with the acidified ZSM-5 (2,3,18,19,113), supporting the transition metal on the acidified ZSM-5 via impregnation (2,3,17,18,112) or crystallizing the ZSM-5 in the presence of the transition metal (9,20). The advantages of placing the transition metal within the zeolite cavity have been discussed by Dodwell (9). These advantages include a highly dispersed metal phase, prevention of coke formation and possible selectivity enhancements stemming from the close proximity of the acid function and the synthesis function.

Rao et al. (18) compared the performance of two Co/ZSM-5 catalysts. The first was prepared by physically mixing Co_3O_4 and H/ZSM-5 while the second was prepared by impregnating ZSM-5 with cobalt nitrate[18]. In both cases, the resulting catalysts were approximately 9 wt% cobalt. These

---

[18] The catalyst prepared by impregnation contained large cobalt oxide crystals on the external surface of the zeolite.

catalysts were reacted under 20 atm CO/H_2 (1/1) at 280°C. The results from this study showed the physically mixed catalyst to yield a much higher aromatic content of the liquid hydrocarbon fraction (C_5-C_{12}); 65% compared to only 20%. This difference was attributed to the lower Bronsted acidity of the catalyst prepared by nitrate impregnation. Appearantly, the acidity was reduced by the cobalt occupying protonoic sites within the ion exchanged zeolite.

Rao (2) and Stencel et al. (3) prepared a 1.2 wt% cobalt ZSM-5 catalyst where the majority of the cobalt was shown to be intrazeolitic. This catalyst was virtually inactive at 280°C under 300 psig CO/H_2 (1/1). Analysis of the catalyst by XPS indicated that the cobalt was in a highly oxidized environment. This cobalt could not be reduced to cobalt metal. These results lead to the conclusion that intrazeoltic cobalt is inactive towards the hydrogenation of CO.

Dodwell (9) demonstrated the most favorable selectivity to gasoline range hydrocarbons. His catalyst was Fe/ZSM-5 prepared by synthesizing ZSM-5 in the presence of $Fe(OH)_2$. The crystalline product was washed to remove the amorphous particles which accompanied the zeolite. The resulting material was reported to be 78.7 (this is not a typographical error) wt% iron. This catalyst, when reacted at 300°C under 300 psig H_2/CO (1/1 to 2/1) yielded up to 92% gasoline range hydrocarbons, which was high in aromatic content. This product distribution is shown in Figure 34. Catalysts prepared by similar techniques employing different transition metals demonstrated non-Schultz-Flory behavior as well.

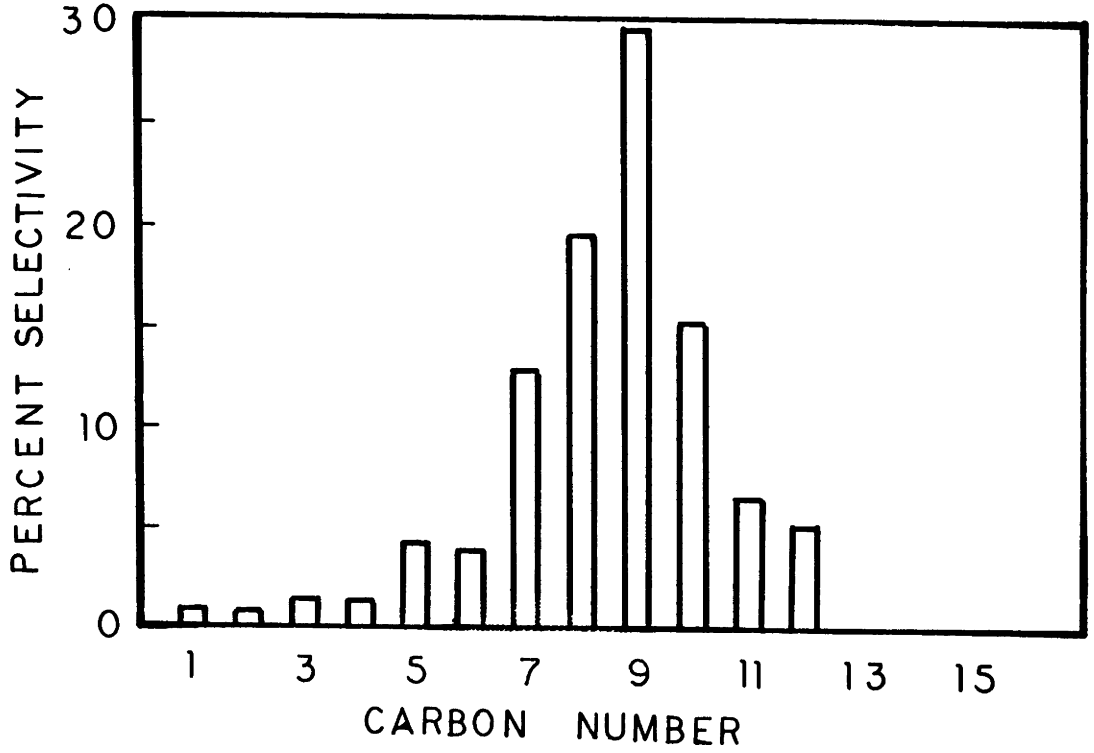

Figure 34: Hydrocarbon Product Distribution Obtained Over Fe/ZSM-5 (9).

Dodwell bases the enhanced selectivity of these materials on the iron being intrazeolitic. However, he reports clumps of transition metal oxides to be present with the crystals (21). It is also doubtful that at a loading of 78.7 wt% iron, the iron was intrazeolitic.

III OBJECTIVES

I. Develop a synthesis procedure for the crystallization of transition metal containing zeolites where the metal is intrazeolitic.

   Case A) High aluminum containing zeolite with no organic cation required for synthesis

   Case B) High silica zeolite with an organic cation required for synthesis.

II. Evaluate the new materials prepared in I in a reaction environment.

   Case A) Catalysis where the metal is in an oxidized state (immobilized homogeneous complex).

   Case B) Catalysis where the metal is in a zero valent state (metal particle).

For objective I.A, zeolite A was chosen. This material possesses a large ion exchange capacity, does not require an organic cation to be present and is synthesized at a relatively low temperature. For objective II.B, ZSM-5 was chosen. This material can be synthesized with virtually no aluminum in the structure and therefore will possess a very low cation exchange potential. Further, an organic cation, which fills the channel system, is essential to the synthesis which is conducted at relatively high temperatures.

The olefin hydroformylation reaction will be used to meet objective II.A. This reaction is thought to proceed by a rhodium(I) complex. The Fischer-Tropsch reaction will be used to meet objective II.B. This reaction is quite unselective and is catalyzed by zero valent metal particles.

IV Equipment and Procedure

IV.A Zeolite A Synthesis

IV.A.1 Zeolite A Synthesis: Sodium A

Zeolite sodium A (Na A) was synthesized as described below. First, 4.9 g of sodium silicate (Fisher Scientific) was dissolved in 20 ml distilled water and heated to 40-50°C. A second solution was prepared by adding 2.50 g sodium aluminate (Fisher Scientific) to 0.92 g sodium hydroxide (50 wt% Fisher Scientific) and 15 ml distilled water. Once the two solutions were completely dissolved, they were combined and stirred to uniform consistency while heating to 40-50°C. The resulting gel composition was:

$$3.5\ Na_2O\text{-}Al_2O_3\text{-}2.0\ SiO_2\text{-}185\ H_2O$$

This composition was used on subsequent batches unless otherwise noted. The resulting gel was added to 15 ml teflon lined autoclaves and heated to 95°C under autogeneous pressure for four hours in a free convection oven. Product crystals were recovered by filtration and washed with distilled water. The X-ray diffraction pattern of the resulting crystals identified the product as zeolite A. This material will be designated as blank zeolite A (does not contain any transition metal).

IV.A.2 Zeolite A Synthesis: Rhodium A using $RhCl_3$-$3H_2O$

Rhodium zeolite A was synthesized following the method outlined for blank zeolite A with the exception that $RhCl_3$-$3H_2O$ (Johnson Matthey) was added to the sodium silicate solution. This procedure is similar to that of Kuehl (78). Zeolite A synthesized in the presence of $RhCl_3$-$3H_2O$ will be designated as zeolite A synthesized from the salt source. Also, zeolite A was synthesized from a gel which contained the rhodium salt and blank zeolite A crystals. $RhCl_3$-$3H_2O$ and zeolite A were added to the sodium silicate solution previously described. The remainder of the synthesis procedure followed that of blank zeolite A.

IV.A.3 Zeolite A Synthesis: Rhodium A using "Seed" Rhodium Material

Below the novel techniques developed here for synthesizing rhodium zeolite A are presented. Rhodium zeolite A was synthesized by three different procedures. The first two techniques involved addition of cation exchanged rhodium zeolite A to the synthesis gel, while the third involved addition of a rhodium containing amorphous aluminosilicate material (to be described later). Rhodium exchanged zeolite A was prepared following the procedure of Arai and Tominaga (128). The crystals were exchanged at various loadings (up to 5.5 wt% rhodium). These "seed" crystals were added to the sodium silicate solution previously described. Next, the sodium aluminate solution was added; forming a thick gel. The resulting gel was then charged into teflon lined autoclaves. The autoclaves were removed and quenched at specified time intervals, and the solid residue filtered and washed. Following this procedure, the crystals

were then dried under flowing air at 110°C. This synthesis technique is subsequently referred to as the "seed" technique. The cation exchanged rhodium zeolite A is referred to as rhodium "seed."

The second technique involved addition of "seed" crystals (4.23 wt% rhodium) to the synthesis gel as described above. The resulting gel was added to a teflon lined autoclave, along with a teflon stirring bar. The vessel was then placed on a hot plate and allowed to react under agitation at approximately 100°C for 5.5 hours. The resulting crystals were washed and dried as before. This synthesis of rhodium zeolite A will be referred to as the "seed" technique with agitation.

The third method of synthesis involved addition of a rhodium containing amorphous aluminosilicate material to the synthesis gel. The amorphous "seed" was prepared by the addition of $RhCl_3$-$3H_2O$ to the zeolite A synthesis gel as previously described; however, the gel was only heated for 1 - 1.5 hours at 95°C. The resulting rhodium material was then filtered, washed with 500 ml of distilled water, dried at 110°C and sieved to below 70 mesh. This material was found to be X-ray amorphous. The rhodium material prepared by this method is referred to as rhodium amorphous "seed." Zeolite A synthesized from this material followed the exact procedure as zeolite A grown from seed crystals except the "seed" material is now the amorphous aluminosilicate.

IV.A.4 Zeolite A Synthesis: Ruthenium A using "Seed" Ruthenium Material

Zeolite ruthenium A was synthesized using RuNa A "seed" crystals. The "seed" crystals employed here were not prepared by cation exchange. Rather, they were prepared from zeolite A crystallized in the presence of $RuCl_3$-$3H_2O$ (follows the procedure of rhodium A grown in the presence of $RhCl_3$-$3H_2O$). This material was synthesized at 90°C for approximately 12 hours.

IV.A.5 Zeolite A: Calcium/Potassium Cation Exchange

Zeolite RhNa A and RuNa A were placed in either the calcium or potassium form by ion exchange. The procedure presented below is for the calcium exchange. Potassium exchange is obtained by substituting $CaCl_2$ (Fisher Scientific) with KCl (Fisher Scientific). A typical calcium exchange procedure involved addition of 2.5 grams zeolite RhNa A or RuNa A to 500 ml of 0.1 N calcium chloride solution. The zeolite cation exchange was carried out at room temperature for 18 hours, after which, a second exchange was performed. Next, the zeolite was filtered and washed with distilled water. Following washing, the zeolite was dried at 110°C overnight.

IV.B ZSM-5 Synthesis

IV.B.1 ZSM-5 Synthesis: Mixed Organic Cations

The synthesis of ZSM-5 typically involved dissolving 0.50 g sodium

aluminate in either 0.64 or 1.83 g sodium hydroxide (50 wt%) and 10 ml distilled water. To this solution, 41.3 g Ludox AS-40 colloidal silica solution (DuPont) was added and the resulting gel was stirred to uniform consistency. Addition of the organic cation was next performed. This involved addition of desired quantities of tetrapropylammonium bromide (TPA) and either tetraethylammonium bromide (TEA) or tetramethylammonium hydroxide (TMA) to the synthesis gel. Each of these organic cations were purchased from Aldrich. The quantities of TPA, TEA and TMA were chosen so that the molar ratios of $(TEA+TPA)/Al_2O_3$ and $(TMA+TPA)/Al_2O_3$ were maintained at a constant 7.2. Following addition of the organic cation, an additional 10 ml distilled water was added to the resulting gel. The gel compositions were:

A) $2.75Na_2O\text{-}Al_2O_3\text{-}120\ SiO_2\text{-}7.2(1\text{-}x)TPA\text{-}7.2x(TEA,TMA)\text{-}1100\ H_2O$
B) $6.00Na_2O\text{-}Al_2O_3\text{-}120\ SiO_2\text{-}7.2(1\text{-}x)TPA\text{-}7.2x(TEA,TMA)\text{-}1100\ H_2O$

where x was varied between 0 and 1 in all cases. Once stirred to uniform consistency, the resulting synthesis gel was added to 15 ml teflon lined autoclaves and heated to 185°C in a forced convection oven. These batches will be referred to as mixed organic cation, with batch A designated as the low sodium system and batch B designated as the high sodium system.

IV.B.2 Co/ZSM-5 Synthesis: $CoCl_2\text{-}6H_2O$

ZSM-5 was synthesized in the presence of $CoCl_2\text{-}6H_2O$. Three gel compositions were utilized, with these being:

C) $2.80\ Na_2O\text{-}96\ SiO_2\text{-}5.77\ TPA\text{-}\ 880\ H_2O\text{-}y\ Co$
D) $3.71\ Na_2O\text{-}Al_2O_3\text{-}90\ SiO_2\text{-}5.75\ TPA\text{-}\ 825\ H_2O\text{-}y\ Co$
E) $5.50\ Na_2O\text{-}Al_2O_3\text{-}70\ SiO_2\text{-}4.20\ TPA\text{-}\ 645\ H_2O\text{-}y\ Co$

with y being varied between 0.0 and 0.50. Composition C is cobalt silicalite, since there is no aluminum added to the synthesis gel. This system will also be referred to as low sodium, as will all batches of Co/ZSM-5 synthesized from here forward with a $NaOH/SiO_2$ ratio of approximately 0.04. Composition D is Co/ZSM-5 with a SiO_2/Al_2O_3 ratio of 90 synthesized with the low sodium system. Composition E is Co/ZSM-5 with a SiO_2/Al_2O_3 ratio of 70 synthesized in the high sodium system. The high sodium system will refer to any batch of Co/ZSM-5 synthesized with a $NaOH/SiO_2$ ratio of approximately 0.08. ZSM-5 syntheses C, D and E follow the same procedure as previously described in the mixed organic cation section with the exception of the addition of $CoCl_2$-$6H_2O$ to the synthesis gel. The addition was accomplished by dissolving the desired amount of $CoCl_2$-$6H_2O$ in the final 10 ml portion of water. This solution was then added to the gel and mixed to uniform consistency.

IV.B.3 Co/ZSM-5 Synthesis: Cobalt Amorphous Material

Below is described the novel procedure developed here for synthesis of cobalt ZSM-5. A cobalt containing amorphous aluminosilicate synthesized for use as a "seed" for ZSM-5 synthesis was prepared by first dissolving 15.2 g sodium silicate in 40 ml distilled water and heating under agitation to approximately 40°C. $CoCl_2$-$6H_2O$ was then added to the above solution. A second solution was prepared by dissolving 5.2 g sodium aluminate in 1.9 g sodium hydroxide (50 wt%) and 30 ml distilled water. Upon combining these solutions the gel composition was:

$$4.5\ Na_2O\text{-}Al_2O_3\text{-}3.0\ SiO_2\text{-}185\ H_2O\text{-}y\ Co$$

For all cases, y was varied between 0.0 (blank amorphous material) and 1.10. The resulting gel was added to a 200 ml teflon jar and heated at 95°C for 1 hour in a forced convection oven. Following removal from the oven, the resulting material was filtered and washed with 500 ml distilled water by pouring the water over the filter cake. The material was then dried at 110°C. After drying, the solid was crushed and sieved to below 70 mesh. Material synthesized by this technique will be referred to as cobalt amorphous "seed."

Four gel compositions which employed cobalt amorphous "seed" were:

F) 2.80 Na_2O-96 SiO_2-5.77 TPA- 880 H_2O-y Co
G) 5.10 Na_2O-96 SiO_2-5.77 TPA- 880 H_2O-y Co
H) 3.00 Na_2O-Al_2O_3-70 SiO_2-4.20 TPA- 645 H_2O-y Co
I) 5.50 Na_2O-Al_2O_3-70 SiO_2-4.20 TPA- 645 H_2O-y Co

The gel compositions do not include the contribution of SiO_2 and Al_2O_3 from the "seed." These batches were synthesized in the same manner as previously described with the exception being the addition of the cobalt amorphous "seed." The "seed" material was added to the solution consisting of sodium hydroxide, water and (when applicable) sodium aluminate. The remainder of the synthesis procedure followed that described previously.

IV.B.4 Co/ZSM-5 Synthesis: Cobalt Ion Exchange

A cobalt ion exchange of ZSM-5 was performed. ZSM-5 was synthesized according to gel composition D with y = 0.0. Ion exchange involved addition of 2.5 g ZSM-5 to 500 ml distilled water. $CoCl_2$-$6H_2O$ (0.525 g) was added to the slurry. The slurry was then heated to 95°C for 22 hours.

Following the exchange, the ZSM-5 was filtered, washed and calcined so as to follow similar pretreatment as Co/ZSM-5 prepared from "seed." Calcination was carried out in a muffle oven at 550°C.

IV.C Zeolite Crystal Growth

Crystal growth data were recorded by removing and quenching the teflon lined autoclaves at various times following heat-up. The solid was filtered and washed with 50-75 ml distilled water after which it was dried at 110°C. Percent crystallinity was determined by ratioing the sum of the intensities of the three major peaks in the 2θ = 20 - 30° range to a standard sodium zeolite A. Percent crystallinity for ZSM-5 was obtained by using the 2θ = 23° peak.

IV.D Chemical Analysis

IV.D.1 Chemical Analysis: Zeolite A

Chemical analysis was performed using a Varian 3800 Atomic Absorption (AA) Spectrophotometer. For zeolite A, the elements analyzed were silicon, aluminum, ruthenium and rhodium. Below, the preparation of standard solutions is first described followed by instrument operation and sample digestion.

Standard solutions were prepared for the purpose of instrument calibration. Silicon and aluminum depress the signal of one another when present in the same solution (129). To account for this behavior, a standard solution was prepared with a Si/Al ratio of 1.0 (similar to the

ratio in the zeolite A structure). Sodium aluminate was used for synthesis of the aluminum standard while Ludox AS-40 was used for the preparation of the silicon standard. Typically, 1.8 g sodium aluminate and 2.5 g Ludox were dissolved in 50 ml HCl (conc) and diluted to 500 ml total volume with distilled water. This procedure gave a solution of approximately 600 moles each of silicon and aluminum per 10^6 moles water. Silicon/aluminum calibration solutions were prepared by further diluting the standard to concentrations of 200, 300, 400, 500 and 600 moles Si,Al per 10^6 moles H_2O. This range provided optimum detection of these elements (129).

The rhodium standard was prepared by dissolving 0.12 g $RhCl_3$-$3H_2O$ (0.4125 wt% Rh) in 225 ml H_2O and 25 ml HCl (conc). The standard solution was approximately 35 moles rhodium per 10^6 moles water (196 µg/ml). From this standard, rhodium calibration solutions were prepared at 5, 10, 15, 20 and 25 µg/ml solution. This range provided optimum detection of rhodium (129). No elements present in the digested zeolite A solution influenced the rhodium absorption signal (129).

The ruthenium standard was prepared from $RuCl_3$-$3H_2O$ with a ruthenium concentration of approximately 120 µg/ml solution. This solution was further diluted to produce calibration solutions of 20, 50, 75, 100 and 120 µg/ml. This calibration range is optimum for detection of ruthenium (129). As with rhodium, no element present in the digested zeolite A solution interfered with the ruthenium absorbance (129).

Operation of the Varian atomic absorption instrument and analysis of silicon, aluminum, ruthenium and rhodium in zeolite A is described below. Silicon was detected at 251.6 nm wavelength with a spectral band path of 0.5 nm. The silicon lamp was operated at 15 mA. The fuel for the AA spectrometer was nitrous oxide/acetylene burning with a strongly reducing flame stoichiometry. Aluminum was detected at 309.3 nm wavelength with a spectral band path of 0.5 nm. The lamp current was 10 mA. The flame stoichiometry was reducing and also employed a nitrous oxide/acetylene fuel.

Rhodium was detected at 307.4 nm wavelength with a spectral band path of 0.5 nm. The lamp current was 10 mA. The flame was air/acetylene burning with a flame stoichiometry of oxidizing. Ruthenium was detected at 349.9 nm wavelength with a spectral band path of 0.2 nm. The lamp current was 10 mA. The flame employed air/acetylene burning with a flame stoichiometry of oxidizing.

Typically, 0.0050 to 0.0500 g zeolite rhodium A were digested in 5-10 ml HCl (conc) diluted to 20 ml total volume with distilled water. For ruthenium A, the quantity of zeolite digested ranged from 0.05 to 0.20 g. By digesting the above quantities of zeolite, the solution could be analyzed for all the elements of interest. A typical analysis is provided in Appendix I.

From the above AA analysis, the Ru or Rh weight loading of the digested zeolite was determined two ways. The first involved calculating

the mass of rhodium/ruthenium in solution, then dividing this quantity by the mass of digested zeolite. A second calculation was performed by using the silicon, aluminum and rhodium/ruthenium concentrations. This computation was accomplished by combining the moles of each of these elements in solution with the unit cell composition of zeolite A. For Ca A, the unit cell composition is given as $Ca_6[(AlO_2)_{12}(SiO_2)_{12}]$-$27H_2O$ (130). This stoichiometrically gives a pseudo-unit cell molecular weight of 2154. Since SiO_2 and AlO_2 are approximately the same molecular weight (60 and 59, respectively) and their ratio was approximately 1.0 in all cases, the above pseudo-unit cell molecular weight was used without further modification. The unit cell composition in the hydrated form was employed due to zeolite A's affinity to adsorb water. The ratio of Rh/(Si+Al) was then calculated. This value enabled the determination of Rh atoms per pseudo unit cell. From this result the weight loading of rhodium could be directly calculated. A sample computation is presented in Appendix I. The weight loading calculated by the two methods usually agreed to within 10%.

IV.D.2 Chemical Analysis: Co/ZSM-5

For all cobalt ZSM-5 materials, only the amount of cobalt was analyzed. Aluminum was below detection limits due to the relatively low quantity present in ZSM-5. Also, silicon could not be analyzed (see below). Cobalt calibration solutions were prepared by diluting a 1000 µg/ml solution of cobalt (Aldrich) to 1, 3, 5, 7 and 10 µg/ml. Cobalt was detected at 240.7 nm wavelength with a spectral band path of 0.50 nm. The lamp current was 9.0 mA. An oxidizing air/acetylene flame was employed.

Typically, 0.01 to 0.03 g Co/ZSM-5 were dissolved in 6 ml HF (conc) and brought to 12 ml total volume with distilled water in a teflon lined autoclave. The vessel was then heated to 185°C for 5 to 7 hours under autogeneous pressure. These conditions were necessary to digest the Co/ZSM-5 material. Following heating, the vessel was removed from the oven, cooled and the contents diluted to 30 ml in a polyethylene jar. The cobalt sensitivity with regards to the AA analysis was not affected by the preparation conditions; however silicon was. The use of HF to dissolve siliceous material leads to formation of volatile silicon tetrafloride (129). Once the vessel is opened, the silicon tetrafloride was released to the atmosphere. Thus the cobalt to silicon ratio of the digested zeolite was determined by assuming the zeolite to be pure SiO_2. AA on Co/ZSM-5 was performed on both the calcined and non-calcined samples. Analysis on non-calcined material assumed the organic cation to occupy 13% of the total weight. The 13% weight loss was based on previous work (98).

IV.E X-Ray Photoelectron Spectroscopy

X-ray photoelectron spectroscopy (XPS) was performed on RhCa A using a KRATOS XSAM 800 spectrometer with MgKα X-rays. XPS spectra for all other materials were performed using a Perkin-Elmer PHI 5300 ESCA system also employing MgKα X-rays. The superficial atomic ratio's were calculated from the equation:

$$\frac{N_1}{N_2} = \frac{I_1}{I_2} * \frac{S_2}{S_1}$$

where N_1/N_2 is the elemental ratio, I is the intensity of the element and S is the sensitivity factor. Often, S is set equal to the cross section (σ) for photoelectron emission from that level (4,5,131). Thus, the escape depth, λ, is not taken into account. Sensitivity factors employed here are listed in Table 14. The machine supplied sensitivity factors refer to the Perkin-Elmer Phi 5300 ESCA and were employed for samples run on this machine. The sensitivity factors used in conjunction with the KRATOS XSAM 800 were calculated from S = σ*(source energy-binding energy)**0.75 (132,133). This equation was used since machine factors were not provided by KRATOS. As the table shows, the two sets of sensitivity factors compare favorably.

The machine supplied sensitivity factors supplied for the Perkin-Elmer Phi 5300 ESCA were evaluated for accuracy by recording XPS spectra on Cab-O-Sil (W. R. Grace). Cab-O-Sil is 99.98% pure SiO_2. Using these factors, the O/Si ratio obtained on the Perkin-Elmer PHI 5300 ESCA was 2.0, verifying the accuracy of the machine supplied sensitivity factors for oxygen and silicon. Other sensitivity factors were not evaluated.

The number of scans varied for the different elements depending on their abundance. Typically, the number of scans varied between 2 and 10 for both instruments. The elements of interest for zeolite A were Na, Ca, Si, Al, Rh, Ru and O. For ZSM-5, the elements of interest were Si,

Table 14
X-Ray Photoelectron Spectroscopy
Sensitivity Factors

Element	Sensitivity Factors Perkin-Elmer[1]	KRATOS[2]
O1s	0.66	0.58
Si2p	0.25	0.25
Al2p	0.18	0.17
Ca2p	1.05	1.24
Co2p(3/2)	2.50	2.20
Ru3d(5/2)	2.15	1.91
Rh3d(5/2+3/2)	----	3.58

[1] Perkin-Elmer PHI 5300 ESCA
[2] KRATOS XSAM 800

Al, O, Co and Na. In all samples, the C1s photoelectron peak was used as a reference for the binding energies. All binding energies reported are referenced to the C1s at 285.0 eV.

When analyzing Co/ZSM-5, overlap between the oxygen auger and cobalt 2p3/2 peak was present. To provide an accurate quantitative representation of superficial cobalt, the area of the oxygen auger was estimated and subtracted from the sum of the Co2p3/2 and oxygen auger area obtained following integration. This calculation was carried out by integrating over the Co2p3/2 photoelectron region (780-787 eV) of blank ZSM-5. The area obtained from the blank sample was ratioed to the O1s area, with the value of O(auger)/O1s being 0.0830. For all cobalt ZSM-5 samples, the O1s area was multiplied by this ratio and the resulting value (units of area) subtracted from the sum of the cobalt 2p3/2 and oxygen auger area. Thus the cobalt 2p3/2 area was obtained. XPS spectra for the oxygen auger region and cobalt plus oxygen auger region are shown in Figure 35.

IV.F Pore Volume Analysis: Oxygen Adsorption

Oxygen adsorption was used to determine the pore volume of various zeolite A and ZSM-5 samples. The system employed here is commonly referred to as a McBain-Bakr balance. The system is constructed entirely of thick wall glass tubing with the exception of the adsorption chamber, which is constructed of vicor. Vicor is a high temperature, low expansion borosilicate which is capable of temperatures in excess of 900°C. The manifold ports employ #7 round joints with O-rings. All valves are Konets

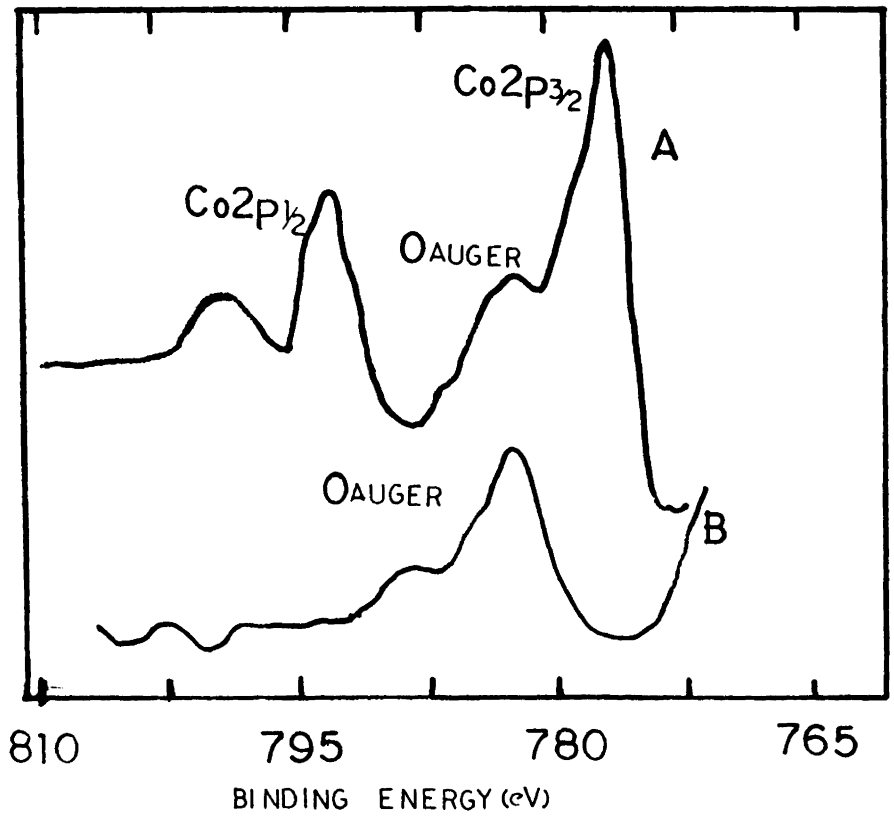

Figure 35: XPS Spectra Showing Co2p(3/2) (A) and Oxygen (KVV) Auger (B) Photoelectron Region.

high vacuum valves. A schematic representation of this system is shown in Figure 36.

Unit A is an oil diffusion pump, constructed by the glass shop at Virginia Tech. It is controlled by a variac set at 67.5 and 140 V. Unit B is a cold trap. Cooling is supplied by liquid nitrogen which is placed in a dewar surrounding the trap. The manifold is divided into two halves (C and D) for independent operation. E is the pressure gauge, which is connected to the pressure transducer. Both the gauge and transducer were purchased from Hastings Instrument Company. The pressure gauge reads from 10^{-4} torr to atmospheric. Unit F is the adsorption chamber. It is connected at the top by a ground glass joint. The chamber is approximately 1.75 inches in diameter. The hook at the top of the chamber extends to just below the ground glass joint. The hook is connected to a quartz spring (500 mg maximum load, 400 mm maximum extention, spring constant 1.25 mg/mm) purchased from Ruska Instrument Company. The spring is attached to a 10 cm quartz extension wire obtained from the glass shop at Virginia Tech. The extention wire is then attached to a 75 mg quartz sample pan (15 mm diameter), also purchased from Ruska Instruments. Units G and H are u-tube manometers with unit J being a mercury trap. The trap is filled with sulfur in order to adsorb mercury vapor.

As designed, the manifold is capable of simultaneously performing adsorption on four separate samples. Its use was limited to only one sample at a time for work performed here. Adsorption work presented here was performed in chamber F as shown in Figure 36. The first step in the

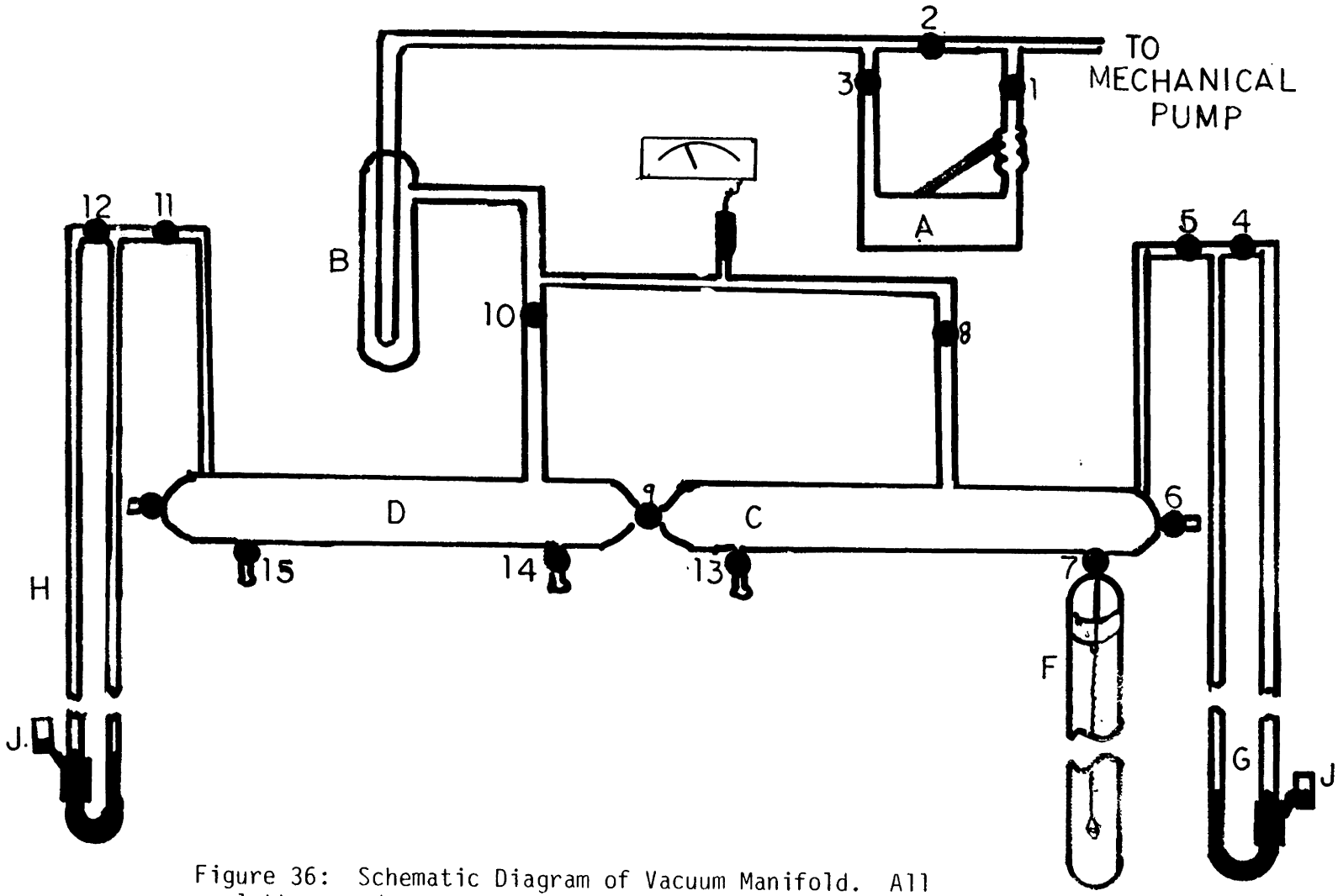

Figure 36: Schematic Diagram of Vacuum Manifold. All letters and numbers are referred to in text.

Attention Patron:

Pages 137-186 omitted from numbering

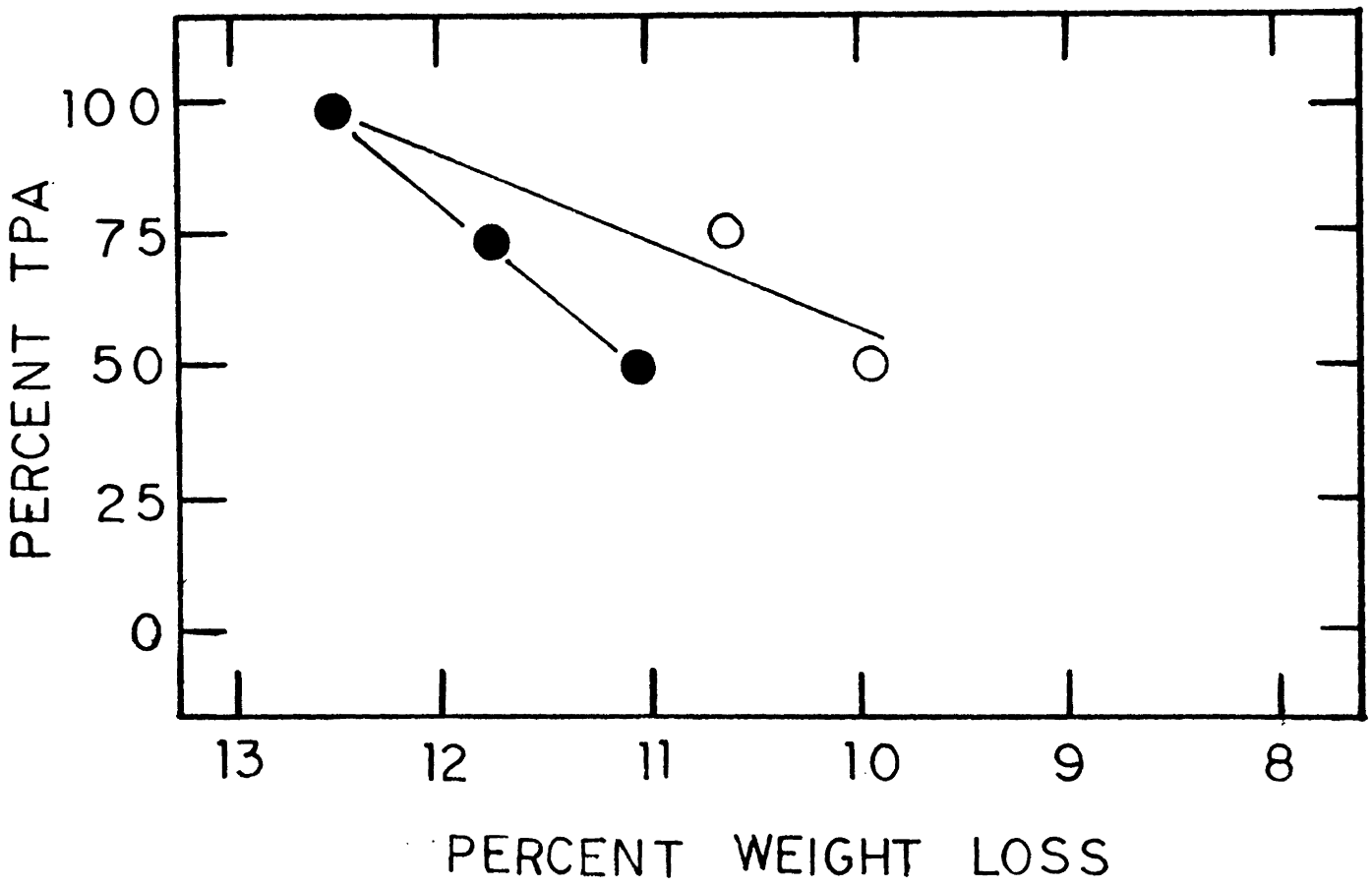

Figure 63: Weight Loss After Calcination versus Percent TPA in the Synthesis Gel for ZSM-5 (Low Sodium, O TMA/TPA and ● TEA/TPA Systems).

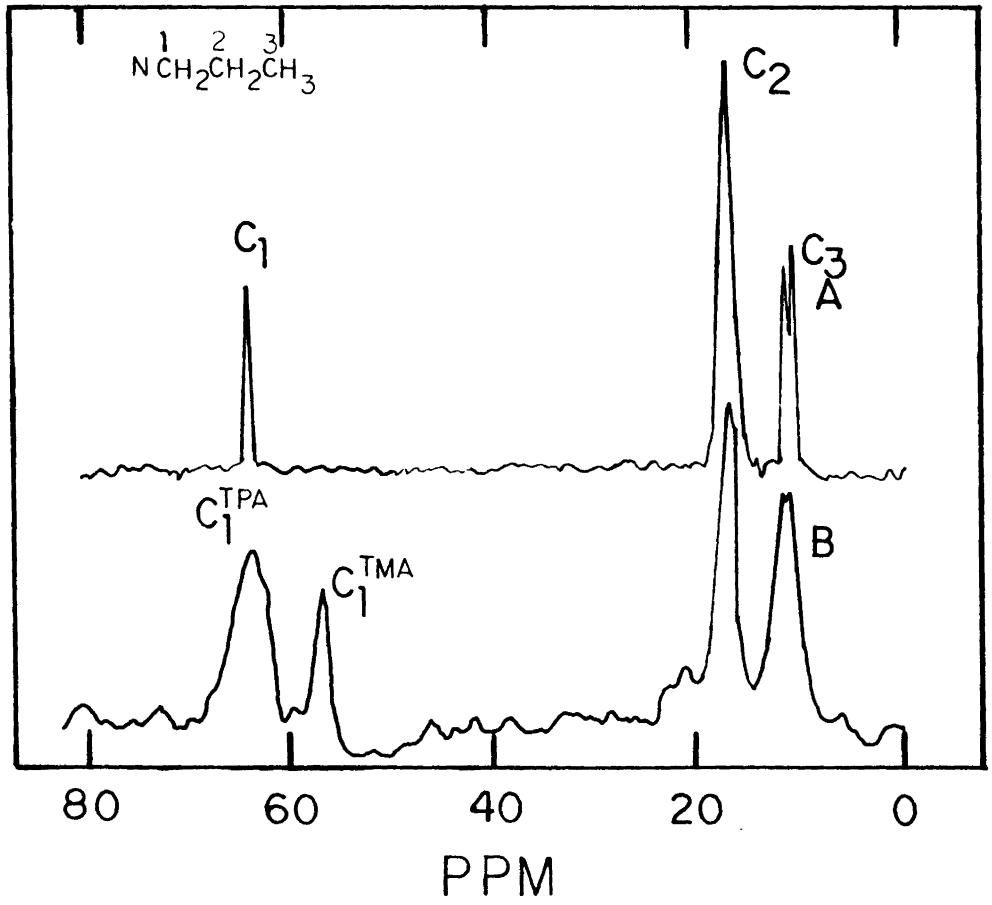

Figure 64: ^{13}C-MASNMR Spectra for ZSM-5. (A) TPA-ZSM-5 and (B) TMA/TPA ZSM-5 (Composition A, x = 0.5). Zero ppm is referenced to tetramethyl silane.

Table 19
Optical Density Ratio for ZSM-5 Synthesized in the Presence of Mixed Organic Cations with a High Sodium System

X[1]	Organic Cation(s)	a/b[2]
0.0	TPA	0.83
0.50	TMA/TPA	0.83
0.75	TMA/TPA	0.84
0.25	TEA/TPA	0.85
0.50	TEA/TPA	0.89
0.75	TEA/TPA	0.92

[1] As referenced in gel composition B
[2] Optical density ratio, see Figure 66

Note: FTIR spectra recorded from a 1% ZSM-5 in KBr pellet. ZSM-5 was not calcined.

absorption of internal vibration of the T-O tetrahedra in the 440-480 cm^{-1} region (136). These bands are labeled in Figure 65. The optical density ratio was used to ascertain the purity of the ZSM-5 samples. Ratios above 0.70 are indicative of high purity ZSM-5 (96). As the table shows, the optical density ratio (a/b) increases as the quantity of TEA in the synthesis gel is increased. The optical density ratio is not altered as the quantity of TMA in the synthesis gel is increased, however.

V.B.2 Cobalt ZSM-5 Synthesis

Figure 66 compares crystal growth data for ZSM-5 (Si/Al_2O_3 ratios of ∞ and 90, gel compositions C and D) synthesized in the presence and absence of $CoCl_2$-$6H_2O$ (gel Co/Si ratio of 0.0048). As shown, the presence of $CoCl_2$-$6H_2O$ in the synthesis gel hinders the rate of crystal growth. Note, however, that the addition of $CoCl_2$-$6H_2O$ does not appear to hinder the nucleation time. Also of note from this figure is that the addition of sodium aluminate results in decreasing the crystal growth rate, and does not allow for complete crystallization of the resulting Co/ZSM-5 crystals.

Figure 67 illustrates the crystal growth data for ZSM-5 synthesized with gel composition F employing the amorphous cobalt "seed" material with values of y up to 1.20. The value of y was increased by increasing the quantity of amorphous "seed" material added to the synthesis gel. As the figure shows, no deviation in crystal growth rate occurs over the range of y studied.

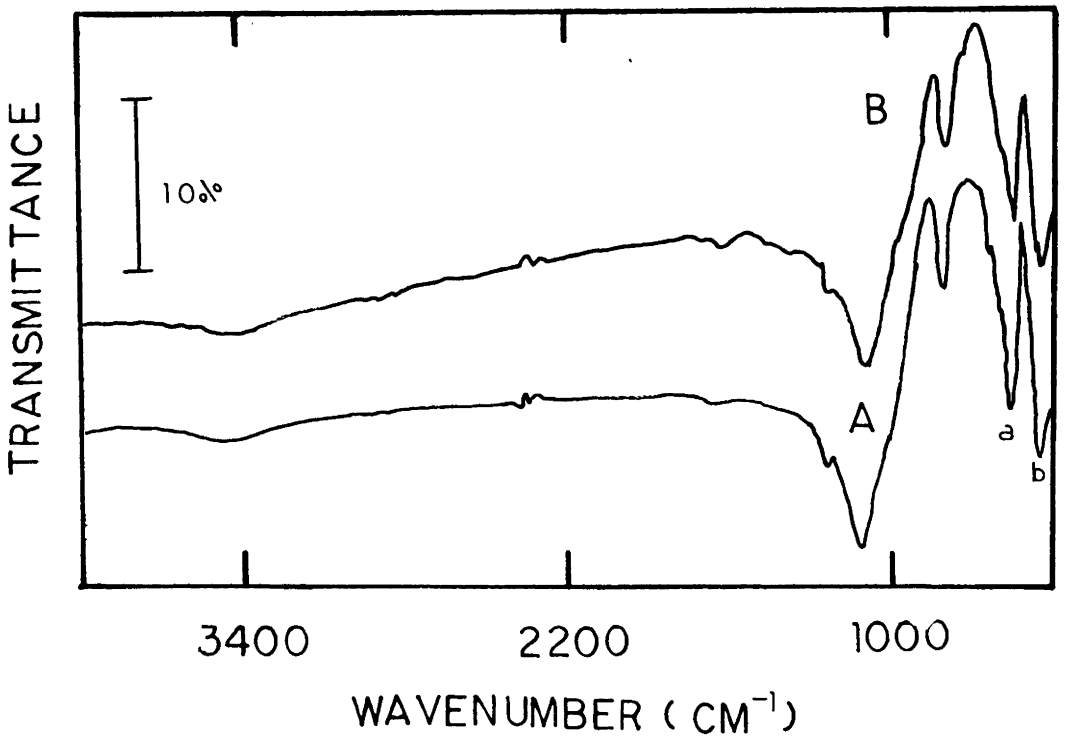

Figure 65: FTIR Spectra of ZSM-5 Synthesized with TPA (Low Sodium System) (A) and ZSM-5 Synthesized with 75% TMA (High Sodium System) (B). (a) and (b) refer to the absorption of framework tetrahedra and internal vibration of the T-O tetrahedra, respectively.

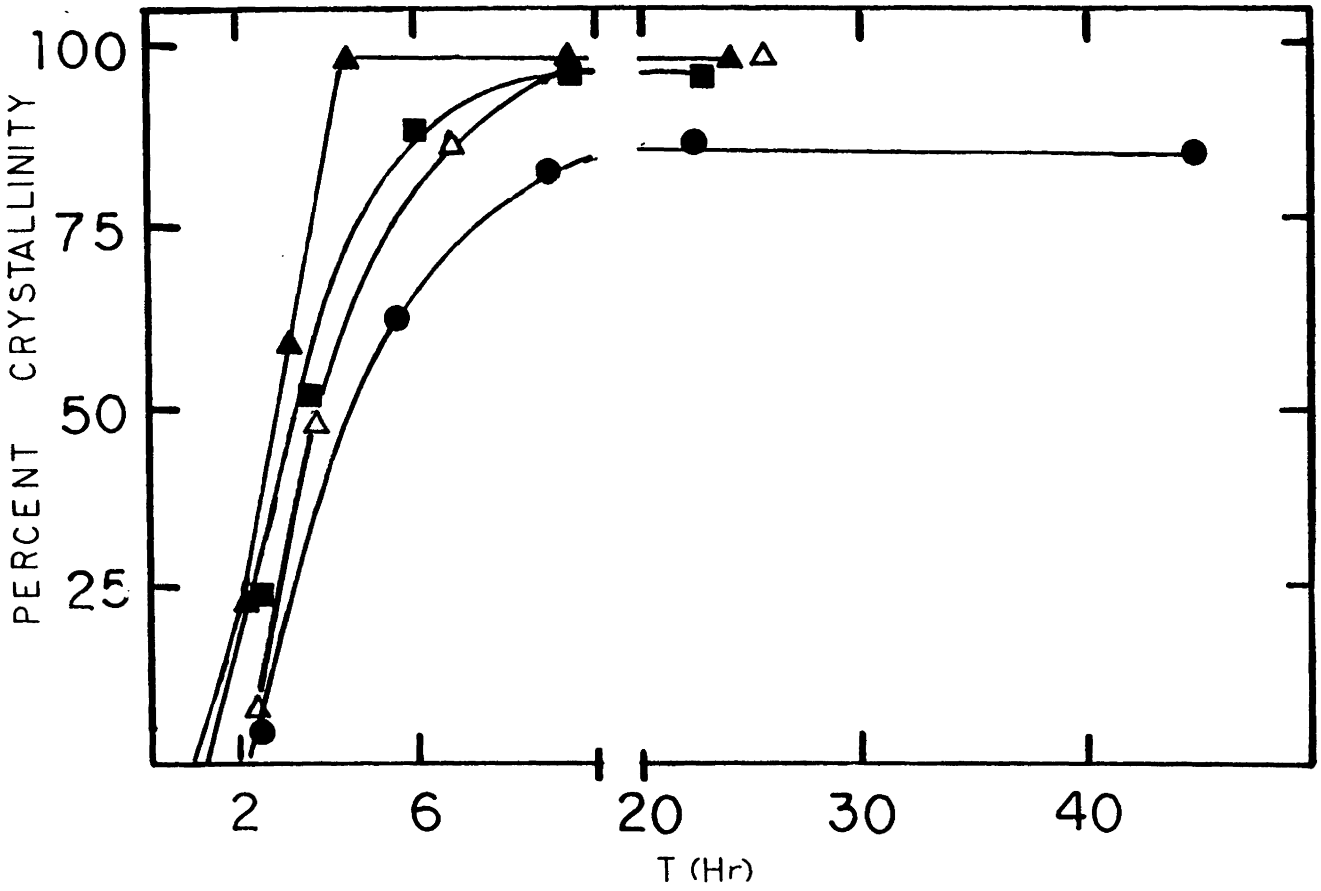

Figure 66: Crystal Growth Data for ZSM-5 synthesized from Gel Compositions C and D in the Presence and absence of $CoCl_2$-$6H_2O$. ● Co/ZSM-5 (Si/Al = 45); △ ZSM-5 (Si/Al = 45); ■ Co/ZSM-5 (Si/Al ≅ infinity); ▲ ZSM-5 (Si/Al = infinity).

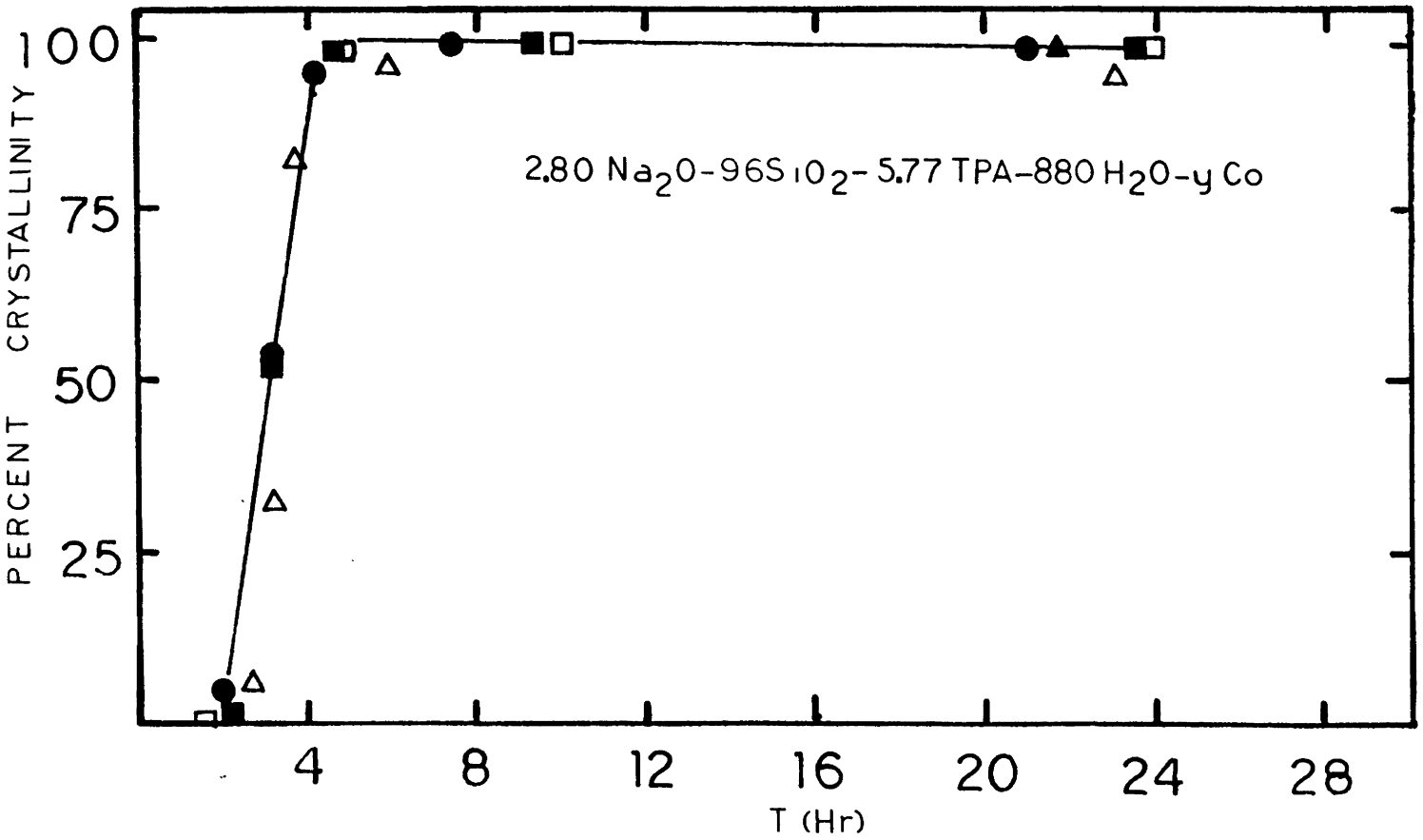

Figure 67: Crystal Growth Data for ZSM-5 Synthesized in the Presence of Amorphous "Seed" Material (Gel Composition F). —— ZSM-5 (Si/Al = infinity); ● Co/Si = 0 (large addition of blank "seed"); ■ Co/Si = 0.00014; ▲ Co/Si = 0.0013; ◘ Co/Si = 0.0049; △ Co/Si = 0.010. Cobalt content varied by increasing the quantity of amorphous "seed" material (12.79 wt% Co).

Figure 68 reports metal utilization data for Co/ZSM-5 synthesized from gel composition F. Amorphous "seed" material (6.21 wt% cobalt) was employed as the cobalt source. As this figure shows, the utilization of cobalt is not altered by increasing the gel Co/Si ratio to 0.0048. Material balances showed all the cobalt to be recovered in the product crystals to within experimental error.

Figure 69 shows an SEM of Co/ZSM-5 synthesized with gel composition F (Co/Si = 0.0082). This figure provides a qualitative indication of the crystal purity and morphology.

XPS and chemical analysis were performed on various Co/ZSM-5 samples prepared from gel compositions C through I. All crystals analyzed by XPS possessed Co/Si ratios of 0.0045 or greater. Table 20 reports binding energies of the elements of interest in the Co/ZSM-5 samples. The binding energies of oxygen (1s), aluminum (2p) and silicon (2p) energy levels are typical of those reported elsewhere (2,137). The binding energy of cobalt corresponds to Co(II) (2) for all cases where the XPS Co/Si ratio was greater than 0.020. For the two cases where the XPS Co/Si ratio was less than 0.020, the binding energy of the Co2p(3/2) photoelectron peak was shifted upfield approximately 1.5 eV. Note from Figure 70 that the Co2p(3/2) peak appears to be a doublet, and is reported as such in Table 20. A similar shift in binding energy has been reported elsewhere (2,3).

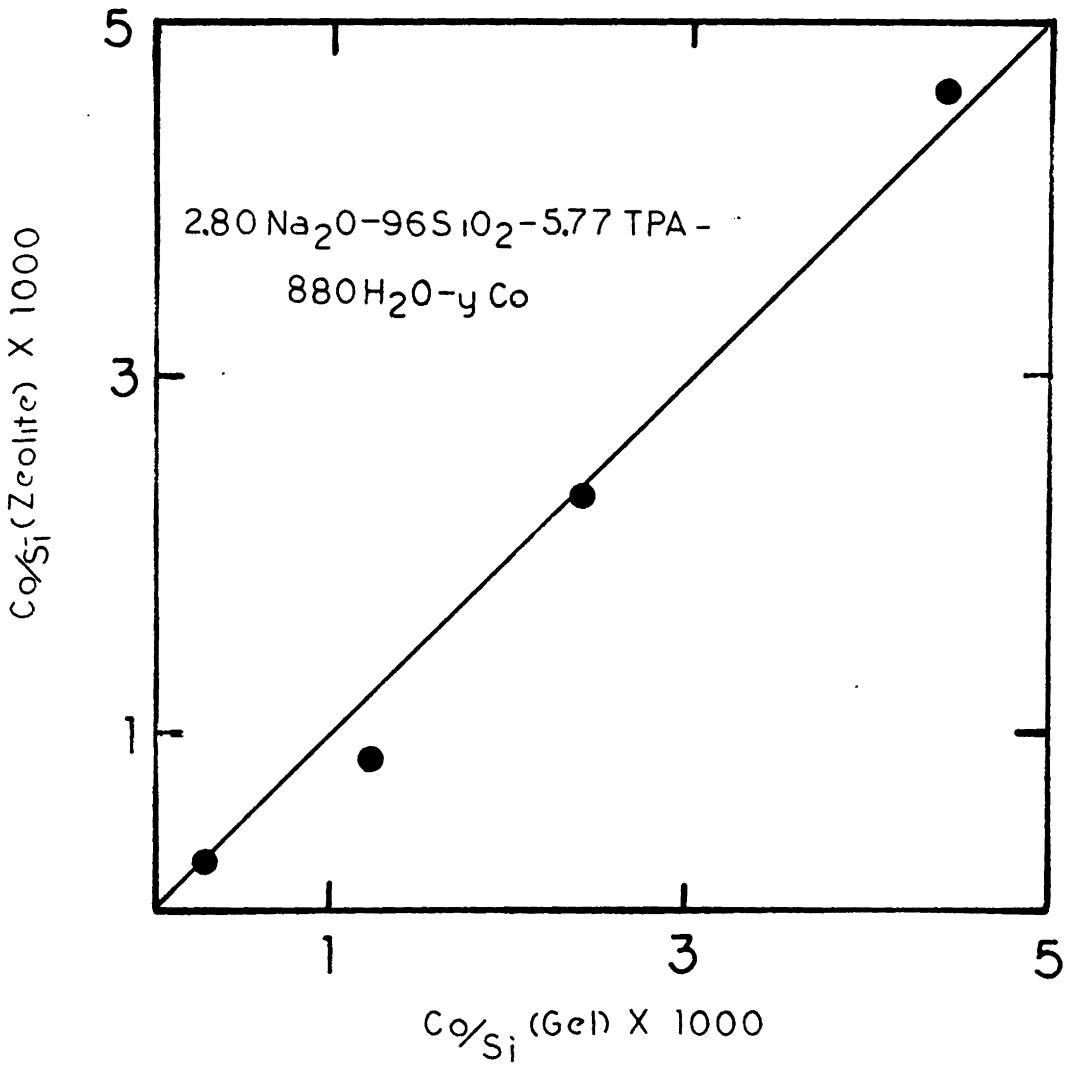

Figure 68: Cobalt Utilization for Co/ZSM-5 Synthesized with Amorphous "Seed" Material (6.21 wt% Co).

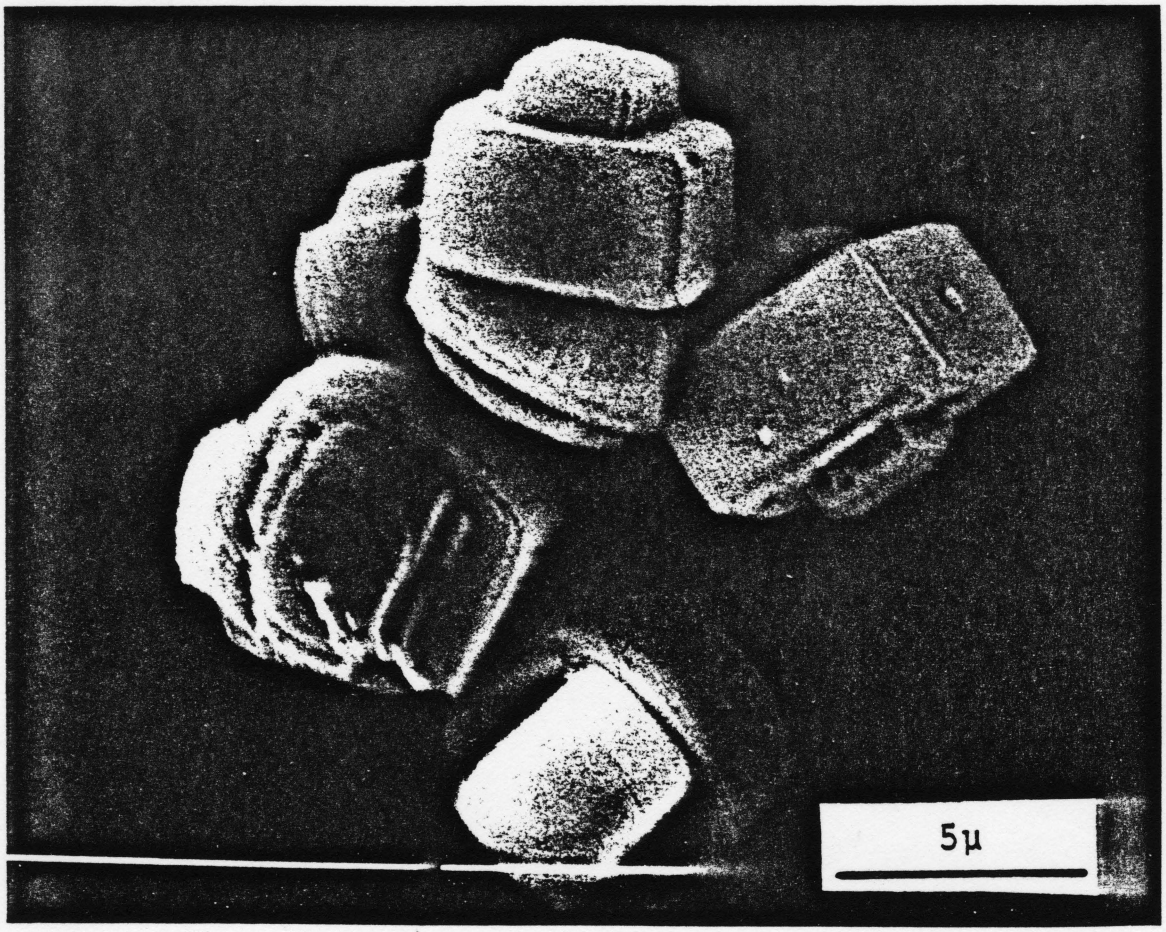

Figure 69: Scanning Electron Micrograph of Co/ZSM-5 Synthesized with Amorphous "Seed" Material (Composition F). Magnification 5000X. Zeolite is 0.80 wt% cobalt.

Table 20
Binding Energies of Elements in Cobalt ZSM-5
(Referenced to C1s at 285.0 eV)

Element	Binding Energy (eV)
O(1s)	532.7±0.1
Al(2p)	74.4±0.1
Si(2p)	103.7±0.1
Co(2p3/2)[1]	781.5±0.3
Co(2p3/2)[2]	782.0, 783.4

[1] Binding energy for all Co/ZSM-5 samples reported in Table 21 with an XPS Co/Si ratios greater than 0.020.

[2] Binding energy for Co/ZSM-5 synthesized from composition I (Co/Si = 0.0046) reported in Table 21.

Table 21 reports the XPS and CA data for Co/ZSM-5 synthesized in the presence of $CoCl_2$-$6H_2O$ and amorphous "seed" material. An ion exchanged Co/ZSM-5 is presented as a reference. As the table shows, the surface cobalt concentration was significantly lower for Co/ZSM-5 synthesized in the presence of the amorphous "seed" cobalt material at the same bulk loading. This table further shows that the addition of sodium aluminate to the synthesis gel increases the superficial cobalt concentration, while increasing the sodium hydroxide content decreased the superficial cobalt concentration. The data also illustrates that increasing the cobalt loading increases the superficial/bulk, Co/Si ratio. The superficial cobalt concentration of Co/ZSM-5 (approximately 0.5 wt%) with XPS Co/Si ratios of 0.1917, 0.0483 and 0.0098 are compared in Figure 26. These values correspond to the cation exchanged Co/ZSM-5, Co/ZSM-5 synthesized from composition C and Co/ZSM-5 (bulk Co/Si = 0.0046) synthesized from composition I as reported in Table 21. A comparison between the relative amount of cobalt present at the surface for each preparation can be made by comparing the intensity of the O(KVV) auger to the intensity of the Co2p(3/2) peak.

Figure 71 shows the Co2p photoelectron region for Co/ZSM-5 (composition I, Co/Si=0.0046) as-synthesized and following calcination at 550°C. As the figure shows, a slight upfield shift in binding energy has occurred. Note that the intensity of the Co2p(3/2) peak to that of the O(KVV) auger has not been altered.

Table 21
XPS Analysis for Cobalt ZSM-5 Prepared from Various Techniques

Cobalt Source	Si/Al[1] (gel)	NaOH[2]	Co/Si XPS	Co/Si CA	Co/Si XPS/CA
Ion exchanged	45	----	0.1917	0.0054	35.50
Salt[3]	∞	low(C)	0.0478	0.0048	9.96
Amorphous "seed"	∞	low(F)	0.0198	0.0048	4.10
Amorphous "seed"	∞	low(F)	0.0402	0.0082	4.88
Amorphous "seed"	∞	high(G)	0.0068	0.0046	1.48
Salt[3]	45	low(D)	0.0708	0.0049	14.49
Amorphous "seed"	35	low(H)	0.0432	0.0047	9.00
Salt[3]	35	high(E)	0.0256	0.0048	5.33
Amorphous "seed"	35	high(I)	0.0098	0.0046	2.13
Amorphous "seed"	35	high(I)	0.0584	0.0085	6.90

[1] Aluminum from sodium aluminate
[2] Low and high sodium batches as referenced in text; letter in brackets refers to gel composition
[3] $CoCl_2$-$6H_2O$ added to synthesis gel

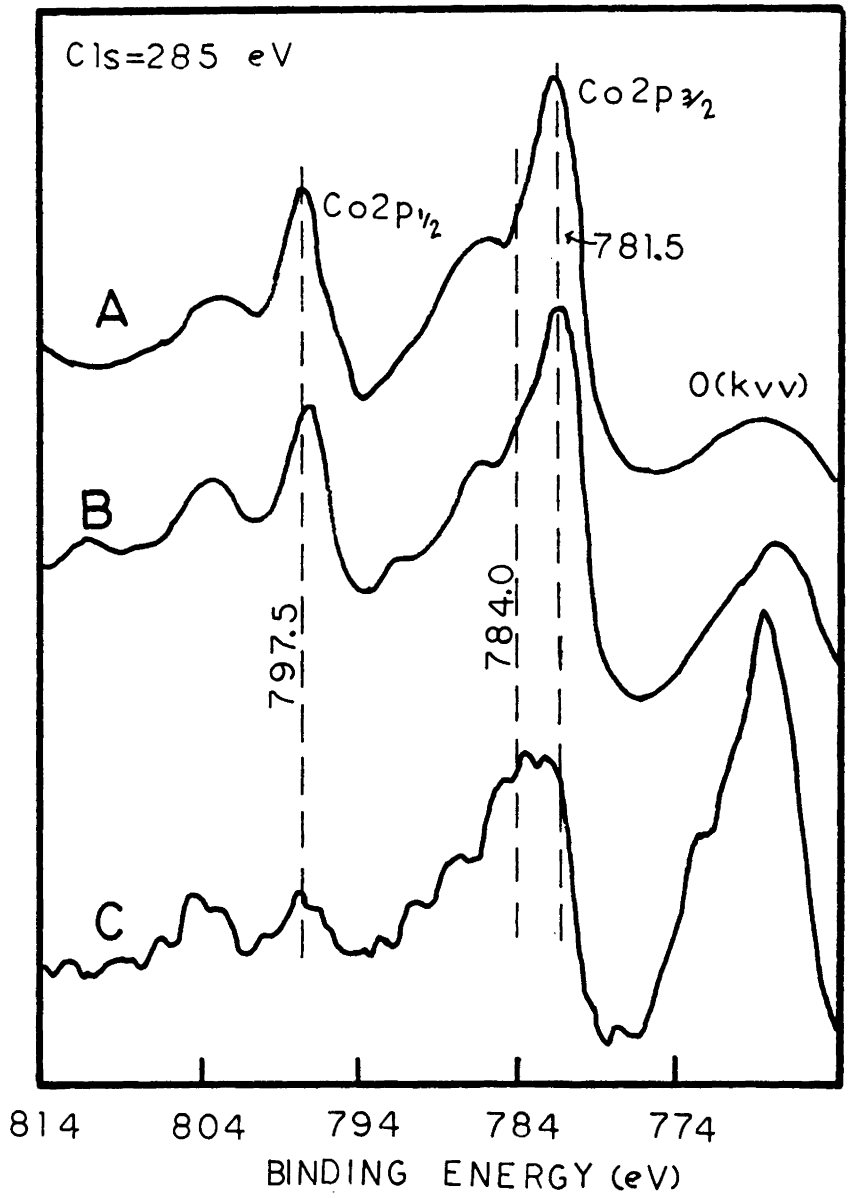

Figure 70: XPS Spectra of the Co2p Photoelectron Region. (A) Co/ZSM-5 (Co/Si = 0.0054) prepared by cation exchange; (B) Co/ZSM-5 (Co/Si = 0.0049) prepared from composition C and (C) Co/ZSM-5 (Co/Si = 0.0046) prepared from composition I.

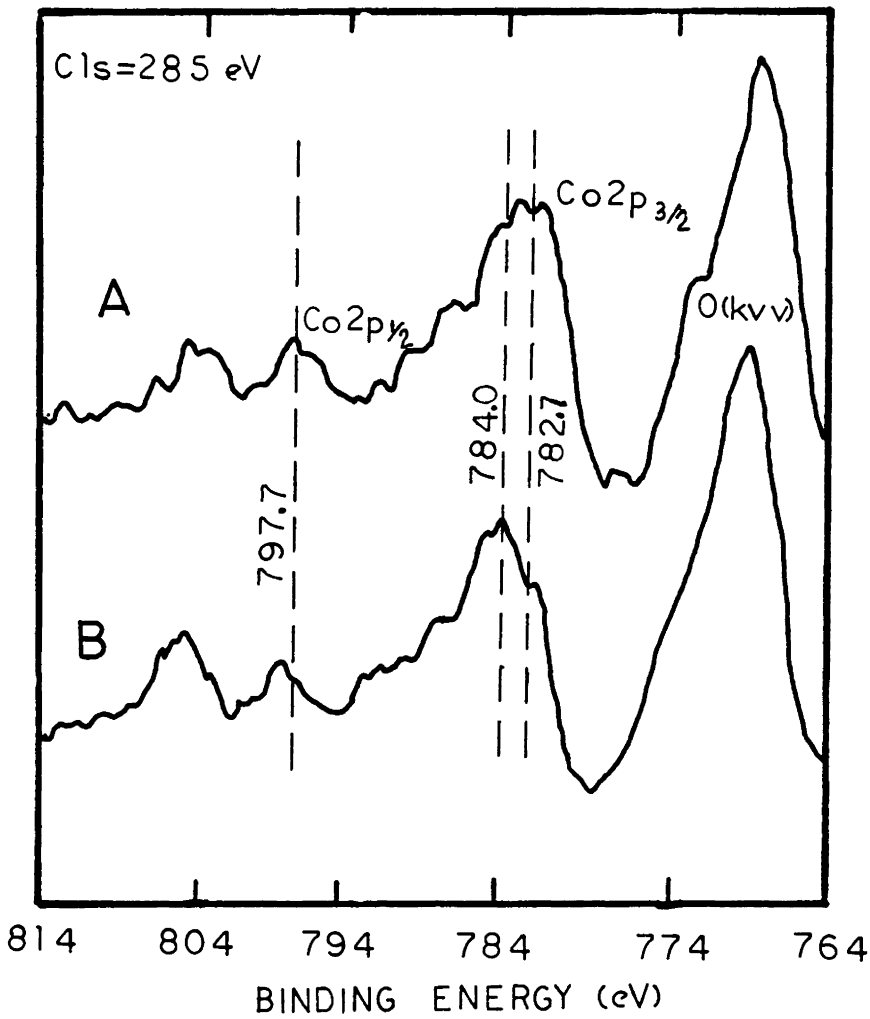

Figure 71: XPS Spectra of the Co2p Photoelectron Region. (A) Co/ZSM-5 synthesized from composition I (Co/Si = 0.0046) and (B) following calcination.

Figures 72 through 75 are electron microprobe images of various Co/ZSM-5 samples. Figures 72 and 73 show the cobalt distribution in ZSM-5 crystals (Co/Si = 0.0082) and single crystal (synthesized from gel composition F). These figures show the presence of regions of high cobalt concentrations. The cobalt distribution of Co/ZSM-5 synthesized from composition I (Co/Si = 0.0046) showed the cobalt to be near evenly distributed among the crystals. Figure 74 reports the aluminum distribution within ZSM-5 synthesized from gel composition F employing a large quantity of blank amorphous "seed" material. This figure shows the aluminum distribution across the crystal to be uniform. Figure 75 shows the cobalt and aluminum metal distribution of cation exchanged Co/ZSM-5 (single crystal). Note the nonuniformity in the cobalt distribution.

V.C Zeolite Rhodium A: Hydroformylation Activity

Table 22 reports the hydroformylation activity of a 0.07 and 0.08 wt% rhodium zeolite A catalyst in the potassium, sodium and calcium forms. As the table shows, the greatest catalytic activity occurred when the zeolite was in the calcium form. These reactions were carried out in the batch reactor system at 50°C under 300 psig H_2/CO (3:1 and 1:1). Table 23 illustrates the effects of rhodium loading on conversion for RhCa A prepared by addition of $RhCl_3$-$3H_2O$ and rhodium "seed" material to the synthesis gel. As this table shows, the reaction rate increased with the increase in catalyst rhodium loading, with the exception of the less than 0.1 wt% rhodium catalysts. The table also shows the catalyst prepared from the rhodium "seed" material to be more reactive than catalyst syn-

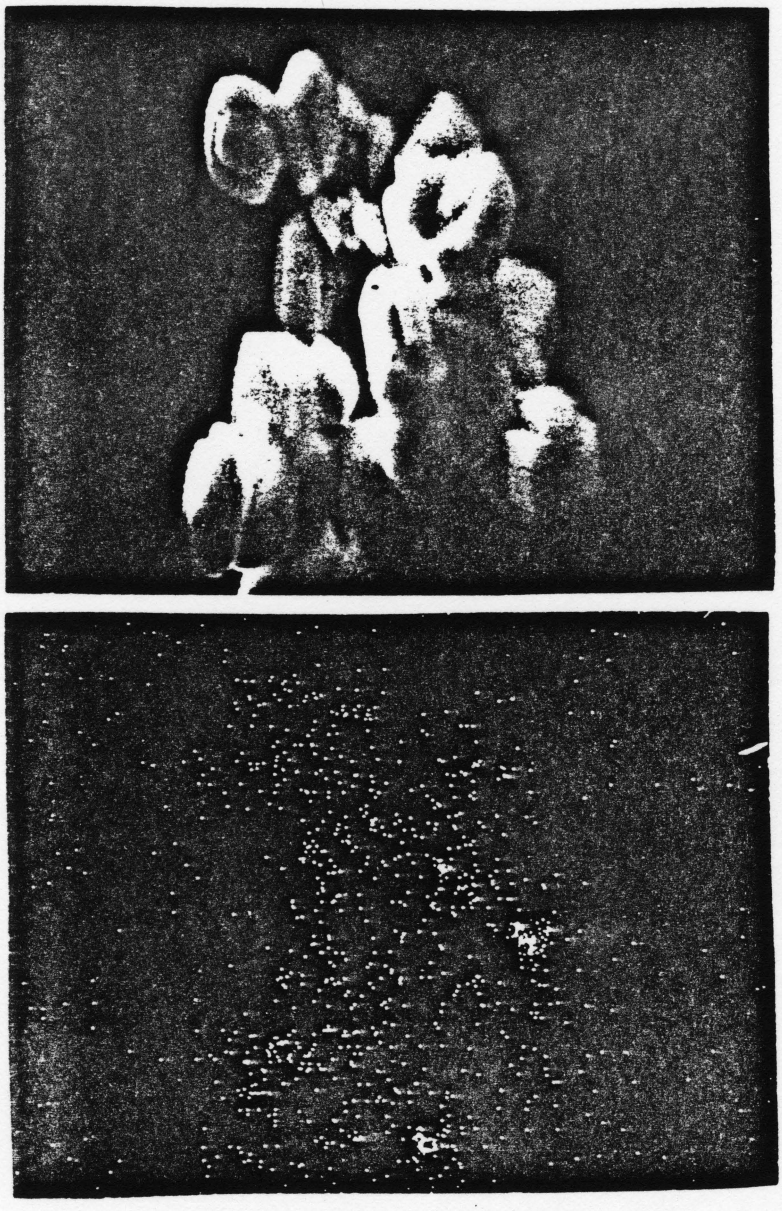

Figure 72: Electron Microprobe Analysis of Co/ZSM-5 (Composition F, Co/Si = 0.0082). Top: SEM of crystals; Bottom: Cobalt distribution. Crystals in as-synthesized form, see Table 21 for XPS and chemical analysis.

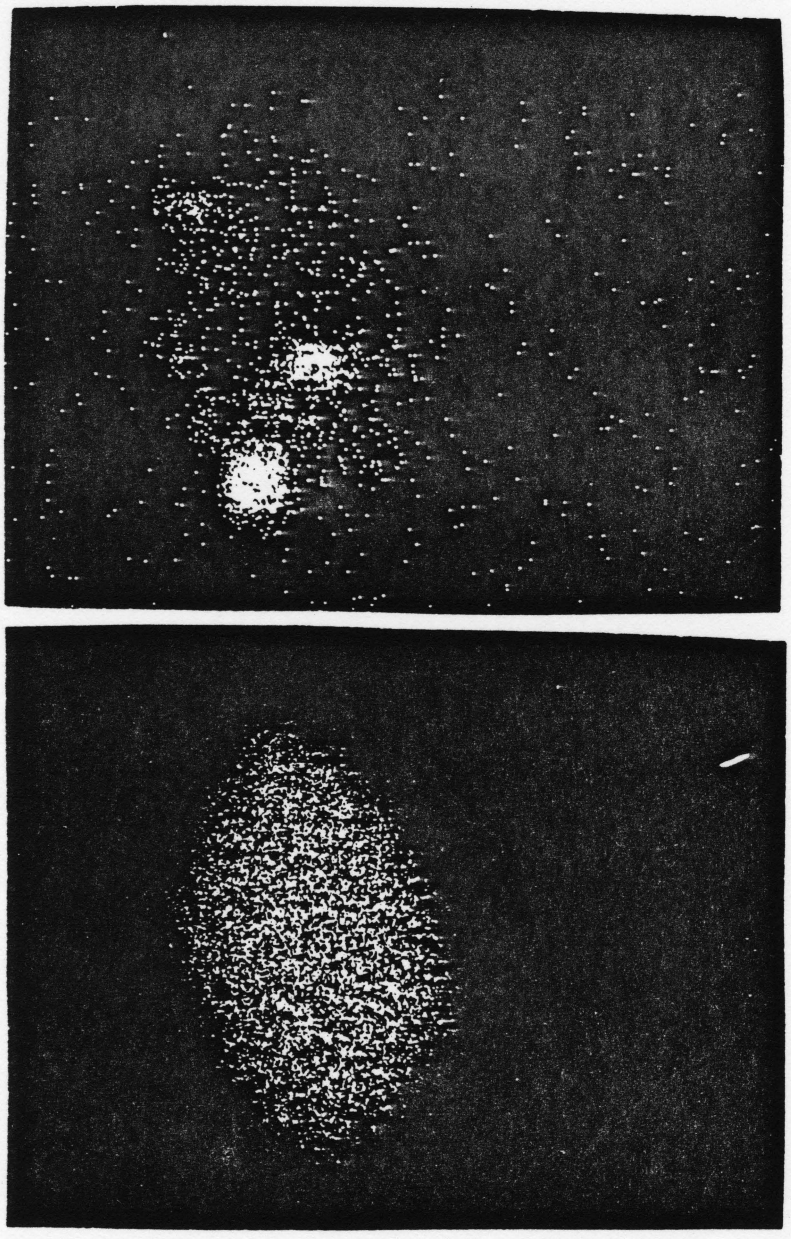

Figure 73: Electron Microprobe Analysis of Co/ZSM-5 Crystal (Composition F, Co/Si = 0.0082). Top: Cobalt distribution; Bottom: Silicon Distribution. Crystal shown following Calcination. See Table 21 for XPS and chemical analysis.

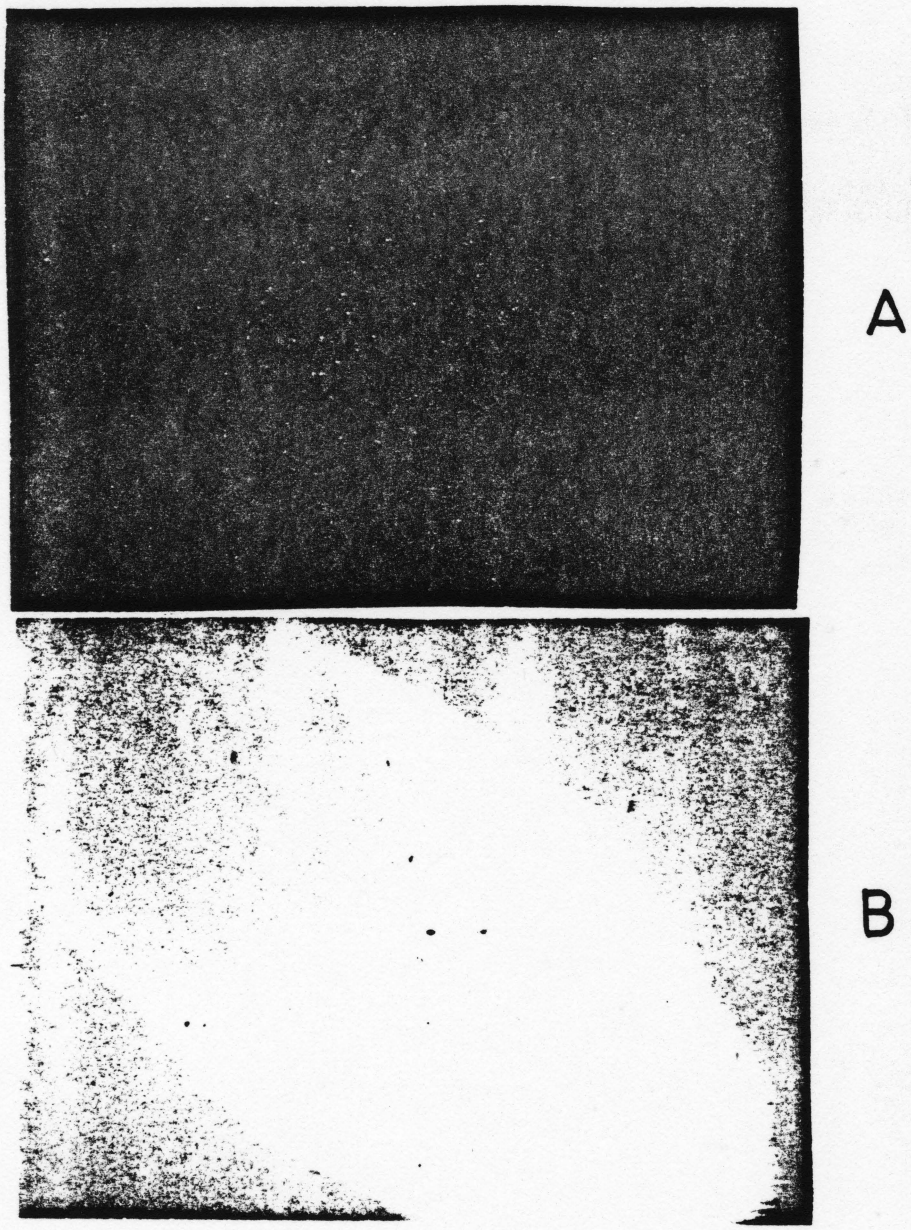

Figure 74: Electron Microprobe Analysis of ZSM-5 Crystal Synthesized with Large Addition of Blank Amorphous "Seed" Material (Composition F). (A) Aluminum Distribution and (B) SEM of single crystal in as-synthesized form.

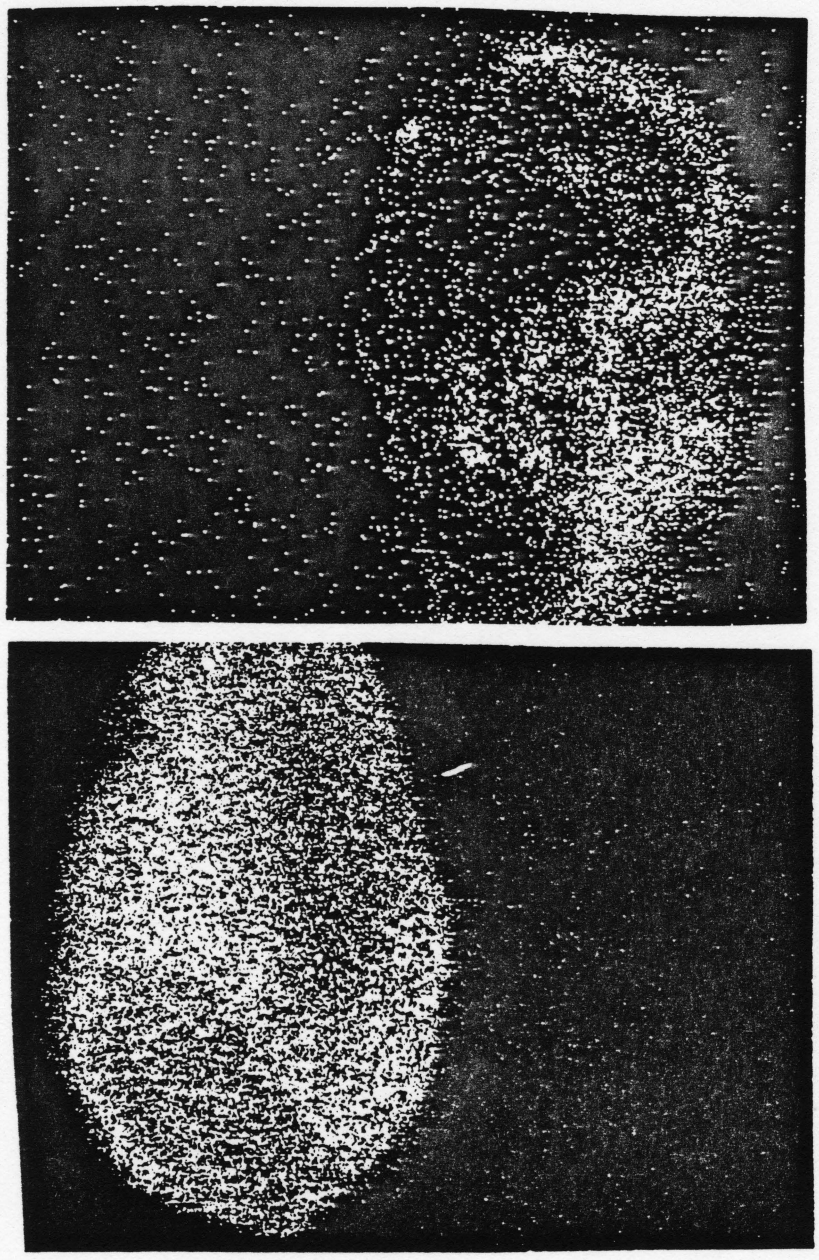

Figure 75: Electron Microprobe Analysis of Co/ZSM-5 Prepared by Cation Exchange (Co/Si = 0.0053). Top: Cobalt distribution Bottom: Aluminum Distribution. See Table 21 for XPS and chemical analysis.

Table 22
Cation Effect on Hydroformylation Activity
of Zeolite Rhodium A Synthesized form "seed"

$H_2/CO = 3/1$

Catalyst	Run	Rh Conc[1]	Conversion[2]	Selectivity[3]	N/B[4]
RhK A	5-22-84	0.035	1.60%	0.46	2.92
RhCa A	5-12-84	0.041	96.0 %	0.31	2.36

Catalyst loading: 0.07 wt % Rh

$H_2/CO = 1/1$

RhNa A	7-31-84	0.025	0.36%	----	----
RhCa A	8-01-84	0.025	21.3 %	0.26	2.73

Catalyst loading: 0.08 wt % Rh

P = 20 atm
T = 50°C
t = 22 hrs
Concentration = 1.0 molar 1-hexene in toluene

[1] mmols Rh/liter toluene
[2] Conversion of 1-hexene
[3] Ratio of aldehydes formed to 1-hexene reacted
[4] Ratio of normal aldehyde to branched aldehyde(s)

Table 23
Reactivity at Various Loadings for Zeolite Rhodium A Synthesized from "Seed" and $RhCl_3$-$3H_2O$

Catalyst Synthesized from Rhodium "Seed" Material

Wt% Rh	Run	Rh Conc	Conversion	Selectivity	N/B	Rate[1]
0.024	10-11-84	0.0097	7.75%	0.36	3.17	0.101
0.08	8-01-84	0.025	21.3 %	0.26	2.73	0.108
0.37	8-24-84	0.060	3.17%	0.36	2.60	0.0067
0.83	8-16-84	0.052	7.90%	0.31	2.92	0.0192
0.96	9-28-84	0.042	13.91%	0.37	2.80	0.0418

Catalyst Crystallized from $RhCl_3$-$3H_2O$

0.27	10-04-84	0.044	1.17%	0.60	2.17	0.0034
0.29	10-10-84	0.036	1.11%	0.43	2.75	0.0039
0.90	10-07-84	0.042	2.20%	0.37	2.93	0.0066
1.06	9-29-84	0.039	1.93%	0.24	2.70	0.0062
1.41	9-26-84	0.041	4.87%	0.42	2.66	0.0150

P = 20 atm
T = 50°C
t = 22 hrs
Concentration = 1.0 molar 1-hexene in toluene

[1]Rate defined as mole 1-hexene reacted per mole rhodium per second.

thesized from $RhCl_3$-$3H_2O$. All reaction data reported in Table 23 were conducted at 50°C under 300 psig CO/H_2 (1:1). Table 24 compares the conversion and activity of RhCa A towards different olefins, 1-hexene and 4-methyl-1-pentene, reacted at 50°C under 300 psig CO/H_2 for 22 hours. This table also compares the selectivity of Rh_6CO_{16} to that of RhCa A at low conversions.

Tables 25 and 26 report the catalyst activity and rhodium loss from the catalyst (elution) over the course of four batch reactions. These catalysts were 0.99 wt % rhodium and 0.065 wt% rhodium prepared from "seed" material; respectively. These runs were performed in the presence of cyclohexylmercaptan (3-4 cm^3) in order to poison solution and surface rhodium. Heptanal was the only product observed in these runs. As the table shows, the conversion per gram of zeolite was not altered significantly following repeated usage. Further analysis showed significant rhodium loss to occur during the first run, following which, the rhodium loss became less severe (illustrated in Figure 76). The comparison of data presented in Tables 25 and 26 show that conversion was not altered significantly when the zeolite rhodium content was decreased from 0.99 wt% to 0.065 wt%.

Table 27 presents spectroscopic (XPS) and chemical analysis of RhCa A prepared from rhodium "seed" material following exposures to carbon monoxide environments. Analysis of the zeolite following pretreatment and vapor phase hydroformylation showed the majority of the rhodium loss to occur during catalyst pretreatment. Analysis of the spent catalyst

Table 24
Hydroformylation Activity of Various Catalysts and Reactants

Catalyst	Reactant	Conversion	N/B	Selectivity
Rh_6CO_{16}	1-hexene	23.16%	2.67	0.31
Rh_6CO_{16}	1-hexene	39.55	2.67	0.29
RhCa A[1]	1-hexene	13.91	2.80	0.37
RhCa A[1]	4-methyl-1-pentene	11.26	2.62	0.33

P = 20 atm CO/H_2 (1:1)
T = 50°C
Concentration = 1.0 molar olefin in toluene

[1] Catalyst 0.96 wt% rhodium

Table 25
Conversion and Rhodium Loss with Repeated Batches

Batch	Run	Conversion[1]	Rh Lost[2]	Rh loading
1	11-28-84	1.46 %	37.4%	0.62 wt%
2	12-02-84	1.21 %	5.5%	0.57
3	12-03-84	1.84 %	1.6%	0.58
4	12-04-84	1.61 %	1.5%	0.55

Initial catalyst loading: 0.99 wt%
Temperature: 120 °C
Pressure: 300 psig
Run time: 22.5 hrs
Cyclohexylmercaptan: 3 - 4 cm^3

[1] Conversion to aldehyde per gram zeolite.
[2] Based on the rhodium loading of the catalyst which entered the reactor. Value calculated based on combination of rhodium,analysis of solution and atomic absorption analysis of solid.

Table 26
Conversion and Rhodium Loss with Repeated Batches

Batch	Run	Conversion[1]	Rh Lost[2]	Rh loading
1	12-07-84	0.87 %	55.4%	0.029 wt%
2	12-08-84	1.05 %	13.0%	0.035
3	12-09-84	1.61 %	---	---
4	12-10-84	1.37 %	---	---

Initial catalyst loading: 0.065 wt%
Temperature: 120 °C
Pressure: 300 psig
Run time: 22.5 hrs
Cyclohexylmercaptan: 3 - 4 cm^3

[1] Conversion to aldehyde per gram zeolite.
[2] Based on the rhodium loading of the catalyst which entered the reactor. Value calculated based on combination of rhodium analysis of solution and atomic absorption analysis of solid.

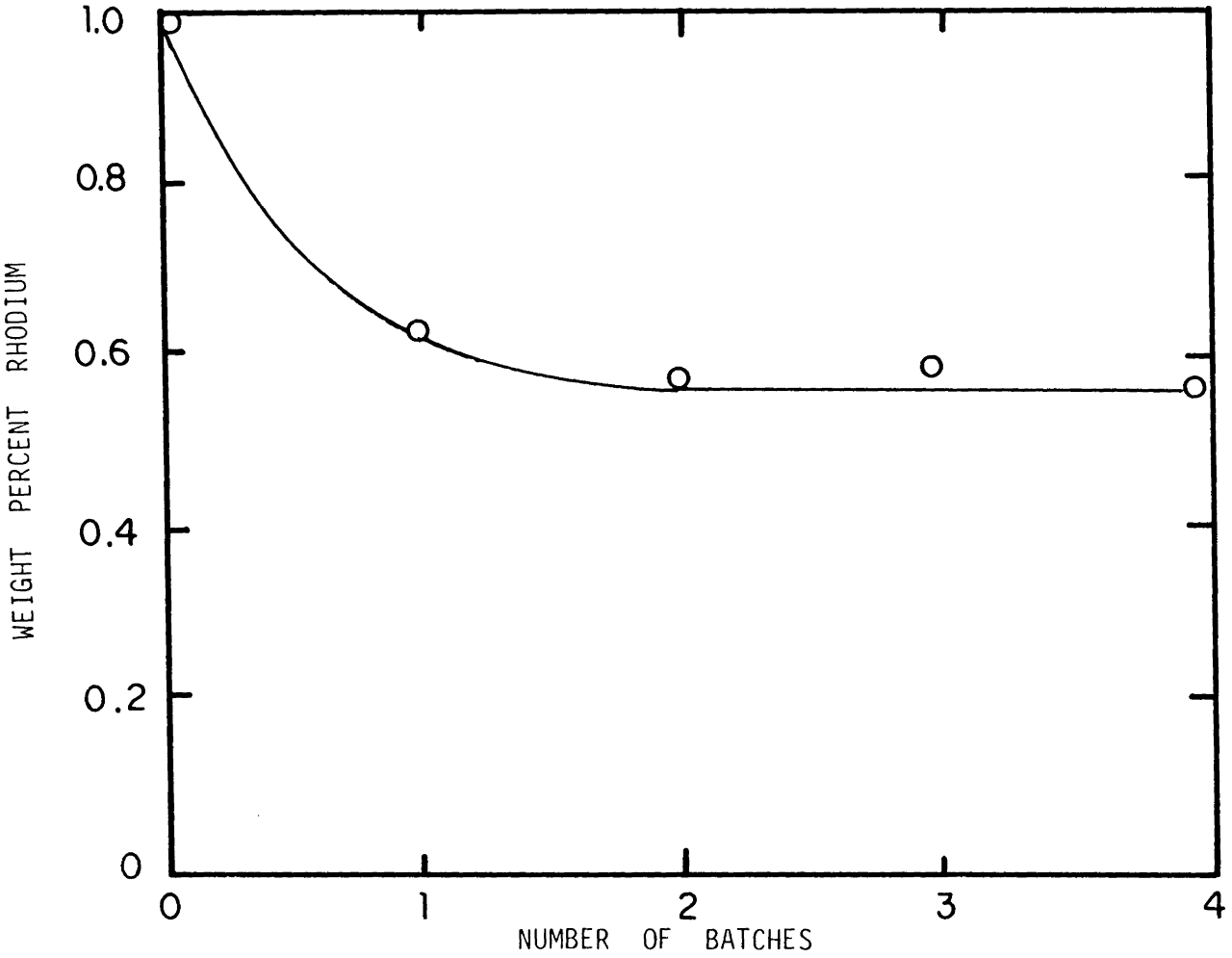

Figure 76: Rhodium Loss from 0.96 wt% RhCa A as a Function of Catalyst Usage.

Table 27
XPS and Chemical Analysis Following Vapor and Liquid Phase Reaction Exposures

Treatment	wt% Rh	Rh/Si XPS/CA	Rh Lost	Si/Al XPS	Si/Al CA
Vapor Phase (137)[1]					
As Synthesized[3]	1.20	0.57	---	1.18	1.07
Pretreat	0.80	1.01	33 %	1.54	1.08
Reaction	0.76	0.26	4 %	1.40	1.12
Liquid Phase (Run 11-04-84)[2]					
As Synthesized[3]	0.96	1.31	---	0.83	1.16
Reaction	0.80	0.90	17.2 %	1.41	1.19

[1] Pretreatment: 30 psig flowing CO for 18 hours at 150°C. Reaction: 120°C under 15 psig total H_2/1-hexene/N_2/CO (3/1/2/1) for 33 hours.

[2] Reacted at 50°C under 300 psig CO/H_2 (1:1) for 22 hrs.

[3] From Table 17.

following the liquid phase reaction also shows a rhodium loss to have occurred. Note that in no case is there a drastic increase (order of magnitude) in surface rhodium. From this analysis it also appears that there is a slight loss of aluminum at the zeolite surface, as evidenced by the increase in the XPS Si/Al ratio.

Figure 77 shows FTIR spectra of RhCa A following 5 minutes and 24 hours of exposure to 30 psig CO at 150°C. These spectra were recorded for the purpose of detecting rhodium carbonyl species. As these spectra show, only one rhodium carbonyl species is present, with the band centered at 2020 cm^{-1}.

V.D Ruthenium Zeolite A: Fischer-Tropsch Reactivity

The XPS spectral region for the Ru3d5/2 energy level of RuCa A (2.16 wt% Ru) in the as synthesized form (A), following hydrogen reduction (B) and following reduction and reaction (run 9-26-85) (C) are shown for comparison in Figure 78. Note that the intensity of the Ru3d5/2 energy level has remained relatively constant over the course of the exposures. The shift of the Ru3d5/2 energy level to a lower binding energy is due to a decrease in oxidation state.

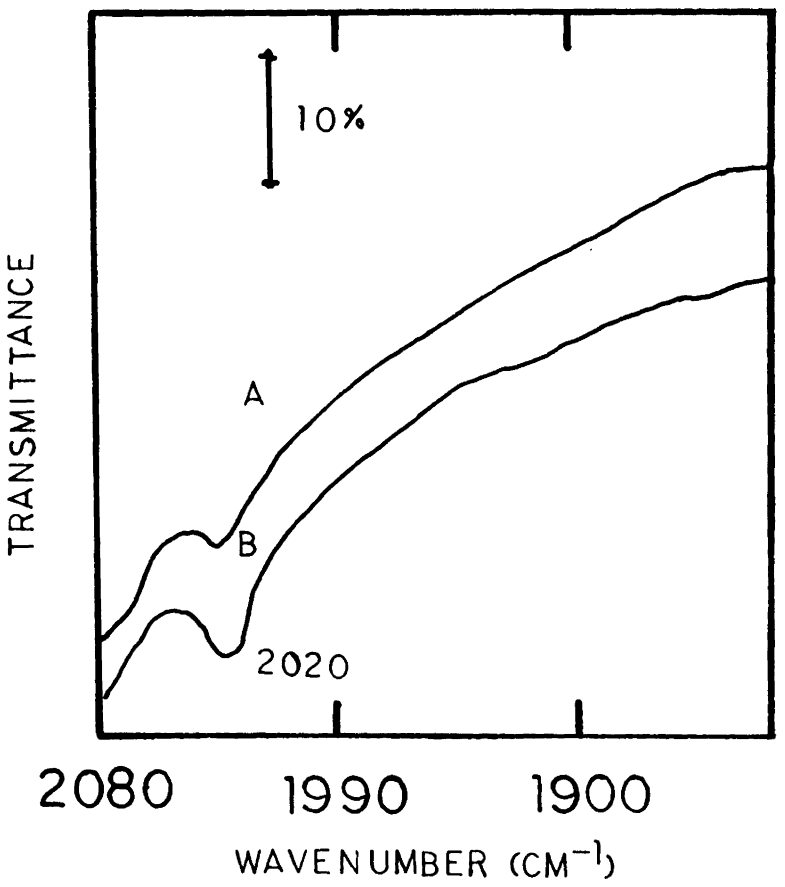

Figure 77: FTIR Spectra of RhCa A Exposed to 30 psig CO at 150 C. (A) Following 5 minutes of exposure and (B) following 24 hours of exposure. Pellet consisted of pure zeolite. (Zeolite 1.20 wt% rhodium, see Table 17 for XPS and chamical analysis).

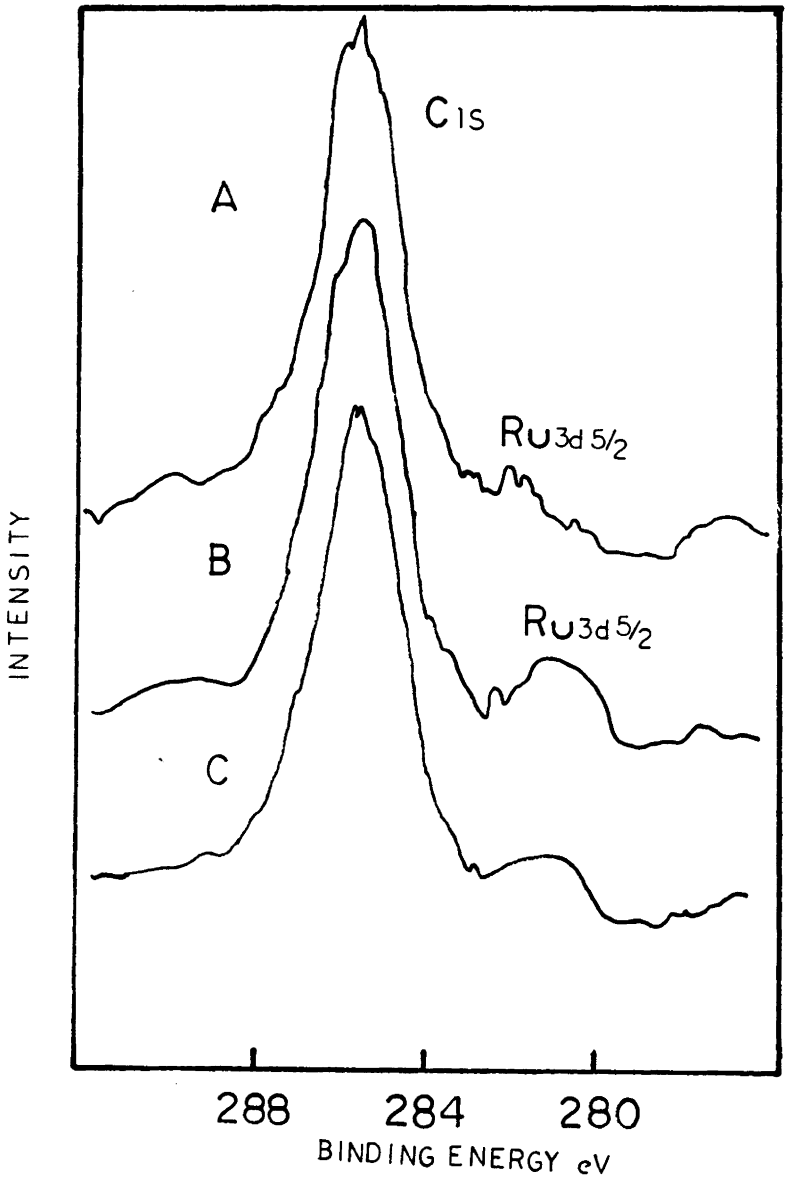

Figure 78: XPS Spectra of the Ru3D5/2 Photoelectron Region for RuCa A (2.16 wt% Ruthenium). (A) As synthesized; (B) follwoing reduction at 275 C and (C) following reaction (run 9-26-85).

Figure 79 reports the IR spectra of RhCa A[19] following exposure to reaction, RuCa A following exposure to reaction and the same catalyst (RuCa A) prior to reaction. Spectrum A is of RuCa A prior to reaction while spectrum B is of RuCa A (1.53 wt%) following exposure to 15 psig CO/H_2 for 22 hours at 255°C followed by exposure at 80 psig (CO/H_2) and 308°C for an additional 22 hours (run 9-21-85). Spectrum C is of RhCa A reacted at 350°C under 80 psig Co/H_2 for approximately 12 hours. The spectrum for RuCa A following hydrogen reduction at 275°C was similar to that of the as synthesized catalyst. Note from comparison of spectrum B and C that important changes are occurring over the 800-650 cm^{-1} region. The band at 658 cm^{-1} decreases in intensity while the bands at 756 and 673 cm^{-1} are gaining intensity. Note also that the 756 and 673 cm^{-1} bands are present in the RhCa A (spectrum A) at 737 and 671 cm^{-1}. From spectrum A note that the intense band shifts from 1011 cm^{-1} to 987 cm^{-1}. Also, there is the absence of the band at 551 cm^{-1} while bands appear at 737, 712, 671 and 438 cm^{-1}. Note also that the band at 468 cm^{-1} is still present.

Pore volume analysis performed on the 1.53 wt% RuCa A catalyst following reduction showed no change in the oxygen adsorption capacity. Following reaction (run 9-21-85); however, a 22 % loss in oxygen adsorption capacity had occurred.

---

[19] This catalyst was 1.20 wt% Rh and was synthesized from the amorphous "seed" material. For XPS and chemical analysis, see Table 18.

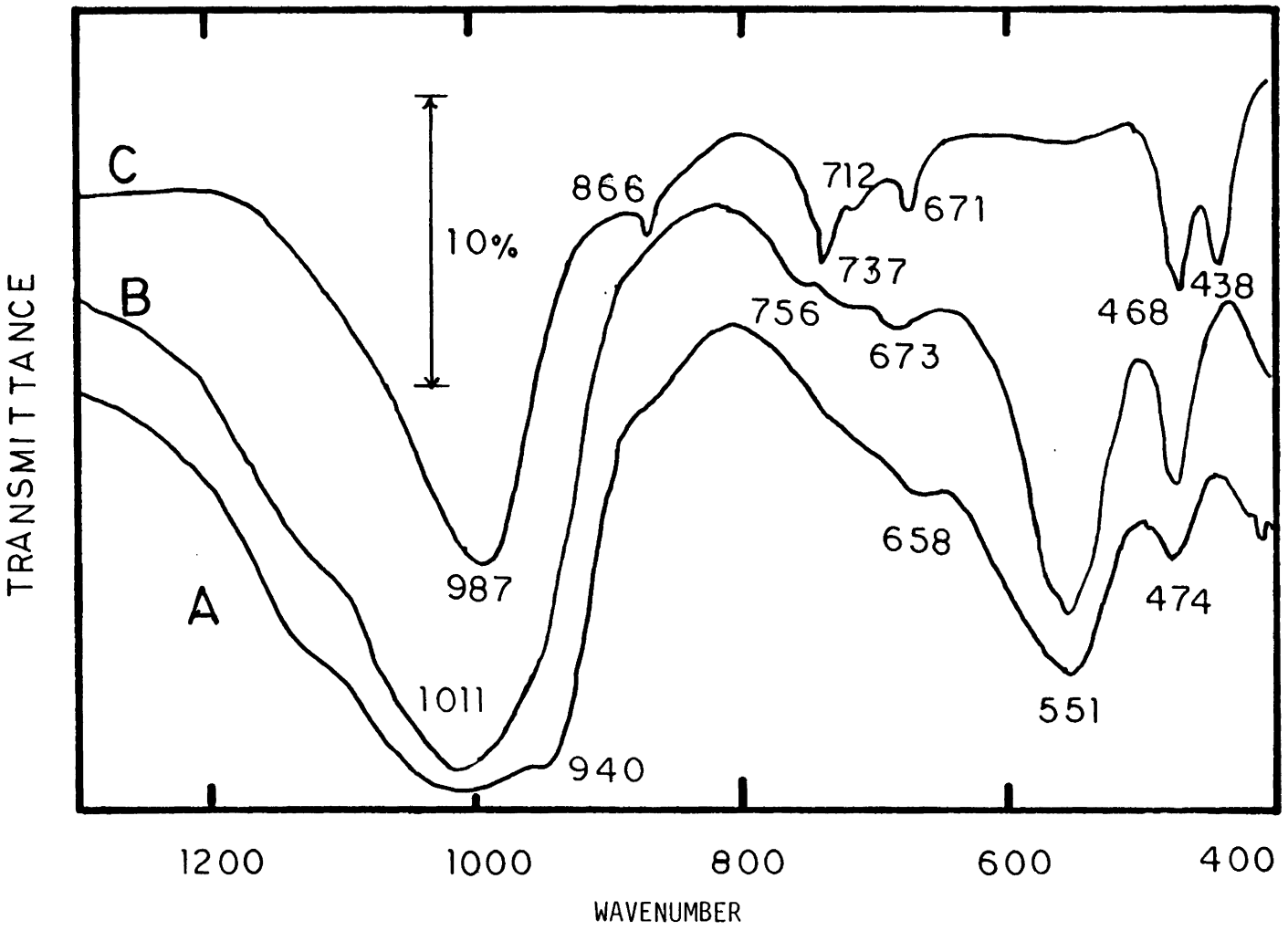

Figure 79: FTIR Spectra of RuCa A (1.53 wt% Ru) and RhCa A (1.20 wt% Rh) following Fischer-Tropsch Reaction. (A) 1.53 wt% RuCa A prior to reaction; (B) RuCa A following Run 9-21-86 and (C) RhCa A following reaction.

Run 9-21-85 was performed with 2.0g RuCa A (1.53 wt% ruthenium). This catalyst was reduced at 275°C for 18 hours under 20 psig hydrogen, after which it was reacted at 255°C under 15 psig CO/H_2 (1:1) for 24 hours. Following 24 hours of exposure to the reaction environment, the pressure was raised to 80 psig and the temperature increased to 308°C. Details of this run are presented in Appendix XI. The hydrocarbon start-up behavior at 255°C is shown in Figure 80 for C_1, C_3, C_4 and C_5. C_2 hydrocarbon start-up behavior was similar to that of methane. Traces of C_6 were observed between 8 and 12 hours after start-up. In no case was C_7 or greater hydrocarbon detected in the product stream, nor were any branched hydrocarbons detected as well. As this figure shows, methane was the only hydrocarbon produced initially. The C_3 production rose sharply to a maximum, followed by decay. The figure shows that as the C_3 production decreased, the production of C_4 rapidly increased. Note that the C_4 production surpasses the C_3 production after approximately 4 hours and follows a similar behavior during declining activity. The rate of production of C_5 did not become significant until approximately 8 hours after start-up. Note that the increase in C_5 production did not interfere with the steady decay of the other hydrocarbon components.

Figure 81 shows the hydrocarbon product distribution (run 9-21-85, 255°C) at times of 72, 280 and 666 minutes into the run. Note that in no case was a log-normal behavior followed. The figure shows that there is a shift in selectivity towards production of longer chain hydrocarbons as the run time is increased. Table 28 shows the initial selectivity is towards C_1 and C_3 hydrocarbons in the 1 to 2 hour time interval. A typical

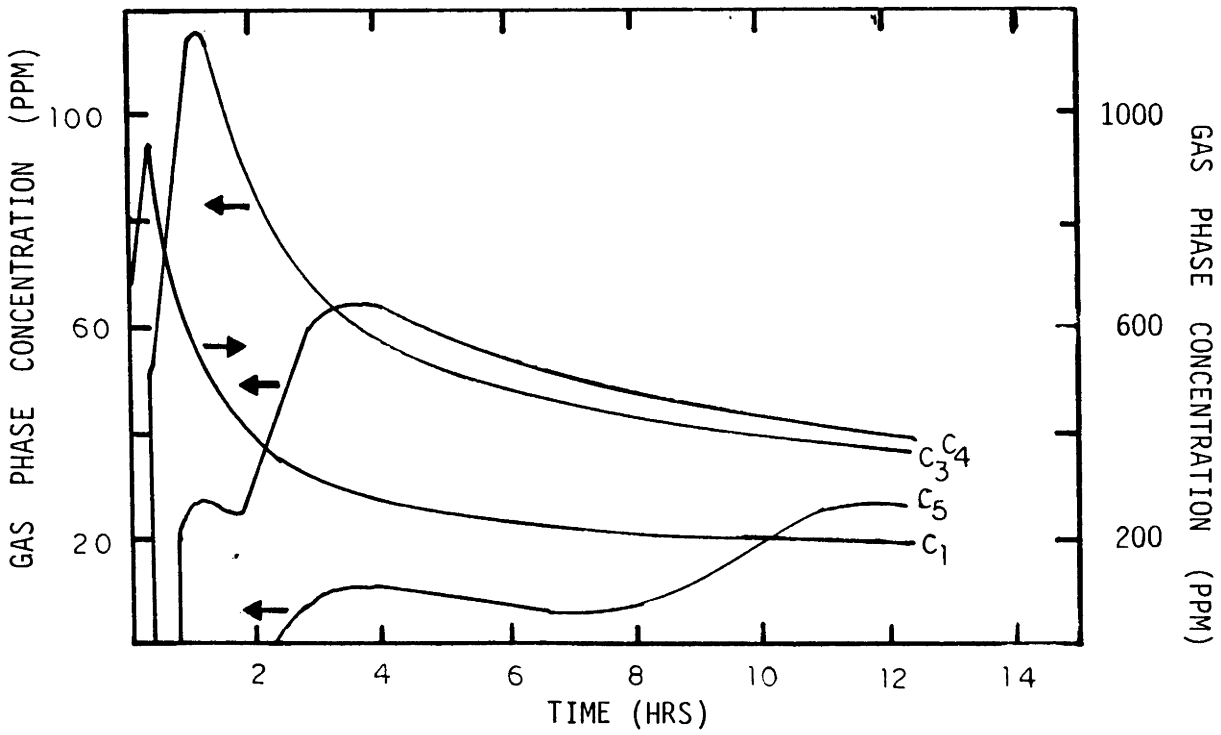

Figure 80: Hydrocarbon Start-up Behavior for Run 9-21-85 (1.53% RuCa A) at 255 C. All hydrocarbons were linear.

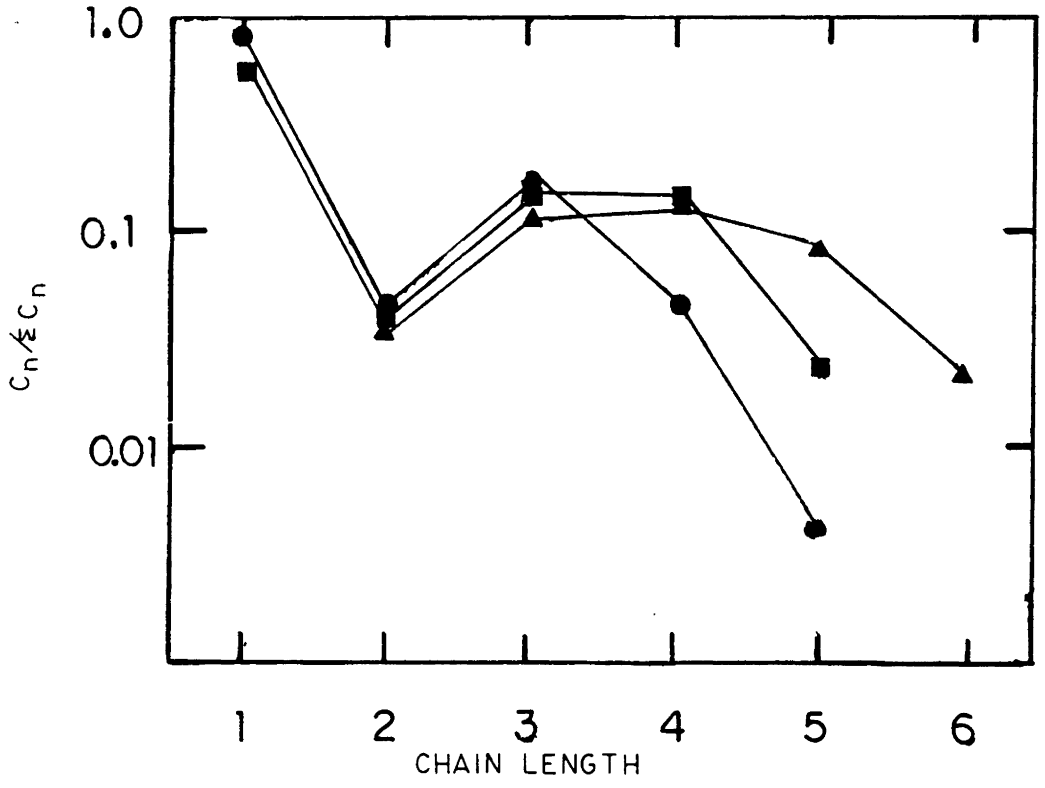

Figure 81: Hydrocarbon Product Distribution for Run 9-21-85 at 255 C. ● t = 72 min; ■ t = 280 min; Δ t = 666 min.

Table 28
Hydrocarbon Product Distribution for 1.53 wt% Ruthenium Zeolite A
(Run 9-21-85)

Hydrocarbon	Wt %	Wt %	Wt %	Wt %
C_1	54.15	52.37	52.51	52.75
C_2	5.08	5.24	5.88	5.88
C_3	30.52	32.06	32.00	30.90
C_4	10.26	10.34	9.62	10.48
Time (hrs)	0:58	1:12	1:27	1:44

Conversion: 0.21 %
Pressure: 15 psig
Temperature: 255 ^{0}C
Flow rate: 6.5 ml/min $CO/H_2 = 1.0$

Note: No C_5 or larger hydrocarbon observed.

product distribution for this run is presented in Table 29. Note that the C_4 fraction is dominated by β-olefins.

Figure 82 reports the hydrocarbon product distribution for run 9-21-85 at 308°C and 80 psig at 160, 399, 545 and 1350 minutes after start-up. Note that for the first three times, two chain growth probabilities, α, are used to fit the data. These values are listed in Table 30. As Figure 82 shows, a shift towards higher hydrocarbon production is occurring, until a log-normal behavior is followed. A typical hydrocarbon product distribution for this run is listed in Table 31. Note again the almost nonexistence of α-olefins and the dominance of the C_4+ fraction by internal olefins. It is also interesting to note from this table that when the high growth probability is followed (C_4-C_6) internal olefins dominate the hydrocarbon fraction. When the lower growth probability is followed, the hydrocarbon fraction is exclusively the normal alkane.

Run 9-26-85 employed 1.75 g of RuCa A (2.16 wt% ruthenium). This run followed the same start-up procedure as run 9-21-85. The start-up behavior of the C_2 through C_5 hydrocarbon fraction are shown in Figure 83. Again, methane was the only hydrocarbon observed over the first 30 minutes of the run. Note that the C_2 and C_3 fractions reach their maximum rates of production at about the same time, while the maximum in the rate of C_4 production occurs as the production of C_2 and C_3 are rapidly declining. The maximum in the rate of C_5 production occurs following the decline in the rate of production of C_4. In no case were C_7 or greater

Table 29
Product Distribution for 1.53 wt% Ruthenium Zeolite A
(Run 9-21-85)

Hydrocarbon	Mole Pct	Carbon Pct
Methane	66.09 %	36.17 %
Ethane	2.00	2.19
Ethylene	2.00	2.19
Propane/ene	13.30	21.84
1-Butene	0.43	0.95
n-Butane	2.98	6.52
t 2-Butene	7.08	15.15
c 2-Butene	3.65	7.80
n-Pentane	2.48	6.80

Time:	3:29 hrs
Temperature:	255°C
Rate:	$15.7X10^{6}$ (1)

1 Moles CO reacted per mole Ru per second

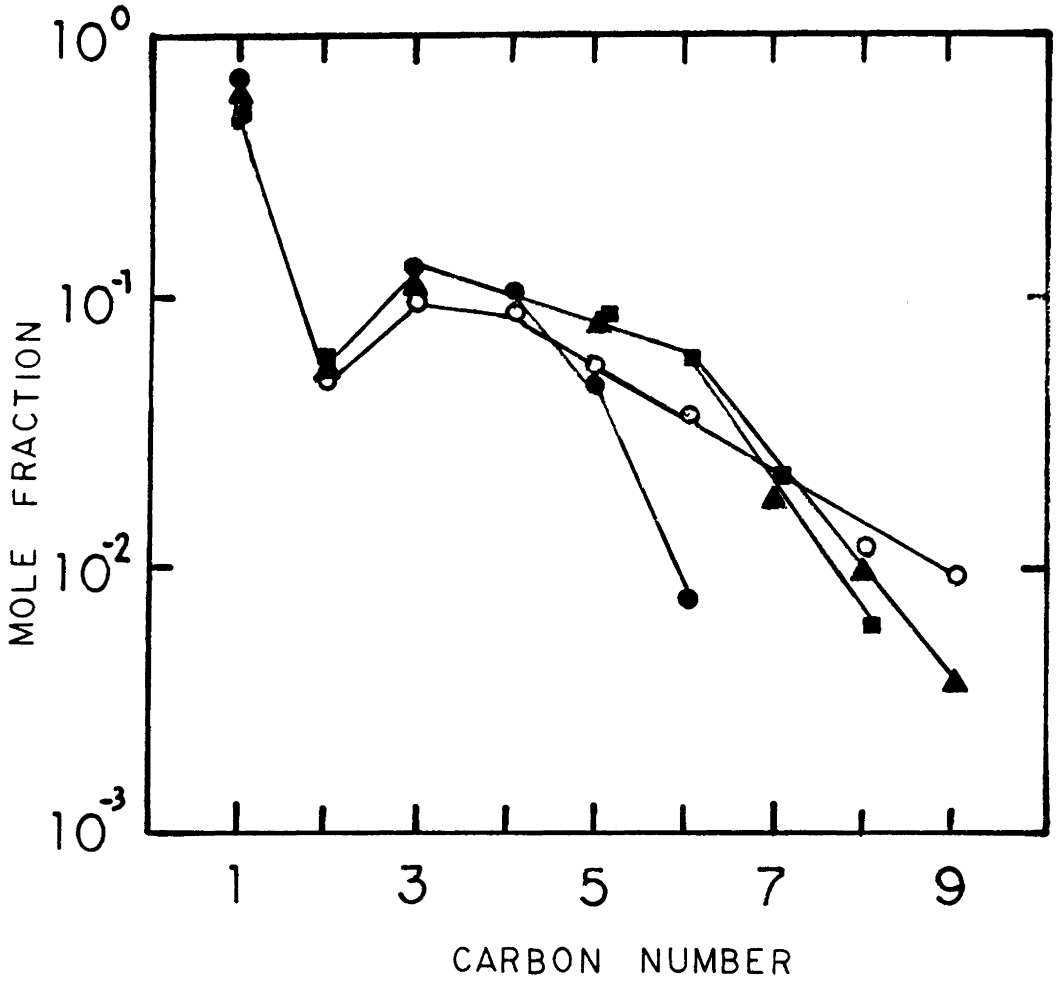

Figure 82: Hydrocarbon Product Distribution for Run 9-21-85 at 308 C. ● t = 160 min, conversion = 0.47%; ■ t = 399 min, conversion = 0.64%; △ t = 545 min, conversion = 0.64%; ○ t = 1350 min, conversion = 0.46%

Table 30
Chain Growth Probability for Different Carbon Numbers at Various Reaction Times[1]
(Run 9-21-85)

Time:	2:40 hrs
α(3-4)	0.840
α(4-6)	0.417
Time:	6:39 hrs
α(4-5)	0.743
α(6-8)	0.349
Time:	9:05 hrs
α(4-6)	0.726
α(6-9)	0.412
Time:	23:30 hrs
α(4-9)	0.639

Conversion:	0.46 to 0.64%
Pressure:	80 psig
Temperature:	308°C
Flow rate:	10.5 ml/min CO/H_2 = 1.0

[1] From Figure 82

Note: Numbers in brackets refers to the carbon numbers over which the value of alpha was computed

Table 31
Product Distribution for 1.53 wt% Ruthenium Zeolite A
(Run 9-21-85)

Hydrocarbon	Mole %	Carbon %
Methane	55.50 %	36.17 %
Ethane	2.84	2.19
Ethylene	2.84	2.19
Propane/ene	11.27	21.84
1-Butene	1.03	0.95
n-Butane	2.74	6.52
t 2-Butene	4.74	15.15
c 2-Butene	2.25	7.80
1-Pentene	0.51	1.07
n-Pentane	2.48	3.90
t 2-Pentene	4.08	8.46
c 2-Pentene	1.49	3.09
n-Hexane	1.26	3.14
C 3-Hexene	0.98	2.42
t 2-Hexene	2.53	6.28
c 2-Hexene	0.90	2.24
n-Heptane	1.75	5.09
n-Octane	1.01	3.33
n-Nonane	0.39	1.47

Time:	9:05 hrs
Temperature:	308°C
Conversion:	0.64 %
Rate[1]:	$72.1X10^{6}$

[1] moles CO reacted per mole Ru per second

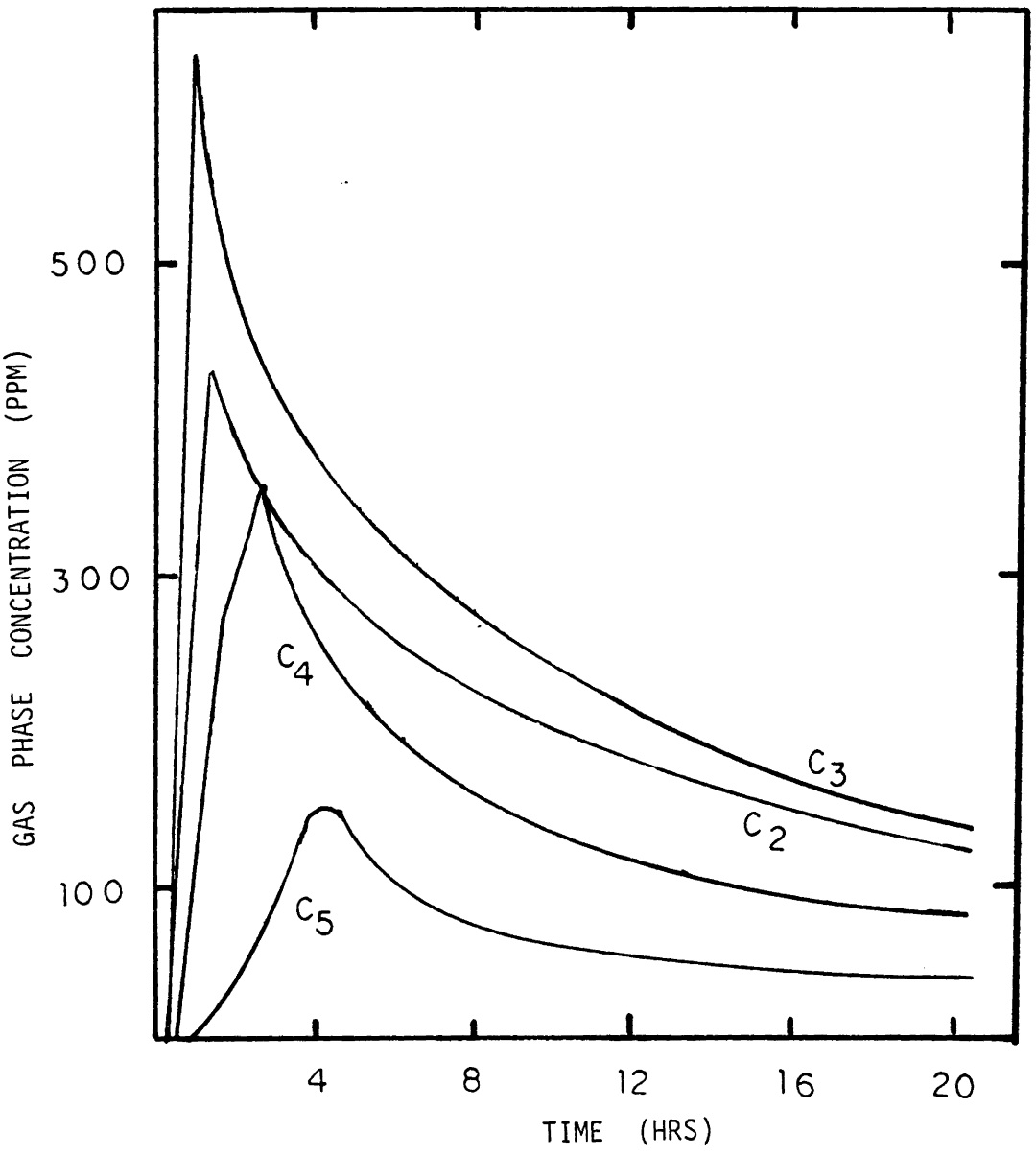

Figure 83: Hydrocarbon Product Start-up Behavior for Run 9-26-85 (2.16 wt% RuCa A) at 255 C.

hydrocarbon observed in the product stream at any time during the run. Figure 84 shows the conversion to hydrocarbons with respect to time for this run. As the figure shows, a sharp initial decline in rate is observed, followed by a constant rate of deactivation. Figure 85 illustrates the hydrocarbon product distribution for this run at various times. Note the non-Schultz-Flory behavior. Table 32 reports a typical product distribution. Table 33 compares the rate data reported here to that of Nijs et al. (123).

V.E Co/ZSM-5 Fischer-Tropsch Reactivity

Cobalt ZSM-5 prepared by ion exchange and by the addition of amorphous "seed" material to the synthesis gel were reacted at temperatures up to 470°C under 300 psig CO/H_2 (1:1) in the flow reactor system. For these runs, the catalyst was first contacted with hydrogen at 450°C for approximately 20 hours for comparison with other studies (2,3,112). Following hydrogen contact, the catalyst was exposed to CO/H_2 (1:1) at temperatures of 300°C, 350°C, 410°C and 470°C. Figure 86 shows the Co2p(3/2,1/2) photoelectron region of the XPS spectrum for Co/ZSM-5 in the as synthesized form (composition I, Co/Si = 0.0046), following hydrogen exposure and after reaction 9-1-85. The figure shows that no significant increase in the superficial cobalt concentration has occurred. It is also of interest to note that no shift in the cobalt binding energy has occurred.

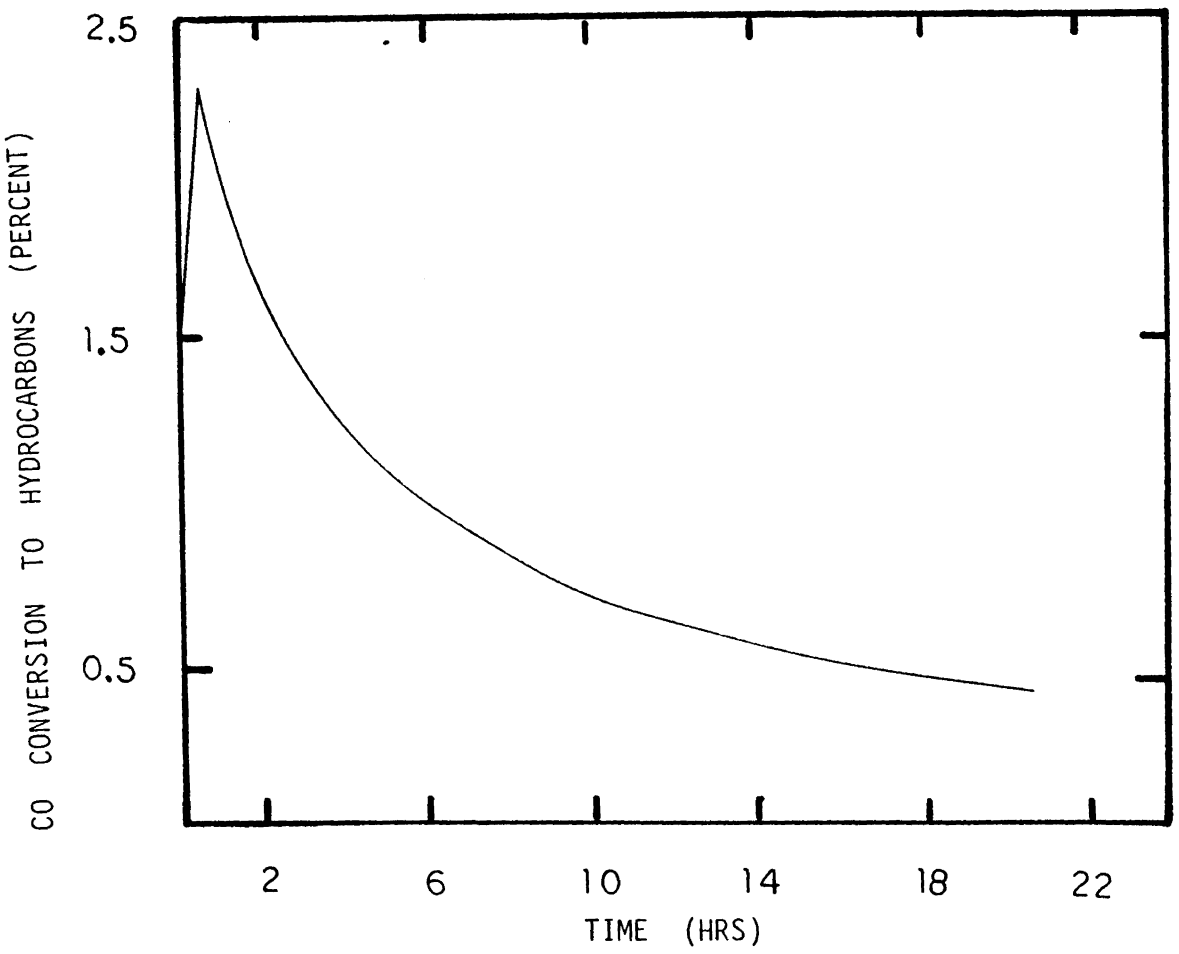

Figure 84: Reaction Behavior of RuCa A at 255 C Under 15 psig CO/H_2 (1:1); Run 9-26-85.

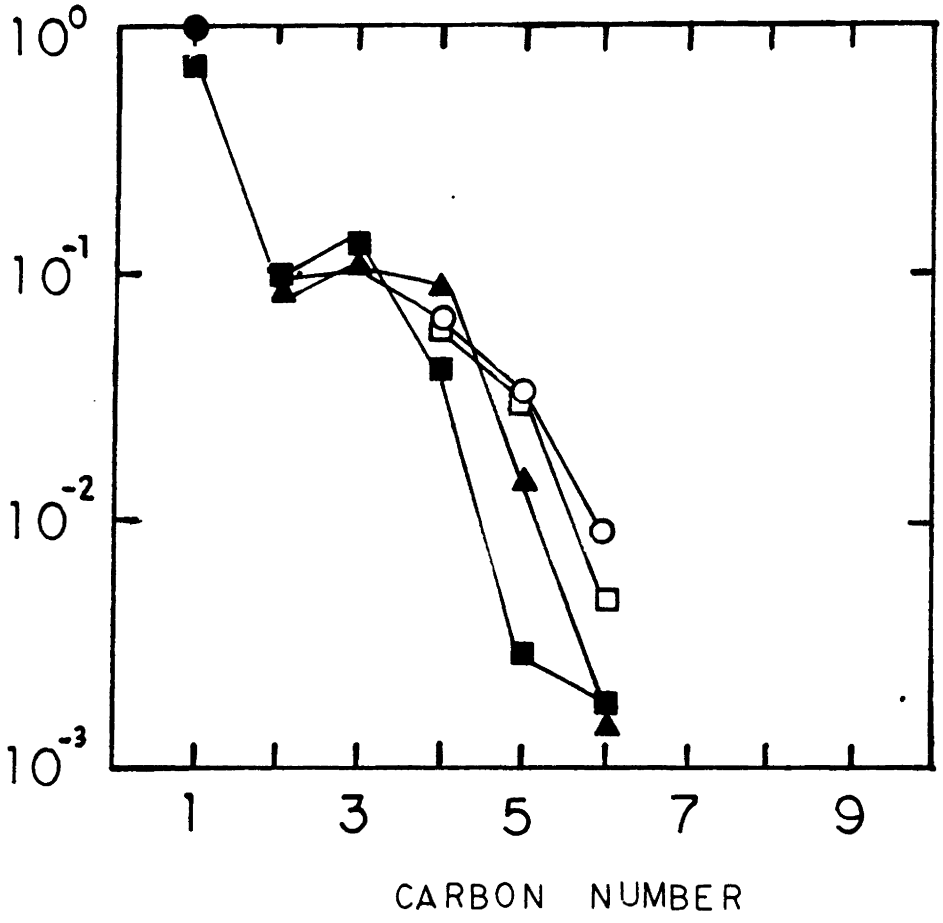

Figure 85: Hydrocarbon Product Distribution for Run 9-26-85 at 255 C. ● t = 10 min, conversion = 2.05 %; ■ t = 78 min, conversion = 1.33%; ▲ t = 162 minutes, conversion = 1.28%; □ t = 338 min, conversion = 0.98%; ○ t = 793 min, conversion = 0.58%.

Table 32
Product Distribution for 2.16 wt% Ruthenium Zeolite A
(Run 9-26-85)

Hydrocarbon	Mole %	Carbon %
Methane	70.36 %	43.12 %
Ethane	4.10	5.02
Ethylene	4.10	5.02
Propane	3.32	6.11
Propylene	7.76	14.26
1-Butene	0.79	2.05
n-Butane	0.79	2.05
t 2-Butene	4.53	11.10
c 2-Butene	2.88	7.07
1-Pentene	----	----
n-Pentane	0.84	2.57
t 2-Pentene	0.33	1.00
c 2-Pentene	0.23	0.69
n-Hexane	0.06	0.19

Time:	2:42 hrs
Temperature:	255°C
Conversion:	1.24 %
Rate[1]:	$176.2X10^{-6}$

[1] moles CO reacted per mole Ru per second

Table 33
Fischer - Tropsch Reaction Rate Comparison

Catalyst	Temperature	Pressure	H_2/CO	Rate[1]
RuCa A[2]	255°C	15 psig	1.0	183.3
Ru_2La Y[3]	200°C	206 psig	1.5	520-140

[1] Moles CO reacted per mole ruthenium per second X 10^{-6}
[2] Rate obtained from steady state deactivation extrapolated to t=0 for run 9-26-85
[3] From reference 123

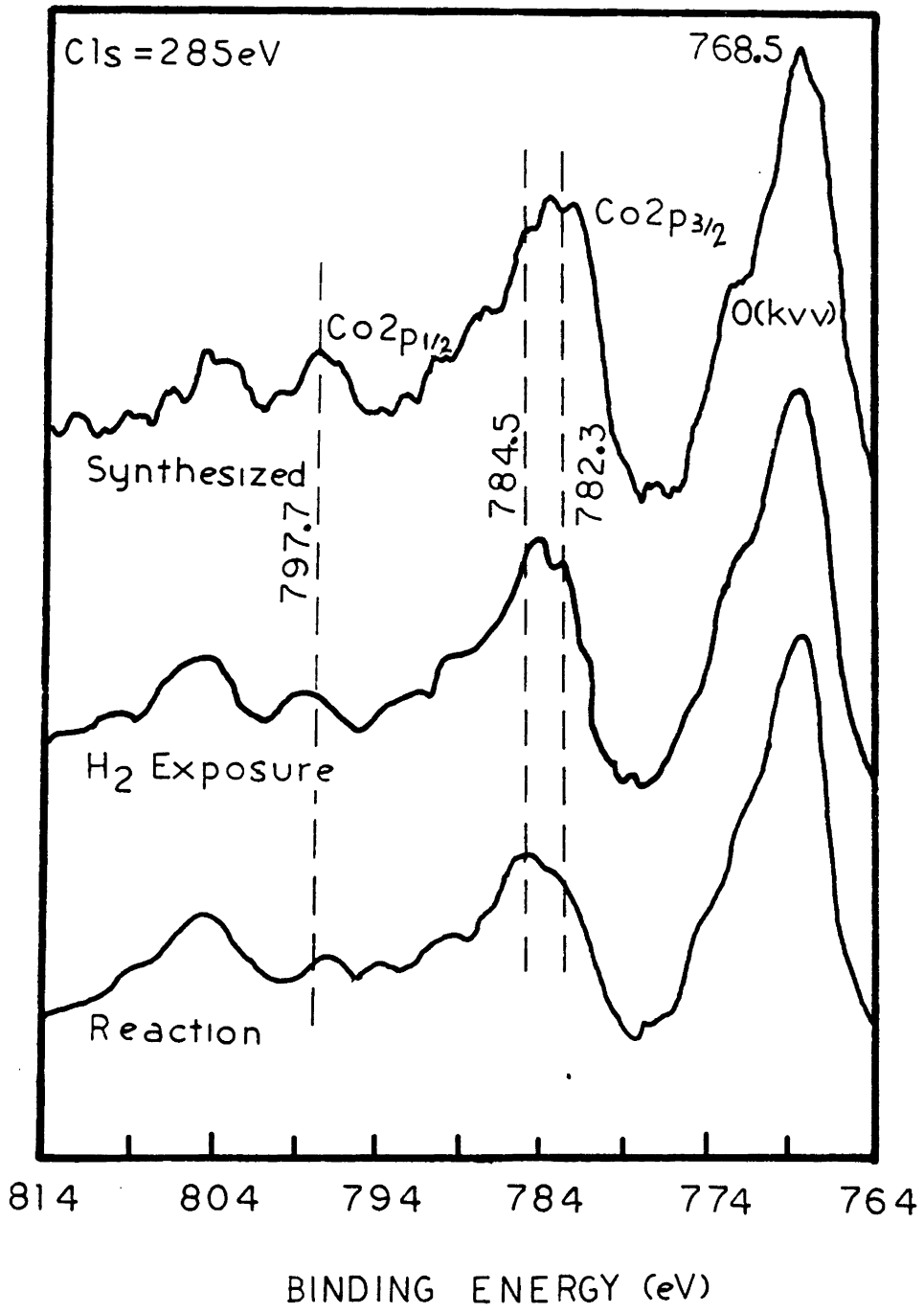

Figure 86: XPS Spectra of the Co2p Photoelectron Region. Zeolite was synthesized from composition I (Co/Si = 0.0046).

Figure 87 shows a plot of conversion versus time for Co/ZSM-5 (Co/Si=0.0046) prepared from composition I and reacted at 410°C. This catalyst was found to be essentially unreactive below this temperature. As the figure shows, there is a slow decline in activity with time. The hydrocarbon product distribution is reported in Table 34. As the table shows, the products were primarially C_1 to C_3 saturates. A log-normal behavior of the products is followed and is illustrated in Figure 88.

The reaction temperature was then raised to 470°C. Again, as shown in Figure 89, the conversion remained essentially constant over the course of the run. Note from this figure that the production of CO_2 is almost equal to the hydrocarbon production. The product distribution for this run is reported in Table 35. Again, C_1 to C_3 dominate the product spectrum. The hydrocarbon distribution is plotted in Figure 90.

Run 9-12-85 followed the same start-up procedure as the previous run. The catalyst employed in this run was prepared by cation exchange (see Table 21 for surface and bulk analysis). This catalyst was slightly reactive at 350°C, and, as reported in Table 36, at 410°C was approximately 8 times more reactive towards hydrocarbon production than the catalyst employed in run 9-1-85. Almost no decline in activity was observed over the course of the run. The ion exchange catalyst produced less methane and carbon dioxide than did the catalyst prepared from the amorphous "seed" material. Also, the ion exchanged catalyst produced hydrocarbons up to C_{10}. Figure 91 shows the product distribution for this run at 410°C.

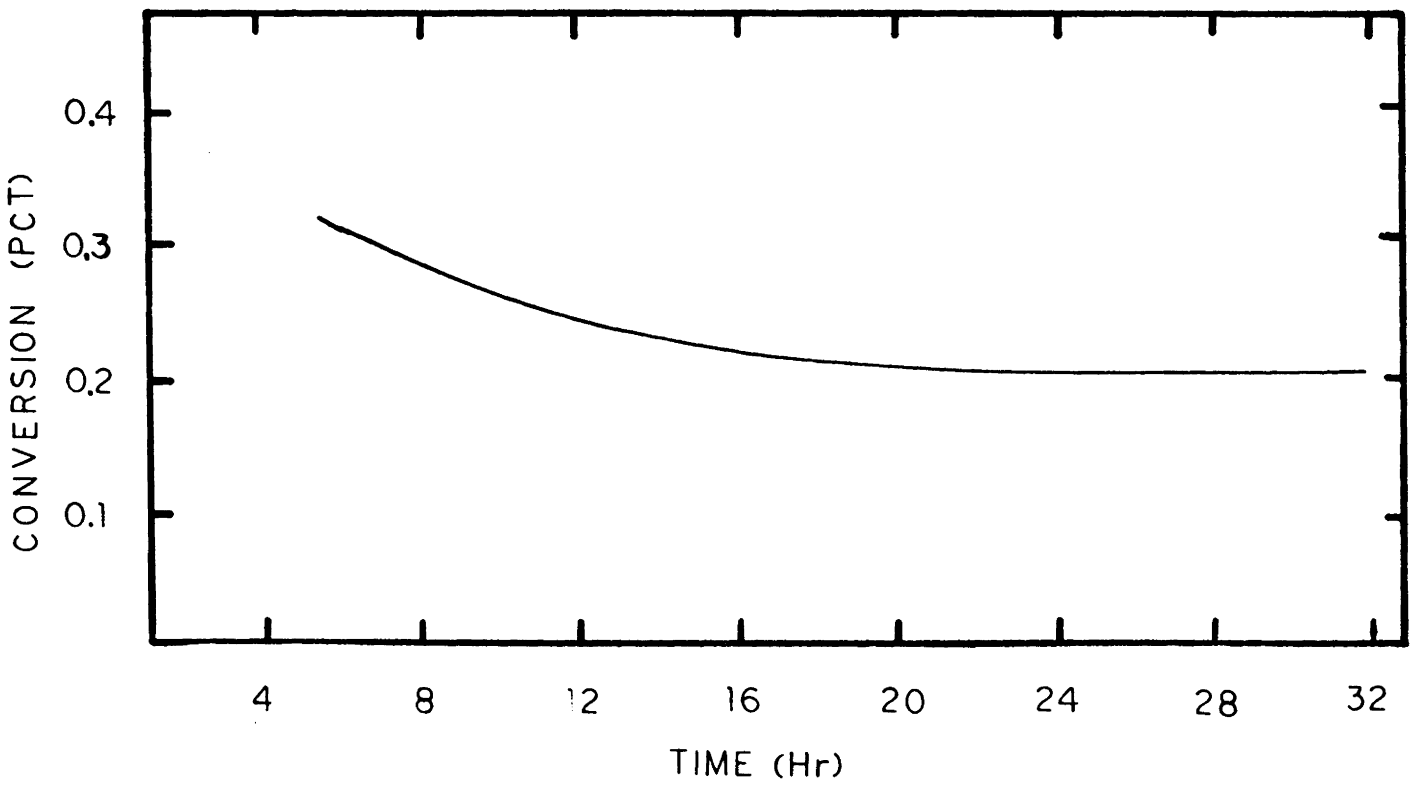

Figure 87: Hydrocarbon Start-up Behavior for Co/ZSM-5 Prepared from Amorphous "Seed" Material at 410 C (Run 9-1-85).

Table 34
Hydrocarbon Product Distribution for Co/ZSM-5 Prepared from Amorphous Cobalt "Seed" Material Reacted at 410°C (Run 9-1-85)

Hydrocarbon	Mole %	Carbon %
Methane	67.97	46.48
Ethane	20.51	28.09
Propane	8.88	18.21
i-Butane	1.58	4.34
n-Butane	1.06	2.88

Pressure:	300 psig
Flow rate:	10.0 ml/min CO/H_2=1.0 (STP)
Conversion:	0.55 %
α:	0.347
$CO_2/(CO_2+HC)$[1]:	0.59
Rate[2]:	159 X 10^{-6}

[1] Ratio of carbon dioxide formed to total conversion
[2] Moles CO reacted per mole cobalt per second

Note: Product distribution obtained following 8 hours after start-up.

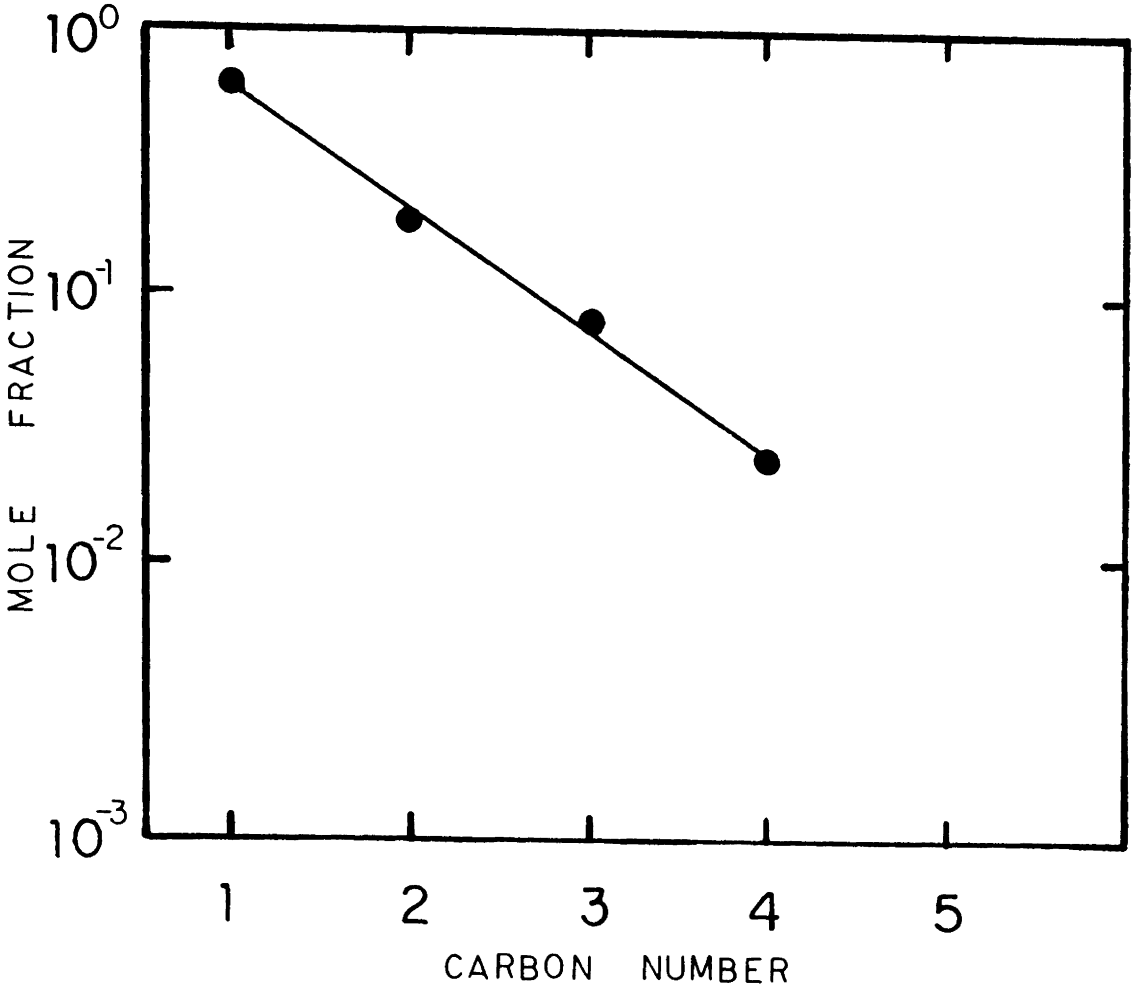

Figure 88: Hydrocarbon Product Distribution for Run 9-1-85 at 410 C (following 5 hours past start-up).

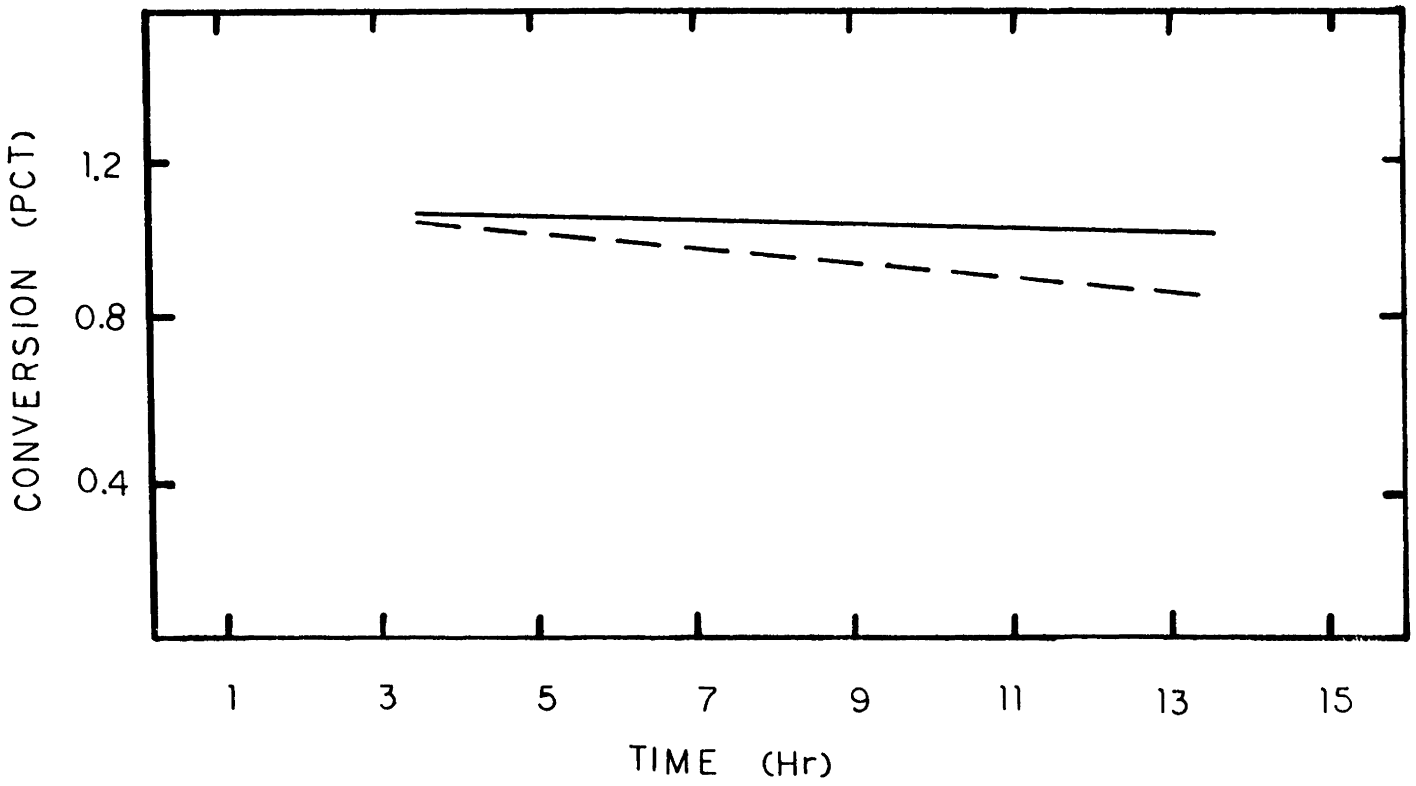

Figure 89: Start-up Behavior for Co/ZSM-5 Prepared from Amorphous "Seed" Material Reacted at 470 C (Run 9-1-85). ---CO_2; — Hydrocarbons.

Table 35
Hydrocarbon Product Distribution for Co/ZSM-5 Prepared from Amorphous Cobalt "Seed" Material Reacted at 470°C
(Run 9-1-85)

Hydrocarbon	Mole %	Carbon %
Methane	65.49	43.62
Ethane	24.35	32.44
Propane	8.04	16.07
i-Butane	0.63	1.68
n-Butane	0.54	1.44
Toluene	0.42	1.95
C8	0.52	2.78

Pressure:	300 psig
Flow rate:	10.0 ml/min CO/H_2=1.0 (STP)
Conversion:	2.03 %
α:	0.350
$CO_2/(CO_2+HC)$[1]:	0.48
Rate[2]:	587 X 10^{-6}

[1] Ratio of carbon dioxide formed to total conversion
[2] Moles CO reacted per mole cobalt per second

Note: Only trace amount of water observed in the product stream.
No C_5 - C_7 hydrocarbons detected.
Product distribution obtained following 5 hours after start-up.

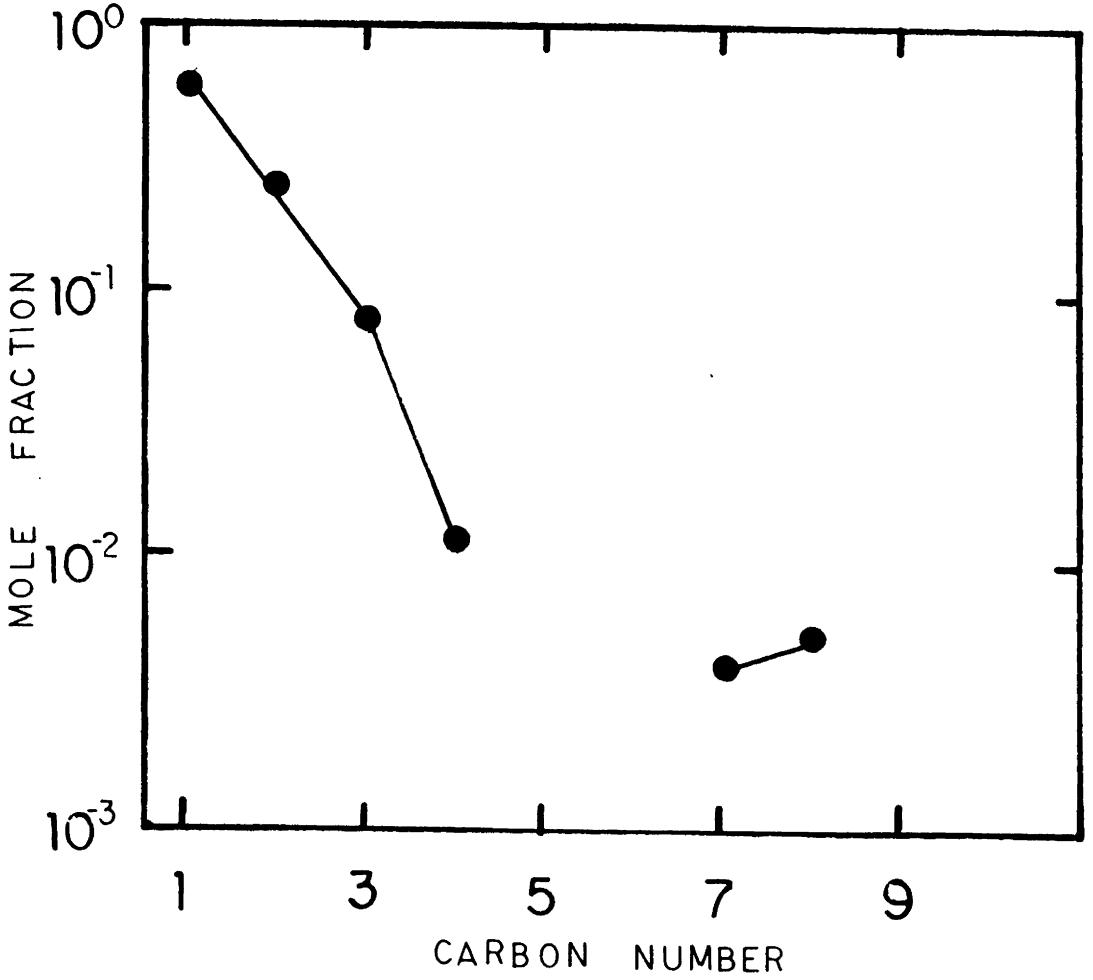

Figure 90: Hydrocarbon Product Distribution for Run 9-1-85 at 470 C (following 5 hours past start-up).

Table 36
Hydrocarbon Product Distribution for Co/ZSM-5 Prepared by Cation Exchange at 410°C
(Run 9-12-85)

Hydrocarbon	Mole %	Carbon %
Methane	58.88	29.36
Ethane	21.52	21.46
Propane	9.42	14.08
i-Butane	1.98	3.95
n-Butane	1.32	2.62
i-Pentane	0.66	1.64
Pentane	0.25	0.62
Benzene	0.36	1.07
C8	1.21	4.67
C9	2.94	13.21
C10	1.45	7.42

Pressure:	300 psig
Flow rate:	10.0 ml/min CO/H_2=1.0 (STP)
Conversion:	2.28 %
α:	0.357
$CO_2/(CO_2+HC)$[1]:	0.23
Rate[2]:	587 X 10^{-6}

[1] Ratio of carbon dioxide formed to total conversion
[2] Moles CO reacted per mole cobalt per second

Note: Product distribution obtained following 5 hours after start-up.

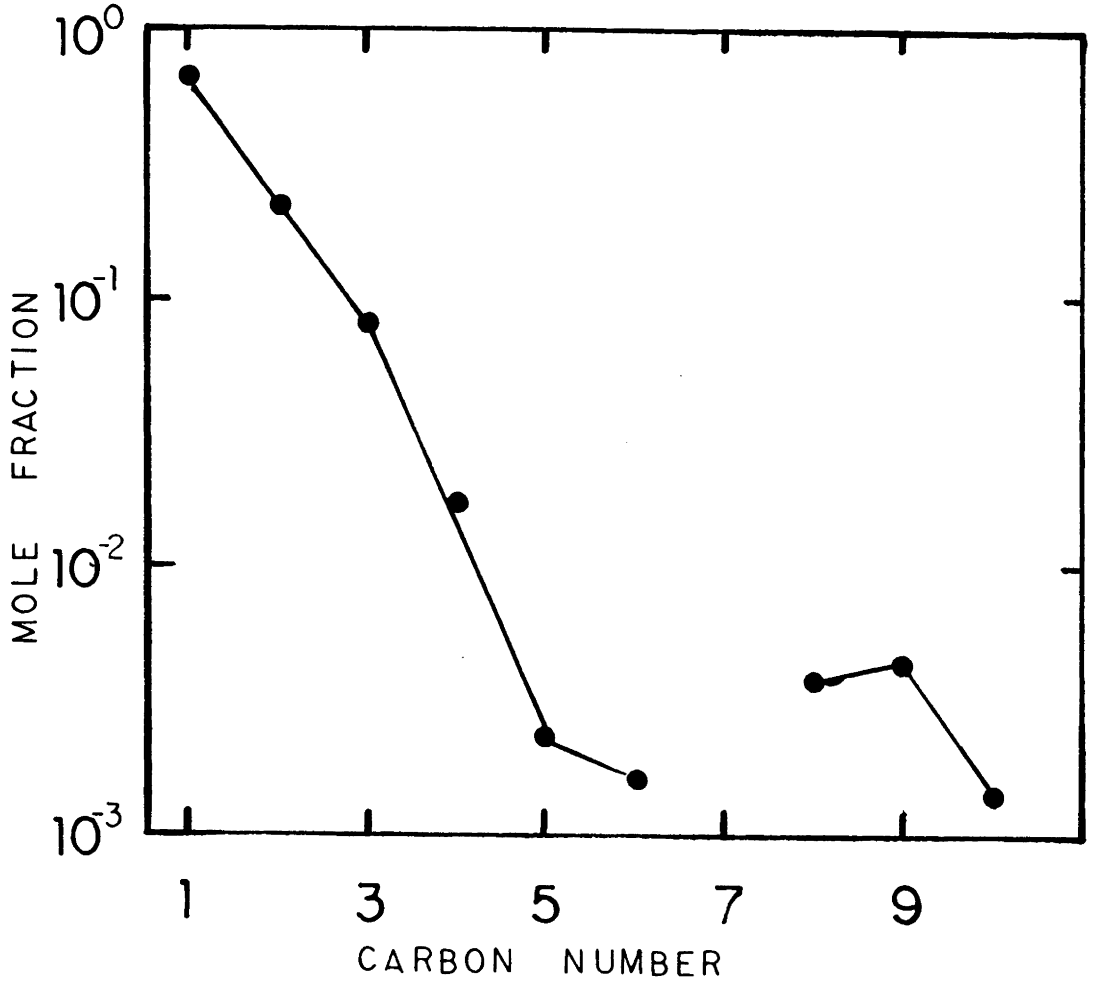

Figure 91: Hydrocarbon Product Distribution for Run 9-12-85 at 410 C (following 5 hours past start-up).

Raising the reaction temperature to 470°C did not alter the product distribution significantly from that observed at 410°C (see Table 37). The catalyst did not loose activity over the course of the run. A comparison of the product distribution from this catalyst to the Co/ZSM-5 synthesized from amorphous "seed" material was made. As these data show, the ion exchanged catalyst was almost 5 time more reactive towards hydrocarbon production. Also, the ion exchanged material was not as selective towards CO_2 formation.

Table 37
Hydrocarbon Product Distribution for Co/ZSM-5 Prepared by Cation Exchange at 470°C
(Run 9-12-85)

Hydrocarbon	Mole %	Carbon %
Methane	66.56	43.52
Ethane	22.21	29.05
Propane	8.16	16.00
i-Butane	0.92	2.40
n-Butane	0.79	2.05
i-Pentane	0.16	0.55
Pentane	0.07	0.24
Benzene	0.17	0.66
C8	0.39	2.02
C9	0.44	2.60
C10	0.14	0.92

Pressure: 300 psig
Flow rate: 10.0 ml/min CO/H_2=1.0 (STP)
Conversion: 7.57 %
α: 0.350
$CO_2/(CO_2+HC)$[1]: 0.33
Rate[2]: 1950 X 10^{-6}

[1] Ratio of carbon dioxide formed to total conversion
[2] Moles CO reacted per mole cobalt per second

Note: Product distribution obtained following 5 hours after start-up. No linear or branched C_6 or C_7 observed.

VI DISCUSSION

VI.A Synthesis of Transition Metal Containing Zeolites

VI.A.1 Rhodium Zeolite A Synthesis

Crystal growth curves reported in Figures 44, 45 and 46 were obtained for the purpose of examining the effects of rhodium upon the crystallization process. The Rh/Al_2O_3 ratio is based upon the aluminate added to the gel from the sodium aluminate only. This ratio does not include any aluminum contribution from the "seed" material. Note that in Figures 45 and 46, the time required for nucleation has decreased from that shown in Figure 44. This reduction in nucleation time results from the presence of the "seed" crystals (47). These figures show that the presence of rhodium in the synthesis gel does not influence this phenomena. As shown in all three figures, the presence of rhodium in the synthesis gel does not affect the crystal growth rate for Rh/Al_2O_3 ratios less than approximately 0.035. From Figure 44 it can be seen that increasing the Rh/Al_2O_3 ratio to 0.256 resulted in an abrupt halt in the crystallization process at approximately 65% crystallinity. It is interesting to note here that the initial rate of crystal growth is not effected by the presence of $RhCl_3$-$3H_2O$.

The increase of the gel Rh/Al_2O_3 ratio to 0.256 resulted in incomplete crystallization. (This high ratio was attainable only from the use of $RhCl_3$-$3H_2O$, as the gel rhodium content was limited by the loading of the "seed" material.) Incomplete crystallization of zeolite A is usually a result of the inability of the synthesis solution to dissolve the gel particles (139). This phenomena is typically associated with a low gel

pH or low reaction temperatures (61). In the case of addition of $RhCl_3$-$3H_2O$ to the synthesis gel, the pH varied from 12.2 to 11.3 as the Rh/Al_2O_3 ratio changed from 0 to 0.343. Since silica is completely dissolved at pH>11.0 it is doubtful that the lowering of gel pH from 12.2 to 11.3 by the $RhCl_3$-$3H_2O$ was the cause of the incomplete crystallinity.

The sodium present in the zeolite A synthesis gel is thought to provide structure direction during crystallization (54). It is possible that the rhodium provides a "structure breaking" effect similar to that proposed for Cs^+ in the synthesis of ZSM-5 (74). That is, at high rhodium concentrations, the Rh^{3+} could interfere with the ability of Na^+ to coordinate gel phase silica and alumina.

The crystallization time was extended to 24 hours for several preparations. Following this time, the resulting material (blank zeolite A) was analyzed by XRD. A portion of this sample was shown to have undergone a mild phase transformation to form sodalite (approximately 12%). The transformation of zeolite A to zeolite P and sodalite in alkaline media is well documented (140-142). For all preparations possessing a Rh/Al_2O_3 ratio greater than 0.0025, regardless of the rhodium source, no phase transformation was observed. Large, multivalent cations are known to stabilize the zeolite A structure (62). Based on this fact, the improved stability of the rhodium A zeolite in the alkaline synthesis solution could be an indication that at least some of the rhodium is cationically associated with the zeolite.

Figure 47 shows the utilization of rhodium for those syntheses illustrated in Figures 44, 45, and 46 which obtained complete crystallinity. The filtrate of various samples were analyzed for rhodium content by AA. In no case was any rhodium detected. This indicated that all the rhodium placed into the synthesis gel is ultimately associated with the product zeolite. Rhodium material balances were typically 100±5%. Figure 47A shows a linear relationship exists between the rhodium in the gel and the rhodium in the product crystals when adding $RhCl_3$-$3H_2O$ to the gel. Since the amount of product crystals in each of these syntheses is relatively constant, a linear relationship is expected if all the gel rhodium is incorporated proportionally into product. When a variable amount of rhodium "seed" is added to the synthesis gels, a linear utilization relationship is not obtained as can be seen in Figure 48B. The observed curvature is the result of the "seed" crystals' contribution to the overall product yield. That is, in order to raise the rhodium content in the gel, increasing amounts of "seed" (3.76 wt% Rh) were added to the gel which consequently resulted in the production of more RhNa A. To prove this result, a constant amount of "seed" was added to the synthesis gels while the rhodium content was varied by changing the rhodium loading of the "seeds." The rhodium utilization results for this case are illustrated in Figure 47C. Notice that a linear relationship is observed. Again, this is due to the fact that a constant amount of product is synthesized.

The binding energies of the elements of interest used for XPS analysis are reported in Table 15. These binding energies are in good agreement

with those reported for other Rh zeolites (143). The binding energy of 310.4 eV for the Rh3d5/2 level indicates that rhodium is in the plus three oxidation state (4,143). It is also important to note from this table that no sodium or chlorine were observed. Thus, at least in the superficial region, chlorine ions are not in the neighborhood of rhodium, and the exchange of Ca^{+2} for Na^{+} is complete. The absence of chlorine is important, as many organic reactions are poisoned by the presence of halides.

The (Si + Al)/O ratio for the zeolite A should equal approximately 0.5 (based on the framework composition of the structure). Values less than 0.5 indicate that there is an excess of oxygen present. In the case of RhNa A prepared by cation exchange (4), a superficial (Si+Al)/O ratio of 0.23 resulted. This indicated to the authors that the surface rhodium probably existed as rhodium oxide. For all preparations reported in this study, the superficial values of (Si+Al)/O were 0.5±0.1. Due to the small quantity of rhodium located on the surface, it can not be determined from these results whether the rhodium is cationically associated with the zeolite or whether it exists as rhodium oxide or both. However, it is believed that at least a portion of the rhodium associated with crystals synthesized in this study is rhodium cationically associated with the zeolite. This is based on the yellow-orange color of the material (rhodium oxides are black). Also, the rhodium zeolite A synthesized by the above mentioned techniques were found to be more difficult to dissolve in acid as the rhodium content was increased. This result could be due to the rhodium cations adding stability to the zeolite A structure (62).

Table 17 reports XPS and chemical analysis data for RhCa A prepared by several synthesis procedures. Zeolite A was exchanged into the calcium form because this form would be used for all reaction studies. Chemical analysis of zeolite A following calcium exchange showed no change in the rhodium content of the zeolite to within experimental error.

The XPS and chemical analysis data were used to determine the amount of rhodium in the superficial area of the zeolite crystals relative to the bulk. The ratio of XPS/CA for Rh/Si was employed in accordance with (4) to provide an indication of the superficial to bulk rhodium content. The results from cation exchanged ($RhCl_3$-$3H_2O$) RhNa A are presented for comparison (XPS/CA Rh/Si = 60). Since the rhodium aquo-complex is too large to penetrate the zeolite A structure, the cation exchange sample provided a representation of surface rhodium. Analysis of all samples from this work showed superficial/bulk Rh/Si ratios far less than 60. From this result it was concluded that all preparations in which rhodium was placed into the synthesis gel resulted in intrazeolitic rhodium.

XPS and chemical analysis were performed on blank zeolite A "seed" crystals and blank zeolite A synthesized from these "seed" crystals. This was for the purpose of observing the effect of the "seed" crystals on the composition of the product crystals. A bulk Si/Al ratio of 0.92 and 0.93 was obtained for the "seed" and final product Na A, respectively, while the superficial Si/Al ratios were 1.18 and 1.24, respectively. These

results indicate that the addition of "seed" crystals to the synthesis gel did not alter the product composition from that obtained in the absence of "seed." With the addition of rhodium (see Table 17), the "seed" technique produced crystals with a greater bulk Si/Al ratio (with the exception of the case where both blank "seed" crystals and $RhCl_3$-$3H_2O$ were added to the synthesis gel). Also for these preparations, the superficial Si/Al ratio was less than one. This result is likely due to occluded aluminum near the surface, as a Si/Al ratio less than one is in violation of Loewenstein's rule (59). It is interesting to note that for zeolite RhCa A prepared from $RhCl_3$-$3H_2O$, the superficial Si/Al ratio was well above one, and is in closer agreement with that of blank zeolite A. Also, for this sample, the bulk Si/Al ratio was over 20% greater than that of blank zeolite A and in agreement with rhodium A synthesized from the "seed" material. These data may be suggesting that the rhodium present in the synthesis gel is responsible for producing a more siliceous zeolite.

The Rh/Si superficial/bulk ratios of the products obtained from the syntheses utilizing "seed" material show that the superficial rhodium content is nearly equivalent to the bulk. Also, there is no apparent affect of agitation on the superficial to bulk rhodium content. The use of an amorphous rhodium "seed" material resulted in reducing the superficial rhodium content to below that of the bulk. When using $RhCl_3$-$3H_2O$ as a rhodium source, the rhodium concentrates towards the surface of the product crystals. Note also that the addition of blank "seed" to the $RhCl_3$-$3H_2O$ synthesis gel increased the superficial rhodium concentration

of the product crystals. It appears that whenever the rhodium is added to the synthesis gel associated with "seed" material, the superficial Rh/Si ratio is in the neighborhood of the bulk.

The presence of "seed" crystals in the zeolite A synthesis gel reduce the time required for nucleation and increase the rate of crystal growth (47). The purpose of adding blank "seed" to the gel containing $RhCl_3$-$3H_2O$ was to observe whether the increased gel reactivity improved the production of intrazeolitic rhodium. As the XPS and chemical analysis data reported in Table 17 have shown, the addition of "seed" crystals here only served to increase the superficial/bulk, Rh/Si ratio. Thus it appears that the increased gel reactivity due to the presence of "seed" crystals in the gel is not responsible for improving the production of intrazeolitic rhodium.

Since the presence of the blank "seed" crystals did not reduce the superficial rhodium content when added to the $RhCl_3$-$3H_2O$ synthesis gel, alternative experiments were investigated in an attempt to understand the crystallization process. It is proposed that the lower superficial rhodium content obtained from the "seed" technique could be due to either a "concentration" effect or a "chemical" effect. The concentration effect was first investigated and is explained as follows. Rhodium on the surface of zeolite A "seed" crystals will be released into the synthesis gel as the "seed" crystals are dissolved by the alkaline media. Evidence that the "seed" crystals did dissolve is obtained from Figure 45, as virtually no crystallinity was observed after 1.5 hours at 90°C. As the "seed"

crystals dissolve, species active for crystal growth are formed and released into the synthesis gel along with rhodium. Thus, it is postulated that the rhodium would be concentrated in a region of active crystal growth. Since the ratio of rhodium to sodium in this region is greater than that of the bulk, the rhodium would be better incorporated during the early stages of the synthesis, resulting in a decrease of the superficial/bulk rhodium concentration. This proposed mechanism is schematically illustrated in Figure 92. In an attempt to test this mechanism, the synthesis was carried out with agitation in order to disrupt the proposed concentration gradient. Analysis of rhodium zeolite A synthesized from "seed" material under agitation showed no change in the superficial/bulk rhodium content. Thus, agitation did not effect the incorporation of rhodium into zeolite A. These data suggest that the lower superficial/bulk rhodium concentration obtained with the "seed" technique was not due to a "concentration" effect, but rather due to the difference in the chemical nature of the gel rhodium species resulting from the addition of the rhodium "seed" material and the $RhCl_3$-$3H_2O$.

It is postulated that as the seed material dissolved a significant quantity of rhodium was associated with species active towards crystal growth, and that these species possibly act as nuclei (139). Rhodium association with these species could be the result of ionic attraction. These species would be able to incorporate into the growing crystals and would thus "carry" rhodium into the growing product. This would account for the lowering of the superficial/bulk rhodium content. This hypothesis was tested by employing a rhodium amorphous "seed" material. Crystals

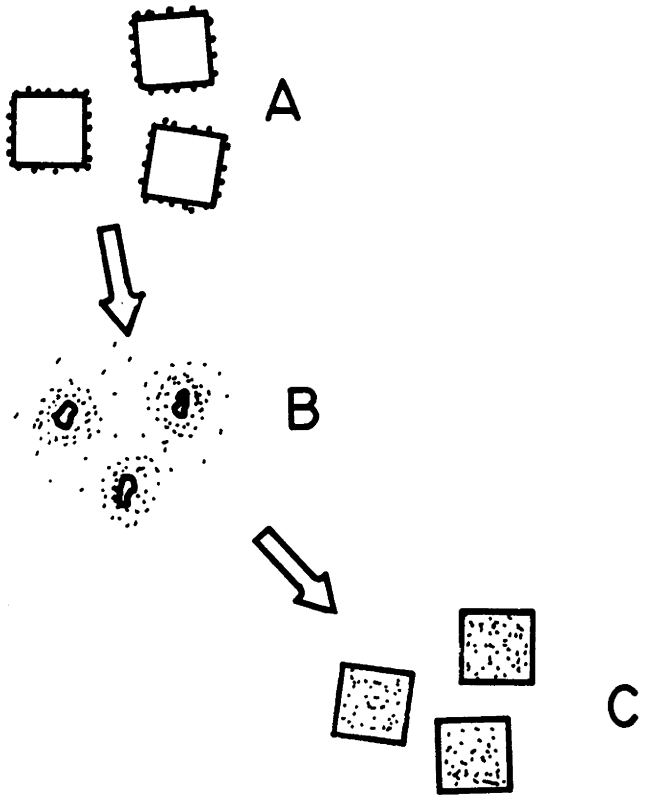

Figure 92: Schematic of Proposed Concentration Effect. Rhodium A seed crystals (A) dissolve in gel releasing rhodium into solution (B). Crystals then form with a lower superficial to bulk rhodium concentration than obtained via $RhCl_3$-$3H_2O$.

synthesized from this material possessed a superficial rhodium to silicon ratio below that of the bulk. This hypothesis is schematically represented in Figure 93. As the figure shows, rhodium "seed" material dissolves into the synthesis gel (A). The rhodium remains associated with species active towards crystal growth, possibly through ionic attractions (B). These species are then incorporated into the growing zeolite A structure (C).

RhCa A (1.06 wt% Rh) prepared by addition of $RhCl_3$-$3H_2O$ to the synthesis gel was examined by electron microprobe for rhodium distribution among the crystals. As Figure 49A shows, the metal distribution was uniform from crystal to crystal, however, particles of rhodium oxide were present (exhibited by the regions of high rhodium concentration). The presence of these particles mixed with the product zeolite is probably the reason that the bulk material appeared darker in color than the RhCa A synthesized from the "seed" technique (at equivalent loadings). Dodwell (21) also observed particles of metal oxides following synthesis of transition metal ZSM-5. The particles were more than likely formed by the reaction of the caustic synthesis solution with the $RhCl_3$-$3H_2O$. These data show that synthesis of rhodium zeolite A by addition of $RhCl_3$-$3H_2O$ to the synthesis gel does not associate all the rhodium with the product zeolite. The presence of non-zeolitic rhodium mixed with the RhCa A could cause problems when using this material as a catalyst.

The presence of the amorphous rhodium oxide particles indicates that the XPS/CA Rh/Si ratio, as presented in Table 17, is not a good indication

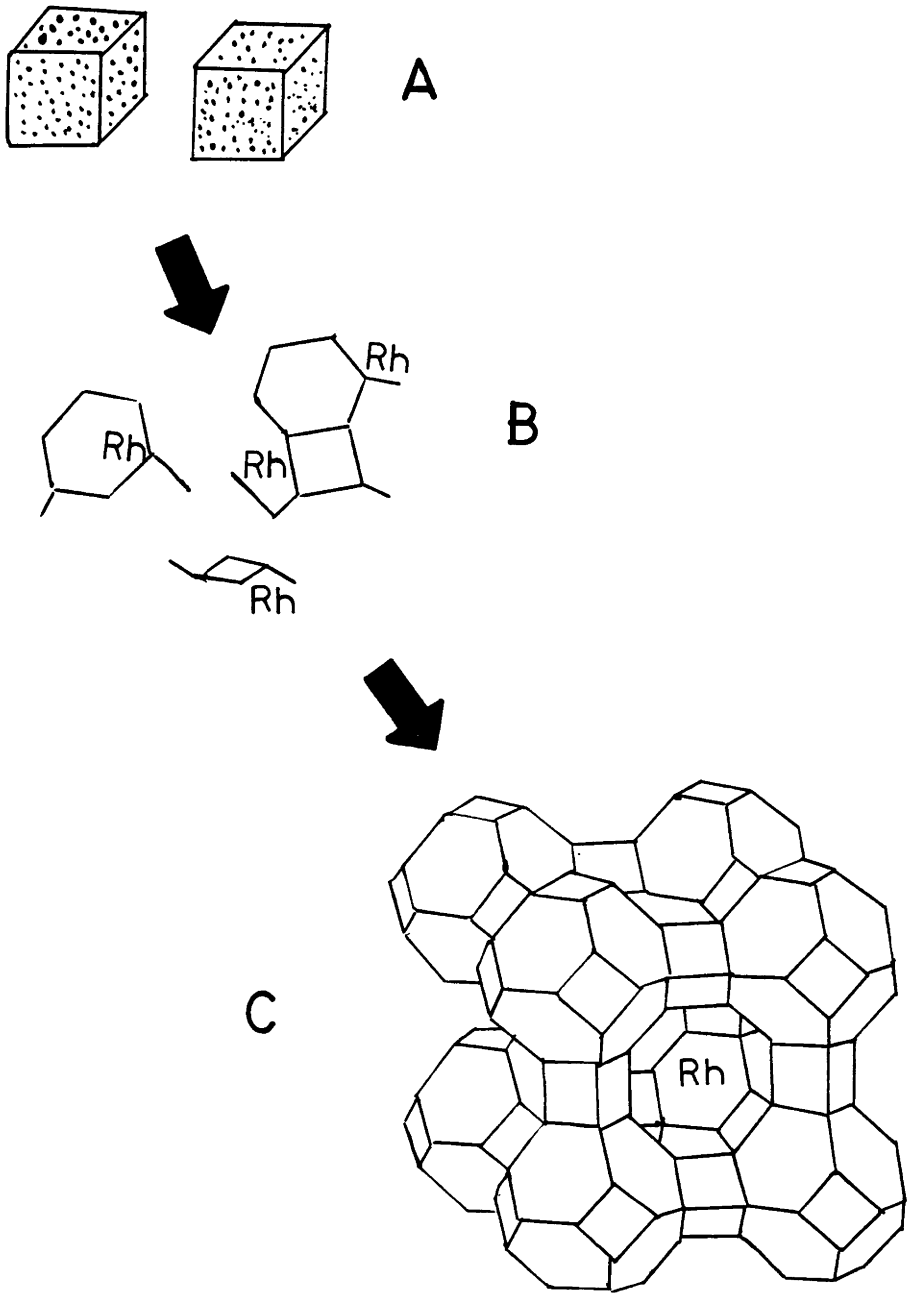

Figure 93: Rhodium Zeolite A Dissolved iuto Synthesis Gel (A), remaining Associated with the Species Active towards Crystal Growth. These Species are then incorporated into the growing structure, resulting in intrazeolitic rhodium (C).

of the degree of rhodium incorporation within the zeolite. Thus, it is not known as to what degree the rhodium zeolite A prepared by this technique incorporated rhodium.

Electron microprobe analyses of RhCa A prepared from the amorphous "seed" material (see Table 17 for XPS and chemical analysis) are shown in Figures 49B and 49C. These figures are of different crystals, and indicate that the rhodium is not uniformly distributed among the crystals. However, no particles of rhodium oxide were observed. This indicates that all the rhodium in the sample is associated with the zeolite. The non-uniform distribution of rhodium among the crystals is more than likely due to a non-uniform distribution of rhodium in the synthesis gel. During the synthesis, the amorphous particles of rhodium "seed" material probably settle, agglomerate, etc., prior to dissolution and the onset of crystallization. Also, the the presence of this material in the synthesis gel reduced the nucleation time, suggesting that the amorphous "seed" material may supply nucleation sites. Thus, the variable rhodium content among the crystals could be a result of crystals grown in the vicinity of the rhodium amorphous "seed" material (leading to a rhodium rich crystal) and away from the material (leading to a rhodium defficient crystal). Since the "seed" rhodium zeolite A is expected to behave similarly to the rhodium amorphous "seed" material in the gel (as far as settling, etc.), it is postulated that rhodium zeolite A produced from this material will also possess a non-uniform rhodium distribution.

Visual inspections of the zeolite A crystals produced in the rhodium systems revealed the following:

1) Crystals produced in the presence of $RhCl_3$-$3H_2O$ (without "seed" addition) were very uniform in size, approximately 1-2μ in size.

2) Crystals produced from the rhodium containing "seed" crystals were not uniform, as crystalline size varied between submicron to approximately 10μ. The majority of crystals were between 1 and 5μ.

3) The use of agitation greatly improved the uniformity of the product crystals when the "seed" technique was employed.

4) The use of the amorphous "seed" material resulted in uniform product crystals between 1-2μ in size.

5) Crystals grown in the presence of $RhCl_3$-$3H_2O$ were much brighter in color (yellow-orange) than those produced via the seed technique.

VI.A.2 Ruthenium Zeolite A Synthesis

The rhodium zeolite A work was extended to include the synthesis of ruthenium zeolite A. Ruthenium A was chosen because it would later be evaluated under Fischer-Tropsch reaction conditions. Based on the rhodium A study, the best technique for synthesizing intrazeolitic transition metals with zeolite A was through the addition of a transition metal containing amorphous "seed" material to the synthesis gel. Ruthenium A was first synthesized by this technique with unpleasant results. Visual examination of the product crystals revealed that dark particles of amorphous material were present along with the product crystals. The crystal growth rate data for this synthesis showed that near complete crystallization was achieved in less than 1:45 hours, as opposed to 2:30 hours in the case of rhodium A. The decrease in

crystallization time was the result of a forced convection oven which was now being employed. (A free convection oven was used for all rhodium zeolite A studies.) The forced convection improved the heat transfer to the synthesis vessel, heating it up at a faster rate. Since the free convection oven was no longer available, the synthesis technique would have to be modified. A variation of the "seed" technique was then used. Ruthenium A "seed" material was not prepared by cation exchange as previously employed, but was prepared by synthesizing ruthenium A through addition of $RuCl_3$-$3H_2O$ to the synthesis gel.

Binding energies for the elements of interest in analyzing RuCa A are presented in Table 16. The binding energy of 281.5 eV associated with the Ru3d5/2 energy level corresponds to ruthenium in the plus three oxidation state (135). Also, the (Si+Al)/O ratio at the surface was very nearly equal to 0.5, and no sodium or chlorine were detected.

XPS and chemical analysis data for a 2.16 and 1.53 wt% ruthenium zeolite A are presented in Table 18. The XPS/CA Ru/Si values presented in this table have an increased amount of error associated with them when compared to the data of rhodium zeolite A. This error is due to the small amount of ruthenium present on the surface, which did not yield a good signal to noise ratio. As a result, these values can only be used as an indication that very little ruthenium is present on the zeolite A surface.

The RuCa A zeolite (2.16 wt% Ru) was examined for metal distribution from crystal to crystal by electron microprobe. As shown in Figure 50,

the ruthenium was not evenly distributed among the crystals; some contained large Quantities of ruthenium, while others contained almost none. The RuNa A "seed" crystals added to the synthesis gel should contain primarially intrazeolitic ruthenium (based on the analogous rhodium A material). Thus, the ruthenium should stabilize the crystal structure against alkaline attack. It is possible that the variation of ruthenium content among product crystals could be due to the "seed" crystals' inability to completely digest into the synthesis gel. Thus, only small Quantities of ruthenium at or near the crystal surface would be released. The "seed" material could then overgrow, producing a crystal rich in ruthenium at the core with little ruthenium at the surface. Crystals which formed independently of the "seed" material would not possess much ruthenium, as very little would be available from the gel phase. Hence, two types of crystals could result, those containing a ruthenium core overgrown by a less concentrated region, and those containing very little ruthenium resulting from solution crystal growth.

VI.A.3 Synthesis of ZSM-5 from Mixtures of Organic Cations

The objective of this work was to study the nature of "foreign" quarternary ammonium cations present in the ZSM-5 synthesis gel. Results of this study would aid in determining whether non-structure directing cations are incorporated into zeolites during crystal growth. The two systems chosen here for investigation are:

A) Two organic cations (TPA,TEA) which produced similar zeolites (ZSM-5, ZSM-8) with different crystallization rates.

B) Two organic cations (TPA,TMA) where one produces zeolite (TPA) and the other does not (TMA).

For system A, the TPA and TEA were used. TPA reacts to produce ZSM-5 while TEA reacts to produce the ZSM-5 like ZSM-8 (2,4). ZSM-8 crystallizes much slower in the presence of TEA than ZSM-5 in the presence of TPA from similar synthesis gels. For system B, TPA and TMA were employed. No references could be found to show that zeolite could be crystallized from the gel compositions reported in this study in the presence of TMA alone.

X-ray diffraction patterns were recorded for all samples synthesized in the mixed organic cation systems (gel compositions A and B). In every case, only one zeolite phase was observed, that being ZSM-5. The X-ray patterns of ZSM-5 and ZSM-8 are extremely similar (144). We were unable to observe any clear differences between the two X-ray patterns. Because of this, the product zeolite synthesized from pure TEA will be referred to as ZSM-5. Representative X-ray diffraction patterns are reported in Figures 58, 59 and 60. All X-ray patterns shown here were obtained on the samples following calcination. The X-ray diffraction patterns clearly identify these materials as ZSM-5 (64).

Of note from the X-ray diffraction patterns was the increase in resolution (splitting) of the 2θ = 23.00 peak and the 2θ = 23.60 to 23.80 region as the quantity of the "foreign" organic cation was increased. The increase in resolution is best observed by comparing Figure 58 (TPA/ZSM-5, x = 0.0) to Figures 59 (TEA-TPA/ZSM-5, x = 0.75) and 60 (TMA-TPA/ZSM-5, x = 0.75). In no case were new peaks observed in any of

the X-ray diffraction patterns. Similar alterations in the X-ray diffraction pattern have been observed elsewhere (78,84,91,92). These works report the increase of the resolution of the 2θ = 23.00 peak along with presence of some additional doublets in the high 2θ region.

The crystal structure of ZSM-5 synthesized with TPA has been indexed to orthorhombic crystal symmetry (70,81). For the crystals where the 2θ = 23.00 peaks were resolved; the authors could not index the crystal structure to orthorhombic crystal symmetry (91). They then lowered the crystal symmetry to monoclinic and were successful in indexing the crystal structure. The loss of resolution in the 2θ = 23.00 region of the ZSM-5 X-ray diffraction pattern is caused by lattice imperfections (78,145). It has been suggested previously (78) that the presence of a doublet in the 2θ = 23.00 region results from a more "perfect" crystal. The ideal crystal structure of silicalite calculated by Flanagen et al. (81) shows the presence of this doublet. The increase in resolution in this region with the increase in the "foreign" organic cation concentration is then suggesting that as the quantity of "foreign" organic cation is increased, the resulting crystal becomes more consistent with that calculated for ZSM-5 and silicalite.

Crystal purity of the resulting ZSM-5 materials synthesized from composition B was investigated by IR spectroscopy. The optical density ratio below 0.7 indicates that the ZSM-5 is not pure (amorphous SiO_2 also present) and/or contains intergrowth of another crystalline phase, typically ZSM-11 (96). Optical density ratios above 0.7 indicate that the

ZSM-5 is of high purity (96). As reported in Table 19, the optical density ratio for all samples is above 0.7 and increases with the fraction of TEA added to the synthesis gel. When the fraction of TMA is increased, no changes in the optical density ratio was observed. Thus, the X-ray and FTIR data suggest that as the ratio of "foreign" organic cation to TPA is increased, the purity of the resulting ZSM-5 material is also increased.

SEM's of various crystals are shown in Figures 55, 56 and 57. These figures show that the addition of the "foreign" organic cation to the synthesis gel reduced the extent of twinning and intergrowth. Twinning and intergrowth of ZSM-5 result from crystallization on lattice faults and defects. Ideally, the morphology of ZSM-5 is lath shape (79).

^{13}C-MASNMR was used to ascertain the presence of the "foreign" organic cation within the product zeolite. The sample chosen for analysis was synthesized from the low sodium, TMA/TPA system ($x = 0.5$). Figure 64 compares the ^{13}C-MASNMR spectrum of ZSM-5 synthesized from composition A ($x = 1.0$) to that of ZSM-5 synthesized from the same composition (TMA/TPA) with $x = 0.5$. The methyl peak associated with the TMA molecule is present at 56 ppm, slightly upfield from the C^1 peak associated with the TPA. These data show that the TMA molecule is present and because of the amount relative to TPA, it must reside within the ZSM-5 channel system. Thus, this result suggests that the ZSM-5 is capable of incorporating non-structure directing cations during the crystal growth process.

TGA was performed on various samples for the purpose of establishing whether or not the "foreign" organic cations had been incorporated. Since the organic weight loss upon calcination did not occur in two stages, it became impossible to determine how much of each organic cation had been incorporated. The results of the TGA, however, were useful in quantifying that the "foreign" organic cation had been incorporated. This was accomplished by combining the weight loss upon calcination with a material balance on the TPA cation. Chemical analysis and crystalline yield showed the conversion of silica in the synthesis gel to be greater than 99.9% (i.e. 99.9%+ of the silica in the gel is ultimately transformed into ZSM-5). This result implies that from the gel composition, the maximum weight loss attributed to the TPA could be calculated and compared to the weight loss obtained from the TGA. An example of this calculation is presented for clarity. For either gel composition with x = 0.5, there are 0.0295 TPA molecules present in the synthesis gel per (Si,Al) atom. 96 T atoms comprise the unit cell of the ZSM-5 zeolite. Since essentially all the T atoms in the synthesis gel are ultimately incorporated in the product crystal structure, then the number of TPA molecules per unit cell can be obtained by multiplying the TPA per T-atom by 96. For this case, there are 2.83 TPA molecules per unit cell. The approximate molecular weight of the cation-free ZSM-5 unit cell is 5760 and the molecular weight of TPA is 186. Thus, for x = 0.5, the maximum organic weight loss which can be attributed to the presence of the TPA is 9.15 wt% [186(2.83)/5760] Whenever the observed organic weight loss was greater than the calculated maximum, the conclusion was that the "foreign" organic cation had been incorporated. This was the case for all batches synthesized in which x

≥ 0.50. Table 38 reports the weight loss upon calcination and the calculated maximum weight loss which could be attributed to TPA. These data show that for all batches prepared with $x \geq 0.5$, sufficient Quantities of "foreign" organic cations have been incorporated within the ZSM-5 channel system during the crystal growth process. Again, the results indicate that the growing ZSM-5 crystal is capable of incorporating non-structure directing cations.

Figure 63 shows the weight loss upon calcination as a function of the percent TPA in the synthesis gel for the low sodium system. As this figure shows, a linear decrease in the weight loss is observed as x is increased. The loss in weight upon calcination is consistent with the incorporation of the "foreign" organic cation, as the TEA and TMA molecules have a lower molecular weight than the TPA. Also since the change in weight loss with increasing x was different for TEA and TMA, the decrease in weight loss with increasing x can not be attributed to only the decline in the incorporation of TPA.

In the high sodium case, an unexpected behavior was observed as can be seen in Figures 61 and 62. Note that the sample grown from pure TPA yields only 3.22 TPA per unit cell (four channel intersections per unit cell). This compares to a value of 4 most commonly reported. However, values this low for TPA per unit cell have been reported (85). Figures 61 and 62 show that decreasing the concentration of TPA in the synthesis gel initially leads to an increase in weight loss upon calcination which is followed by a linear decrease. One possible explanation for the in-

Table 38
Organic Weight Loss and Maximum Calculated Weight Loss for ZSM-5 Materials Synthesized in the Mixed Organic Cation Systems

Low Sodium System

Cation	x	Wt Loss[1]	Maximum Wt Loss[2]
TPA	0.00	12.58%	12.90%
TEA/TPA	0.25	11.76	12.90
TMA/TPA	0.25	10.65	12.90
TEA/TPA	0.50	11.11	9.15
TMA/TPA	0.50	9.85	9.15

High Sodium System

Cation	x	Wt Loss[1]	Maximum Wt Loss[2]
TPA	0.00	10.24%	12.90%
TEA/TPA	0.25	11.58	12.90
TMA/TPA	0.25	11.88	12.90
TEA/TPA	0.50	11.58	9.15
TMA/TPA	0.50	10.92	9.15
TEA/TPA	0.75	10.44	4.57
TMA/TPA	0.75	8.25	4.57
TEA	1.00	8.55	0.00

[1] Weight loss upon calcination
[2] Maximum weight loss which could be attributed to the TPA

crease in the organic weight loss observed over the x = 0.0 to 0.25 region is that the small quantities of "foreign" organic cation present in the synthesis gel have increased the number of cations incorporated per unit cell. Over the x = 0.0 to 0.25 region, it was not determined whether the "foreign" organic cation had been incorporated. The decrease in organic weight loss upon calcination observed as x was increased past 0.25 is a result of the lower molecular weight associated with the "foreign" organic cation.

Quantitative analysis of the ^{13}C-MASNMR spectra illustrated in Figure 64 shows the TPA molecule to be preferentially incorporated into the ZSM-5 structure (69% of the organic cation in the solid was TPA). This material was synthesized from gel composition A with x = 0.5. It was not surprising that TPA was preferentially incorporated into the product ZSM-5, as it is the most reactive organic cation employed in the synthesis of ZSM-5. Based on the organic weight loss obtained upon calcination (see Figure 63), 91% of the TPA in the synthesis gel had been incorporated into the product crystal, as opposed to only 41% of the TMA. Further calculations show that there are 3.75 organic cations present per unit cell.

As shown in Figures 51 and 53, the crystal growth rate was not affected by the presence of the "foreign" organic cation up to the values of x reported in these figures. The compositions with $x \geq 0.50$ are of special interest. For these batches, there is not enough TPA present in the synthesis gel to achieve complete crystallization. This was demonstrated by attempts to synthesize ZSM-5 with half the TPA utilized in

compositions A and B with x = 0.0. For these batches, crystallization was halted at 40 and 55%, respectively. Furthermore, the TGA and the ^{13}C-MASNMR analyses showed that the "foreign" organic cation is indeed incorporated into the product crystal. For values of x reported in these figures, the "foreign" organic cation is able to react with the growing crystals without affecting the crystal growth rate.

Figure 52 compares the crystal growth rate of ZSM-5 synthesized with x = 0.75 in the low sodium system (both TMA and TEA) to that of ZSM-5 synthesized in the same system with x = 0.0. Figure 54 compares the growth rate of ZSM-5 synthesized in the high sodium, TEA (x = 1.0) and TMA/TPA (x = 0.75) systems to that of ZSM-5 synthesized in the same system with x = 0.0. In all the aforementioned cases which utilized "foreign" organic cations, complete crystallization was not achieved. However, it is of interest to note that the initial stages of crystal growth rate are not affected by the presence of "foreign" organic cations (with the exception of the pure TEA cases).

Crystal growth data reported in Figures 52 and 54 show that for x = 0.75, the initial rate of crystal growth does not deviate from that of ZSM-5 synthesized with pure TPA. However, later in the crystallization process the deviation in crystal growth rate becomes significant. Figure 54 shows also that composition B prepared with pure TEA required over 8 hours to nucleate, while the same composition required approximately 3 hours to achieve nucleation when prepared with pure TPA. The pure TMA systems were unable to produce any zeolite material. Since: 1) the TEA

required a much greater time to nucleate than the TPA, 2) the TMA did not cause nucleation with the gel composition investigated here and, 3) the time required to achieve nucleation was not altered by the presence of the "foreign" organic cation (up to x = 0.75), it is most probable that the TPA is responsible for initiating crystal growth in these mixed organic cation systems.

It appears that the caustic (NaOH) catalyzes the crystal growth process, as complete crystallization was achieved in the high sodium compositions at greater values of x. Sodium is known to enhance the reactivity of the ZSM-5 synthesis gel. It has also been shown that sodium is capable of directing the synthesis of ZSM-5, because the growth of ZSM-5 from seed crystals alone has been reported (83,84). Thus, the quantity and type of "foreign" organic cation incorporated into the ZSM-5 during synthesis is directly related to the amount of caustic present in the synthesis gel.

One of the accepted growth mechanism for pentasil type zeolites involves silica and alumina clathration of the hydrophobic organic cation (77,81,146). The alkylammonium cation forms complexes with gel phase silica and aluminum via hydrogen bonding interactions. The clathrated silica complex then causes replication of the structure (crystal growth) by a stereospecific hydrogen bonding interaction with framework oxygen of the growing structure.

If the two organic cations (TPA, TEA) behaved independently, two distinct crystalline phases would result; one occurring via the TPA and appearing first and the other stemming from the TEA and appearing much later. The two phases would be easily recognized by two crystalline morphologies. For the TMA/TPA system, one would expect a halt in crystal growth well short of completion as the TPA supply would be exhausted. Because uniform crystals were produced while incorporating significant Quantities of "foreign" organic cation, these results probably indicate that the Si,Al atoms are able to clathrate the "foreign" organic cations. This is consistent with data reported by Boxhoorn et al. (82). These clathrated species appear to preferentially react with the ZSM-5 structure or structure units rather than nucleate another material. It appears that since the TPA dominated nucleation, it has determined the crystal structure.

Figures 51 and 53 suggest that when a certain quantity of TPA is present in the synthesis gel (x = 0.5) the species formed with the "foreign" organic cations are active towards crystal growth. This is evidenced by the inclusion of the "foreign" organic cation within the product crystal and the observation of complete crystallinity when there was not enough TPA in the synthesis gel to alone produce complete crystallinity. These species may be double-ring structures as has been proposed by Boxhoorn et al. (82). Figure 52 shows that the species formed with the "foreign" organic cation alone cannot form the ZSM-5 structure.

An attempt to explain the observed crystal growth behavior is given below. It is assumed that the TPA cation forms a species which initiates crystal growth. This assumption has been previously discussed. A further assumption is made that the "foreign" organic cations order around themselves Si,Al atoms so as to yield a second species. This assumption appears valid, as the addition of quarternary ammonium cations (including TMA and TEA) to a ZSM-5 synthesis gel without TPA have produced double ring structures (82). From these assumptions, it is postulated that the TPA species serves as a building block which initiates the crystallization of ZSM-5. These TPA initiated units interact with the species formed from the "foreign" organic cation so as to replicate or form structure units (or at least parts of these units). Thus, structure direction during crystallization is not supplied by the "foreign" organic cation Si,Al species but rather is being supplied by the structure itself. The fact that crystallization was halted short of completion in the low sodium system (for all batches prepared with x = 0.75, see Figure 54) suggests that the TPA may be involved in the interaction between the double ring structures formed by the "foreign" organic cation and the growing crystal structure. [If TPA is not involved in this interaction, then only small quantities of TPA would be required for complete crystallinity. The TPA would initiate crystal growth by supplying structure direction in the form of nuclei. The species formed from the "foreign" organic cation would then interact with the structure to form replicating units, which would be incorporated continuously. This would lead to complete crystallization, which was not observed at high values of x.]

Interactions between species formed from the TPA and the "foreign" organic cation may occur early in the crystallization process. Scholle et al. (87) have shown that the crystallization of ZSM-5 occurs first by formation of double five ring structures brought about by coordination of gel phase Si,Al atoms with TPA^+ and Na^+. The ring structures join together and stabilize the TPA cations. However, these secondary units are small, approximately 20-50A, and are thus X-ray amorphous (87,88). These units have also been shown to be completely formed prior to the formation of large crystals (88). The X-ray amorphous structures then combine to form large ZSM-5 crystals during the completion of the crystal growth process. It is postulated here that when the double ring structures join to form the secondary building units (X-ray amorphous structures) that the TPA and the "foreign" organic cation interact. That is, the double five ring structures (or groups of them) formed from the TPA coordinate with the double ring structures formed from the "foreign" organic cations to form the secondary building units. When the TPA supply is small, a limited number of X-ray amorphous structures are formed, and this number is below that required to achieve complete crystallinity. These structures, associated with both the TPA and the "foreign" organic cation, then react to form large crystals, as proposed previously (87). The sudden halt in crystal growth would then be the result of exhausting the supply of X-ray amorphous structures and the clathrated "foreign" organic cations' inability to react with the large crystal structure. This behavior is consistent with the data presented in Figures 51 and 52.

Figure 53 shows that increasing the NaOH content of the synthesis gel results in achieving complete crystallinity in the presence of greater quantities of "foreign" organic cations. Derouane et al. (74) have shown that both Na^+ and TPA^+ possess "structure forming effects." The structure forming effect of sodium has been further highlighted by the synthesis of ZSM-5 from seed crystals (83,84). It has also been suggested that sodium favors the formation of the secondary building units (80). It is possible that the increased Na^+ content (of composition B) aids in coordinating and reacting solution species associated with the "foreign" organic cation.

Batches similar to composition A were prepared, except that sodium hydroxide is now replaced by potassium hydroxide. For these batches, the K_2O/Al_2O_3 ratio was held constant (1.75) while the SiO_2/Al_2O_3 ratio was varied according to 120, 90, 30, 20 and 10. The two quaternary ammonium cations employed here were TPA and TMA with x = 0.5. This gel composition was selected because it can yield ZSM-5 in the high silica system (147) while producing TMA-offretite in the low silica system (148-151). X-ray analyses of the resulting crystalline products showed the phases to be ZSM-5, ZSM-5, ZSM-5 and α-quartz, no crystalline yield and TMA-offretite, respectively. In no case were ZSM-5 and offretite simultaneously present. In the high silica case, it is suspected that TPA dominated the nucleation process and hence ZSM-5 was produced. When the TMA was suspected to dominated the nucleation process, as in the SiO_2/Al_2O_3 = 10 case, the crystalline yield was offretite. TGA could ascertain the presence of the TMA within the ZSM-5 (see previous discussion for technique), but was

unable to show that the TPA had been incorporated into the TMA-offretite. This example shows that the species which dominates nucleation will determine the ultimate crystal structure. Following nucleation, crystal growth becomes less dependent on the nature of the organic cation as structure direction from the structure is supplied. These observations are similar to that of Aiello and Barrer (148), who observed the same trends in mixed base (inorganic) systems with low silica zeolites.

VI.A.4 Cobalt ZSM-5 Synthesis

The objective of this work was to extend the synthesis procedure for incorporating transition metals into zeolite A to ZSM-5. Zeolite A and ZSM-5 are synthesized from two very different synthesis gel chemistries. The ZSM-5 synthesis gel employed in this study contained very little aluminum and OH^- relative to the zeolite A gel. In addition, the ZSM-5 synthesis (for the gel compositions utilized in this study) requires an organic cation. Also, the synthesis temperatures used to produce ZSM-5 were almost 100°C greater than that of zeolite A. Because of the tremendous difference in synthesis conditions, the ZSM-5 would aid in evaluation of the applicability of the "seed" technique to other zeolite systems.

The basis of the synthesis technique developed for zeolite A involved associating the transition metal with framework atoms, namely silicon and aluminum. It has been shown that ZSM-5 will grow in the presence of seed crystals (83,84,152). In our laboratories initial attempts to grow ZSM-5 from seed crystals failed, and the procedure was not persued further.

Instead, cobalt was associated with framework aluminum by cation exchange of sodium aluminate with $CoCl_2$-$6H_2O$. This material was added to the ZSM-5 synthesis gel and served as the carrier of cobalt. ZSM-5 synthesized in the presence of this material contained dark particles of an amorphous cobalt material visible via light microscopy. Because of this result, the procedure was not studied further. The next cobalt source investigated was an amorphous cobalt silica-aluminate material. The preparation of this amorphous material is presented on page 123. This material was similar to the amorphous rhodium material employed in the synthesis of rhodium zeolite A. Visual examination (light microscopy and SEM) of Co/ZSM-5 synthesized in the presence of this amorphous material did not reveal particles of amorphous cobalt material. Thus, this technique was chosen for subsequent Co/ZSM-5 synthesis studies and serves as the extention of the principles of the "seed" technique developed for zeolite A to ZSM-5.

Crystal growth data for blank ZSM-5 (Si/Al = ∞ and 45) and Co/ZSM-5 (Si/Al = ∞ and 45) synthesized in the presence of $CoCl_2$-$6H_2O$ are reported in Figure 66. As the figure shows, the initial rate of crystal growth is not altered by the presence of the $CoCl_2$-$6H_2O$. Following this period in growth, severe deviation from the growth rate of blank ZSM-5 is observed for the cobalt containing gel. Note also that the deviation between the growth rate of the blank ZSM-5 and Co/ZSM-5 becomes more prevalent as the Si/Al ratio is decreased from ∞ to 45. It has been shown elsewhere that the addition of salts, even NaCl, to the ZSM-5 synthesis gel effects the crystal growth rate (69,74). Thus, the deviation in the

crystal growth rate resulting from the addition of $CoCl_2$-$6H_2O$ to the synthesis gel could be expected. Aluminum added to the ZSM-5 synthesis gel lowers the gel reactivity [observed by increases in the nucleation time and decreases in the rate of crystal growth]. The data reported in Figure 66 may be suggesting that as the gel reactivity decreases, the crystal growth process becomes more susceptible to the influence of non-structure directing cations. However, the deviation in growth rate may also be due to the influence of the chlorine ions on the synthesis gel chemistry.

The Co/ZSM-5 produced from these compositions appeared speckled with particles of amorphous cobalt material. These observations were similar to those of Dodwell's (21) for metal/ZSM-5 synthesized by addition of metal chlorides and hydroxides to the synthesis gel. Also, the halt in crystallinity may be due to the gel's inability to react these amorphous particles.

Figure 67 compares the crystal growth data of blank ZSM-5 (Si/Al = ∞) to that of Co/ZSM-5 synthesized at various cobalt loadings. In this case, the Co/ZSM-5 was prepared by addition of amorphous cobalt "seed" material to the synthesis gel. As the figure shows, the amorphous cobalt material does not alter the crystal growth rate up to a Co/Si ratio (gel) of 0.010 for the composition (F) employed here. The data reported in this figure show that cobalt added to the synthesis gel associated with framework molecules (namely silicon and aluminum) does not effect the crystal growth rate up to the limits reported. Contrary to the case where

the cobalt was introduced to the synthesis gel as $CoCl_2$-$6H_2O$, traces or no particles of amorphous cobalt material were observed via light microscope or SEM. These results suggest that the cobalt associated with the "seed" material does not alter the gel chemistry to the extent of the $CoCl_2$-$6H_2O$, thereby allowing for completion of the crystallization process.

From the visual observations and the crystal growth data, the addition of amorphous "seed" material appears to be superior to that of $CoCl_2$-$6H_2O$ for the synthesis of Co/ZSM-5 in that it does not alter the growth rate and does not appear to aggregate the cobalt in large amorphous particles. It should also be noted here that Co/ZSM-5 synthesized in the presence of the amorphous "seed" material was a much lighter blue in color than the Co/ZSM-5 synthesized in the presence of $CoCl_2$-$6H_2O$, which was a very deep blue color.

A sample of the Co/ZSM-5 synthesized from the amorphous "seed" material was further checked for crystal purity by oxygen adsorption. The analysis showed this material to possess a pore volume of 17.8 cm^3/100 g zeolite, which compares favorably to the value reported for silicalite (18.7 cm^3/100 g zeolite, ref. 81) and ZSM-5 (18.0 cm^3/100 g zeolite, refs. 95,153). The slight discrepancy in the measured pore volume could be attributed to many factors, including the presence of cobalt within the

channels[20], occluded aluminate ions and minute traces of amorphous particles.

Cobalt recovery in the product Co/ZSM-5 synthesized via the amorphous "seed" material was next evaluated. Analysis of the synthesis solution following crystallization showed the solution to be free of cobalt. This indicated that all the cobalt which was initially placed into the synthesis gel was ultimately associated with the product crystals. As shown in Figure 68, a linear relation exists between the gel and zeolite phase Co/Si ratio. The gel phase Co/Si ratio does not include any silicon contribution from the amorphous material. However, the amorphous material was not present in a large enough quantity to significantly influence the concentration of silicon. The slope of this line is one, as would be expected since virtually all the silicon and cobalt present in the synthesis gel are incorporated into the product zeolite.

Figure 69 shows an SEM of Co/ZSM-5 crystals synthesized from composition F (gel Co/Si = 0.0082). As the figure shows, crystals synthesized from the amorphous "seed" material are clean and uniform.

Table 20 reports the binding energies for the elements of interest in this study. As the table shows, all samples reported in Table 21 with an XPS Co/Si ratio greater than 0.02 possessed a binding energy of

---

[20] Wu and Ma (103) have shown the adsorption capacity of various hydrocarbons in ZSM-5 to decrease as the size of the cation is increased.

781.5±0.3 eV for the Co2p(3/2) electron level. This binding energy is in excellent agreement with those reported elsewhere for supported cobalt (126) and cation exchanged Co/ZSM-5 (2,3). When the XPS Co/Si ratio was less than 0.02, as was the case for Co/ZSM-5 synthesized from compositions G and I (bulk Co/Si = 0.0046), the binding energy of the cobalt 2p(3/2) photoelectron peak was shifted upfield approximately 1.5 to 2.0 eV. This shift in binding energy is shown in Figure 70. Chin and Hercules (126) have shown that for cobalt supported on γ-alumina (Co/Al_2O_3) an increase in the binding energy of the Co2p(3/2) photoelectron peak was observed (780.7 to 781.7 eV) as the loading of the catalyst was decreased from 30 to 2 wt% cobalt. This shift was attributed to an interaction between the cobalt and the alumina support. Rao (2) and Stencel et al. (3) have reported binding energies for the Co2p(3/2) photoelectron peak as high as 783.4 eV, similar to those reported here. This material was prepared by cation exchange of Na/ZSM-5 with $CoCl_2$-$6H_2O$ followed by extensive washing of the catalyst with water so as to remove surface cobalt. The resulting material was 1.20 wt% cobalt. They also noted a very strong shoulder at 787.0 eV, which was also present in this study, as shown in Figure 70. Stencel et al. (3) assigned this shoulder to bare Co^{+2} ions. The binding energy of cobalt in their studies (2,3) compared to binding energy of 782.0±0.3 eV for cation exchanged Co/ZSM-5 (9.0 and 5.1 wt% cobalt). Rao (2) and Stencel et al. (3) concluded that the 1.2 wt% Co/ZSM-5 must possess a different form of cobalt than the higher loaded materials. The XPS spectra of the Co2p(3/2) photoelectron region for the 1.2 wt% Co/ZSM-5 reported by Stencel et al. (3) is shown in Figure 94A and can be compared to that of Co/ZSM-5 synthesized from composition I (Co/Si=0.0046) which

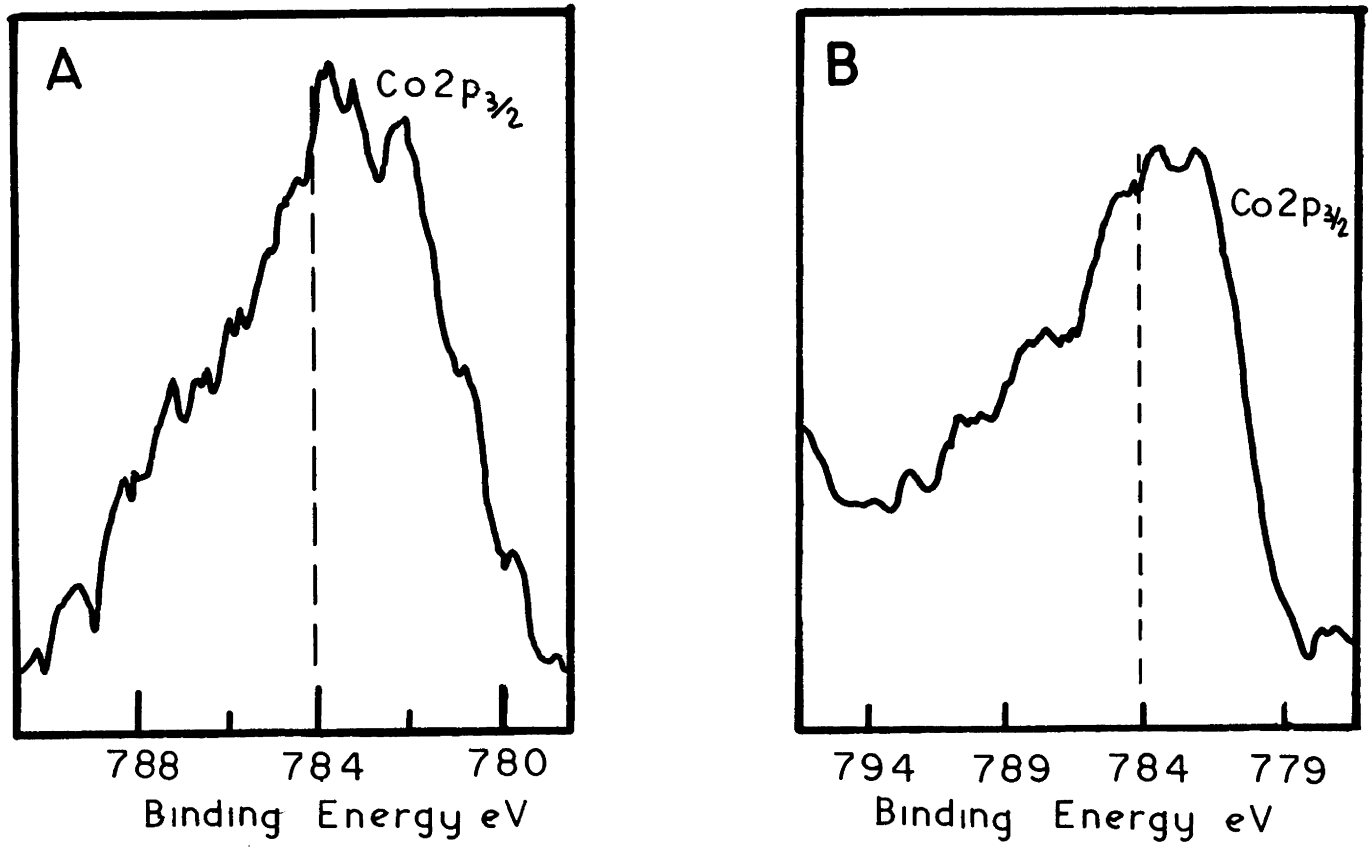

Figure 94: XPS Spectra of Co/ZSM-5. A) Co2p(3/2) photoelectron peak from Stencel et al. (3); and B) from composition I (Co/Si = 0.0046).

is shown in Figure 94B. The higher than normal binding energy reported in their studies and in this study may indicate that the cobalt is in a highly oxidized environment. This may be the result of the interaction between the cobalt and the ZSM-5 support (3). A higher than normal binding energy for ruthenium located in the cages of Na Y has also been reported (3). The higher than normal binding energy reported in this study for Co/ZSM-5 synthesized from compositions G and I (at a bulk Co/Si ratio of 0.0046) suggest that these materials may contain highly dispersed cobalt atoms in intimate contact with the ZSM-5 support.

Table 21 reports XPS and chemical analysis data of cobalt and silicon for Co/ZSM-5 prepared from various procedures. All materials were examined in the as synthesized form. For all materials reported in this table, including the cation exchanged Co/ZSM-5, the Si/O ratio was 0.50±0.02.

Cation exchange of ZSM-5 with $CoCl_2$-$6H_2O$ appears to locate most of the cobalt on the surface of the zeolite (based on the XPS analysis). This provides a surface/bulk, Co/Si ratio from which the various preparations could be compared. As Table 21 shows, all the techniques which utilized cobalt in the synthesis gel resulted in producing ZSM-5 with at least some of the cobalt within the channel system. This is evident by the much lower XPS/CA Co/Si ratio obtained for these samples. This table shows that Co/ZSM-5 synthesized in the presence of the amorphous "seed" material possesses a lower superficial cobalt concentration than the zeolite prepared by addition of $CoCl_2$-$6H_2O$ to the synthesis gel (at

equivalent loadings). Figure 70 provides an indication as to the relative amounts of cobalt present at the zeolite surface for different XPS Co/Si ratios. This is done by comparing the intensity of the O(KVV) aguer line to the intensity of the Co2p(3/2) photoelectron line[21]. For cation exchanged Co/ZSM-5 (Figure 70A), the Co2p(3/2) peak towers above the O(KVV) line. For this material, the XPS Co/Si ratio was 0.1917. Figure 70B is for Co/ZSM-5 synthesized from composition C. In this case, the XPS Co/Si ratio was 0.0478. Note that the differences in intensities between the Co2p(3/2) and O(KVV) has decreased compared to the the cation exchanged material. Finally, for Co/ZSM-5 synthesized from composition I (bulk Co/Si=0.0046), the intensity of the O(KVV) has become greater than the intensity of the Co2p(3/2), as shown in Figure 70C. Here, the XPS Co/Si ratio is 0.0098. Table 21 further shows the effects of the sodium aluminate, sodium hydroxide, and sodium aluminate + sodium hydroxide content of the synthesis gel on the superficial cobalt content.

Figure 71 compares the XPS photoelectron spectra of Co/ZSM-5 synthesized from composition I (Co/Si = 0.0046) in the as-synthesized form and following calcination. As the figure shows, the relative intensity of the Co2p(3/2) peak to the O(KVV) is not altered by the calcination. This indicates that intrazeolitic cobalt has not migrated to the external surface of the zeolite during calcination.

---

[21] The intensity of the O(KVV) auger is directly related to the quantity of zeolitic oxygen in the superficial region.

Electron microprobe studies of various Co/ZSM-5 crystals were performed. Figures 72 and 73 are X-ray images of Co/ZSM-5 synthesized from composition F with a Co/Si ratio of 0.0082 (see Table 21 for XPS analysis)[22]. As the figures show, the cobalt is not evenly distributed among the crystals as regions of high cobalt concentration are present. These regions may be the result of small particles of cobalt oxide or cobalt associated with amorphous silica present on the surface of the crystals. The Co/ZSM-5 syntheiszed from composition I with a Co/Si ratio of 0.0046 was also examined by electron microprobe. The analysis shows the cobalt to be almost uniformly distributed among the crystals. Also, regions of high cobalt concentration were scarce.

An X-ray image of cobalt for cation exchanged Co/ZSM-5 is shown in Figure 75. The figure shows the cobalt to be unevenly distributed on the crystal. However, all the cobalt is associated with the zeolite and does not exist as large (0.1 micron) particles of cobalt oxide.

The aluminum distribution within a ZSM-5 crystal synthesized from the "blank" amorphous material is shown in Figure 74. As the figure shows, the aluminum is distributed evenly among the crystal. XPS analysis of this material showed a high (relative to the bulk) aluminum concentration to exist at the surface. For this material, the SiO_2/Al_2O_3 ratio in the superficial region was 30 while that of the bulk was 104 as meas-

---

[22] Figure 72 is of the material in the as-synthesized form, Figure 73 is of the same material following calcination.

ured by electron microprobe analysis. Also, if the amorphous material had not completely dissolved, pockets of aluminum rich areas would be observed. These results suggest that the amorphous material dissolved completely so as to produce crystals which possessed an aluminum rich surface.

As can be seen in Table 21, increasing the quantity of aluminum in the synthesis gel (from a Si/Al ratio of ∞ to 35) increased the superficial cobalt content (at equivalent loadings) of the resulting crystals with the low sodium system. The effects of aluminum on the surface cobalt concentration with the high sodium system were not as severe. It is postulated here that the cobalt is associated with the growing zeolite through ionic attractions. Thus, it was expected that increasing the number of anionic sites of the zeolite (by addition of aluminum to the synthesis gel) would result in a lower surface cobalt concentration[23]. As the data reported in Table 21 shows, the direct opposite occurred. The fact that the presence of aluminum did not significantly reduce the superficial cobalt concentration (at equivalent loadings) was surprising since the framework Al^- requires a cation to balance the charge. These results tend to indicate that the cobalt may not be associated with the structure during synthesis exclusively through ionic attractions with framework aluminum.

---

[23] It should be noted that increasing the aluminum content of the product crystals will place more anionic aluminum sites in the superficial region. However, the quantity of aluminum in this region will be much much less than the quantity of aluminum in the remainder of the crystal.

Dodwell synthesized silicalite in the presence of transition metal salts (21). His results showed that the transition metals were incorporated during the synthesis. He concluded that the metals were occluded as complex hydroxides rather than cations. Dodwell did not provide an explanation as to the driving force behind the metal incorporation. In a recent paper by Chester et al. (102), it was shown that ZSM-5 and ZSM-11 possess aluminum independent cation exchange sites. The nature of these sites was postulated to be occluded silicate ions, i.e. trapped OH^- or $SiOH^-$ species. It is suspected that sites of this nature (independent of aluminum concentration) are responsible for the incorporation of the cobalt into the ZSM-5 material synthesized here, as these sites would provide an ionic force which would attract the cobalt.

Crystal growth data reported in Figure 66 shows aluminum to hinder the crystal growth rate. Also, growth data presented here show the influence of cobalt on the crystallization rate to be enhanced by the presence of aluminum in the synthesis gel. The lowering of the reactivity of the synthesis gel by the aluminum may be responsible for increasing the surface cobalt concentration of the resulting ZSM-5 material as a less reactive gel could be greater effected by non-structure directing cations.

Based on the previous postulate that the cobalt becomes associated with the ZSM-5 structure through ionic attractions, it would be expected

that increasing the sodium hydroxide content of the synthesis gel would result in more cobalt in the superficial region of the crystals. This is because cobalt and sodium would compete for the anionic sites. Appearantly, this was not the case, as increasing the sodium hydroxide content of the synthesis gel decreased the superficial/bulk Co/Si ratio in all cases (at equivilent loadings; see Table 21).

Product crystals synthesized in the presence of "seed" material at various sodium hydroxide contents were examined for cobalt position both visually and by electron microprobe analysis. A Co/ZSM-5 synthesis gel was prepared with a $Na_2O/(96\ SiO_2)$[24] ratio of 1.4 utilizing the amorphous "seed" material. Following completion of the synthesis, the contents of the synthesis vessel were examined. At the bottom of the vessel, a layer of dark blue material was present with a layer of light blue Co/ZSM-5 directly above. The dark blue material was not crystalline and is believed to be undigested "seed" material. For this composition, it appears that there was not enough caustic present in the synthesis gel to completely digest the amorphous cobalt "seed" material. When the $Na_2O/(96\ SiO_2)$ was increased to 2.80, no dark particles of non-zeolite cobalt particles were visible via the light microscope or by SEM. Further analysis of one of these materials (composition F, Co/Si = 0.0082) by electron microprobe analysis showed regions of high cobalt concentration to exist, as can be seen in Figure 72. Microprobe analysis also showed the aluminum to be uniformly distributed among the crystals, and that the

---

[24] Na_2O per 96 silicon atoms

cobalt rich regions were not aluminum rich. Based on these results, it appears that the amorphous cobalt "seed" material was completely digested by the synthesis gel. [If the material had not been completely digested, then the regions rich in cobalt would also be rich in aluminum since the amorphous "seed" material contained appreciable quantities of aluminum.] The regions rich in cobalt may be amorphous SiO_2 associated with cobalt or small cobalt oxide particles existing on the surface of the zeolite. Upon further increasing the $Na_2/(96\ SiO_2)$ ratio to 7.00, the superficial/bulk Co/Si ratio decreased to 1.48 (composition G, Co/Si = 0.0046). Microprobe analysis was not performed on this sample, however, it is believed that since the XPS/CA Co/Si ratio has decreased, the presence of cobalt particles on the zeolite surface has also decreased. From examination of the crystals synthesized at various sodium hydroxide levels, it appears that increasing the pH of the synthesis gel reduced the agglomeration of cobalt (either cobalt oxides or amorphous cobalt silicon species) thereby making more cobalt available for intrazeolitic sites.

Increasing the sodium aluminate concentration of the synthesis gel with the high sodium system did not severely effect the surface cobalt concentration in the product Co/ZSM-5 as can be seen by comparison of the materials synthesized from compositions G and I prepared from the amorphous "seed" material with Co/Si ratios of 0.0046. In the case of composition G, it appears that ample sodium hydroxide was present to prevent formation of cobalt "agglomerates" while maintaining high gel reactivity. These data show that the SiO_2/Al_2O_3 ratio may be varied in the ZSM-5

crystal without significantly altering the surface cobalt concentration (at equivilent loadings). This is an important result, as the properties of ZSM-5 are drastically altered by changes in the aluminum content.

Increases in the cobalt content of the synthesis gel resulted in increasing the XPS/CA Co/Si ratio of the product Co/ZSM-5; i.e. as more cobalt is placed into the synthesis gel, a greater percentage of cobalt becomes located in the superficial region of the product. This can be seen by comparing the results from the two materials synthesized from compositions F (Co/Si = 0.0048 and 0.0082) and I (Co/Si = 0.0046 and 0.0082) whose XPS analyses are reported in Table 21. These date could be suggesting that a greater percentage of the cobalt becomes intrazeolitic as the cobalt content of the synthesis gel is reduced. The reason for this behavior could be due to a limited number of sites available which can accommodate cobalt within the zeolite or the possibility of forming more cobalt "aggreates" as the quantity of cobalt in the synthesis gel is increased.

Calcination of the Co/ZSM-5 did not alter the chemical or XPS analysis of the parent material. Electron microprobe analysis showed that the cobalt "agglomerates" remained present on the crystal surface, as can be seen in Figure 73. These data indicate that calcination to remove the organic cation does not alter the position of the cobalt, i.e. cobalt does not migrate to the surface and surface cobalt does not disperse or sinter.

Following synthesis, selected materials reported in Table 21 were calcined in a muffle oven at 550°C so as to remove the organic cation (TPA in these cases). It is reported in (102) that calcination to remove the organic cation does not effect the aluminum independent cation exchange sites. If the cobalt is associated with these sites in a charge balancing manner, then calcination should not effect the nature of the cobalt; i.e. cobalt cationically associated with these sites would remain cationically associated following calcination. Thus, little change in color of the crystal should result following this treatment provided the majority of the cobalt is intrazeolitic. Calcination of all materials synthesized from compositions C, D, E, and F reported in Table 21 resulted in the material changing from a blue in color to dark brown. The blue colored crystals may be the result of Co^{2+} hydroxide ions, e.g., $[Co(OH)_4]^{2-}$ (154), with the hydroxide ions supplied from the synthesis solution. It should be noted, however, that many tetrahedral cobalt complexes are blue in color (155). Oxidizing agents (oxygen in this case) cause Co^{2+} to form black CoO_2 and Co_3O_4 (156). [Cobalt oxide (CoO) is olive green in color and is obtained by heating metallic cobalt in oxygen at 1100°C (157).] Thus, calcination of these materials resulted in the transformation of the cobalt(II) tetrahedral complexes to cobalt oxides.

Calcination of Co/ZSM-5 synthesized from batches G and I (Co/Si = 0.0046) did not change color significantly. These materials possessed the lowest superficial to bulk, Co/Si ratios and were a light powder blue color in the as-synthesized form. They became slightly darker following calcination, but not nearly as dark as the previously mentioned Co/ZSM-5.

Thus, a portion of the cobalt associated with these samples was probably not transformed into cobalt oxide. It was also of interest to note that the lower the surface cobalt content, the lighter blue in color the resulting crystal.

A portion of the Co/ZSM-5 prepared from composition F (Co/Si = 0.0082) was slurried in a dilute (about 1.0 wt%) HF solution for 6 hours at room temperature. This material was in the as-synthesized form. Analysis of the Co/ZSM-5 following this treatment showed 77% of the cobalt to have been removed from the crystal[25]. XPS analysis of this material showed virtually no trace of cobalt to be present in the superficial region while microprobe analysis showed no large cobalt particles. Upon calcination of this material, no change in color was observed. It is believed that after the acid washing, all the cobalt associated with this sample is intrazeolitic. Therefore, it appears that intrazeolitic cobalt associated with this sample will not form oxides upon calcination. From this result it is probable that the color change observed upon calcination of unwashed Co/ZSM-5 materials was likely due to the formation of oxides with surface cobalt (namely the aggreates as shown by the microprobe).

VI.B Transition Metal Containing Zeolite Catalysis

---

[25] The possibility that cobalt was exchanged from the interior of the zeolite does exist, as sodium has been cation exchanged from as-synthesized ZSM-5 (95).

VI.B.1 Rhodium Zeolite A Catalysis

The first materials exposed to hydroformylation reaction conditions were of very low rhodium loadings, typically about 0.07 wt% rhodium. These catalysts were prepared via the "seed" technique. Unless otherwise noted, all catalysts used in this study were RhCa A prepared via the "seed" technique. The effect of the primary charge balancing cation (Ca^{+2},Na^{+},K^{+}) was first investigated. These experiments were conducted for the purpose of establishing the location of the active rhodium (surface or intrazeolitic). If the majority of the active rhodium is present on the zeolite surface, the reactivity of the resulting material will be independent of the charge balancing cation[26]. If the majority of the active rhodium is intrazeolitic, virtually no reactivity will be observed when the zeolite is in the sodium or potassium form. The synthesized RhNa A catalyst was placed into either the potassium or calcium form via ion exchange. The RhNa A catalyst was exchanged with NaCl so as to be consistent with the other preparations. These cation exchanges did not alter the rhodium content of the crystal to within experimental error nor did the exchange affect the crystallinity. Hydroformylation activity results using the various cation forms of rhodium zeolite A are reported in Table 22. As the table shows, the RhK A catalyst was essentially unreactive while the RhCa A was very reactive when the overhead gas was 3/1 H_2/CO. When the ratio of the H_2/CO was decreased to 1/1 only trace conversion was observed from the RhNa A while the RhCa A still remained fairly ac-

---

[26] Both K A and Na A exclude 1-hexene. Only Ca A will allow 1-hexene to penetrate the 8-membered rings.

tive. The lower conversion obtained upon reducing the H_2/CO from 3/1 to 1/1 was expected, as this behavior has been reported for homogeneous hydroformylation of 1-hexene (158).

For all cases reported in Table 22, the production of 2-methylhexanal was observed. This product must be formed from solution or surface rhodium, as 2-methylhexanal is too large to have diffused from within the zeolite A structure. Table 24 reports the activity of RhCa A when reacted with 4-methyl-1-pentene. As the table shows, the conversion and N/B ratio observed for this reactant are similar to that of 1-hexene reacted over the same catalyst. Since 2-methyl-1-pentene is excluded from zeolite A, the conversion of this material must result from surface and/or solution rhodium. Also, note from this table that the N/B ratio obtained from reaction of 1-hexene with RhCa A is similar to that obtained from $Rh_6(CO)_{16}$ at similar levels of conversion. This is an important observation. If a portion of the reactivity occurred as a result of intrazeolitic rhodium, then the N/B ratio would be greater than that obtained for $Rh_6(CO)_{16}$. This is because only the linear aldehyde would be able to diffuse from within the zeolite A structure. Since 2-methylhexanal was produced and the RhCa A material did not alter the selectivity (compared to $Rh_6(CO)_{16}$), it is suspected that the majority of the observed catalytic activity is due to surface and/or solution rhodium.

Analysis of the solvent for rhodium content following reaction with a 0.96 wt% RhCa A catalyst was performed. This reaction was carried out

at the same conditions as discussed before. The catalyst loading was increased to improve the chance of detecting solution rhodium[27]. The analysis showed that 17.2% of the rhodium originally associated with the zeolite had been eluted into solution (see Table 27). To poison solution and surface rhodium, approximately 3-4 cm^3 of cyclohexylmercaptan were added to the reaction mixture. Mercaptans are known to poison rhodium catalysts (159). Cyclohexylmercaptan is too large to penetrate the zeolite A structure. Due to its size, it will not be able to poison intrazeolitic rhodium. Examination of the reaction mixture following this experiment showed no conversion of 1-hexene to have occurred. Thus, it appears that all the catalytic activity observed at these conditions is due to solution and/or surface rhodium.

Analyses of the catalyst and the reaction mixture following reaction for rhodium content have shown that a significant portion of the rhodium is lost from the RhCa A. Spectroscopic analysis of the catalyst following synthesis, as discussed previously, has shown that only trace quantities of rhodium are present on the catalyst surface. Further, analysis of the catalyst following liquid phase reaction at 50°C, as reported in Table 27, shows that small quantities of rhodium are still present on the zeolite surface while 17.2% of the initial rhodium content has been eluted. There is not sufficient rhodium on the zeolite surface to account for this rhodium loss, thus it appears that the RhCa A has leached

---

[27] No rhodium could be detected in solution from the catalysts reported in Table 22. This was more than likely due to the quantity of rhodium present in solution being below the detection limits.

intrazeolitic rhodium into solution. This postulate can be further verified from the data reported in Table 22. If all the rhodium loss is attributable to surface rhodium, then the catalytic activity would be independent of the cation exchange form of the catalyst. The primary charge balancing cation, potassium, sodium or calcium, results in changing the effective pore diameter to 3, 4 and 5 Å, respectively. Therefore, it appears that the lack of activity from the sodium and potassium forms of this catalyst is due to rhodium not being able to migrate out of the catalyst due to physical constraints. Thus, the rhodium species which migrated from the RhCA A zeolite must be greater than 4Å and less than 5Å.

Table 27 reports the rhodium content and distribution for RhCa A following exposure to flowing CO at 120°C (pretreatment) and following pretreatment and vapor phase hydroformylation reactivity. These data show that the vast majority of the rhodium loss occurs during the pretreatment. Examination of the XPS/CA analyses shown in Table 12 provides insight to the fate of the rhodium. Initially, the superficial to bulk ratio of Rh/Si is 0.57. After carbonylation, one third of the rhodium is lost from the zeolite (1.20 to 0.80 wt% rhodium). Also note that the superficial to bulk Rh/Si ratio has increased to 1.01. These data indicate that during carbonylation rhodium migrates to the surface of the zeolite where it is lost into the flowing CO. Upon exposure to 33 hours of 1-hexene hydroformylation, the superficial to bulk Rh/Si ratio decreased to 0.26 while the bulk rhodium content remained essentially unchanged.

Rhodium carbonyls could be volatile at pretreatment and reaction conditions. If so, rhodium could be lost from the surface of the zeolite by sublimation as a carbonyl. At reaction conditions (150°C and 2 atms), rhodium carbonyls would be expected to sublime faster than at carbonylation conditions (120°C and 3 atms). Thus, during carbonylation rhodium could migrate to the surface and sublime as a carbonyl. This phenomena would account for the lowering of the bulk rhodium content and also the XPS/CA obtained at the end of carbonylation. At reaction conditions, rhodium may be sublimed faster than it can migrate to the surface and therefore the superficial to bulk Rh/Si ratio would be less than that obtained following carbonylation. Also, the migration of rhodium is probably greatly impaired by adsorbed reactants and products (vide infra).

Rode (25) has shown that rhodium may bond with CO to form a number of rhodium carbonyl species. In an attempt to identify the rhodium species which migrates from within the zeolite to the surface, an <u>in situ</u> FTIR experiment was performed. Spectra A shown in Figure 77 was obtained following 5 minutes of CO exposure[28], while spectra B was obtained following 24 hours of exposure. Only one rhodium carbonyl band was present, that being at 2020 cm^{-1}. This band was assigned to a monocarbonyl species and has not been previously identified by other investigators. If the

---

[28] 30 psig CO at 150°

rhodium species is a monocarbonyl, it is possible for it to diffuse through the 8-membered rings of Ca A.

Table 23 reports the reactivity of various RhCa A catalysts prepared by the "seed" technique and by addition of $RhCl_3$-$3H_2O$ to the synthesis gel. As this table shows, the catalysts prepared from the "seed" technique are more active, at equivilent loadings, than catalysts prepared by addition of $RhCl_3$-$3H_2O$ to the synthesis gel. The reason for the difference in reactivity of the two materials may be due to the nature of the rhodium associated with each catalyst. As previously discussed, the catalyst prepared by addition of $RhCl_3$-$3H_2O$ to the gel contained large particles of rhodium oxide in addition to the zeolite material. These particles are probably able to form rhodium carbonyls, however, the carbonyls will only form on the surface. This means that only a very small fraction of the rhodium associated with these particles will probably become active in the hydroformylation of 1-hexene. Therefore, in these cases there was less rhodium available to form active species than in the case of the catalyst prepared from the "seed" technique.

Regardless of the method of preparation, the activity appears to have increased with an increase in the rhodium loading, with the exception of the very low loaded (0.0024 and 0.08 wt%) RhCa A prepared from the "seed" technique. It was previously shown that the catalytic activity observed under these conditions is the result of intrazeolitic rhodium leaching into solution. Based on this observartion, it appears that, with the

exception of the very low loaded materials, an increase in the catalyst rhodium content may lead to an increase in the rhodium elution.

In an effort to observe activity from intrazeolitic rhodium, the reaction temperature was raised to 120°C and the reactions were performed in the presence of 3-4 cm^3 cyclohexylmercaptan[29]. In addition, the reactant concentration was reduced to 0.1M with all other conditions remaining the same. Two RhCa A catalysts prepared from the "seed" technique (0.065 and 0.99 wt% rhodium) were investigated in this study. The vast difference in catalyst loadings would allow for observing the effects of catalyst loading on the reaction rate. For these cases, only one product was observed, that being heptanal. Conversions, however were very low; 0.87 and 1.46% respectively (see Tables 25 and 26). The fact that only heptanal appeared in the product indicates that it was produced from intrazeolitic rhodium. This is because the mercaptan poisons all solution and surface rhodium, and only heptanal can diffuse from the zeolite A structure.

Following reaction, the above catalysts were recovered from the reaction mixture and re-used an additional three times. As listed in Tables 25 and 26, neither catalyst loading or conversion varied significantly[30] after the first use. It should also be noted that the 0.065 wt% catalyst,

---

[29] Increasing the quantity of cyclohexylmercaptan did not effect the catalyst reactivity.

[30] The low reactivity increased the error associated with the reported conversion when compared to conversions above 10%.

which contained over 15 times less rhodium than the 0.99 wt% catalyst, yielded almost the same conversion per gram of zeolite as the higher loaded catalyst. The fact that the change in rhodium loading did not significantly alter the catalytic activity suggests that diffusion limitations may exist; 1.e. diffusion of 1-hexene into the zeolite or diffusion of aldehyde from the zeolite.

The rhodium loss at 120°C was greater than that observed at 50°C. It is of interest to note that the rhodium loss was not significant following the first usage. For the 0.99 wt% rhodium zeolite, a plot of rhodium loss versus usage is shown in Figure 76. The decrease in rhodium elution following the first use is more than likely due to the pores of the catalyst being filled with product and reactant.

VI.B.2 Ruthenium A Fischer-Tropsch Reactivity

The two ruthenium zeolite A materials whose synthesis have been discussed in section VI.A.2 were evaluated under Fischer-Tropsch reaction conditions. The focus of this study was not to design a Fischer-Tropsch catalyst, but rather to probe the RuCa A for metal position and possible migration, zeolite stability and catalytic activity.

Product selectivity observed over the course of the reaction will provide an indication of the metal position, metal migration and support stability. The analysis of the RuCa A prior to reactivity showed the ruthenium to be mainly intrazeolitic (see Table 18). Cyclic and branched hydrocarbons are not able to penetrate the pores of Ca A. Thus, the ap-

pearance of these hydrocarbons in the product stream would indicate that they are being formed via surface ruthenium or that the zeolite lattice has been altered such that it is no longer selective. It has been reported that straight chain hydrocarbons as large as n-tetradecane can be adsorbed into Ca A (47). Thus the appearance of long, straight chain hydrocarbons would not necessarily imply their formation via surface ruthenium.

The hydrocarbon start-up behavior for the two RuCa A materials are shown in Figures 80 (1.53 wt% Ru) and 83 (2.16 wt% Ru). In both cases the reaction pressure was 15 psig and the reaction temperature was 255°C. Notice from these figures that the production of C(n)[31] rapidly increases, followed by rapid decline. Also, note that the maximum rate of production of all hydrocarbons do not occur at the same time. For example, as shown in Figure 83, the maximum in the rate of C_3 production is observed at about 1.5 hours into the run, while the maximum in the rate of C_4 production occurs after approximately 3.5 hours. This behavior suggests that alterations in the catalyst are occurring with time.

Figures 81 and 85 show the hydrocarbon product distribution at various times for runs 9-21-85 (1.53 wt% Ru) and 9-26-85 (2.16 wt% Ru), respectively. These figures show that a log-normal behavior of the products is not followed. In no case were branched hydrocarbons or hydrocarbons of length C_7 or greater observed in the product stream. Notice also from

---

[31] This notation is used to signify hydrocarbon of length n.

these figures the shift towards the production of higher hydrocarbons with time.

The start-up behavior of these materials are quite unusual. A minimum of 6 hours was required for the steady-state product distribution to be achieved. Fe_2O_3 catalysts do require excessive start-up times, but this is due to the formation of iron carbides (160). Supported ruthenium, especially at differential conversions, require very short start-up times, usually 30 to 120 minutes (33,115,120,123,161) regardless whether a zeolite or non-zeolite support is employed. The catalyst used in run 9-21-85 required almost 12 hours to achieve the steady-state product distribution. The steady-state product distribution is defined as the selectivity of the catalyst which remained essentially constant, even though the catalytic activity did not.

The raising of the reaction temperature to 308°C and the pressure to 80 psig following 22 hrs at 255°C (run 9-21-85) resulted in the product distribution reported in Figure 82. As the figure shows, an initial hydrocarbon cut-off exists at C_6 which is consistent with the low temperature runs. Notice also that the product distribution did not change initially. Further into the run, longer chain hydrocarbons were observed (up to C_9). Also, note from this figure that the data can be described by two chain growth probabilities, one from C_3 to C_6 and the other from C_6 to C_8 (present at the intermediate times). At the end of the run, a log-normal behavior was followed, as is typical of ruthenium Fischer-Tropsch catalysts. This behavior again suggests that ruthenium metal has

migrated to the surface of the zeolite or a loss in the structure of the zeolite has occurred or both to a greater extent than observed at lower temperatures.

It is also of interest to note from the runs conducted at 255°C that methane was the only hydrocarbon observed over the first 20 to 30 minutes of reaction. Following this time, the rates of production of C_2 and C_3 were observed to quickly rise, proceed through a maximum, then decay according to a steady rate. As shown in Figure 80 (run 9-21-86, 1.53 wt% Ru), once the maximum in the rate of C_3 production was reached, the rate of C_4 production began to increase, proceed through a maximum, then decay at a steady rate consistent with methane, C_2 and C_3. Further into this run (approximately 9 hours) the rate of production of C_5 began to increase and appears to reach a maximum at about 12 hours into the run. It is also interesting to note from this plot that the rise in C_5 production does not appear to influence the steady rate of decay of the other hydrocarbon products. Run 9-26-85 displayed a similar behavior, with the maximums in rates of production occurring over a shorter time period (see Figure 83). Again, the rate of production of C_4 increases following the decline in the rates of C_2 and C_3 production. When the maximum rate of C_4 production is achieved, it quickly declines giving way to the production of C_5. For both these runs, the selectivity appears to be towards procuction of hydrocarbons of greater chain length. This behavior may be attributed to the sintering of ruthenium particles, as Nijs and Jacobs (109) have shown that metal particle size can greatly influence the selectivity in Fischer-Tropsch reactions.

Studies by Peter Jacobs and his co-workers (41,116,123,127) and others (115,120) conducted on zeolite Ru Y showed this catalyst to deviate from Schultz-Flory behavior; i.e. their hydrocarbon product distributions did not follow log-normal behavior. Log-normal behavior is typical of ruthenium supported catalysts, either zeolite or non-zeolite (10,33,161-163). In Jacobs' work, very small particles (10 to 15Å) of ruthenium, as measured by chemisorption (129) and temperature programmed oxidation (TPO) (41,123) were present. The size of these particles is larger than the α-cage of zeolite Y (11.8Å). When reacted at Fischer-Tropsch conditions, a sharp cut-off in production of hydrocarbons at C_9 existed. Here, we observed a cut-off at C_6. The results from Jacobs et al. suggest that they were observing selectivity enhancements from intrazeolitic ruthenium, and since the metal particles were larger than the α-cages, zeolite alterations were suspected. Examination of the zeolite Y by X-ray diffraction showed the zeolite to have remained crystalline (123). STEM analysis showed the contrary, as "holes" were present within the zeolite structure, with the center of each hole being occupied by small ruthenium particles.

In this study, X-ray diffraction analysis following reaction of both RuCA A catalysts showed no loss in crystallinity to have occurred over the course of the reaction. Examination of the catalyst purity by oxygen adsorption following run 9-21-85 showed a 22% loss in pore volume. This loss may be the result of hydrocarbons trapped within the structure, or

support degradation invisible to XRD. Analysis of zeolite A via STEM is impossible, as the electron beam will destroy the zeolite.

Figure 80 compares the FTIR spectra of RuCa A and RhCa A[32] following reduction and subsequent Fischer-Tropsch reaction to that of RuCa A (1.53 wt% Ru) prior to reaction. The spectra reported for RuCa A before reaction agrees well with the pattern of zeolite A reported by Flanigen et al. (60). No change in the IR spectrum was observed following reduction of this material by hydrogen. Note that important changes in the 800-650 cm^{-1} region have occurred following reaction of the 1.53 wt% RuCa A zeolite. In this region, the band at 658 decreases in intensity while the bands at 756 and 673 gain intensity. These alterations suggest that changes in the zeolite have occurred over the course of the reaction. These changes in the zeolite A structure may be due to the presence of "holes," similar to those observed by Jacobs. Note from the spectra of RhCa A that the intense band at 1011 has shifted to 987 cm^{-1}. Note also the absence of the band at 551 cm^{-1}, the appearance of the triplet at 737, 712 and 671 cm^{-1}, and the appearance of the bands at 468 and 438 cm^{-1}. This spectrum is not characteristic of zeolite A but is characteristic of sodalite (60). Thus, the exposure of the RhCa A to the reaction mixture at the previously stated conditions resulted in collapse of the α-cages, leaving only β-cages, which are the structure units of sodalite.

---

[32] Spectrum of 1.53 wt% RuCa A following run 9-21-85. Spectrum of 1.20 wt% RhCa A obtained following reduction at 275°C under 20 psig H_2 for 17 hours followed by exposure to 80 psig CO/H_2 (1/1)at 250°C for 17 hrs, 310°C for 12 hrs and 350°C for 12 hours.

Figure 78 compares the XPS spectra of the Ru3d(5/2) photoelectron region for the 2.16 wt% ruthenium catalyst in the as-synthesized form, following hydrogen reduction and following Fischer-Tropsch reaction (run 9-26-85). As the figure shows, the amount of ruthenium on the zeolite surface remained essentially unchanged following both reduction and reaction. This indicates that the intrazeolitic ruthenium did not migrate to the surface of the catalyst. Comparison of spectra A and B of this figure reveal that the binding energy of ruthenium has decreased approximately 1.5 to 2.0 eV. This decrease is due to the reduction of Ru(III) to Ru(0) via the hydrogen. Spectra C shows that the ruthenium remained in the reduced state over the course of the reaction. Since an increase in the ruthenium content at the surface of the zeolite did not occur, the change in selectivity observed over the course of these runs is not the result of ruthenium migrating to the zeolite surface.

Localized support degradation, leading to the formation of "holes" is postulated to be due to the metal reduction and the water formed by the reaction. The reduction of ruthenium in a zeolite proceeds by the following reaction (127):

$$Ru^{+3}(ZO^{-})_3 + (3/2)H_2 \text{ ===> } Ru^{0} + 3ZOH$$

where ZO^{-} refers to an anionic zeolite site and ZOH refers to the protonated form of this site. Thus, the reduction of ruthenium creates three acid sites. Breck notes for zeolite A (62) that the stability of the structure decreases drastically as the cationic radii of the

monovalent cation is decreased. He further notes the inability of the protonated zeolite to withstand water attack (93). Formation of acid sites by the reduction of ruthenium, followed by Fischer-Tropsch chemistry (forms water) in the neighborhood of the acid sites could result in destroying the structure, thus producing the "holes" like those observed by Jacobs (41,123,127).

Based on Jacobs' work, the formation of "holes" in the catalysts studied here seems likely. This is due to the fact that the structure stability of zeolite A is lower than that of the Y zeolite employed by Jacobs. Zeolite Y is more siliceous than zeolite A making it (zeolite Y) more stable to attack from water vapor.

Initially, 100% selectivity to methane was observed during the first 20-30 minutes of start-up. High selectivity to methane (95%) was observed by Jacobs (41,123) using a Ru_2La Y catalyst. The La served to stabilize the zeolite Y in order to minimize the production of "holes." He concluded from this study that the particles within the supercage of zeolite Y must be small and thus only produce methane. XPS analysis of the RuCa A following H_2 reduction (shown in Figure 78) indicates that the ruthenium did not migrate to the zeolite surface. Based on Jacobs' observation, the high initial selectivity towards methane observed here is believed to be due to reaction of CO/H_2 with very small metal particles present in the α-cage prior to the zeolite degradation.

The shift in selectivity away from methane after a few minutes into the run is more than likely due to localized zeolite degradation resulting from the water formed via the Fischer-Tropsch reaction. The degradation results in the formation of holes by which ruthenium particles in adjacent cages join, forming larger particles. The larger particles then alter the hydrocarbon selectivity towards the production of higher hydrocarbons, as postulated by several authors (109,115,120,123,127).

Nijs and Jacobs (109) have shown that any metal particle of a given size imposes a strict maximum upon the chain length of the hydrocarbon which can be formed upon it. This could be the reason for the cut-off at C_6 observed in these runs conducted at 255°C. The cut-off is felt to be due to a particle size effect rather than a molecular sieving effect. This reasoning is based on reports that hydrocarbons as large as n-tetradecane have been adsorbed into Ca A (58). Also, Eberley (163) has shown that n-hexane and n-heptane readily desorb from Ca A, with the desorption diffusion coefficient of n-hexane being about twice that of n-heptane at 93°C. Since the temperatures employed in this study were greater than those employed by Eberly, it is safe to assume that n-C_7 hydrocarbons would easily desorb from the catalysts.

In run 9-21-85, the ruthenium appears to sinter slower than in run 9-26-85 since greater times between the maximum rates of production of the various hydrocarbons of chain length n are observed in run 9-26-85. The lower metal loading of this material would lead to the formation of less acid sites causing the zeolite to be more stable to water attack.

It is interesting to note that for hydrocarbons other than methane, the 1.53 wt% RuCa A was 67% selective (wt basis) to C_3 over the 1 to 2 hour start-up interval (see Table 28).

The increase in reaction temperature and pressure (to 308°C and 80 psig) resulted in the product distribution following a log-normal behavior (illustrated in Figure 82). This behavior occurred well into the run, however. For this case, the IR spectra showed that the zeolite degradation was more severe than for the catalyst employed in run 9-26-86. This was more than likely due to the increased effects of water attack at the elevated temperature. Again, the XPS spectra indicated that the ruthenium did not migrate to the surface of the zeolite. The shift in selectivity observed here is more than likely the result of increased support degradation leading to the formation of larger metal particles. The $n\text{-}C_9^+$ hydrocarbons observed in this case can still diffuse from the RuCa A (58). These results indicate that there is an upper bound of temperature which limits the usefulness of this catalyst.

In summary, the start-up behavior of the RuCa A is believed to be due to metal sintering brought about by zeolite degradation. Localized zeolite degradation resulting in the formation of holes produced by the interaction of water with the acid sites (formed via ruthenium reduction), leads to the sintering of the ruthenium. The large particles form and give rise to a greater average hydrocarbon chain length with time on stream (Figures 81, 82 and 85).

It is also interesting to note that the data shown in Figure 82 can be represented by two growth probabilities, α, as reported in Table 30. Bell (10) also observed similar behavior using Ru/Al_2O_3 and attributed this to sampling artifacts, i.e. line condensation. His change in α occurred at C_{12}. Hydrocarbons present in this work were too light and in too small of quantity to condense in line. Jacobs and Wouwe (116) attributed the presence of two chain growth probabilities to a particle size effect. They indicated the existence of chain growth with a different α on a distinct set of sites. This may explain the change in growth probabilities observed here.

Fischer-Tropsch chemistry over metal catalysts yields predominantly α-olefins (10). Here, α-olefins of C_4 and greater were rarely observed. Whenever a hydrocarbon number was associated with the high growth probability ($\alpha > 0.7$), the predominant hydrocarbons were β-olefins. This behavior is best illustrated from the product distributions obtained during runs 9-21-85 at 308°C and 9-26-85 at 255°C, as reported in Tables 29 and 31. When the hydrocarbon number was associated with the low growth probability, it was exclusively (except during the transition region) a normal alkane. Internal olefins have usually been attributed to oligomerization and cracking/isomeration reactions. Zeolite A, with a Si/Al ratio of 1, is not a strong acid catalyst. It is not believed that internal olefins produced here resulted from reaction with an acid site, as it has been reported (41) that 1-decene is inert to reduced Ru Y at conditions more severe than those employed here. The formation of β-olefins must therefore be attributed to a chemical effect associated with

the intrazeolitic ruthenium. This observation is consistent with that of Smith et al. (37). In that study, rhodium carbonyls were sublimed onto alumina. This resulted in rhodium particle sizes of less than 20Å (38). The product distribution reported from this study is listed in Table 11. Note the large fraction of C_4 internal olefins.

VI.B.3 Cobalt ZSM-5 Fischer-Tropsch Reactivity

The cobalt ZSM-5 catalyst prepared from composition I with a Co/Si ratio of 0.0046 (see Table 21 for XPS analysis) was evaluated under Fischer-Tropsch reaction conditions. The behavior of this catalyst was compared to that of a cation exchanged Co/ZSM-5 prepared with a similar cobalt loading. As with the rutheniunm zeolite A catalysts discussed earlier, the focus of this study was to probe the Co/ZSM-5 for metal position, metal migration, and catalytic activity.

The Co/ZSM-5 catalyst prepared from composition I will be referred to as synthesized Co/ZSM-5 through the remainder of this section. The catalyst pretreatment involved first calcining the catalyst in air at 550°C so as to remove the orgainc cation. As the analysis in section VI.A.4 has shown, the calcination did not alter the superficial cobalt concentration. Following calcination, the catalyst was exposed to flowing hydrogen at 30 psig and 470°C for 21 hours. 1.60 g of this catalyst was then exposed to 10 ml/min (STP) flowing CO/H_2 (1/1) at the various reaction temperatures. This catalyst was essentially inactive at temperatures of 350°C and below. It was not until the reactor temperature was raised to 410°C that a detectable conversion was achieved. This be-

havior was unexpected since supported Co/ZSM-5 catalysts have been activated at or below 350°C (2,3,17,18,112,113). The reason why the synthesized Co/ZSM-5 catalyst could not be activated below 410°C will be discussed later.

Table 34 reports the catalytic activity of synthesized Co/ZSM-5 reacted at 410°C. As the table shows, all hydrocarbons detected in the product stream were alkanes, with no hydrocarbons greater than C_4 being observed. In this case, the cut-off at C_4 may be due to detection limits rather than to physical-chemical effects of the catalyst as the conversion was very low. It is interesting to note from this table that the ratio of CO_2 formed to CO reacted was 0.59. Also, only traces of water were detected in the product stream. These results may suggest that the water-gas-shift (WGS) reaction is very active at these conditions. Figure 88 shows a Flory plot of the data presented in Table 34. As the plot shows, a log-normal behavior is followed over the entire hydrocarbon product range. This product distribution is typical of Schultz-Flory kinetics. Figure 87 reports the catalytic activity (in terms of CO conversion) as a function of time on stream. As the figure shows, the activity decays slowly with time.

The temperature of the reactor was then increased to 470°C. The hydrocarbon product distribution obtained after five hours at 470°C is reported in Table 35. As the table shows, the majority of the hydrocarbon production (92.13 wt%) was methane, ethane or propane. Traces of butanes, along with small quantities of toluene and C_8 hydrocarbons constituted the remainder to the hydrocarbon fraction. Toluene and the C_8 fraction

may have been formed via dehydrogenation/oligomerization reactions occurring over the acid sites. The acid sites on the ZSM-5 may dehydrogenate the alkane, followed by oligomerization of the resulting alkene. Garwood (8) has shown that light olefins may readily undergo oligomerization to higher order hydrocarbons over ZSM-5 at temperatures as low as 250°C and atmospheric pressure. Although no light olefins were observed in the product stream, they may have been formed by the cobalt only to have immediately undergone oligomerization. At this temperature, the ratio of CO_2 per mole CO reacted was 0.48, indicating that the WGS reaction may again be very active. As shown in Figure 90, a log-normal behavior was obtained for C_1-C_4 hydrocarbons. After reaction, the catalyst was a light brown color indicating that some coke formation had occurred.

Figure 89 shows a plot of CO conversion to hydrocarbons and to CO_2 as a function of time on stream at 470°C. As the figure shows, the conversion to hydrocarbons deactivates slowly while the decline in the rate of CO_2 production occurs at a slightly greater rate.

A reaction study was performed with the synthesized Co/ZSM-5 catalyst which had been washed with acid to remove any surface cobalt. This material possessed only slight traces of cobalt in the superficial region. Further analysis of this material showed the cobalt to be uniformly distributed among the crystals with no particles of cobalt oxide present. This catalyst was reacted in a similar manner as as the synthesized Co/ZSM-5 catalyst previously discussed. No conversion what-so-ever was

observed at temperatures of 425°C and 300 psig CO/H_2. Thus, it appears that the intrazeolitic cobalt associated with this catalyst is not active towards CO hydrogenation. This data may suggest that the trace reactivity observed in run 9-1-86 at 410°C may be due to small quantities of surface cobalt or the cobalt associated with the amorphous oxide particles.

The cation exchanged cobalt ZSM-5 catalyst was first calcined in air at 550°C followed by exposure to 30 psig H_2 at 470°C. This pretreatment is similar to that of the synthesized Co/ZSM-5 catalyst. Upon exposure to syn-gas, the cation exchanged catalyst yielded only trace conversion at 300°C. Upon raising the reaction temperature to 350°C, approximately 0.45% conversion of carbon monoxide was obtained, with 30% of the CO being reacted to CO_2 This compared with a conversion of less than 0.05% for the synthesized Co/ZSM-5 at the same conditions.

Table 36 reports the CO hydrogenation activity of cation exchanged Co/ZSM-5 reacted at 410°C. As the data shows, the light hydrocarbon fraction (C_1-C_5) consists exclusively of alkanes. Unlike the synthesized Co/ZSM-5, larger hydrocarbons, up to C_{10}, were also observed. The presence of the larger hydrocarbons more than likely resulted from the acid properties of the ZSM-5 support as previously discussed. For this catalyst, note that the percentage of CO_2 in the product fraction was much less than that of synthesized CO/ZSM-5 (23% as opposed to 59%). This may indicate that the activity of this catalyst towards the WGS reaction was less than that of the synthesized Co/ZSM-5 catalyst. A proper comparison between the activities of these two catalysts cannot be made, however,

due to the differences in the level of conversion. When compared to the synthesized Co/ZSM-5 catalyst reacted at this temperature, the ion exchanged Co/ZSM-5 was almost eight times more reactive towards the production of hydrocarbons than the synthesized Co/ZSM-5.

Figure 91 reports a Flory weight distribution for the data presented in Table 36. As the figure shows, a log-normal behavior is not followed, as a greater than expected fraction of C_8, C_9 and C_{10} hydrocarbons are present. This behavior could be due to the coupling of the Fischer-Tropsch properties of the cobalt with the oligomerization properties of the ZSM-5. This behavior has been well documented by Dodwell (9).

The temperature of the reaction was then raised to 470°C with the other conditions remaining constant. The hydrocarbon product distribution obtained at this temperature is reported in Table 37. A product distribution similar to that reported in Table 36 was obtained. Note that increasing the temperature resulted in increasing the ratio of CO_2 formed to CO reacted from 0.23 to 0.33. This is more than likely the result of the WGS reaction becoming more active as the temperature is increased. At this temperature, the cation exchanged Co/ZSM-5 was approximately five times more active towards the formation of hydrocarbons than the synthesized Co/ZSM-5. Visual examination of this catalyst following the reaction showed it to be heavily coked, as evidenced by the pitch black color.

The low reactivity of the cation exchanged Co/ZSM-5 may be the result of a finely dispersed cobalt phase brought about by the low cobalt loading. This is based on studies by Fu and Bartholomew (11) and Reuel and Bartholomew (34) who have shown the activity of Co/Al_2O_3 catalyst (as measured in terms of moles CO reacted per mole Co per unit time) to decrease drastically as the cobalt loading is decreased. Their study also noted that the cobalt particle size decreased with a decrease in cobalt loading. This lead the authors to conclude that the CO hydrogenation activity of Co/Al_2O_3 is dependent upon the cobalt particle size. Reuel and Bartholomew (34) have shown that low loaded, highly dispersed Co/Al_2O_3 catalysts require temperatures in excess of 400°C to activate. The low activity of the Co/ZSM-5 prepared by cation exchange and the synthesized Co/ZSM-5 observed in this study may be the result of this effect.

Figure 86 shows the XPS spectra of the Co2p(3/2,1/2) photoelectron region of the Co/ZSM-5[33] synthesized from the amorphous seed material, following hydrogen exposure[34] and following exposure to CO/H_2 (run 9-1-85). The peak present at 768.5 eV is the O(KVV) auger line. The intensity of this line may be used as a reference as to the relative intensity of the cobalt 2p(3/2) peak. This is because the O(KVV) intensity will be proportional to the intensity of the oxygen photoelectron peak, which is directly related by stoichiometry to the silcon photoelectron

---

[33] For XPS and chemical analysis, see Table 21, composition I, Co/Si=0.0048.

[34] 450°C under 30 psig H_2 for 17 hours.

peak. This figure indicates that the amount of cobalt in the superficial region has not been altered by the various treatments, as the relative intensities of the Co2p(3/2) peak to the O(KVV) peak has remained essentially constant. The slight loss in intensity of the Co2p(3/2) peak observed following reaction exposure may be due to carboneous deposits present at the zeolite surface. Thus, it does not appear that intrazeolitic cobalt migrated to the surface of the zeolite following the different exposures. Chemical analysis of this catalyst following reaction showed no cobalt to have been lost during the reaction to within experimental error.

Figure 86 yields further information regarding the chemical state of the cobalt following the various exposures. As the spectra for the synthesized Co/ZSM-5 shows, the cobalt appears to be in the +2 oxidation state (2,3). Following exposure to hydrogen, the color of the catalyst changed from powder blue to a clear white. The clear white color is indicative of cobalt metal (157). However, the XPS spectra of this material indicates otherwise, as no change in the binding energy of the Co2p(3/2) peak is observed. Cobalt metal displays a photoelectron peak at approximately 778.4 eV (2,3). Therefore, if any of the cobalt was reduced, the XPS spectra would clearly show this shift. Following exposure of this material to the reaction environment, the majority of the cobalt has remained in the +2 oxidation state. It does not appear from this spectrum that a significant quantity of cobalt had been reduced.

The information in Figure 86 is consistent with that reported by Rao (2) and Stencel et al. (3) for a 1.20 wt% Co/ZSM-5. Their catalyst was prepared by ion exchange of Co/ZSM-5 with $CoCl_2$-$6H_2O$ followed by extensive washing to remove any surface cobalt. Similar to the results obtained here, their catalyst could not be reduced by exposure to 300 psig H_2 at 450°C for 24 hours. Stencel et al. (3) concluded that cobalt located within ZSM-5 could not be reduced due to strong interactions with the zeolite. Reuel and Bartholomew (34) have reported that poorly reduced cobalt catalysts are very selective towards the WGS reaction. This may explain the high yield of CO_2 produced from the synthesized Co/ZSM-5 catalyst.

Reuel and Bartholomew (43) and Fu and Bartholomew (11) have shown that the activity of supported cobalt catalysts decrease as dispersion is increased. Since the synthesized Co/ZSM-5 was inactive towards the Fischer-Tropsch reaction, it appears that the cobalt associated with this material is highly dispersed.

Chin and Hercules (26) have reported that Co^{+2} in tetrahedral coordination cannot be reduced by hydrogen. Since no change in binding energy was observed following exposure of the synthesized Co/ZSM-5 to hydrogen at 450°C, the state of the cobalt associated with this material may be Co^{+2} in tetrahedral coordination. This may indicate that the Co^{+2} is associated with the zeolite framework. However, due to the small quantities of cobalt present in the sample, no physical evidence could be obtained to support the previous statement. The catalytic activity ob-

served may be the result of small quantities of reducable cobalt associated with the particles of cobalt oxide (see section VI.A.4).

VII CONCLUSIONS

1) The "seed" technique can be used to produce intrazeolitic rhodium and ruthenium within zeolite A and intrazeolitic cobalt within ZSM-5.

2) All the transition metal placed into the synthesis gel is recovered by the product crystal when the "seed" technique is employed.

3) In the case of Co/ZSM-5, the "seed" technique can be applied over a range of gel phase SiO_2/Al_2O_3 ratios.

4) High purity ZSM-5 may be grown in the presence of large quantities of either TEA or TMA. These cations are incorporated into the product crystal.

5) Intrazeolitic rhodium migrates to the external surface of zeolite A during hydroformylation at the conditions reported in the text.

6) Intrazeolitic rhodium can selectively hydroformylate 1-hexene to heptanal. However, the reactivity of this catalyst is very low.

7) Ruthenium does not migrate to the external surface of zeolite A during hydrogen exposure and subsequent contact with CO/H_2 (1/1) at the conditions given in the text.

8) Cobalt present within ZSM-5 does not migrate to the external surface when exposed to hydrogen and CO/H_2 (1/1).

9) Hydrogen will not reduce intrazeolitic cobalt (ZSM-5) at the conditions reported in text.

10) Cobalt is present within ZSM-5 in a highly oxidized environment.

VIII RECOMMENDATIONS

1) Investigate the influence of the composition of the amorphous "seed" material in an attempt to synthesize zeolite with a uniform metal distribution among the crystals.

2) Extend the "seed" technique to include additional transition metals. Also extend this technique to include additional zeolite systems.

3) Investigate the use of different forms of the transition metal species contained on the "seed" material.

4) Investigate the applications of high silica rhodium containing zeolite A analogs (e.g. NA, zeolite α, etc.) towards hydroformylation of olefins. These high silicon analogs will be more hydrophobic and thus will allow the aldehydes to diffuse from the zeolite more readily.

5) Employ a different reducing agent (e.g. Cd vapor) when reducing ruthenium zeolite A. Investigate the applications of this material as a Fischer-Tropsch catalyst. This will yield a more stable zeolite support.

6) Investigate the applications of high silica ruthenium containing analogs of zeolite A as a Fischer-Tropsch Catalyst. This will result in a more stable zeolite support.

7) Investigate Ru/ZSM-5 as a Fischer-Tropsch catalyst.

REFERENCES:

1) D. Breck; "Zeolite Molecular Sieves," Wiley, 492-497 (1974).

2) V. U. S. Rao; Physica Scripta; **T4**, 71 (1983).

3) J. M. Stencel, V.U. S. Rao, J. D. Diehl, K. H. Rhee, A. G. Dhere and R. J. DeAngelis; J. Catal., **84**, 109 (1983).

4) R. D. Shannon, J. C. Vedrine, C. Naccache and F. Lefebvre; J. Catal., **88**, 431 (1984).

5) F. Steinbach, J. Schutte, R. Krall, C. Minchev, V. Kanazrev and V. Penchev; in "Proceedings of the Sixth International Zeolite Conference," Butterworth, 417 (1984).

6) A. G. Dhere and R. J. Deangelis; J. Catal., **92**, 392 (1985).

7) C. Chang and J. Silvestri; J. Catal., **46**, 249 (1977).

8) W. E. Garwood; in "Intrazeolite Chemistry," ACS #218, 383 (1983).

9) G. Dodwell, "Bifunctional Transition Metal-Zeolite Catalyst for Synthesis Gas to Gasoline Conversion," Ph.D. Dissertation Worchester Polytechnic Institute, P. 331-347 (1984).

10) C. S. Kellner and A. T. Bell; J. Catal, **75**, 251 (1982).

11) L. Fu and C. H. Bartholomew; J. Catal., **92**, 376 (1985).

12) P. Chu and F. G. Dwyer; in "Intrazeolite Chemistry," ACS #218, 59 (1983).

13) D. Breck; "Zeolite Molecular Sieves," Wiley, 537-540 (1974).

14) N. Y. Chen; U. S. Patent #3,373,110 assigned to Mobil Oil Corporation (1968).

15) N. Y. Chen and P. B. Weisz; Chem. Eng. Progr., SymSer., **63**, 86 (1967).

16) G. Keuhl; U. S. Patent #4,191,663 (1980).

17) T. Lin; "Zeolite Supported Iron-Cobalt Catalyst for Fischer-Tropsch Synthesis," Ph.D. Dissertation, Northwestern University, (1985).

18) V. U. S. Rao, R. J. Gormley, R. R. Schehl, K. H. Rhee, R. D. Chi and G. Pantages;"Metal Zeolite Catalysis for the Conversion of Syn-Gas to Selected Hydrocarbon Products," U. S. Departent of Energy paper, (1981).

19) F. G. Dyer and W. E. Garwood; "Conversion of Syn-Gas to Olefins over Physical Mixture of High SiO2/Al2O3 ZSM-5 and Fe(K)," (1981).

20) T. Sano, K. O. Kabe, Y. Kohtoku, Y. Shimazaki, K. Saitot, H. Takaya and K. Bando; Zeolites, **5**, 194 (1985).

21) G. Dodwell, "Bifunctional Transition Metal-Zeolite Catalyst for Synthesis Gas to Gasoline Conversion," Ph.D. Dissertation Worchester Polytechnic Institute, P. 295-297 (1984).

22) L. A. Rankal and K. W. Valyocalk; US Patent # 4,388,285 assigned to Mobil Oil Corporation (1983).

23) I. Wender and P. Pino; "Organic Synthesis via Metal Carbonyls," Whiley, 45, (1977).

24) E. Mantovani, N. Pallaudino and A. Zanobi; J. Mol. Catal., **3**, p.285 (1977/78).

25) E. J. Rode;"Rhodium-Zeolite Hydroformylation of Proplyene," Ph.D. Dissertation, Virginia Tech, (1985).

26) J. Schnitzer; "Liquid Phase Hydroformylation by Zeolite Supported Rhodium," M.S. Thesis, Virginia Tech (1984).

27) M. E. Davis, J. Schnitzer and J. A. Rossin; J. Catal., in press.

28) N. Takahashi and M. Kobayashi; J. Catal., **85**, 89 (1984).

29) M. E. Davis, E. J. Rode, B. E. Hanson and D. Taylor; J. Catal., **86**, 67 (1984).

30) G. A. Huff; "Fischer-Tropsch Synthesis in a Slurry Reactor," Ph.D. Dissertation, Massachusetts Institute of Technology, 55-58.

31) P. J. Jacobs; "Catalysis by Zeolites," 293 (1980).

32) Y. Y. Shah and A. J. Perrotta; Ind. Chem. Prod. Res. Dev., **15**, 123 (1976).

33) M. A. Vannice; J. Catal, **37**, 449 (1975).

34) R. C. Reuel and C. H. Bartholomew; J. Catal, **85**,

78 (1984).

35) R. F. Probstein and R. E. Hicks; "Synthetic Fuels," McGraw-Hill, (1982).

36) D. L. King, J. A. Cusumano and R. L. Garten; Catal. Rev. - Sci. Eng., **23**, 233 (1981).

37) A. K. Smith, A. Theolier, J. M. Basset, R. Ugo, D. Commereuc and Y. Chaovin; J. Am. Chem. Soc., Chem. Commun., 2590 (1978).

38) A. Brenner; J. Am. Chem. Soc., Chem. Commun., P. 251 (1979).

39) D. Commereuc, Y. Chauvin, F. Hugues, J. M. Basset and D. Olivier; J. Am. Chem. Soc., Chem. Commun., 154 (1980).

40) D. Fraenkel and B. Gates; J. Am. Chem. Soc., Chem. Commun., 2478 (May 26,1980).

41) G. T. Kerr; Inorg. Chem.; **5**, p. 1537 (1966).

42) R. M. Barrer, J. W. Baynam, F. W. Bultitude and R. M. Meier; J. Chem Soc.; 195 (1959).

43) A. J. Regis, L. B. Sand, C. Calmon and M. E. Garwood; J. Am. Chem. Soc.; **64**, p. 1567 (1960).

44) G. T. Kerr; J. Phys. Chem., **70**, 1047 (1966).

45) J. Ciric; J. Coll. Int. Sci., **28**, 315 (1968).

46) R. M. Barrer and P. J. Denny; J. Chem. Soc.; 971 (1961).

47) R. W. Thompson and A. Dyer; Zeolites, **5**, 302 (1985).

48) D. Breck; "Zeolite Molecular Sieves," Wiley, 270-287 (1974).

49) J. A. Rossin and M. E. Davis; J. Am. Chem. Soc., Chem. Commun., in press.

50) J. A. Kostinko; in "Intrazeolite Chemistry," ACS #218, 3 (1983).

51) R. M. Barrer and E. A. D. White; J. Chem. Soc.; 1267 (1951).

52) R. M. Barrer and P. J. Denny; J. Chem. Soc., 983 (1961).

53) G. H. Keuhl; Inorg. Chem.; **10**, 2488, (1971).

54) D. Breck; "Zeolite Molecular Sieves," Wiley, 333-344 (1974).

55) T. B. Reed and D. W. Breck; J. Am. Chem. Soc.; **78**, 5972 (1956).

56) L. Broussard and D. P. Shoemaker; J. Am. Chem. Soc, **82**, 1041 (1960).

57) D. Breck; "Zeolite Molecular Sieves," Wiley, 83-89 (1974).

58) D. W. Breck, W. G. Eversole, R. M. Milton, T. B. Reed and L. T. Thomas; J. Am. Chem. Soc., **78**, P. 5963 (1956.

59) J. M. Bennett, C. S. Blackwell and D. E. Cox; ACS Sym. Series, **218**, 143 (1983).

60) E. M. Flanigen, H. Khatami and H. A. Szymanski; in "Molecular Seive Zeolites-I," Adv. Chem. Ser. 101, 201 (1971).

61) D. Breck; "Zeolite Molecular Sieves," Wiley, 454 (1974).

62) D. Breck; "Zeolite Molecular Sieve," Wiley, 492 (1974).

63) D. Breck; "Zeolite Molecular Sieve," Wiley, 571 (1974).

64) R. J. Argauer and G. R. Landolt; Us Patent #3,702,886 (1972).

65) R. Mostowicz and L. B. Sand; Zeolites, **2**, P. 143 (1982).

66) D. Breck; "Zeolite Molecular Sieves," Wiley, 353 (1974).

67) H. Nakamoto and H. Takahashi; Chem. Letts., 1739 (1981).

68) V. N. Romannikov, V. M. Mastinkhin, S. Hocevar and B. Drzaj; Zeolites, **3**, 311 (1983).

69) R. Mostowicz and L. B. Sand; Zeolites, **3**, 219 (1983).

70) H. Lermer, M. Draeger, J. Steffen and K. K. Unger; Zeolites, **5**, 131 (1985).

71) V. N. Romannikov, V. M. Mastikhin, S. Hocevar and B. Drzaj; Zeolites, **3**, 311 (1983).

72) M. Ghamami and L. B. Sand; Zeolites, **3**, 155 (1983).

73) L. Y. Hou and L. B. Sand; in "Proceedings of the Sixth International Zeolite Conference," Butterworth, P. 887 (1984)

74) E. C. Derouane, J. B. Nagy, Z. Gabelica and N. Blom; Zeolites, **2**, 299 (1982).

75) R. von Ballmoos, R. Gubser and W. M. Meier; in "Proceedings of the Sixth International Zeolite Conference," Butterworth, 803 (1984).

76) S. B. Kulkarni, V. P. Shiralkar, A. N. Kotashane, R. B. Borade and P. Ratnasamy; Zeolites, **2**, 313 (1982).

77) R. M. Lok, T. R. Cannon and C. A. Messina; Zeolites, **3**, 282 (1983)

78) H. Nakamoto and H. Takahashi; Chem. Letts., 169 (1981).

79) A. Nastro and L. B. Sand; Zeolites, **3**, 57 (1983).

80) A. Nastro, Z. Gabelica, P. Bodart and J. B. Nagy; in "Catalysis on the Energy Scene," Elsevier, 131 (1984).

81) E. M. Flanigen, J. M. Bennett, R. W. Grose, J. P. Cohen, R. L. patton, R. M. Kirchner and J. V. Smith; Nature, **271** 512 (1978).

82) G. Boxhoorn, O. Sudmeijer, P. H. G. vna Kasterem; J. Am. Chem. Soc., Chem. Commun., 1416 (1983).

83) C. J. Planlk, E. S. Rosinski and M. K Rubin; U. S. Patent # 4,175,114 (1979) assigned to Mobil Oil Cor

84) E. Narita, K. Sato and T. Okabe; Chem. Letts., 1056 (1984).

85) J. B. Nagy, Z. Gabelica and E. G. Dourane; Zeolites, **2**, 43 (1983).

86) G. Boxhoorn, R. A. van Santen, W. A. van Erp, G. R. Hays, R. Huis and D. Clague; J. Chem. Soc., Chem. Commun., 264 (1982).

87) K. F. M. G. J. Scholle, W. S. Veeman, P. Frenken and G. P. M. van der Velden; Appl. Catal., **17**, 233 (1985).

88) P. A. Jacobs, E. G. Derouane adn J. Weitkamp; Chem. Comm., 591 (1981).

89) B. T. Kokotailo, S. L. Lawton, D. H. Olson and W. M. Meier; Nature, **272**, 437 (1978).

90) D. G. Hay and H. Yaeger; J. Chem. Soc., Chem. Commun., 1433 (1984).

91) E. L. Wu, S. L. Lawton, D. H. Olson, A. C. Rohamn and G. T. Kokotailo; J. Phys. Chem., **83**, 2777 (1979).

92) H. Nakamoto and H. Takahashi; Chem. Letts., 1013 (1981).

93) C. E. Lyman, P. W. Betteridge and E. F. Moran; in "Intrazeolite Chemistry," ACS # 218 (1983).

94) K. Foger, J. V. Sanders and D. Seddon; Zeolites, **4**, 337 (1984).

95) D. H. Olson, W. O. Haag and R. M. Lago; J. Catal., **61**, 390 (1980).

96) G. Courdurier, C Naccache and J. C. Vedrine; J. Am. Chem. Soc., Chem. Commun., 1413 (1982).

97) F. J. Van der Gaag, J. C. Jansen and H van Belkum; Appl. Catal., **17**, 261 (1985).

98) S. Namba, N. Hosonuma and T. Yashima; J. Catal, **72**, 16 (1981).

99) H. Rastelli, B. M. Lok, J. A. Duisman, D. E. Earls and J. T. Mullhaupt; Can. J. of Chem. Eng., **60**, 44 (1982)

100) W. W. Kaeding, C. Chu, L. B. Young and S. A. Butter; J. Catal., **69**, 392 (1981).

101) P. Dejaifve, A. Auroux, P. Gravelle, J. Vedrine, Z. Gabelica and E. G. Derouane; J. Catal., **70**, 123 (1981).

102) A. W. Chester, Y. F. Chu, R. M. Dessau, G. T. Kerr and C. T. Kresge; J. Chem. Soc., Chem. Commun., 289 (1985).

103) P. Wu and T. H. Ma; in "Proceedings of the Sixth International Zeolite Conference," Butterworth, 251 (1984).

104) H. Arai and H. Tominaga; J. Catal., **75**, p. 188 (1982).

105) M. E. Davis, P. M. Buttler, J. A. Rossin, B. E. Hanson; J. Mol. Catal., **31**, 385 (1985).

106) Y. Amenomiya and G. Pleizer; J. Catal., **76**, 345 (1982).

107) M. Niwa and J. H. Lunsford; J. Catal., **75**, 302 (1982).

108) J. A. Amelse, L. H. Schwartz and J. B. Butt; J. Catal., **72**, 95 (1981).

109) H. H. Nijs and P. A. Jacobs; J. Catal, **65**, p. 328 (1980).

110) H. H. Nijs, P. A. Jacobs, J. J. Verdonck and J. B. Uytterhoeven; "Proceedings from the Fifth International Zeolite Conference," 633 (1981).

111) H. Arai, K. Mitsuishi and T. Seiyama; Chem. Letts., 1291 (1984).

112) V. U. S. Rao and R. J. Gormley; Hrdro. Proc. (Nov, 1980).

113) H. W. Pennline, V. U. S. Rao, R. J. Gromley and R. D Schehl; "Synthesis Gas Conversion with a Transition Metal-Zeolite Catalyst," Depatrment of Energy paper (1981).

114) S. L. Suib, K. C. McMahon, L. M. Tau and C. O. Bennett; J. Catal., **89**, 20 (1984).

115) I. R. Leith; J. Catal, **91**, 283 (1985).

116) P. A. Jascobs and D. van Wouwe; J. Mol. Catal, **17**, 145 (1982).

117) G. A. Huff; "Fischer-Tropsch Synthesis in a Slurry Reactor," Ph.D. Dissertation, Massachusetts Institute of Technology, 269-278.

118) G. A. Huff; "Fischer-Tropsch Synthesis in a Slurry Reactor," Ph.D. Dissertation, Massachusetts Institute of Technology (1982).

119) S. Novak, R. J. Madon and H. Shul; J. Catal, **77**, 141 (1982).

120) Y. W. Chen, H. T. Wang and J. G. Goodwin; J. Catal., **83**, 415 (1983).

121) C. S. Kellner and A. T. Bell; J. Catal, **70**, 418 (1981).

122) B. M. Harney and G. A. Mills; Hycarbon Proc., **67**, (Febuary, 1978).

123) H. H. Nijs, P. A. Jacobs, J. J. Verdonck and J. B. Uytterhoeven; "Proceedings from the Fifth International Zeolite Conference," 633 (1981).

124) F. Huges, B. Besson and J. M. Basset; J. Am. Chem. Soc., Chem. commun., 719 (1980).

125) R. C. Reuel and C. H. Bartholomew; J. Catal, **85**, 63 (1984).

126) R. L. Chin and D. M. Hercules; J. Phys. Chem.; **86**, 360 (1982).

127) J. J. Verdonck, P. A. Jacobs, M. Genet and G. Ponclet; J. Chem. Soc., Faraday I, **76**, 403 (1980).

128) H. Arai and H. Tominaga; J. Catal., **75**, 188 (1982).

129) Varian handbook

130) D. Breck; "Zeolite Molecular Sieves," Wiley, 133 (1974).

131) L. A. Pedersen and J. A. Lunsford; J. Catal., **61**, 39 (1980).

132) J. Dillard; "Surface Chemistry," class notes (11-21-84).

133) G. E. Lawson; "XPS Sensitivity Factors," Dept. Mat. Eng., Va. Tech (1984).

134) E. J. Rode; "Rhodium-Zeolite Hydroformylation of Proplyene," Ph.D. dissertation, Va Tech, 34 (1985).

135) C. D. Wagner, W. M. Riggs, L. E. Davis, J. F. Moulder and G. E. Mulilinberg; "Handbook of X-Ray Photoelectron Specroscopy," Perkin-Elmer Corp., 106 (1979).

136) E. M. Flanigen, H. Khatami and H. Szymanski; Adv. Chem. Series, **101**, 201 (1971).

137) F. Fajula, R. G. Anthony and J. H. Lunsford; J. Catal.; **73**, 237 (1982).

138) R. J. Davis, J. A. Rossin and M. E. Davis; J. Catal., Submitted (1985).

139) J. Ciric; J. Coll. Int. Sci., **28**, 315 (1968).

140) D. Breck; "Zeolite Molecular Sieves," Wiley, 276 (1974).

141) B. Subotic, I. Smit, O. Madzija and L. Sekovanic; Zeolites, **2**, 135 (1982).

142) H. Borer and W. M. Meier; Adv. Chem. Series, **101** 122 (1971).

143) S. L. T. Anderson, R. F. Howe; J. Catal., **71**, 233 (1981).

144) D. Breck; "Zeolite Molecular Sieve," Wiley, 373 (1974).

145) Rollman, L. D.; Advances in Chemistry Series #173, 387 (1979)

146) E. M. Flanigen; Pure and Applied Chem, **52**, 2192 (1980).

147) A. Erdam and L. B. Sand; J. Catal., **60**, 241 (1979).

148) R. Aiello and R. M. Barrer; J. Chem. Soc. (A), 1470 (1970).

149) M. L. Occelli, R. A. Innes, T. A. Apple and B. C. Gerstein; "Surface Properties of Offretite and ZSM-34 Zeolites," presented at the Sixth International Zeolite Conference (1983).

150) T. E. Whyte, E. L. Wu, G. T. Kerr and P. B. Venuto; J. Catal. **20**, 88 (1971).

151) M. L. Occelli and A. J. Perrotta; in "Intrazeolite Chemistry," ACS #218, 21 (1983).

152) R. W. Grose and E. M. Flanigen; U. S. Patent 4,257,885, (1981).

153) A. Paravar and D. Hayhurst; in "Proceedings of the Sixth International Zeolite Conference," Butterworth, 217 (1984).

154) F. A. Cotton and G. Wilkinson; "Advanced Inorganic Chemistry," John Whiley and Sons, 768 (1980), 4th ed.

155) F. A. Cotton and G. Wilkinson; "Advanced Inorganic Chemistry," John Whiley and Sons, 770 (1980), 4th ed.

156) F. A. Cotton and G. Wilkinson; "Advanced Inorganic Chemistry," John Whiley and Sons, 779 (1980), 4th ed.

157) F. A. Cotton and G. Wilkinson; "Advanced Inorganic Chemistry," John Whiley and Sons, 766 (1980), 4th ed.

158) J. Dwyer; Chem. Ind. (London), **7**, 258 (1984).

159) K. G. Allum, R. D. Hancock, I. V. Howell, T. E. Lester, S. McKenzie, R. C. Pitkethyl and P. J. Robinson; J. Catal., **43**, 331 (1976).

160) G. A. Huff; "Fischer-Tropsch Synthesis in a Slurry Reactor," Ph. D. Dissertation, Massachusetts Institute of Technology, 94 (1982).

161) R. D. Gonzalea and M. Hiroshi; J. Catal, **77**, 332 (1982).

162) T. Okuhara; Chem. Letts., 1491 (1984).

163) J. G. Eckerdt and A. T. Bell; J. Catal., **58**, 170 (1979).

164) P. E. Eberly; Ind. Eng. Chem, Prod. Res. Develop.,8, 140 (1969).

Appendix I: Atomic Absorption Analysis

Typical AA analysis: Cobalt ZSM-5 Solution Preparation

	Sample 1	Sample 2
Co/ZSM-5	0.0417 g	0.0257 g
HF solution	28.1758 g	27.9398 g

Note: Two samples of the same material were prepared so as to provide confidence in the analysis. The quantity of Co/ZSM-5 digested in the HF solution should be chosen so that the cobalt concentration falls within the instrument calibration range. In this case, the range of calibration is linear between 1 and 10 µg/L cobalt. The HF solution is approximately 1/3 HF (concentrated) and 2/3 distilled water.

Cobalt Solution Analysis

The calibration samples were prepared by diluting a 1000µg/ℓ cobalt solution (Aldrich) to the following concentrations with the HF solution prepared above.

Calibration Solution	µg/ℓ Coblat
Co-1	1.244
Co-2	4.454
Co-3	2.597
Co-4	6.887
Co-5	9.628

Instrumental Analysis

Wavelength:	240.7 nm
Spectral Band Path:	0.50 nm
Lamp Current:	9.0 Ma

Sample	Reading
Co-1	20.33
Co-2	69.33
Co-3	43.33
Co-4	102.33
Co-5	129.67
sample 1	95.33
sample 2	57.33

Note: reading is average of three readings

The readings from the calibration samples are then plotted as a function of µg/L cobalt (see Figure 95) and the points are joined by linear regression fit with a stright line. Points which appear to be out of place (Co-5 in this case) are not used in the linear regression model. For this case, the linear model was:

$$\mu g/L = 0.0693*(\text{reading}) - 0.2826$$
$$(r = 0.9989)$$

For sample 1, the cobalt concentration was 6.3238 µg/L. The density of the HF solution used to digest the zeolite was approximately one. Thus there were 0.1782 mg cobalt in the solution. The weight loading of the Co/ZSM-5 was obtained by dividing the grams of cobalt in the solution by the grams of Co/ZSM-5 in solution. In this case, the weight loading was 0.1782 mg Co/41.7 mg Co/ZSM-5, or 0.43 wt% cobalt. In this case, the sample analyzed had not been calcined; i.e. the sample still contained the organic cation. Previous TGA analysis has shown the ZSM-5 to be approximately 13 wt% organic cation (98). Thus, the cobalt loading of this particular ZSM-5 material was 0.49 wt%. Similar calculations for sample 2 produced a weight loading of the Co/ZSM-5 as 0.46 wt% cobalt. THese two analyses are in very good agreement, and are averaged together to determine the final cobalt loading, 0.475 in this case.

The cobalt to silicon ratio is determined by assuming the ZSM-5 to be pure SiO_2. The unit cell of ZSM-5 consists of 96 TO_2 units. Thus, based on the previous assumption, the unit cell molecular weight is 5760. For the 0.475 % cobalt material analyzed above, the number of cobalt atoms per unit cell is 0.4643. Dividing this number by 96 (number of T-atoms/unit cell) yields the Co/Si ratio of the sample, 0.0048 in this case. This is the value reported in Table 21 for Co/ZSM-5 synthesized from composition F.

The cobalt to silicon ratio could not be obtained directly due to the formation of volatile SiF_4.

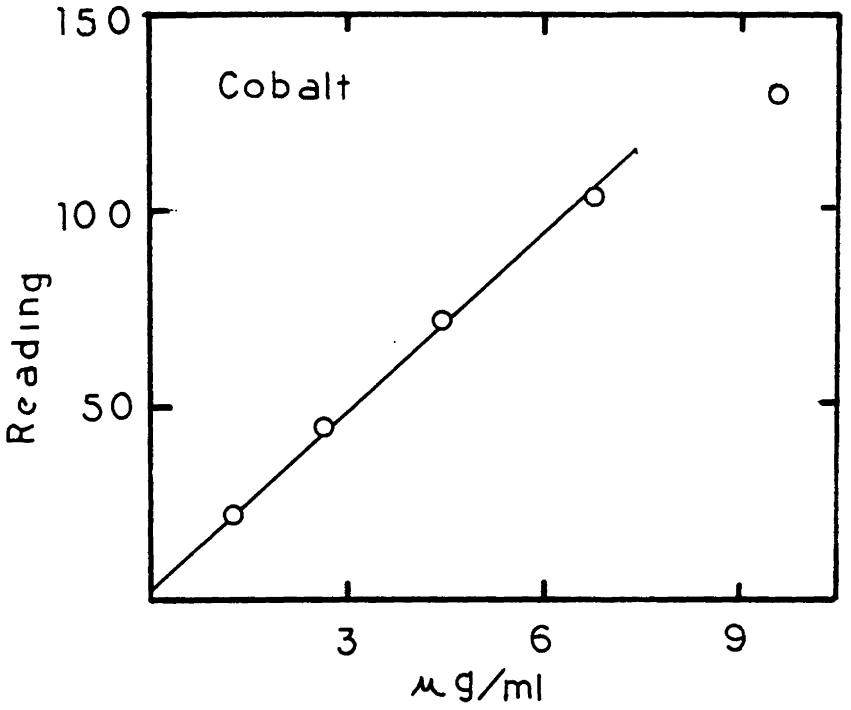

Figure 95: AA Calibration for Cobalt.

Rhodium Zeolite A Chemical Analysis

	Sample 1	Sample 2
RhNa A	0.0291 g	0.0268 g
HCl Solution	21.4876 g	17.5064 g

Note: Quanity of zeolite digested was chosen so as to provide optimal detection of Si, Al and Rh. The solution used to digest the zeolite was 1/3 HCl (conc) and 2/3 distilled water. For rhodium, the optimal detection range is 3 to 25 µg/ℓ while for silicon and aluminum, this range is from 200 to 750 moles silicon or aluminum per 10^6 moles water (ppm).

Calibration Solutions

Rhodium calibration solutions were prepared by dilution a 219 µg/ℓ rhodium solution prepared from $RhCl_3$-$3H_2O$ to the following concentrations. These solutions were approximately 7% HCl.

Calibration Solution	µg/ℓ Rhodium
Rh-1	4.478
Rh-2	7.004
Rh-3	10.434
Rh-4	17.503
Rh-5	19.966

The calibration solution for silicon and aluminum analyses contained both of these elements in 1/1 ratio. This was for the purpose of eliminating matrix effects. Ludox AS-40 and sodium aluminate were used in preparation of the standard solution. The standard solution was prepared by digesting the sodium aluminate in an equal portion of sodium hydroxide. The standard solution was 607 ppm silicon and 610 ppm aluminum and was diluted to the following concentrations:

Calibration Solution	Si (ppm)	Al (ppm)
Si/Al-1	216.4	217.4
Si/Al-2	291.2	292.6
Si/Al-3	405.0	407.0
Si/Al-4	471.7	474.0
Si/Al-5	607.0	610.0

Rhodium Analysis

Solution	Reading
Rh-1	39.6
Rh-2	53.4
Rh-3	71.6
Rh-4	127.8
Rh-5	155.0
Sample-1	185.8
Sample-2	191.4

These readings are plotted in Figure 96A versus µg/ℓ rhodium. These points were fit to the equation:

$$\mu g/\ell = 0.1334R - 0.0585 \qquad r=0.9940$$

Following calculations similar to those for Co/ZSM-5, the samples were found to be 1.83 and 1.66 wt% rhodium (by wt.)

Silicon and Aluminum Analyses

Solution	Reading (Si)	Reading (Al)
Si/Al-1	116.3	184.5
Si/Al-2	156.7	227.0
Si/Al-3	211.2	275.7
Si/Al-4	246.7	294.0
Si/Al-5	315.0	350.0
Sample-1	99.5	128.0
Sample-2	116.7	146.7

Silicon and aluminum calibration curves are shown in Figure 96B and C. These curves were fit to the following equations:

Silicon: $ppm = 1.9744(R) - 14.76$

Aluminum: $ppm = 1.2558(R) - 2.2544$

The aluminum calibration used the zero, Si/Al-1 and Si/Al-2 points only due to the detection range. The sample analysis, presented in ppm, are listed below:

	Rhodium	Silicon	Aluminum
Sample-1	4.32	181.7	158.7
Sample-2	4.45	215.8	182.3

The weight percent rhodium was then calculated from the unit cell composition for zeolite A: $12Na[(SiO_2)_{12}(AlO_2)_{12}]\text{-}27H_2O$. The unit cell molecular weight is 2190. For sample 1, the Rh/(Si+Al) ratio was calculated to be 0.0127. There are 24 T-atoms per unit cell, therefore, 0.3048 rhodium atoms are present per unit cell also. The molecular weight of rhodium per unit cell is 31.37, the weight percent rhodium is obtained

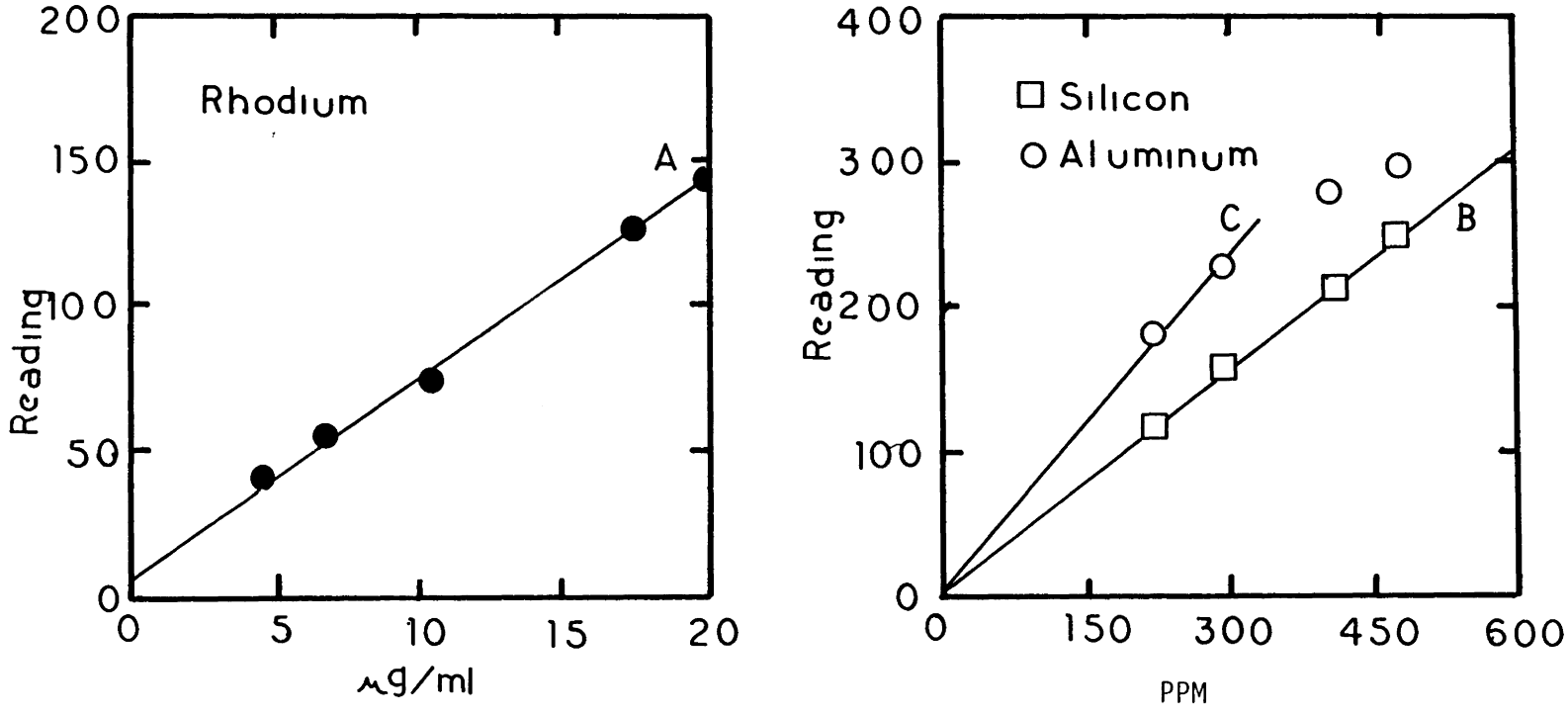

Figure 96: AA Calibration for (A) Rhodium; (B) Silicon and (C) Aluminum.

by dividing this value by the molecular weight of the unit cell. In this case, the sample is 1.46 wt% Rh. A similar calculation for sample-2 yields 1.28 wt% rhodium. These four values of rhodium loading (these two plus the two based on the weight of material dissolved) are averaged together. This material is 1.56 wt% rhodium. This is the chemical analysis for composition 2-10-84, as reported in Appendix II.

Appendix II: Rhodium A Compositions, "Seed" Technique

Batch 7-22-84A

Sodium silicate	2.438g	
Rh A seed	0.049g	(3.76 wt% Rh)
Water	10 ml	
Sodium aluminate	1.252g	
Sodium hydroxide	0.500g	
Water	8 ml	

3.54 Na_2O-Al_2O_3-2.0 SiO_2-186 H_2O-0.0035 Rh

Rhodium loading: 0.093 wt% Rh

Batch 7-24-84

Sodium silicate	2.880g	
Rh A seed	0.157g	(3.76 wt% Rh)
Water	12.197g	
Sodium aluminate	1.479g	
Sodium hydroxide	0.610g	
Water	10.057g	

3.56 Na_2O-Al_2O_3-2.0 SiO_2-192 H_2O-0.0085 Rh

Rhodium loading: 0.295 wt% Rh

Chemical Analysis:

Si/Al	Rh/Al	Rh/Si	Rh/(Si+Al)	WT%(CA)	Wt%(wt)
1.01	0.0051	0.0049	0.0025	0.29	0.30

Wt%(CA) is defined as weight percent rhodium as determined from the atomic ratios and unit cell composition of zeolite A, as discussed in Appendix I. Wt%(wt) is defined as weight percent rhodium as determined from the rhodium analysis and amount of sample digested.

Batch 7-22-84B

Sodium silicate	2.446g	
Rh A seed	0.218g	(3.76 wt% Rh)
Water	15.764g	
Sodium aluminate	1.269g	
Sodium hydroxide	0.583g	
Water	3.008g	

3.63 Na_2O-Al_2O_3-2.0 SiO_2-189 H_2O-0.0137 Rh

Rhodium loading: 0.335 wt% Rh

Chemical Analysis:

Si/Al	Rh/Al	Rh/Si	Rh/(Si+Al)	WT%(CA)	Wt%(wt)
1.17	0.0063	0.0054	0.0029	0.33	0.34

Batch 7-15-84

Sodium silicate	3.836g	
Rh A seed	0.279g	(3.76 wt% Rh)
Water	16 ml	
Sodium aluminate	1.969g	
Sodium hydroxide	0.796g	
Water	11.5 ml	

3.55 Na_2O-Al_2O_3-2.0 SiO_2-185 H_2O-0.0113 Rh

Rhodium loading: 0.372 wt% Rh

Time	Temperature	Crystallinity (%)
1:25 hrs	93 C	Trace
1:45	94	21
2:20	94	77
3:55	94	100
26:25	93	100

Chemical Analysis:

Si/Al	Rh/Al	Rh/Si	Rh/(Si+Al)	WT%(CA)	Wt%(wt)
1.28	0.0071	0.0031	0.0036	0.36	0.38

Batch 7-16-84

Sodium silicate	3.591g	
Rh A seed	0.786g	(3.76 wt% Rh)
Water	15 ml	
Sodium aluminate	1.839g	
Sodium hydroxide	0.764g	
Water	11 ml	

3.57 Na_2O-Al_2O_3-2.0 SiO_2-187 H_2O-0.0340 Rh

Rhodium loading: 0.835 wt% Rh

Time	Temperature	Crystallinity (%)
1:25 hrs	92 C	7
1:55	93	23
2:45	95	100
5:30	95	100
23:05	95	100

Chemical Analysis:

Si/Al	Rh/Al	Rh/Si	Rh/(Si+Al)	WT%(CA)	Wt%(wt)
1.25	0.0164	0.0131	0.0073	0.84	0.83

Batch 8-19-84

Sodium silicate	3.490g	
Rh A seed	0.863g	(3.76 wt% Rh)
Water	15 ml	
Sodium aluminate	1.248g	
Sodium hydroxide	0.505g	
Water	10 ml	

3.57 Na_2O-Al_2O_3-2.0 SiO_2-187 H_2O-0.0387 Rh

Rhodium loading: 0.955 wt% Rh

	90°	30°	10°
Rh/Si	0.0201	0.0170	---
Rh/Al	0.167	0.0180	---
Rh/(Si+Al)	0.0091	0.0086	---
Rh/O	0.0057	0.0056	---
(Si+Al)/O	0.63	0.64	0.56
Si/Al	0.83	1.06	1.04
Ca/Al	0.33	0.40	0.40

Chemical Analysis:

Si/Al	Rh/Al	Rh/Si	Rh/(Si+Al)	WT%(CA)	Wt%(wt)
1.16	0.0177	0.0153	0.0082	0.94	0.97

Batch 7-09-84 Zeolite A

Sodium silicate	4.875g	
Water	20 ml	
Sodium aluminate	2.502g	
Sodium hydroxide	1.011g	
Water	15 ml	

3.50 Na_2O-Al_2O_3-2.0 SiO_2-185 H_2O

Time	Temperature	Crystallinity (%)
0:50 hrs	90 C	-0-
1:45	92	trace
2:35	94	15
3:50	95	100
5:05	95	100
24:20	95	88

Batch 10-14-84 Zeolite A with Agitation

Sodium silicate	1.043g
Rh A Seed	0.551g
Water	18 ml
Sodium aluminate	0.539g
Sodium hydroxide	0.250g
Water	3.757g

3.63 Na_2O-Al_2O_3-2.0 SiO_2-225 H_2O-0.0590 Rh

Rhodium loading: 1.32 wt% Rh

XPS Analysis:

Rh/Si	0.0259
Rh/Al	0.0266
Rh/(Si+Al)	0.0131
(Si+Al)/O	0.54
Si/Al	0.97
Ca/Al	0.24

Chemical Analysis:

Si/Al	Rh/Al	Rh/Si	Rh/(Si+Al)
1.16	0.0248	0.0214	0.0115

Rhodium A Compositions, "Seed" Technique with Variable Seed Loading

Batch 12-15-85A

Sodium silicate	3.504g	
Rh A seed	0.802g	(2.50 wt% Rh)
Water	15 ml	
Sodium aluminate	1.793g	
Sodium hydroxide	0.744g	
Water	10 ml	

3.57 Na_2O-Al_2O_3-2.0 SiO_2-184 H_2O-0.0237 Rh

Rhodium loading: 0.80 wt% Rh

Time	Crystallinity (%)
1:00 hrs	10
1:45	28
2:30	62
23:15	100

Chemical Analysis:

Si/Al	Rh/Al	Rh/Si	Rh/(Si+Al)	WT%(CA)	Wt%(wt)
1.03	0.0122	0.0124	0.0061	0.70	0.89

Batch 12-15-84B

Sodium silicate	3.501g	
Rh A seed	0.808g	(1.25 wt% Rh)
Water	15 ml	
Sodium aluminate	1.785g	
Sodium hydroxide	0.751g	
Water	10 ml	

$$3.57\ Na_2O\text{-}Al_2O_3\text{-}2.0\ SiO_2\text{-}185\ H_2O\text{-}0.0122\ Rh$$

Rhodium loading: 0.37 wt% Rh

Time	Crystallinity (%)
1:00 hrs	15
1:45	29
2:15	34
22:45	100

Chemical Analysis:

Si/Al	Rh/Al	Rh/Si	Rh/(Si+Al)	WT%(CA)	Wt%(wt)
0.96	0.0063	0.0066	0.0032	0.37	0.37

Batch 12-12-84

Sodium silicate	3.515g	
Rh A seed	0.813g	(3.25 wt% Rh)
Water	15 ml	
Sodium aluminate	1.791g	
Sodium hydroxide	0.758g	
Water	10 ml	

3.58 Na_2O-Al_2O_3-2.0 SiO_2-185 H_2O-0.0313 Rh

Rhodium loading: 0.84 wt% Rh

Time	Crystallinity (%)
1:00 hrs	10
1:45	55
2:30	83
5:15	100
21:45	100

Chemical Analysis:

Si/Al	Rh/Al	Rh/Si	Rh/(Si+Al)	WT%(CA)	Wt%(wt)
1.01	0.0141	0.0140	0.0070	0.80	0.87

Batch 12-10-84

Sodium silicate	3.500g	
Rh A seed	0.796g	(5.25 wt% Rh)
Water	15 ml	
Sodium aluminate	1.790g	
Sodium hydroxide	0.757g	
Water	10 ml	

3.58 Na_2O-Al_2O_3-2.0 SiO_2-185 H_2O-0.0525 Rh

Rhodium loading: 1.55 wt% Rh

Time	Crystallinity (%)
1:00 hrs	10
1:45	17
2:30	86
5:15	100
23:00	100

Chemical Analysis:

Si/Al	Rh/Al	Rh/Si	Rh/(Si+Al)	WT%(CA)	Wt%(wt)
1.14	0.02372	0.0238	0.0127	1.46	1.83
1.18	0.0244	0.0206	0.0112	1.28	1.66

Appendix III: Rhodium A compositions, $CoCl_2$-$6H_2O$

Batch 7-11-84

Sodium silicate	6.314g
$RhCl_3$-$3H_2O$	0.0047g
Water	26 ml
Sodium aluminate	3.239g
Sodium hydroxide	1.282g
Water	19 ml

3.54 Na_2O-Al_2O_3-2.0 SiO_2-187 H_2O-0.0013 Rh

Rhodium loading: 0.06 wt% Rh

Time	Temperature	Crystallinity (%)
1:40 hrs	93 C	0
2:50	95	20
3:35	92	100
4:20	95	100
6:00	95	100
24:00	95	100

Batch 7-12-84

Sodium silicate	5.576g
$RhCl_3$-$3H_2O$	0.0207g
Water	23 ml
Sodium aluminate	2.870g
Sodium hydroxide	1.106g
Water	16.5 ml

3.53 Na_2O-Al_2O_3-2.0 SiO_2-183 H_2O-0.0063 Rh

Rhodium loading: 0.24 wt% Rh

Time	Temperature	Crystallinity (%)
1:40 hrs	94 C	0
2:25	93	6
3:40	93	86
4:40	94	100
6:45	93	100
24:00	95	76

Chemical Analysis:

Si/Al	Rh/Al	Rh/Si	Rh/(Si+Al)	WT%(CA)	Wt%(wt)
1.20	0.0047	0.0039	0.0021	0.24	0.23

Batch 7-13-84

Sodium silicate	5.238g
$RhCl_3$-$3H_2O$	0.0973g
Water	22.5 ml
Sodium aluminate	2.695g
Sodium hydroxide	1.021g
Water	16 ml

3.52 Na_2O-Al_2O_3-2.0 SiO_2-188 H_2O-0.0315 Rh

Rhodium loading: 1.06 wt% Rh

Time	Temperature	Crystallinity (%)
1:35 hrs	94 C	0
2:35	93	27
3:35	93	100
4:35	94	100
51:35	95	91

Chemical Analysis:

Si/Al	Rh/Al	Rh/Si	Rh/(Si+Al)	WT%(CA)	Wt%(wt)
1.32	0.0219	0.0165	0.0094	1.08	1.04

Batch 8-19-84

Sodium silicate	2.441g
$RhCl_3$-$3H_2O$	0.0570g
Water	15 ml
Sodium aluminate	1.250g
Sodium hydroxide	1.164g
Water	10 ml

3.55 Na_2O-Al_2O_3-2.0 SiO_2-187 H_2O-0.0382 Rh

Rhodium loading: 1.41 wt% Rh

	XPS Analyses		
	90°	30°	10°
Rh/Si	0.0866	0.1056	0.029
Rh/Al	0.1144	0.1256	0.045
Rh/(Si+Al)	0.0493	0.0571	0.018
Rh/O	0.0203	0.0241	0.009
(Si+Al)/O	0.4668	0.4221	0.487
Si/Al	1.32	1.20	1.54
Ca/Al	0.216	0.195	0.182

Chemical Analysis:

Si/Al	Rh/Al	Rh/Si	Rh/(Si+Al)	WT%(CA)	Wt%(wt)
1.12	0.0259	0.0231	0.0122	1.40	1.56
1.20	0.0252	0.0210	0.0115	1.31	1.38

Batch 7-20-84

Sodium silicate	3.009g
$RhCl_3$-$3H_2O$	0.450g
Water	14.5 ml
Sodium aluminate	1.538g
Sodium hydroxide	0.639g
Water	9.5 ml

3.57 Na_2O-Al_2O_3-2.0 SiO_2-204 H_2O-0.2560 Rh

Rhodium loading: 8.39 wt% Rh

Time	Temperature	Crystallinity (%)
3:00 hrs	96 C	21
3:30	95	67
3:55	93	70
4:35	94	61
25:05	95	77

Chemical Analysis:

Si/Al	Rh/Al	Rh/Si	Rh/(Si+Al)	WT%(CA)	Wt%(wt)
1.87	0.231	0.125	0.0815	n/a	8.39

Batch 8-15-84A

Sodium silicate	2.500g
$RhCl_3$-$3H_2O$	0.0300g
Water	10.778g
Sodium aluminate	1.296g
Sodium hydroxide	0.523g
Water	7.638ml

3.55 Na_2O-Al_2O_3-2.0 SiO_2-285 H_2O-0.0194 Rh

Rhodium loading: 0.71 wt% Rh

Batch 9-25-84 Zeolite A: Blank Seed and Rhodium Trichloride

Sodium silicate	3.033g
$RhCl_3$-$3H_2O$	0.1020g
Seed (blank)	0.771
Water	18 ml
Sodium aluminate	1.565g
Sodium hydroxide	0.649g
Water	11 ml

3.57 Na_2O-Al_2O_3-2.0 SiO_2-227 H_2O-0.0570 Rh

Rhodium loading: 1.19 wt% Rh

XPS Analysis

Rh/Si	0.114
Rh/Al	0.066
Rh/(Si+Al)	0.042
Rh/O	0.082
(Si+Al)/O	0.66
Si/Al	0.62
Ca/Al	0.24

Chemical Analysis:

Si/Al	Rh/Al	Rh/Si	Rh/(Si+Al)	WT%(CA)	Wt%(wt)
0.91	0.0170	0.0188	0.0089	1.02	1.20
0.82	0.0203	0.0247	0.0112	1.28	1.25

Appendix IV: Synthesis of Ruthenium Zeolite A

Batch 9-17-85

Sodium silicate	4.275 g
Ru amorphous	0.5577 g
Water	20 ml
Sodium aluminate	2.190 g
Sodium hydroxide	2.578 g
Water	15 ml

$$4.60\ Na_2O\text{-}Al_2O_3\text{-}2.0\ SiO_2\text{-}185\ H_2O$$

Rhodium loading: 1.53 wt% Rh

Notes: Small trace of ruthenium amorphous clumps present. Crystals removed following 7 hours at 100°C. Crystallization performed in teflon jar under agitation (hot plate as heating source). This material was exchanged into the calcium form and employed in Run 9-21-85. The XPS and chemical analysis data are presented in Table 4.

Batch 9-24-85

Sodium silicate	17.317g	
Water	70 ml	
Sodium aluminate	8.859g	
Ru A seed	5.015g	(9-24-85)
Sodium hydroxide	3.289g	
Water	60 ml	

$$3.51\ Na_2O\text{-}Al_2O_3\text{-}2.0\ SiO_2\text{-}193\ H_2O$$

Rhodium loading: 2.16 wt% Rh (calcium form)

Notes: Gel added to 200 ml teflon jar and placed in oven at 97°C. Removed following 11 hours. The aqueous layer above the gel appeared clear, indicating all ruthenium in gell associated with product zeolite. Product washed through filtration with 2.4ℓ of distilled water. The amorphous seed material could not be digested for chemical analysis.

This material was calcium exchanged by adding 5.50 g $CaCl_2$ to 1ℓ flask so as to produce 0.1N Ca soution. Zeolite removed from this solution following 7 hours of exchange. A second exchange was performed with a 0.1 N Ca solution. This exchange lasted 16 hours. Following this, a third exchange was performed for 7 hours. Following the three exchanges, the zeolite was washed through filtration with four liters of distilled water. The resulting catalyst was employed in run 9-26-85. The chemical analysis and XPS data are reported in Table 18.

Appendix V: ZSM-5 Synthesis with Mixed Organic Cations

Batch 2-2-85A: 100% TPA Low Sodium System

Sodium aluminate	0.408g
Sodium hydroxide	0.528g
Water	6.439g
Ludox AS-40	33.639g
TPABr	3.388g
Water	10.138g

2.76 Na_2O-Al_2O_3-120 SiO_2-6.80 TPA- 1100H_2O

Temperature: 187°C

Time	Crystallinity (%)
2:00 hrs	10
3:00	55
4:20	74
6:05	98
7:30	100
24:30	100

Batch 2-2-85B: 75% TPA Low Sodium System

Sodium aluminate	0.403g
Sodium hydroxide	0.519g
Water	6.486g
Ludox AS-40	33.287g
TPABr	2.508g
TEABr	0.659g
Water	9.887g

2.75 Na_2O-Al_2O_3-120 SiO_2-5.09 TPA-1.71 TEA-1100 H_2O

Temperature: 187°C

Batch 1-17-85: 50% TPA Low Sodium System

Sodium aluminate	0.440g
Sodium hydroxide	0.628g
Water	9.025g
Ludox AS-40	34.793g
TPABr	1.727g
TEABr	1.356g
Water	9.073g

2.75 Na_2O-Al_2O_3-120 SiO_2-3.50 TPA-3.50 TEA-1081 H_2O

Temperature: 187°C

Time	Crystallinity (%)
3:00 hrs	15
5:00	90 ??
6:00	89
6:30	98
9:30	100
24:00	100

Batch 2-7-85: 25% TPA Low Sodium System

Sodium aluminate	0.720g
Sodium hydroxide	0.972g
Water	12.261g
Ludox AS-40	62.620g
TPABr	1.589g
TEABr	3.759g
Water	15.309g

2.75 Na_2O-Al_2O_3-120 SiO_2-1.80 TPA-5.40 TEA-1100 H_2O

Temperature: 187°C

Time	Crystallinity (%)
3:00 hrs	5
5:15	11
7:00	16
11:30	36
23:30	53
48:45	73
73:00	81
95:00	74
144:30	61

X-ray data reported for this sample is at 144:30 hrs.

Batch 2-05-85II: 75% TPA Low Sodium System

Sodium aluminate	0.455g	
Sodium hydroxide	0.609g	
Water	7.517g	
Ludox AS-40	37.573g	
TPABr	2.997g	
TMAOH	1.372g	(25% in H_2O)
Water	9.936g	

2.82 Na_2O-Al_2O_3-120 SiO_2-5.39 TPA-1.80 TMA-1100 H_2O

Temperature: 187°C

Time	Crystallinity (%)
3:00 hrs	28
4:15	64
6:00	93
9:00	100
22:00	100
46:00	100

Batch 2-5-85I: 50% TPA Low Sodium System

Sodium aluminate	0.476g	
Sodium hydroxide	0.616g	
Water	7.744g	
Ludox AS-40	39.305g	
TPABr	2.093g	
TMAOH	2.880g	(25% in H_2O)
Water	9.434g	

2.75 Na_2O-Al_2O_3-120 SiO_2-3.60 TPA-3.59 TMA-1150 H_2O

Temperature: 187°C

Time	Crystallinity (%)
2:30 hrs	14
4:30	67
5:30	81
6:30	90
9:00	96
22:00	98

Batch 2-11-85: 25% TPA Low Sodium System

Sodium aluminate	0.594g	
Sodium hydroxide	0.788g	
Water	9.920g	
Ludox AS-40	49.038g	
TPABr	1.309g	
TMAOH	5.379g	(25% in H_2O)
Water	10.156g	

2.81 Na_2O-Al_2O_3-120 SiO_2-1.80 TPA-5.41 TMA-1099 H_2O

Temperature: 187°C

Time	Crystallinity (%)
4:00 hrs	12
6:45	31
10:30	22
23:00	64
47:00	72
71:00	--
120:00	81
168:00	78

Note: X-ray data recorded at 71 hours.

Batch 2-12-85: 100% TPA High Sodium System

Sodium aluminate	0.436g
Sodium hydroxide	1.625g
Water	6.936g
Ludox AS-40	36.002g
TPABr	3.835g
Water	10.312g

6.08 Na_2O-Al_2O_3-120 SiO_2-7.20 TPA-1100 H_2O

Temperature: 187°C

Time	Crystallinity (%)
2:45 hrs	14
4:10	62
5:05	88
7:15	100
23:00	100

Batch 2-7-85: 75% TPA High Sodium System

Sodium aluminate	0.500g
Sodium hydroxide	1.835g
Water	7.890g
Ludox AS-40	41.286g
TPABr	3.298g
TEABr	0.868g
Water	11.835g

6.00 Na_2O-Al_2O_3-120 SiO_2-5.40 TPA-1.80 TEA-1100 H_2O

Temperature: 187°C

Batch 2-14-85II: 50% TPA High Sodium System

Sodium aluminate	0.514g
Sodium hydroxide	1.882g
Water	8.098g
Ludox AS-40	42.260g
TPABr	2.206g
TEABr	1.782g
Water	12.228g

5.99 Na_2O-Al_2O_3-120 SiO_2-3.60 TPA-3.60 TEA-1100 H_2O

Temperature: 187°C

Time	Crystallinity (%)
2:15 hrs	27
3:30	97
4:45	85
9:30	100
22:30	100

Batch 2-19-85I: 25% TPA High Sodium System

Sodium aluminate	0.635g
Sodium hydroxide	2.350g
Water	9.999g
Ludox AS-40	52.437g
TPABr	1.396g
TEABr	3.304g
Water	15.044g

6.04 Na_2O-Al_2O_3-120 SiO_2-1.80 TPA-5.40 TEA-1100 H_2O

Temperature: 187°C

Time	Crystallinity (%)
2:05 hrs	8
3:25	26
4:35	43
7:30	100
9:30	100
22:30	100

Batch 2-11-85: 100% TEA High Sodium System

Sodium aluminate	0.719g
Sodium hydroxide	2.639g
Water	11.371g
Ludox AS-40	59.362g
TEABr	5.003g
Water	16.997g

6.00 Na_2O-Al_2O_3-120 SiO_2-7.22 TEA-1100 H_2O

Temperature: 187°C

Time	Crystallinity (%)
5:00 hrs	-0-
23.30	64
34:00	93 ??
49:30	68
70:40	60
94:00	64

Batch 2-17-85: 75% TPA High Sodium System

Sodium aluminate	0.528g	
Sodium hydroxide	1.943g	
Water	8.390g	
Ludox AS-40	43.590g	
TPABr	3.488g	
TMAOH	1.585	(25% in H_2O)
Water	11.252g	

6.01 Na_2O-Al_2O_3-120 SiO_2-5:41 TPA-1:79 TMA-1100 H_2O

Temperature: 187°C

Time	Crystallinity (%)
2:35 hrs	33
3:45	73
4:40	91
20:00	100

Batch 2-18-85I: 50% TPA High Sodium System

Sodium aluminate	0.486g	
Sodium hydroxide	1.786g	
Water	7.688g	
Ludox AS-40	40.126g	
TPABr	2.135g	
TMAOH	2.915g	(25% in H_2O)
Water	11.491g	

6.00 Na_2O-Al_2O_3-120 SiO_2-3.60 TPA-3.59 TEA-1128 H_2O

Temperature: 187°C

Time	Crystallinity (%)
3:10 hrs	32
3:45	66
5:00	91
22:00	100

Batch 2-20-85: 25% TPA High Sodium System

Sodium aluminate	0.673g	
Sodium hydroxide	2.482g	
Water	10.481g	
Ludox AS-40	55.560g	
TMAOH	6.072g	(25% in H_2O)
Water	11.521g	

6.02 Na_2O-Al_2O_3-120 SiO_2-1.80 TPA-5.39 TMA-1100 H_2O

Temperature: 187°C

Time	Crystallinity (%)
3:05 hrs	45-
4:30	35
6:40	40
8:50	41
23:00	68
47:00	84
72:00	96

Appendix VI: Mixed Organic Cation X-ray Data

TABLE 39
MIXED TEMPLATE X-RAY ANALYSIS
LOW SODIUM SAMPLES

ZSM-5		25% TEA		50% TEA		75% TEA	
2-Theta	I/I'	2-Theta	I/I'	2-Theta	I/I'	2-Theta	I/I'
7.80	94	7.80	108	7.80	69	7.80	95
8.70	78	8.70	80	8.65	61	8.70	93
8.95	16	8.90	20	8.95	15	8.95	18
13.10	7	13.10	7	13.05	5	13.05	8
13.75	15	13.80	15	13.80	11	13.80	11
14.70	19	14.70	21	14.65	17	14.65	20
15.40	11	15.45	12	15.40	9	15.40	8
15.80	15	15.80	17	15.85	13	15.80	13
16.40	4	16.40	5	16.40	4	16.45	5
17.60	12	17.65	12	17.55	19	17.55	8
						17.70	10
19.10	7	19.15	6	19.15	6	19.15	8
20.25	10	20.25	7	20.25	6	20.25	6
20.75	15	20.85	17	20.75	17	20.75	16
22.10	5	22.05	5	22.10	6	22.05	6
23.00	100	23.00	100	23.05	100	23.00	100
						23.15	76
23.60	34	23.60	39	23.60	sh	23.65	33
23.80	46	23.80	51	23.80	47	23.80	36
24.30	32	24.25	38	24.30	30	24.30	22
24.70	5	24.65	5	24.65	5	24.65	6
25.50	7	25.40	6	25.40	5	25.50	6
25.80	10	25.80	9	25.80	11	25.80	7
		26.50	11				
				26.65	17		
26.85	12	26.80	13			26.80	12
27.35	5	27.30	8	27.25	6	27.40	6
29.20	13	29.15	13	29.15	13	29.20	13
29.85	17	29.85	16	29.80	17	29.80	16

NOTES:
1) All intensities normalized with respect to peak at 23.00
2) Sh ===> Shoulder
3) All samples calcined

TABLE 40
MIXED TEMPLATE X-RAY ANALYSIS
LOW SODIUM SAMPLES

ZSM-5		25% TMA		50% TMA		75% TMA	
2-Theta	I/I'	2-Theta	I/I'	2-Theta	I/I'	2-Theta	I/I'
7.80	94	7.80	126	7.80	76	7.80	109
8.70	78	8.65	136	8.65	57	8.70	112
8.95	16	8.95	22	9.00	11	8.95	20
13.05	7	13.00	8	13.05	6	13.10	15
13.75	15	13.75	19	13.85	10	13.80	23
						14.10	13
14.70	19	14.65	19	14.85	17	14.70	28
15.40	11	15.40	10	15.45	9	15.40	15
15.80	15	15.75	18	15.85	13	15.80	17
16.35	4	16.45	3	16.45	3	16.40	4
						17.20	13
17.60	12	17.60	24	17.70	13	17.60	23
						18.15	15
19.10	7	19.15	7	19.15	6	19.10	9
20.25	10	20.25	13	20.25	7	20.25	10
20.75	15	20.70	19	20.75	13	20.75	26
22.10	5	22.10	5	22.10	4	22.10	5
23.00	100	23.00	100	23.05	100	23.00	95
						23.10	100
23.60	34	23.60	37	23.60	sh	23.65	53
23.80	46	23.80	49	23.80	46	23.80	58
24.30	32	24.25	30	24.30	30	24.35	30
24.70	5	24.55	6			24.70	4
25.50	7	25.45	8	25.45	6		
25.80	10	25.80	11	25.80	6		
		26.55	12	26.55	11	26.45	56
		26.70	16				
26.85	12			26.85	11	26.80	13
27.35	5	27.40	5			27.40	5
29.20	13	29.20	10	29.20	10	29.25	13
29.85	17	29.85	15	29.85	15	29.75	13

NOTES:
1) All intensities normalized with respect to peak at 23.00
2) Sh ===> Shoulder
3) All samples calcined form

TABLE 41
MIXED TEMPLATE X-RAY ANALYSIS
HIGH SODIUM SAMPLES

25% TEA		50% TEA		75% TEA		100% TEA	
2-Theta	I/I'	2-Theta	I/I'	2-Theta	I/I'	2-THETA	I/I'
7.80	116	7.80	180	7.80	126	7.80	102
8.70	64	8.70	144	8.70	235	8.65	120
9.00	28	8.95	27	8.95	22	8.95	21
						9.70	4
						10.35	9
13.10	9	13.10	12	13.10	11	13.05	11
13.80	17	13.80	22	13.80	19	13.75	14
14.65	26	14.70	31	14.70	21	14.65	23
15.40	12	15.40	16	15.40	9	15.40	11
15.80	17	15.70	24	15.80	18	15.75	20
16.40	4	16.45	5	16.40	4	16.45	5
						17.50	9
		17.65	15	17.70	31	17.70	9
19.10	5	19.15	8	19.15	4	19.15	5
20.20	14	20.25	10	20.25	10	20.20	8
20.70	21	20.75	17	20.75	13	20.75	16
21.65	4					21.45	4
22.05	7	22.10	7	22.10	5	22.10	6
23.00	100	23.05	100	23.05	100	23.00	100
23.10	sh	23.15	92	23.15	86	23.15	77
23.60	39	23.65	37	23.65	33	23.60	42
23.80	56	23.85	52	23.80	48	23.80	50
24.30	32	24.35	31	24.30	28	24.30	23
24.65	7	24.70	4	24.70	4	24.60	4
25.40	7	25.50	6	25.50	5	25.50	5
25.75	9	25.80	8	25.80	7	25.80	11
						26.15	4
26.50	6	26.60	8	26.55	14	26.50	13
26.85	11	26.80	10	26.80	18	26.80	12
27.30	5	27.40	4	27.40	3	27.35	5
						27.95	4
						28.35	4
29.15	11	29.15	10	29.20	11	29.15	12
29.75	18	29.95	15	29.85	13	29.80	13

NOTES:
1) All intensities normalized with respect to peak at 23.00
2) Sh ===> Shoulder
3) All samples calcined
4) 100% TEA sample contained traces of layered silicates, as evidenced by SEM.

TABLE 42
MIXED TEMPLATE X-RAY ANALYSIS
HIGH SODIUM SAMPLES

ZSM-5		25% TMA		50% TMA		75% TMA	
2-Theta	I/I'	2-Theta	I/I'	2-Theta	I/I'	2-Theta	I/I'
7.80	121	7.80	205	7.80	148	7.80	113
8.70	89	8.70	159	8.70	114	8.70	94
8.95	23	8.95	35	8.95	24	8.95	19
13.10	8	13.10	14	13.10	8	13.05	5
13.75	16	13.80	26	13.80	17	13.80	16
14.65	24	14.70	30	14.65	25	14.65	24
15.35	11	15.45	14	15.40	12	15.40	14
15.75	17	15.75	24	15.80	15	15.75	16
16.35	4	16.30	4	16.40	5	16.40	4
17.60	10	17.65	16	17.70	15	17.65	11
19.15	6	19.15	6	19.20	6	19.15	5
20.25	7	20.25	11	20.25	8	20.25	6
20.75	14	20.75	14	20.75	16	20.70	16
21.70	3			21.70	3		
22.10	5	22.05	4	22.10	5	22.10	5
23.00	100	23.00	100	23.00	sh	23.00	100
				23.15	100	23.15	74
23.65	33	23.65	37	23.65	37	23.60	33
23.85	47	23.85	53	23.80	44	23.80	45
24.30	29	24.30	33	24.30	30	24.20	33
24.70	6	24.70	5			24.70	4
25.45	6	25.50	6	25.55	7	25.50	6
25.80	7	25.85	10	25.85	8	25.80	10
26.55	9					26.55	10
26.85	10	26.90	14	26.75	12	26.80	11
27.40	4	27.40	5	27.40	4	27.40	5
29.15	9	29.20	10	29.20	11	29.20	10
29.80	16	29.90	14	29.90	16	29.85	12

NOTES:
1) All intensities normalized with respect to peak at 23.00
2) Sh ===> Shoulder
3) All samples calcined

Appendix VII: Synthesis of Cobalt ZSM-5

Cobalt Amorphous "Seed" Chemical Analysis

Material	Wt% Si	Wt% Al	Wt% Co
5-06-85	20.91	14.72	0.00
5-12-85	14.21	10.33	6.21
7-04-85 I	18.33	14.15	7.40
7-04-85 II	25.64	15.53	1.91
7-04-85 III	26.27	14.90	0.21
7-09-85 II	17.77	9.96	12.89

Batch 7-09-85 II: Cobalt Amorphous

Sodium silicate	31.084	g
$CoCl_2$-$6H_2O$	13.071	g
Water	100	ml
Sodium aluminate	10.670	g
Sodium hydroxide	4.026	
Water	60	ml

$$4.52\ Na_2O\text{-}Al_2O_3\text{-}3.0\ SiO_2\text{-}1.115\ Co\text{-}200\ H_2O$$

Notes: Gel heated for 1 hour at 100°C, following which the contents were cooled and filtered. Following filration, the product was dried at 100°C and sieved to below 70 mesh. The chemical analysis of this material is listed above. The remaining amorphous materials listed above were prepared following a similar procedure.

Batch 7-9-85I: Silicalite

Sodium hydroxide	0.922 g
Water	8.321 g
Ludox AS-40	29.637 g
TPABr	3.158 g
Water	6.058 g

Temperature: 190°C

$2.80Na_2O$-96 SiO_2-5.76 TPABr-880 H_2O

Time (hr)	Crystallinity
2:15	21 %
3:10	63
4:35	100
9:15	100
23:30	100

Notes: Gel very thick. Crystals are euhedral, approximately 25 to 30μ in length. Composition C as referenced in Procedure.

Batch 7-17-85: ZSM-5 (90)

Sodium Aluminate	0.576 g
Sodium hydroxide	1.143 g
Water	6.928 g
Ludox AS-40	35.672 g
TPABr	3.802 g
Water	10.369 g

Temperature: 190°C

$3.70Na_2O$-Al_2O_3-90 SiO_2-5.40 TPABr-826 H_2O

Time (hr)	Crystallinity
2:30	7 %
3:40	46
6:20	86
23:00	100

Note: This is composition D as referenced in Procedure synthesized without cobalt.

Batch 7-7-85II: ZSM-5 from Blank Amorphous

Blank amorphous	0.856 g (5-6-85; 20.9% Si, 14.72% Al)
Sodium hydroxide	1.008 g
Water	6.281 g
Ludox AS-40	32.401 g
TPABr	3.450 g
Water	9.400 g

Temperature: 190°C

$2.72Na_2O$-1.02 Al_2O_3-96 SiO_2-5.59 TPABr-854 H_2O

Time (hr)	Crystallinity
2:00	7 %
3:10	54
4:15	95
7:20	100
21:00	100

Note: This is composition F as referenced in Procedure synthesized without cobalt. Oxygen adosortion isotherm reported in Table 43.

Batch 7-9-85II: Co/ZSM-5 from Amorphous

Cobalt amorphous	0.856 g (7-4-85 III, 0.21 wt% cobalt)
Sodium hydroxide	1.347 g
Water	9.179 g
Ludox AS-40	43.297 g
TPABr	4.610 g
Water	11.890 g

Temperature: 190°C

$2.70Na_2O$-1.03 Al_2O_3-96 SiO_2-5.55 TPABr-850 H_2O-0.0133 Co

Time (hr)	Crystallinity
2:15	2 %
3:10	51
4:35	98
9:15	100
23:30	100

Notes: Amorphous carrier was 26.27 % Si, 14.90% Al and 0.21% cobalt. The cobalt to silica ratio of the product zeolite was 0.00016 while this ratio was 0.00014 for the synthesis gel. Batch synthesized from composition F as referenced in Procedure.

Batch 7-7-85I: Co/ZSM-5 from Amorphous

Cobalt amorphous	1.164 g (7-4-85II; 0.191% Co)
Sodium hydroxide	1.354 g
Water	8.473 g
Ludox AS-40	43.521 g
TPABr	4.636 g
Water	12.623 g

Temperature: 190°C

$2.70Na_2O$-1.07 Al_2O_3-96 SiO_2-5.56 TPABr-849 H_2O-0.120 Co

Time (hr)	Crystallinity
2:00	0 %
3:05	29
4:10	95
7:15	100
21:00	100

Notes: Amorphous material was 25.64% Si, 15.53% Al and 1.91% cobalt. The zeolite Co/Si ratio was 0.0013 while that of the gel was 0.0013. Batch synthesized from composition F as referenced in Procedure.

Batch 7-5-85: Co/ZSM-5 from Amorphous

Cobalt amorphous	1.258 g (7-4-85I, 7.40 wt% cobalt)
Sodium hydroxide	1.465 g
Water	9.132 g
Ludox AS-40	47.089 g
TPABr	5.023 g
Water	13.679 g

Temperature: 190°C

$2.73Na_2O$-0.98 Al_2O_3-96 SiO_2-5.62 TPABr-857 H_2O-0.471 Co

Time (hr)	Crystallinity
1:40	2 %
4:30	98
5:30	100
10:00	100
23:30	100

Notes: Amorphous material was 18.33% Si, 14.15% Al and 7.40% cobalt. Small clumps, possibly cobalt oxide supported on amorphous material, were present. Quantities are small but are visible under a light microscope. The cobalt to silica ratio of the product zeolite was 0.0044 while that of the gell was 0.0049. This material was synthesized from composition F as referenced in procedure.

Batch 7-17-85II: Co/ZSM-5 from Amorphous

Cobalt amorphous	1.348 g (7-9-85II; 12.89% Co)
Sodium hydroxide	1.358 g
Water	13.470 g
Ludox AS-40	43.654 g
TPABr	4.650 g
Water	7.698 g

Temperature: 190°C

$2.77Na_2O$-0.81 Al_2O_3-96 SiO_2-5.70 TPABr-870 H_2O-0.96 Co

Time (hr)	Crystallinity
2:30	8 %
3:40	81
5:50	94
23:00	96

Notes: Amorphous material was 17.77% Si, 9.96% Al and 12.89% cobalt. The Co/Si ratio of the synthesis gel was 0.010. Dark clumps of amorphous particles were present, more than in the case of batch 4-16-85. Crystals were dark but turned blue upon drying. Batch synthesized from composition F as reported in Procedure.

Batch 8-29-85: Co/ZSM-5 from Amorphous

Cobalt amorphous	0.632 g (7-9-85II, 12.89 wt% cobalt)
Sodium aluminate	0.493 g
Sodium hydroxide	1.673 g
Water	4.541 g
Ludox AS-40	23.749 g
TPABr	2.529 g
Water	6.550 g

Temperature: 190°C

$5.52Na_2O$-Al_2O_3-70 SiO_2-4.20 TPABr-643 H_2O-0.611 Co

Note: Cobalt to silica ratio of gel was 0.0087 while that of the product crystal was 0.0085. This batch was synthesized from composition I and the XPS and chemical analysis data are reported in Table 21.

Batch 8-2-85: Co/ZSM-5 from Amorphous

Cobalt amorphous	0.741 g (7-9-85II, 12.89 wt% cobalt)
Sodium aluminate	1.055 g
Sodium hydroxide	3.477 g
Water	9.515 g
Ludox AS-40	50.814 g
TPABr	5.411 g
Water	14.180 g

Temperature: 190°C

$5.49Na_2O$-Al_2O_3-70 SiO_2-4.20 TPABr-642 H_2O-0.335 Co

Notes: Vessels removed following 30 hours at 190°C. No dark clumps were visible under the light microscope. Crystals light (powder) blue in color. Crystals approximately 5μ in size, appear somewhat spherical. The gel Co/Si ratio was 0.0048 while that of the product zeolite was 0.0046. This batch was synthesized from composition I as referenced in Procedure. The XPS and chemical analysis of the product crystals are reported in Table 21. This material was also employed as a catalyst in run 9-1-85. Oxygen adsorption isotherm reported in Table 43.

Batch 8-5-85: Co/ZSM-5 from Amorphous

Cobalt amorphous	0.593 g (7-9-85II, 12.89 wt% cobalt)
Sodium aluminate	0.759 g
Sodium hydroxide	1.114 g
Water	7.546 g
Ludox AS-40	36.559 g
TPABr	3.891 g
Water	10.196 g

Temperature: 190°C

$3.00Na_2O$-Al_2O_3-70 SiO_2-4.20 TPABr-642 H_2O-0.378 Co

Notes: Vessels removed from oven following 48 hours at 190°C. Small traces of amorphous particles were still present with the product crystals (about 5%). Dark clumps also present. For this batch, the Co/Si ratio was 0.0053 while the ratio of the product zeolite was 0.0047. This batch was synthesized from composition H and the XPS and chemical analysis data are reported in Table 21.

Batch 4-10-85: Co/ZSM-5 from Amorphous

Cobalt amorphous	0.544 g (12.20 wt% cobalt)
Sodium hydroxide	1.106 g
Water	13.419 g
Ludox AS-40	35.546 g
TPABr	3.785 g
Water	3.816 g

Temperature: 190°C

$2.79Na_2O$-0.434 Al_2O_3-96 SiO_2-5.73 TPABr-886 H_2O-0.456 Co

Notes: Vessels removed following 24 hours at 190°C. Slight trace of amorphous particles also present. Crystals less than 10μ in size, very uniform with slight amount of twinning. The gel Co/Si ratio was 0.0048 while that of the product zeolite was 0.0048. This batch was synthesized from composition F as referenced in Procedure. The XPS and chemical analysis of the product crystals are reported in Table 21. The amorphous material employed in this synthesis was 14.02% Si, 10.70% Al and 12.20% Si as determined by atomic absorption. Oxygen adsorption isotherm reported in Table 43.

Batch 4-16-85: Co/ZSM-5 from Amorphous

Cobalt amorphous	0.965 g (12.20 wt% cobalt)
Sodium hydroxide	1.130 g
Water	7.039 g
Ludox AS-40	36.320 g
TPABr	3.862 g
Water	10.539 g

Temperature: 190°C

$2.77Na_2O$-0.75 Al_2O_3-96 SiO_2-5.70 TPABr-872 H_2O-0.777 Co

Notes: Crystals appear complete following 24 hours at 190°C. Crystals very uniform with slight amount of penetration twinning. Crystals about 7μ in length. The cobalt to silica ratio of the final zeolite was 0.0083 while that of the product zeolite was found to be 0.0082. The amorphous material employed in this study was 14.02% Si, 10.70% Al and 12.20% cobalt. This material was synthesized from composition F and the XPS and chemical analysis results are reported in Table 21. Electron microprobe images are shown in Figure 72. Following synthesis, this material was washed with a 5-7% HCl solution for 3 hours at room temperature. The coblat to silica ratio of the zeolite following this treatment was 0.0025. Thus, only 30% of the cobalt remained with the crystal. Oxygen adsorption isotherm reported in Table 43.

Batch 5-19-85b: Co/ZSM-5 from Amorphous

Cobalt amorphous	0.048 g (5-12-85; 6.21 wt% cobalt)
Sodium hydroxide	0.948 g
Water	6.097 g
Ludox AS-40	30.474 g
TPABr	3.247 g
Water	8.682 g

Temperature: 190°C

$2.80Na_2O$-0.043 Al_2O_3-96 SiO_2-5.76 TPABr-880 H_2O-0.024 Co

Notes: Crystallization complete following 18 hours at 190°C. Crystals euhedral, approximately 25 to 30μ in length. The gel cobalt to silica ratio was 0.00025 while that of the product zeolite was 0.00028. This batch was synthesized from composition F and the metal recovery data were plotted in Figure 68.

Batch 5-20-85I: Co/ZSM-5 from Amorphous

Cobalt amorphous	0.228 g (5-12-85; 6.21% Co)
Sodium hydroxide	0.942 g
Water	6.199 g
Ludox AS-40	30.279 g
TPABr	3.266 g
Water	8.473 g

Temperature: 190°C

$2.80Na_2O$-0.21 Al_2O_3-96 SiO_2-5.60 TPABr-880 H_2O-0.114 Co

Notes: Crystallization complete following 22.5 hours at 190°C. Crystals approximately 25-30μ with penetration twin. The gel Co/Si ratio was 0.0012 while that of the product zeolite was 0.00085. This batch was synthesized from composition F. Cobalt recovery data was plotted in Figure 68.

Batch 5-20-85Ii: Co/ZSM-5 from Amorphous

Cobalt amorphous	0.461 g (5-12-85; 6.21 wt% cobalt)
Sodium hydroxide	0.936 g
Water	5.837 g
Ludox AS-40	30.086 g
TPABr	3.204 g
Water	8.748 g

Temperature: 190°C

$2.80Na_2O$-0.422 Al_2O_3-96 SiO_2-5.76 TPABr-880 H_2O-0.228 Co

Notes: Crystallization complete following 22 hours at 190°C. Crystals euhedral, approximately 20 by 20μ. These crystals are smaller than those synthesized from batch 5-20-85I. The gel cobalt to silica ratio was 0.0024 while that of the product zeolite was 0.0023. This batch was synthesized from composition F and the metal recovery data were plotted in Figure 68.

Batch 5-21-85: Co/ZSM-5 from Amorphous

Cobalt amorphous	1.133 g (5-12-85; 6.21% Co)
Sodium hydroxide	1.278 g
Water	7.998 g
Ludox AS-40	41.075 g
TPABr	4.378 g
Water	11.906 g

Temperature: 190°C

$2.80Na_2O$-0.762 Al_2O_3-96 SiO_2-5.76 TPABr-880 H_2O-0.419 Co

Notes: Crystals complete following 21 hours at 190°C. Crystals about 5-10μ in length, euhedral and very uniform. A very small amount of cobalt clumps are present. The gel phase cobalt to silica ratio was 0.0044 while that of the product zeolite was 0.0046. This batch was synthesized from composition F and the cobalt utilization data is plotted in Figure 68.

Batch 7-22-85I: Co/ZSM-5 from Amorphous

Cobalt amorphous	0.534 g (7-9-85II; 12.89 wt% cobalt)
Sodium hydroxide	2.076 g
Water	8.332 g
Ludox AS-40	36.498 g
TPABr	3.888 g
Water	8.886 g

Temperature: 190°C

$5.19Na_2O$-0.777 Al_2O_3-96 SiO_2-5.76 TPABr-880 H_2O-0.461 Co

Notes: Crystallization complete following 22 hours at 190°C. Crystals spherical, approximately 7-10μ in size. The gel cobalt to silica ratio was 0.0048 while that of the product zeolite was 0.0046. This batch was synthesized from composition G and the XPS and chemical analysis data are reported in Table 21.

Batch 9-2-85: Co/ZSM-5 from $CoCl_2$-$6H_2O$

Sodium aluminate	0.532 g
Sodium hydroxide	1.749 g
Water	4.789 g
Ludox AS-40	25.626 g
TPABr	2.733 g
Water	7.247 g
$CoCl_2$-$6H_2O$	0.195 g

Temperature: 190°C

$5.48Na_2O$-Al_2O_3-70 SiO_2-4.21 TPABr-644 H_2O-0.336 Co

Notes: Vessels removed following 48 hours at 190°C. Crystallization approximately 85 to 90% complete. No further evidence of crystal growth following 24 hours. Crystals deep blue in color, much deeper than 8-2-85 (same composition but different cobalt source). The cobalt to silica ratio of the gel was 0.0048 while that of the product crystal was also 0.0048. This batch was crystallized according to composition E, and the XPS and chemical analysis data are reported in Table 21.

Batch 7-15-85I: Co/ZSM-5 from $CoCl_2$-$6H_2O$

Sodium hydroxide	1.071 g
Water	6.669 g
Ludox AS-40	34.429 g
TPABr	3.672 g
Water	9.998 g
$CoCl_2$-$6H_2O$	0.263 g

Temperature: 190°C

$2.80Na_2O$-Al_2O_3-96 SiO_2-5.77 TPABr-880 H_2O-0.462 Co

Time (hr)	Crystallinity
2:30	23 %
3:40	52
6:00	90
9:30	95
22:00	95

Notes: Amorphous particle present following 22 hours, and there did not appear to be a decrease in particle concentration when compared to the 9:30 sample. The cobalt ot silica ratio of the gel was 0.0048 while that of the product zeolite was 0.0048. This batch was synthesized from composition C and the XPS and chemical analysis data are presented in Table 21.

Batch 7-15-85II: Co/ZSM-5 from $CoCl_2$-$6H_2O$

Sodium aluminate	0.893 g
Sodium hydroxide	1.667 g
Water	10.055 g
Ludox AS-40	51.959 g
TPABr	5.900 g
Water	15.085 g
$CoCl_2$-$6H_2O$	0.393 g

Temperature: 190°C

$3.71Na_2O$-Al_2O_3-90 SiO_2-5.76 TPABr-825 H_2O-0.429 Co

Time (hr)	Crystallinity
2:30	5 %
5:30	63
9:00	82
33:30	87
44:30	84

Notes: Crystals appeared covered with an amorphous layer. Amorphous particles also present. Crystals very deep blue in color. The cobalt to silica ratio of the synthesis gel was 0.0048 while that of the zeolite was 0.0049. This batch was prepared according to composition D, and the XPS and chemical analysis data are reported in Table 21.

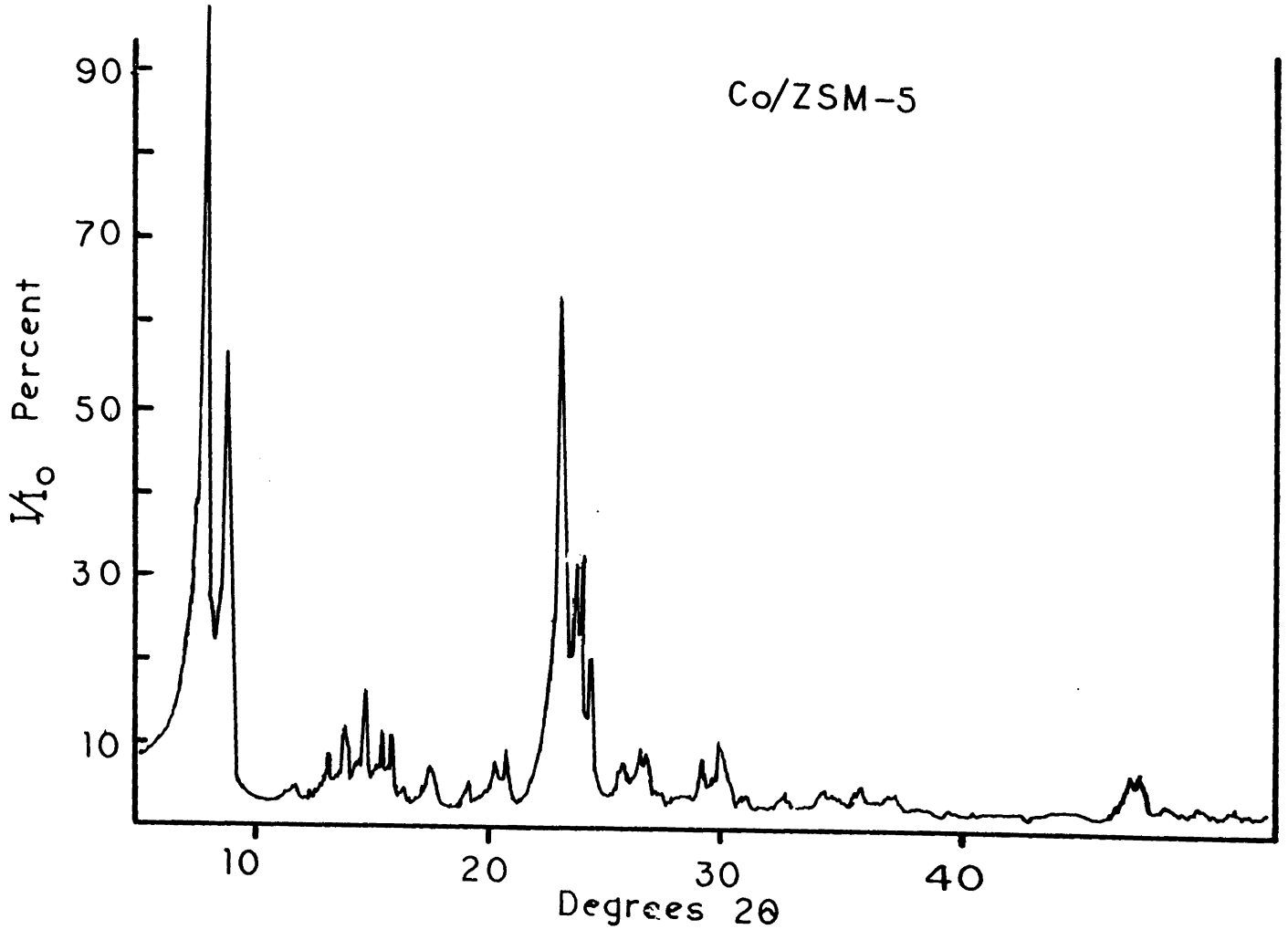

Figure 97: X-Ray Diffraction Pattern of Co/ZSM-5 (Batch 8-2-85)

Table 43

Oxygen Adsorption Isotherms: Co/ZSM-5

Batch 7-7II-85	197.6 Mg	Batch 4-10-85	101.1 mg
Pressure	$cm^3/100g$-Z	Pressure	$cm^3/100g$-Z
>2 torr	10.22	>2 torr	12.89
28	16.52	12	16.28
72	17.26	68	17.66
100	17.46	100	17.82
Purity: 97%		Purity: 99%	

Batch 4-16-85	197.6 Mg	Batch 8-2-85	101.1 mg
Pressure	$cm^3/100g$-Z	Pressure	$cm^3/100g$-Z
>2 torr	12.42	>2 torr	11.86
21	16.14	18	15.46
67	17.07	70	17.23
99	17.18	101	17.41
Purity: 95%		Purity: 97%	

Note: Purity based on pore volume of $18.0cm^3/100g$-Z at 100 torr.

Appendix VIII: Purchasing Information

Tantalum tubing: Rick Stevens
C/O Tevo Indurstries
(216) 425-3505

LUDOX: DuPont
C/O Marcella Jacobs
(302) 999-3926
Ask for sample (free)

Catapal SB Alumina: Vista Chemical Company
C/O Duane Lewis
(405) 767-2763
Ask for sample (free)

Mass Flow Meter: Dynamations, Inc.
C/O Dave Jewett, III
P. O. Box 3191
Richmond, VA 23235
(804) 794-7667

Appendix IX: MMD1 Program Listing

Line	Address
000	076 001
002	323 000
004	315 061 003
007	076 000
011	323 000
013	036 044
015	315 061 003
020	035
021	302 015 003
024	076 002
026	323 000
030	315 061 003
033	076 000
035	323 000
037	076 002
041	036 300
043	315 061 003
046	035
047	302 043 003
052	075
053	302 041 003
056	303 000 003
061	006
063	315 073 003
066	005
067	302 063 003
072	311
073	016 035
075	026 177
077	025
100	302 077 003
103	015
104	302 075 003
107	311
110	000
111	000

Note: the sample time may be varied by changing line 40 as Follows:

Time	Address
:35 hr	002
:51	003
1:07	004
1:23	005
1:39	006
1:55	007

As the program is written, it will delay 10 seconds before activating the sampling valve. The valve will then sample, holding that position for three minutes, followed by returning to the inactive position until simpling is again required.

Appendix X: Rhodium Elution Calibration

A 10 µg/ℓ solution of Rh/2N HCl/1N $SnCl_2$ was prepared for calibration of rhodium by UV visible spectroscopy. Preparation of this solution involved dissolving 0.0242g of $RhCl_3$-$3H_2O$ in 100 mℓ of 2N HCl. 5 mℓ of this solution was added to 5 mℓ concentrated HCl and 10 mℓ 1N $SnCl_2$ solution. The resulting solution was heated on a hot plate under agitation for 30 minutes, followed by cooling to room temperatre. 5 mℓ of 1N $SnCl_2$ solution was then added, and the contents brought to 50 mℓ through addition of 2N HCl. Similar solutions were prepared of 8, 5, 3 and 1 µg/ℓ. These solutions served to calibrate the UV for the rhodium elution experiments. The calibration data are presented below.

µg/ℓ	Absorbance
10	0.355
8	0.275
5	0.173
3	0.105
1	0.038

Appendix XI: Details of Fischer-Tropsch Runs

Run 9-26-86: RuCa A

Catalyst: 1.753g (40-70 mesh), 2.16 wt% Ru

Dry: 1.5 hours at 125°C
Reduction: 14 hours at 275°C
20 psig H_2; 30 ml/Min

Reaction: 21.5 hours at 255°C
15 psig, 10.5 ml/Min CO/H_2 (1/1)

Run 9-26-86: RuCa A

Catalyst: 1.753g (40-70 mesh), 1.53 wt% Ru

Dry: 2.0 hours at 125°C
Reduction: 14 hours at 275°C
20 psig H_2; 25 ml/Min

Reaction: 21.0 hours at 255°C
15 psig, 6.5 ml/Min CO/H_2 (1/1)

25.5 hours at 308°C
80 psig, 10.5 ml/Min CO/H_2 (1/1)

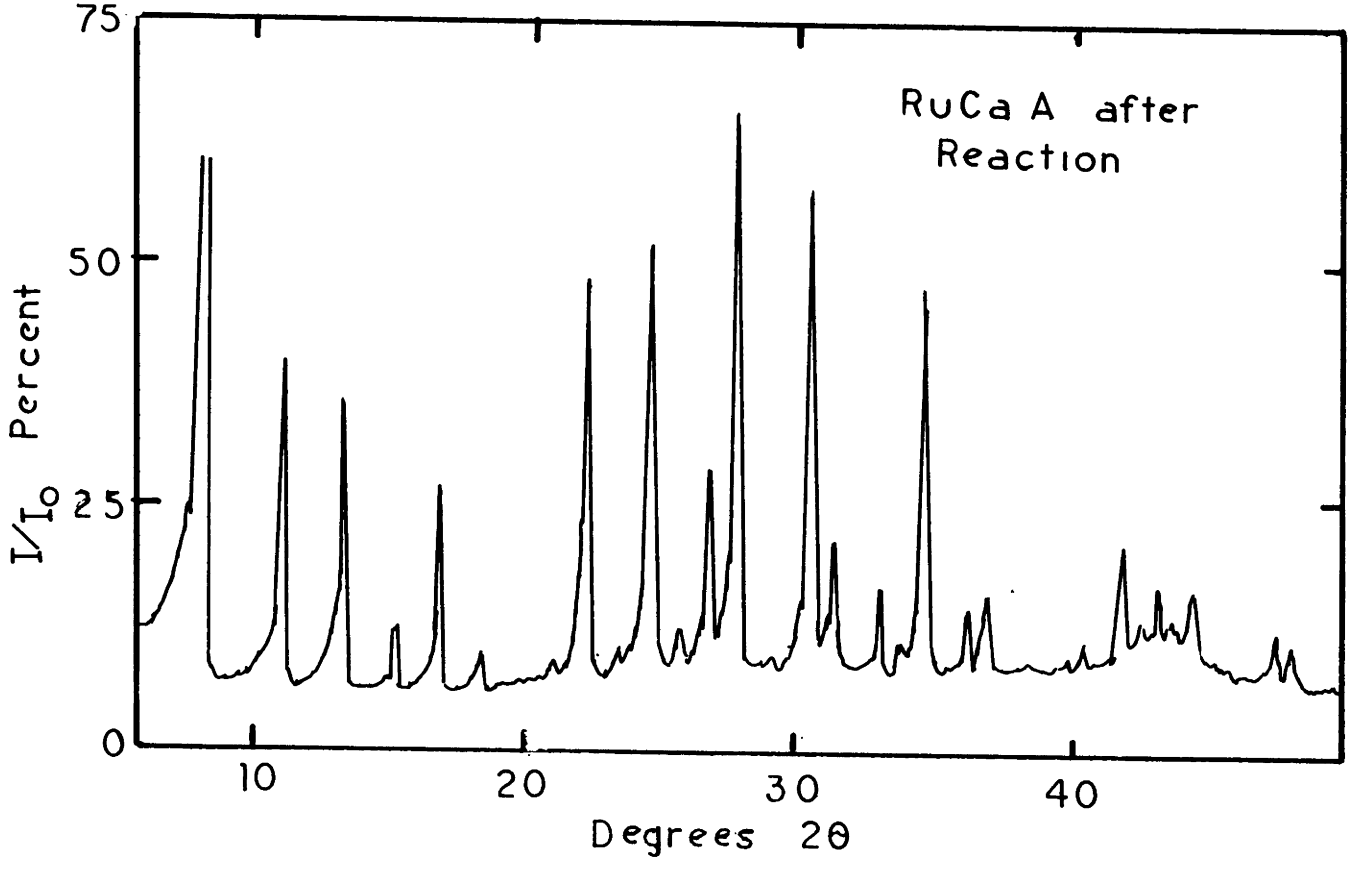

Figure 98: X-ray Diffraction Pattern of 2.16% RuCa A Following Run 9-26-85.

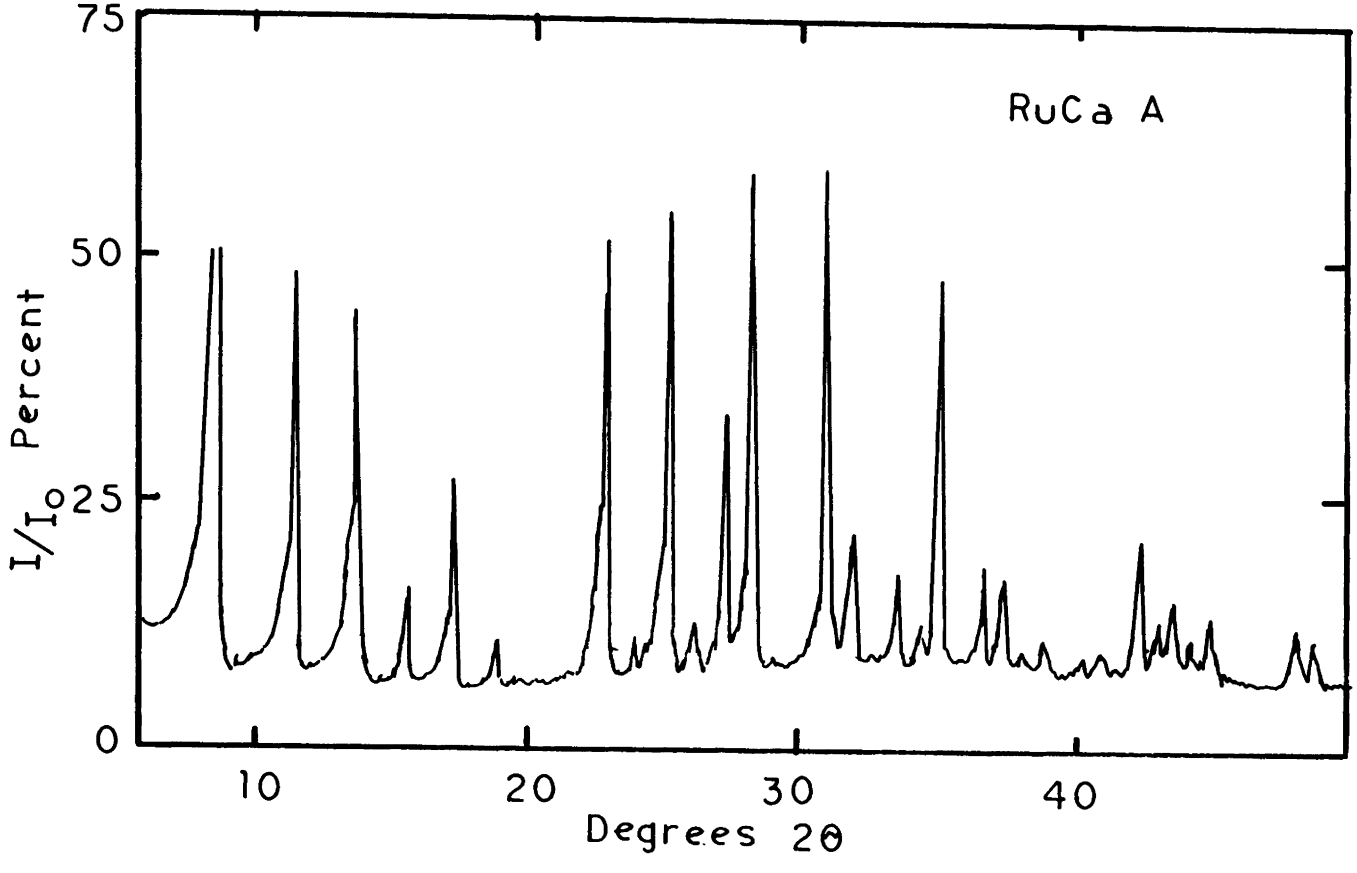

Figure 99: X-ray Diffraction Pattern of RuCa A.

Run 9-1-86: Co/ZSM-5

Catalyst: 1.60g 0.48 wt% Co (catalyst added as powder)
Batch 8-2-85

Dry: 1.0 hours at 125°C
Reduction: 21 hours at 470°C
30 psig H_2; 13 ml/Min (maximum flow through bed)

Reaction: 300 psig, 10.0 ml/Min CO/H_2 (1/1)
300°C for 6.5 hours
350°C for 13 hours
410°C for 22 hours
470°C for 16.5 hours

Run 9-16-85

Catalyst: 1.64g 0.56 wt% Co (catalyst added as powder)
Catalyst prepared by cation exchange.

Dry: 1.0 hours at 125°C
Reduction: 20 hours at 470°C
30 psig H_2; 15 ml/Min

Reaction: 300 psig, 10.0 ml/Min CO/H_2 (1/1)
235°C for 25 hours
300°C for 9 hours
350°C for 17.5 hours
410°C for 20 hours
470°C for 14 hours

Reactor Notes

1) Following approximately 4 months of operation at both low and high temperature, the Tantalum reactor became brittle and broke. This may indicate that the tantalum, although totally inert to CO/H_2 (in a reaction scence), is not the ideal reactor material choice.

Appendix XII: Calculation of Conversion for Fischer-Tropsch Reactions

The concentration of carbon monoxide in the product stream could not be accurately determined. Because of this, conversion of CO had to be estimated indirectly from the hydrocarbon concentration of the output stream and the stoichiometry of the reaction. This estimation was performed as follows:

Assume a basis of 500,000 units of CO fed into the reactor (inlet stream 50/50 CO/H_2). All hydrocarbon concentrations were measured in ppm. The reaction stoichiometry was assumed in all cases to be:

$$CO + H_2 = -CH_2- + H_2O$$

From this, the concentration of CO in the product stream was estimated to from:

$$(10^6 - \Sigma[\text{ppm of } C(n)]/2 = \text{ppm CO in product stream} \qquad (1)$$

Since 500,000 units of CO enter the reactor, 500,ooo units must also exit. To account for the volume change during the reaction:

$$CO(out) + \Sigma n^*[\text{ppm of } C(n)]/500{,}000 = f^{-1} \qquad (2)$$

The conversion is then:

$$f^*\Sigma n^*[\text{ppm of } C(n)]/500{,}000 \qquad (3)$$

The following example will illustrate these calculations and serve to evaluate the accuracy of the assumptions:

Assume that 500,000 units of each CO, H_2 enter the reactor. 20,000 units each of CO are converted to methane, ethylene and 1-butene. The product stream is as follows:

	Units	PPM	
CO	440,000	491,621	
Hydrogen	360,000	402,235	
Methane	20,000	22,346	measured
Ethylene	10,000	11,173	measured
1-butene	5,000	5,587	measured
water	60,000	67,039	
	------	------	
Total	895,000	1,000,000	

Based on the lumped reaction stoichiometry, 50% of the non-hydrocarbons present in the product stream is calculated to be 480,447 units of CO. The atoms of carbon in the product stream can be determined from

$$C \text{ (product)} = CO + \Sigma n^*[C(n)] = 547{,}487 \text{ units}$$

Since only 500,000 units enter, the correction factor becomes 0.9137. Thus, from eq. 3, the conversion would be estimated at 12.24%. This is a 2% error, as the actual conversion in this example was 12%.

Appendix XIII: GC Calibration

Both the capillary and packed gas chromatographs were calibrated in terms of gas phase concentration, ppm. Calibration was accomplished through the use of analyzed gases purchased from Scott Chemical Company. The composition of these gases is listed in Table 46. Response factors were determined for CO, CO_2 and light hydorcarbons (C_1 through C_6). For the packed column gas chromatograph, the gas phase concentration of CO and C&sub2, hydrocarbons were determined from the following equation:

(Integrated area)*(factor) = Concentration (ppm)

Factor = 0.6455 for $CO_2$and 0.5845 for C_2

The packed column was used to determine only the concentration of CO_2 and C_2. Methane could not be determined due to the signal being swamped by the CO signal. Hydrocarbons of C_3 and above were analyzed based on signals from the capillary chromatograph. The packed column GC was also used to determine the relative fractions of propylene, propane and propyne.

The gas phase concentration of all remaining hydrocarbons was determined using the capillary GC from the equation:

Gas phase concentration (ppm) = Area/(N*factor)

where N is the hydrocarbon chain length. For methane, the reponse factor was 7.4082, while for all other hydrocarbons, the reponse factor was determined to be 8.7422. It should be stressed that these response factors are only valid when the flow through the column splitter is 25.7 ml/min. This flow rate was periodically checked and adjusted as required. Also, approximately, every 1 month, the calibration was re-checked.

Appendix XIV: Chromatograph Retention Times

Chromatograph retention times for hydrocarbons of C_4 and below were determined by gas injections. Retention times for hydrocarbons above C_4 were determined by liquid injections. Results are reported in Tables 44 and 45.

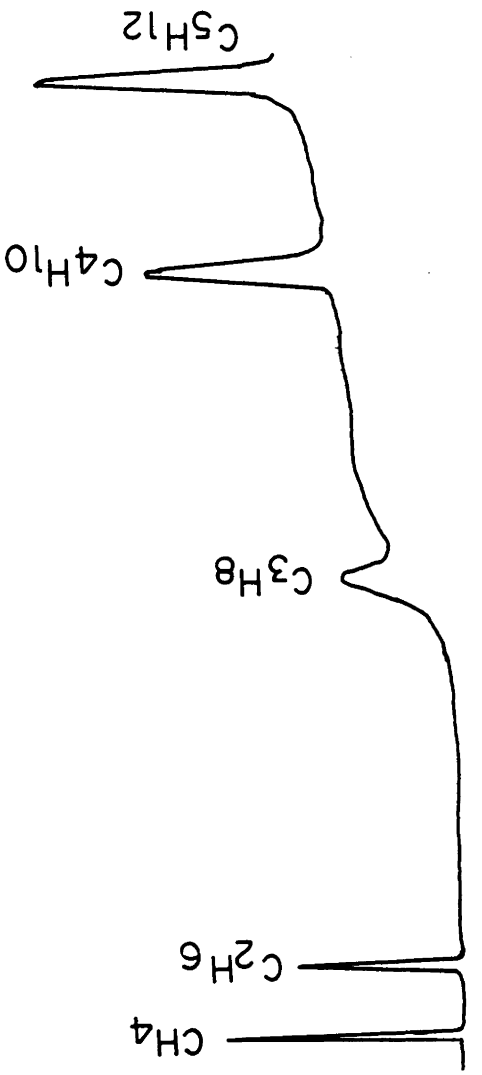

Figure 100: GC Calibration Trace of Light Hydrocarbons (Packed Column).

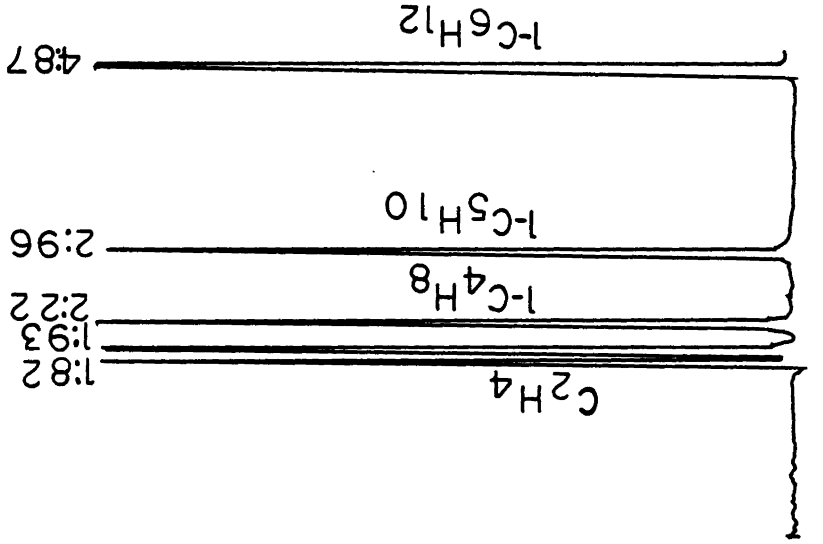

Figure 101: GC Calibration Trace of Light Hydrocarbons (Capillary Column).

Table 44
RETENTION TIMES: CAPILARY COLUMN

30 meter by 0.25mm, 1.0µ SPB-5 fused silica column (supelco)

Time 1: 9:00
Temp 1: 40 C
Rate: 12 C/min
Temp 2: 165 C

Methane:	1:76
Ethane:	1:76
ethylene:	1:76
Propane:	1:93
Propyene:	1:93
Methanol:	2:18
1-butene:	2:22
Butane:	2:31
c,t 2-butene:	2:40
1-pentene:	2:95
Pentane:	3:05
t 2-pentene:	3:18
c 2-pentene:	3:29
1-hexene:	4:85
hexane:	5:11
t 2-hexene:	5:34
c 2-hexene:	5:69
Benzene:	8:00
1-heptene:	9:62
heptane:	10:12
t 2-heptene:	10:53
c 2-heptene:	10:97
Toluene:	13:26
1-octene:	14:00
octane:	14.28
t 2-octene	14:49
c 2-octene:	14:75
p-xylene:	16:17
Ethylbenzene:	16:28
m-xylene:	16:37
1-nonene:	16:80
o-xylene:	16:99
Nonane:	17:00
t 2-nonene:	17:13
c 2-nonene:	17:34
1-decene:	18:93
decane:	19:08
t 2-decene:	19:19
c 2-decene:	19:37
Durene:	21:67

Table 45
Retention Times for Packed column

3 feet by 1/8 inch Porapak Q column[1]

Time 1:	6:00
Temp 1:	40 C
Rate:	12 C/min
Temp 2:	165 C
Flow:	25 ml/min, 23 ml/min reference column
Pressure:	20 psig
Current:	225 mA
Sample:	500 µℓ

Methane	0:37
Carbon Dioxide	0:74
Ethtlene	1:08
Ethane	1:37
Propylene	7:00
Propane	7:75
1-butene	12:30
n-butane	12:60
1-pentene	15:40
n-pentane	15:75

[1] Tubing used for this column is a special high grade 316 stainless steel purchased from Supelco.

Table 46
Analyzed Gas Compositions

Gas	Concenrtation (ppm)	Gas	Concentration (ppm)
Ethylene	993.4	Methane	1002
Propylene	1003	Ethane	1108
1-butene	881.5	Propane	1057
1-pentene	1074	n-butane	1047
1-hexene	1115	n-pentane	1036
		n-hexane	1085

Gas	Volume Percent
CO	5.0241
CO_2	4.9999
N_2	5.0058
O_2	5.0006
CH_4	3.9981
H_2	3.9984

Note: all gases diluted in helium

The vita has been removed from the scanned document